
**THEORETICAL PREDICTION FOR PROBING MAGNON
TOPOLOGY**

Dissertation

zur Erlangung des Doktorgrades der Naturwissenschaften
(Dr. rer. nat.)

der

Naturwissenschaftlichen Fakultät II
Chemie, Physik und Mathematik

der

Martin-Luther-Universität
Halle-Wittenberg

vorgelegt von

Herrn Robin Richard Neumann

Erstgutachterin: Prof. Dr. Ingrid Mertig
Zweitgutachter: Prof. Dr. Steffen Trimper
Drittgutachter: Prof. Dr. Piet Brouwer

Tag der Eröffnung des Promotionsverfahrens: 22.05.2024
Tag der öffentlichen Verteidigung: 23.10.2024
Vorsitzender der Promotionskommission: Prof. Dr. Detlef Reichert

ABSTRACT

In this thesis, potential hallmarks of topological magnons in macroscopic observables of magnetic insulators are investigated. The magnon band structure for various models of two-dimensional ferromagnets, collinear and noncollinear antiferromagnets are characterized for their topological properties. The signatures of magnetic and topological phase transitions in the thermal HALL effect of magnons are analyzed in collinear antiferromagnets. On the basis of experimental data for the collinear antiferromagnet $\text{Na}_2\text{Co}_2\text{TeO}_6$, the magnon transport theory is validated and extended to include magnon polarons. The extended theory explains important qualitative features of the transport measurements highlighting the importance of magnon polarons in the thermal HALL effect. Beyond the study of transport properties, the electric dipole moment of topological magnons is predicted, which causes an electric edge polarization in topological magnon insulators in equilibrium. Despite their charge neutrality, topological magnons are shown to respond to alternating electric fields rendering them electrically active. Those *topological electromagnons* are predicted to bring about unique footprints in the electrical absorption spectra at THz frequencies.

In dieser Doktorarbeit werden mögliche Kennzeichen von topologischen Magnonen in makroskopischen Observablen von magnetischen Isolatoren untersucht. Dabei werden die Magnonenbandstrukturen für verschiedene Modelle von Ferromagneten, kollinearen und nichtkollinearen Antiferromagneten nach deren topologischen Eigenschaften charakterisiert. In kollinearen Antiferromagneten werden die Signaturen von magnetischen und topologischen Phasenübergängen im thermischen HALL-Effekt von Magnonen identifiziert. Anhand experimenteller Daten für den kollinearen Antiferromagneten $\text{Na}_2\text{Co}_2\text{TeO}_6$ wird die Magnontransporttheorie überprüft und um Magnonpolaronen erweitert. Die erweiterte Theorie hebt die Bedeutung von Magnonpolaronen im thermischen Transport hervor, indem sie wichtige qualitative Merkmale der Transportmessungen mit ihrer Hilfe zu erklären vermag. Über die Transporteigenschaften hinaus wird ein elektrisches Dipolmoment von topologischen Magnonen vorhergesagt, das sich in einer elektrischen Randpolarisation in topologischen Magnonenisolatoren äußert. Es wird demonstriert, dass topologische Magnonen trotz ihrer Ladungsneutralität mit elektrischen Feldern wechselwirken und somit elektrisch aktiv sind. Insbesondere wird vorhergesagt, dass diese *topologischen Elektromagnonen* oszillierende elektrische Felder absorbieren, wodurch sie in der Terahertz-Spektroskopie in Erscheinung treten.

CONTENTS

1	Introduction	1
2	Quantum Theory of Magnetic Solids	5
2.1	Born-Oppenheimer Approximation	6
2.2	Theory of Lattice Excitations: Phonons	8
2.3	Theory of Spin Excitations: Magnons	21
2.4	Theory of Spin-Lattice Excitations: Magnon Polarons	36
3	Band Topology of Bosonic Quasiparticles	43
3.1	Adiabatic Time Evolution	43
3.2	Geometric Concepts in Band Structure Theory	46
3.3	Chern Insulators and Chiral Edge States	51
4	Linear Response Theory	57
4.1	General Kubo Formula	58
4.2	Statistical Forces	61
4.3	Intrinsic Thermal Hall Conductivity	63
5	Magnetoelectric Effects	69
5.1	Vacuum Magnetoelectric Effect	70
5.2	Exchange Striction Model	71
5.3	Spin Current Model	73
5.4	Spin-Dependent p - d Hybridization Model	75
6	Publications	77
6.1	Orbital Magnetic Moment of Magnons	77
6.2	Thermal Hall Effect in Magnetic Insulators	87
6.3	Electrical Activity of Topological Magnons	105
7	Conclusion and Outlook	113
8	List of Publications	115

INTRODUCTION

Are insulators always insulating? It is well known that the quintessential distinction between a metal and an insulator are band gaps in the electronic structure [1, 2].¹ If a material exhibits fully occupied bands and a nonzero energy gap between the occupied and unoccupied states, it does not conduct charge currents. However, in certain materials, the band gap exists only in their bulk and vanishes at the surface, where edge states appear. Those edge states cannot exist with nor without the bulk. On the one hand, they cannot exist with the bulk because they are localized at the edges and do not exist in infinite systems. On the other hand, they cannot exist without the bulk because their existence is determined by the bulk band structure and does not depend on the details of the edges. In particular, it is the existence of the bulk band gap, which implies the existence of the edge states. Consequently, the edge states are robust with respect to distortions of the lattice, impurities, and other perturbations as long as the bulk band gap remains stable. Since the existence of the edge states does not depend on geometrical details, they are considered to be *topologically protected*.

The topologically protected edge states of such an insulator, called *topological insulator*, allow for a unique transport signature – the quantum (anomalous) HALL effect [3–5].² In response to an applied longitudinal electric field, a transverse current flows. The transverse conductivity is quantized depending on the number of edge states [6–9]. The first experimental observation has been reported by KLAUS VON KLITZING [6], who was awarded the NOBEL Prize in 1985 for his discovery. Hence, some insulators are not insulating.

This work occupies itself with analogous topological phases of magnetic insulators, in which electrons are bound to the atomic nuclei. Although electrons themselves cannot conduct charge, heat, or spin, their spins interact with each other giving rise to collective spin excitations – the magnons. Magnons are bosonic quasiparticles that quantize spin waves [10–12]. Because of the mutual interactions of the electrons’ spins, the dynamics of one spin incites the dynamics of surrounding spins, thereby forming spin waves. Similar to electrons, magnons can feature topological gaps in their band structure that entail magnonic edge states [13–21]. These *topological magnon insulators* have been predicted in 2013 by ZHANG *et al.* [14] and SHINDOU *et al.* [15], however, no conclusive experiment has been conducted that proves their existence to date.

There are several complications compared to electrons. While the quantum (anomalous) HALL effect serves as a reliable footprint for topological edge states of electrons, magnons generally do not exhibit quantized transport coefficients. Firstly, magnons correspond to *excitations* of the magnetic ground state. They do not exist at zero temperature for their creation warrants finite energies. Electrons, on the other hand, may occupy different states at nonzero temperatures, but exist already in the ground state. Secondly, magnons are bosons and, as such, do not have a FERMI level. Magnons are generated

¹Here, I confine myself to band insulators.

²More specifically, I refer to CHERN insulators, which host chiral edge states.

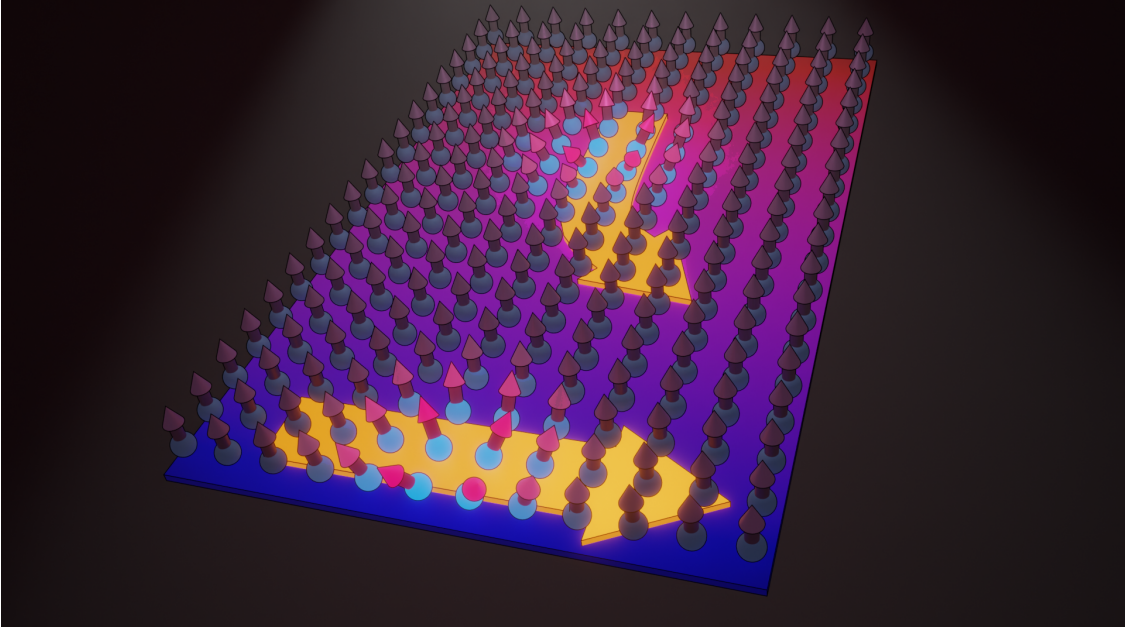


Figure 1.1: Transverse magnon transport in a temperature gradient by bulk and edge states. As an example, the thermal HALL effect denotes the transverse heat transport in a temperature gradient.

according to the BOSE distribution, which occupies the magnonic states depending on their energy levels. The higher the energy, the smaller the average number of magnons at that energy. This disadvantages topological magnons because, in general, they are not the lowest-energy excitations. Since they exist between two magnon bulk bands, lower-energy magnons *must* exist. As a result, the magnonic transport is always governed by both bulk and edge modes and shows no quantization (cf. Fig. 1.1).

Electronic edge states can be probed more directly by spectroscopic methods such as angle-resolved photoemission spectroscopy. Magnons, however, lack the charge of an electron and, thus, are invisible to these techniques [22]. One established technique for the measurement of magnon band structures is inelastic neutron scattering, where a fraction of the neutrons exchanges energy and momentum with magnons due to the magnetic interaction between the spins of the neutrons and the spins in the magnet. The change of energy and momentum then can be related to the magnon band structure [23]. Since the magnetic interaction underlying inelastic neutron scattering is weak compared to charge-based spectroscopic methods, edge modes do not provide the necessary scattering intensities to directly probe them. Consequently, inelastic neutron scattering is of avail for identifying topological magnon insulator candidates by detecting gaps in bulk magnon spectra, but is insufficient for providing direct evidence for the topological edge modes [24, 25]. To summarize, the experimental detection of charge-neutral topological bosons in general, and magnons in particular, tremendously challenges state-of-the-art techniques.

Acknowledging these intricacies, this thesis aims at theoretically studying new hallmarks for probing topological magnons based on transport properties and THz spectroscopy taking practical restrictions into consideration. As an overarching pattern, the starting point constitutes a microscopic description of the ground state and the low-energy

excitations of a magnetic insulator. This description involves certain degrees of freedom of magnons such as their spin and their energy. Beyond these well-known properties, less explored traits of magnons like the orbital magnetic moment or the electric dipole moment are addressed. The understanding of the microscopic physics is employed to identify the signatures of magnons in macroscopic observables. In particular, emphasis is put on the differentiation between effects that are independent of magnon topology and those that originate from it to help to assess the practicability of the new routes for the detection.

The structure of the thesis comprises two main parts. In the first part, the theoretical foundations for describing the relevant quasiparticles in magnetically ordered insulators, which are phonons and magnons (and their hybrids), are delineated. Starting from a many-body Hamiltonian of a crystal, it is demonstrated how magnons and phonons emerge as low-energy degrees of freedom and how their interaction leads to another type of quasiparticles – magnon polarons (Chapter 2). A section on bosonic topology (Chapter 3) introduces how (bosonic) band structures can be classified in terms of a topological invariant – the CHERN number. Chapter 4 is devoted to linear response theory, which is an essential tool for predicting and explaining macroscopic observables. The magneto-electric effects presented in Chapter 5 provide the basis for the study of electric properties of magnons.

The cumulative second part combines those theories and applies them to concrete models of ferromagnets (Sections 6.1 and 6.3), collinear antiferromagnets (Sections 6.2.1 and 6.2.2), and noncollinear antiferromagnets (Section 6.1). Publication [RN1] of Section 6.1 revisits the magnetic moment of magnons and predicts an additional contribution beyond the magnon spin. The additional contribution, which is attributed to the orbital magnetic moment, renormalizes not only the magnetization and the transport of magnetic moment in temperature gradients, but also affects their symmetry, i.e., qualitative ramifications in macroscopic properties.

Both Publications [RN2] and [RN3] of Section 6.2 investigate how the transverse heat transport evolves with an external magnetic field in collinear antiferromagnets. While Publication [RN2] focuses on the magnon transport, which shows signatures of magnetic and topological phase transitions, Publication [RN3], which has been a collaborative effort involving experimental groups, demonstrates that magnons by themselves cannot explain the transport properties of the insulating antiferromagnet $\text{Na}_2\text{Co}_2\text{TeO}_6$. Instead, magnon polarons have to be considered to reproduce the qualitative features of the experimental data.

Finally, a major part of the thesis is concerned with the electric properties of magnons that has been condensed in Publication [RN4] of Section 6.3. The paper attributes an electric dipole moment to topological magnons, which directly depends on their topological properties. The microscopic electric dipole moment is shown to contribute to the electric edge polarization in a ferromagnet. Moreover, the electric dipole allows alternating electric fields to couple to topological magnons causing peaks in the electric absorption spectrum when the frequency of the external field is tuned in resonance to the topological magnons.

In Chapter 7, a conclusion is drawn and potential future research projects are proposed.

QUANTUM THEORY OF MAGNETIC SOLIDS

The prediction and understanding of macroscopic phenomena in the solid state generally requires a quantum theoretical description of its microscopic constituents – the electrons and the nuclei. One of the most fundamental description of their coupled dynamics is given by the SCHRÖDINGER equation

$$i\hbar \frac{\partial \Psi}{\partial t} = \hat{\mathcal{H}}\Psi \quad (2.1)$$

(i imaginary unit, \hbar Planck constant), where the wave function Ψ is a function of time and all the positions \mathbf{r}_i and \mathbf{R}_l of roughly 10^{23} electrons and nuclei, respectively. While electrons have a negative charge $-e$, e being the elementary charge, nuclei have a positive charge of $Z_k e$, where Z_k is the integer-valued atomic number, that lead to electromagnetic interactions. Thus, the many-body Hamiltonian [2]

$$\hat{\mathcal{H}} = \sum_k \frac{\hat{\mathbf{P}}_k^2}{2M_k} + \sum_i \frac{\hat{\mathbf{p}}_i^2}{2m} + \sum_{i<j} \frac{e^2}{4\pi\epsilon_0|\mathbf{r}_i - \mathbf{r}_j|} + \sum_{k<l} \frac{Z_k Z_l e^2}{4\pi\epsilon_0|\mathbf{R}_k - \mathbf{R}_l|} - \sum_{ik} \frac{Z_k e^2}{4\pi\epsilon_0|\mathbf{r}_i - \mathbf{R}_k|} \quad (2.2)$$

(ϵ_0 vacuum permittivity) comprises their kinetic energies, which depend on the electrons' and nuclei's masses m and M_k as well as their momenta $\hat{\mathbf{p}}_i$ and $\hat{\mathbf{P}}_k$, respectively, and their pairwise Coulomb interactions due to their charges. The relativistic corrections such as spin-orbit coupling and the inner structure of the nuclei are neglected.

Although the full description treats electrons and nuclei on equal footing, empirically the physical properties can be divided into those governed by the electrons, such as electric conductivity, and those governed by the nuclei, such as thermal expansion [26]. As will be discussed in Section 2.1, this observation can be mathematically justified by the *BORN-OPPENHEIMER approximation* that allows to decouple the dynamics of the lattice and the electrons. This separates the nuclei's lattice vibrations – the phonons – from the electronic degrees of freedom.

The electrons localize and become correlated if the repulsive interactions dominate over the kinetic energies. The strong correlation often promotes magnetic order at low temperatures so that the electronic degrees of freedom can be described by an effective spin Hamiltonian, where the excited states correspond to collective excitations of localized spins – magnons. While Section 2.2 is devoted to the mapping of the lattice dynamics to phonons, Section 2.3 reviews how the spin dynamics of the correlated electrons can be described by magnons. In the final section, the coupling between nuclei and electrons is effectively restored by spin-lattice coupling, which causes the hybridization of phonons and magnons. Those hybrid quasiparticles – called magnon polarons – turn out to play an important role in transversal transport properties of magnetic insulators, as highlighted in Publication [RN3] (cf. Section 6.2.2).

2.1 Born-Oppenheimer Approximation

The BORN-OPPENHEIMER approximation, also called adiabatic approximation, was introduced by MAX BORN and JULIUS ROBERT OPPENHEIMER in 1927 [27]. They realized that the atomic and molecular spectra comprise terms of different orders of magnitudes:

$$E_{\text{tot}} = E_{\text{el}} + E_{\text{vib}} + E_{\text{rot}}. \quad (2.3)$$

The largest contribution comes from the electronic motion E_{el} , whereas the energies associated with the vibrations and the rotations of nuclei, E_{vib} and E_{rot} , possess smaller magnitudes. The reason for this hierarchy lies in the difference between electronic and nuclear masses. Below, I cover the arguments of the adiabatic approximation following Refs. [1, 2, 28–31]. For the ease of notation, I assume that the masses M_k and atomic numbers Z_k of all nuclei are identical. The arguments can be directly extended to the most general case.

The full Hamiltonian [Eq. (2.2)] can be divided into three parts:

$$\hat{\mathcal{H}}_{\text{e}} = \sum_i \frac{\hat{\mathbf{P}}_i^2}{2m} + \sum_{i<j} \frac{e^2}{4\pi\epsilon_0|\mathbf{r}_i - \mathbf{r}_j|}, \quad (2.4a)$$

$$\hat{\mathcal{H}}_{\text{n}} = \sum_k \frac{\hat{\mathbf{P}}_k^2}{2M} + \sum_{k<l} \frac{Z^2 e^2}{4\pi\epsilon_0|\mathbf{R}_k - \mathbf{R}_l|}, \quad (2.4b)$$

$$\hat{\mathcal{H}}_{\text{e-n}} = - \sum_{ik} \frac{Ze^2}{4\pi\epsilon_0|\mathbf{r}_i - \mathbf{R}_k|}, \quad (2.4c)$$

for which the solutions of the stationary SCHRÖDINGER equation

$$\hat{\mathcal{H}}\Psi_i(\mathbf{r}, \mathbf{R}) = E_i\Psi_i(\mathbf{r}, \mathbf{R}) \quad (2.5)$$

have to be found. These solutions can be expanded in any complete basis set. For fixed nuclear coordinates \mathbf{R} , such a complete basis set is formed by the eigenfunctions of the Hamiltonian $\hat{\mathcal{H}}_{\text{e}} + \hat{\mathcal{H}}_{\text{e-n}}$, which satisfy

$$\left[\hat{\mathcal{H}}_{\text{e}}(\mathbf{r}) + \hat{\mathcal{H}}_{\text{e-n}}(\mathbf{r}, \mathbf{R}) \right] \psi_j(\mathbf{r}, \mathbf{R}) = \varepsilon_j(\mathbf{R})\psi_j(\mathbf{r}, \mathbf{R}). \quad (2.6)$$

Here, the nuclei coordinates \mathbf{R} are treated as parameters. By representing

$$\Psi_i(\mathbf{r}, \mathbf{R}) = \sum_j \chi_{ij}(\mathbf{R})\psi_j(\mathbf{r}, \mathbf{R}) \quad (2.7)$$

in the basis of ψ_j , the chosen basis set depends on the (frozen) nuclear coordinates \mathbf{R} . Consequently, the coefficients χ_{ij} must depend on those parameters as well. The ansatz for Ψ_i is inserted into the stationary SCHRÖDINGER equation of the full Hamiltonian [Eq. (2.2)] to obtain¹

$$\begin{aligned} \sum_j \psi_j(\mathbf{r}, \mathbf{R}) \left[\hat{\mathcal{H}}_{\text{n}} + \varepsilon_j(\mathbf{R}) \right] \chi_{ij}(\mathbf{R}) + \sum_j \hat{\mathcal{C}}_j(\mathbf{r}, \mathbf{R}) \chi_{ij}(\mathbf{R}) \\ = E_i \sum_j \chi_{ij}(\mathbf{R}) \psi_j(\mathbf{r}, \mathbf{R}), \end{aligned} \quad (2.8)$$

¹This intermediate result does not fully agree with Ref. [30], where the mixed first derivatives of the electronic and the nuclei wave functions do not appear contrary to Refs. [1, 28, 29]. For it will be disregarded as an approximation, the final results match each other.

where the operator

$$\hat{C}_j(\mathbf{r}, \mathbf{R}) = \frac{\left[\hat{\mathbf{P}}^2 \psi_j(\mathbf{r}, \mathbf{R}) \right] + 2 \left[\hat{\mathbf{P}} \psi_j(\mathbf{r}, \mathbf{R}) \right] \cdot \hat{\mathbf{P}}}{2M} \quad (2.9)$$

acts on the nuclear coordinates of χ_{ij} . The operator $\hat{\mathbf{P}}$ comprises the momenta $\hat{\mathbf{P}}_k$ of all nuclei k . Operators within brackets only act on a wave function inside the same bracket. Multiplying with $\psi_k^*(\mathbf{r}, \mathbf{R})$ and integrating over the electron coordinates \mathbf{r} yields

$$\left[\hat{\mathcal{H}}_n + \varepsilon_k(\mathbf{R}) \right] \chi_{ik}(\mathbf{R}) + \sum_j \hat{C}_{kj}(\mathbf{R}) \chi_{ij}(\mathbf{R}) = E_i \chi_{nk}(\mathbf{R}), \quad (2.10)$$

where $\int d^d \mathbf{r} \psi_k^* \psi_j = \delta_{kj}$ has been used (d is the dimension of the electronic configuration space). Now all that remains of the electronic wave functions in the nuclear SCHRÖDINGER equation is comprised in

$$\hat{C}_{kj}(\mathbf{R}) = \int d^d \mathbf{r} \psi_k^*(\mathbf{r}, \mathbf{R}) \hat{C}_j(\mathbf{r}, \mathbf{R}), \quad (2.11a)$$

$$\begin{aligned} &= \frac{1}{2M} \left[\int d^d \mathbf{r} \psi_k^*(\mathbf{r}, \mathbf{R}) \hat{\mathbf{P}}^2 \psi_j(\mathbf{r}, \mathbf{R}) \right] \\ &+ \frac{1}{M} \left[\int d^d \mathbf{r} \psi_k^*(\mathbf{r}, \mathbf{R}) \hat{\mathbf{P}} \psi_j(\mathbf{r}, \mathbf{R}) \right] \cdot \hat{\mathbf{P}}. \end{aligned} \quad (2.11b)$$

This term in the Hamiltonian allows for transitions between electronic states j and k due to the nuclear dynamics.² If one assumes loosely bound electrons, the dependence of ψ_j on \mathbf{R} is weak and $\hat{C}_{kj}(\mathbf{R})$ can be neglected. For strongly localized electrons the electronic and nuclear coordinates are coupled so that the actions of $\hat{\mathbf{p}}$ and $\hat{\mathbf{P}}$ on ψ_j are equivalent. For illustration, I assume that there is one electron per nucleus so that the wave function can be expressed as $\psi_j(\mathbf{r}, \mathbf{R}) = \psi_j(\mathbf{r} - \mathbf{R})$ and evaluate the first term of $\hat{C}_{kj}(\mathbf{R})$,

$$\frac{1}{2M} \int d^d \mathbf{r} \psi_k^*(\mathbf{r} - \mathbf{R}) \hat{\mathbf{p}}^2 \psi_j(\mathbf{r} - \mathbf{R}), \quad (2.12)$$

which corresponds to m/M times the kinetic energy of the electrons for $j = k$. Because of the mass difference between electrons on one hand and protons and neutrons on the other hand, this ratio has a magnitude between $1/1836$ and $1/500\,000$ (depending on the atomic number and the mass defect) rendering the energy correction negligible. The second term comprises

$$\int d^d \mathbf{r} \psi_k^*(\mathbf{r}, \mathbf{R}) \hat{\mathbf{P}} \psi_j(\mathbf{r}, \mathbf{R}), \quad (2.13)$$

the diagonal components ($j = k$) of which are effectively acting like a vector potential for the nuclear wave function as it couples to the nuclear momentum. This already hints at the geometric phase associated with adiabatic processes that I address in detail in Chapter 3, where it is rederived in a general context. In the literature it is often

²In the case of a crystal, which is the focus of this work, the nuclei order in a lattice and the deviations from the equilibrium positions are described by phonons (cf. Sections 2.2.1 and 2.2.2) and the electronic transitions can be described by electron-phonon scattering.

dismissed, which is only justified if time-reversal symmetry is present so that the wave function is real. Then, the integral of $\psi_k^*(\mathbf{r}, \mathbf{R}) \hat{P} \psi_k(\mathbf{r}, \mathbf{R}) = \hat{P} |\psi_k(\mathbf{r}, \mathbf{R})|^2 / 2$ vanishes due to the normalization of ψ_k . The nondiagonal entries of $\hat{C}_{kj}(\mathbf{R})$, corresponding to interstate transitions, are small as long as the electronic energies $\varepsilon_j(\mathbf{R})$ display large splitting compared to the timescale of the nuclear motion.

In the adiabatic approximation, all terms comprising $\hat{C}_{kj}(\mathbf{r}, \mathbf{R})$ are truncated from the Hamiltonian and the nuclear wave function can be obtained from solving³

$$\left[\frac{\hat{P}^2}{2M} + \mathcal{W}_k(\mathbf{R}) \right] \chi_{nk}(\mathbf{R}) = E_n \chi_{nk}(\mathbf{R}). \quad (2.14)$$

Since now the electronic quantum number k is a good quantum number in the approximate nuclear SCHRÖDINGER equation [Eq. (2.14)], the expansion of the full wave function [Eq. (2.7)] can be restricted to

$$\Psi_{nk}(\mathbf{r}, \mathbf{R}) = \chi_{nk}(\mathbf{R}) \psi_k(\mathbf{r}, \mathbf{R}) \quad (2.15)$$

and the eigenstates can be labeled by the electronic (k) and nuclear (n) quantum numbers.

Here, the electronic degrees of freedom have essentially been removed from the nuclear dynamics and only enter as a modified potential energy in the nuclear Hamiltonian. If the electrons start in a state k , they give rise to a *potential energy surface* $\mathcal{W}_k(\mathbf{R}) = \sum_{i < j} \frac{Z^2 e^2}{4\pi\epsilon_0 |\mathbf{R}_i - \mathbf{R}_j|} + \varepsilon_k(\mathbf{R})$ that governs the nuclear dynamics. Physically, the electrons move much faster due to the relative smallness of their masses and can follow the nuclear positions instantaneously. Displacing the nuclei from their equilibrium positions causes a new electronic distribution with higher energy while maintaining the electronic state k . Upon relaxing the nuclei, the electrons assume their previous energy. This corresponds to a reversible process, in which the electrons remain in the k -th state during the full time evolution of \mathbf{R} . When electron-phonon scattering becomes important or the electronic energies $\varepsilon_k(\mathbf{R})$ become degenerate for some \mathbf{R} so that electronic transitions only require infinitesimal energies, the adiabatic approximation is expected to fail and nonadiabatic processes must be included.

2.2 Theory of Lattice Excitations: Phonons

Phonons are the bosonic quasiparticles of the collective lattice dynamics. They play a central role for many macroscopic properties of crystals. Some examples include [2]:

- the heat capacity, thermal expansion, and the thermal conductivity of insulators,
- the temperature dependence of the electric resistivity of metals,
- the superconductivity of metals,

³Strictly speaking the diagonal elements of $\hat{C}_{kj}(\mathbf{r}, \mathbf{R})$ are compatible with an adiabatic approximation in the sense that they do not allow for electronic transitions, but merely renormalize the effective potential energy for the nuclei. However, as demonstrated above, these renormalizations are either relatively small (first term) or they become important as geometric phases (second term), which have physical consequences in topologically nontrivial systems (cf. Chapter 3). While some authors consider them part of the approximate nuclear Hamiltonian [30], others do not [1, 28, 29].

- the dielectric properties of ionic crystals, and
- the inelastic light and neutron scattering.

In Section 2.1, the BORN-OPPENHEIMER approximation was introduced that allows a separate treatment of the lattice and electron dynamics. A simplification of the decoupled lattice dynamics given by the harmonic approximation is discussed in Section 2.2.1 and the resulting differential equations are solved classically in Section 2.2.2. Based on the classical solutions the phonons can be quantized using a similar mapping as in the algebraic solution of the harmonic oscillator, which is presented in Section 2.2.3.

2.2.1 Harmonic Approximation

Having separated the electronic and nuclear dynamics, it is possible to study the structure of the solutions of the Hamiltonian $\frac{\hat{\mathbf{P}}^2}{2M} + \mathcal{W}(\mathbf{R})$. In the following, I consider the electronic quantum number as arbitrary but fixed. At this point, one faces the problem of having to compute the electronic energies $\varepsilon(\mathbf{R})$, which requires solving the electronic SCHRÖDINGER equation [Eq. (2.6)], for each possible configuration of \mathbf{R} first, in order to determine $\mathcal{W}(\mathbf{R})$ even if one is not interested in the electronic properties. This is where the harmonic approximation comes to the rescue. In this section, I partly present arguments from Refs [1, 2, 26, 30, 32].

First, I confine myself to crystalline solids, in which the nuclei only take positions on lattice points $\mathbf{R}_n = n_1 \mathbf{a}_1 + n_2 \mathbf{a}_2 + n_3 \mathbf{a}_3$, where $n_i \in \mathbb{Z}$ are integers and \mathbf{a}_i are primitive translation vectors ($i = 1, 2, 3$). This describes the case of a BRAVAIS lattice, where each unit cell exactly comprises one nucleus. More generally, a crystal may feature multiple *sublattices* that are displaced by basis vectors \mathbf{b}_i ($i = 1, \dots, \mathcal{N}_{\text{sl}}$), where \mathcal{N}_{sl} is the number of sublattices. Hence, the position of a nucleus can be written as

$$\mathbf{R}_{im} = \mathbf{R}_{im}^{(0)} + \mathbf{u}_{im}, \quad (2.16)$$

where $\mathbf{R}_{im}^{(0)} := \mathbf{R}_m + \mathbf{b}_i$ is the equilibrium position and \mathbf{u}_{im} is the displacement of the nucleus of the i -th sublattice in the m -th unit cell from its equilibrium position.

The equilibrium positions are characterized by local minima of the potential energy surface, which means that the first derivative $\hat{\nabla}_{\mathbf{R}} \mathcal{W}(\mathbf{R}) \Big|_{\mathbf{R}^{(0)}}$ evaluated at the equilibrium positions of all nuclei, $\mathbf{R}^{(0)}$, vanishes so that

$$\mathcal{W}(\mathbf{R}) = \mathcal{W}(\mathbf{R}^{(0)}) + \frac{1}{2} \sum_{mn} \sum_{ij} \sum_{\alpha\beta} C_{i\alpha}^{j\beta} \left(\mathbf{R}_n^{(0)} - \mathbf{R}_m^{(0)} \right) u_{im}^{\alpha} u_{jn}^{\beta} + \dots \quad (2.17)$$

($\alpha, \beta = x, y, z$ Cartesian components) can be expanded in a TAYLOR series without a linear term. The second partial derivatives, i.e., the entries of the Hessian

$$C_{i\alpha}^{j\beta} \left(\mathbf{R}_n^{(0)} - \mathbf{R}_m^{(0)} \right) = \left. \frac{\partial^2 \mathcal{W}}{\partial R_{im}^{\alpha} \partial R_{jn}^{\beta}} \right|_{\mathbf{R}^{(0)}} \quad (2.18)$$

at $\mathbf{R}^{(0)}$ are the *elastic constants*.⁴ Here, I implicitly use the translational invariance of the potential energy surface \mathcal{W} , which must only depend on the difference vector $\mathbf{R}_n^{(0)} - \mathbf{R}_m^{(0)}$

⁴Alternative designations in the literature are force constants or spring constants.

between the unit cells, but not the absolute position within the lattice. Since the partial derivatives can be commuted (for doubly continuously differentiable functions, which is implicitly presumed in the TAYLOR expansion), the indices of the elastic constants can be interchanged under simultaneous inversion of the argument:

$$C_{i\alpha}^{j\beta}(\mathbf{R}_n^{(0)} - \mathbf{R}_m^{(0)}) = C_{j\beta}^{i\alpha}(\mathbf{R}_m^{(0)} - \mathbf{R}_n^{(0)}). \quad (2.19)$$

The harmonic approximation truncates the TAYLOR expansion of \mathcal{W} beyond quadratic (or bilinear) order so that the nuclei move within a harmonic potential about their equilibrium positions. This approximation holds if the displacements \mathbf{u}_{mi} are small compared to the interatomic distances ($|\mathbf{a}_i|$ and $|\mathbf{b}_j|$).⁵ Moreover, in order for $\mathbf{R}^{(0)}$ to be a minimum of the truncated \mathcal{W} , the Hessian needs to be positive semidefinite so that no deformation of the lattice can decrease the energy. Note that an increase of energy upon arbitrary deformation (i.e., a positive definite Hessian, which is sufficient for an isolated local energy minimum) cannot be required, since any rigid global translation can be conceived as a change of coordinates and must not change the energy.

The tedious task of solving for the electronic SCHRÖDINGER equation for infinitely many configurations of the nuclei has been mapped to computing only the potential energy surface at the lattice positions and the elastic constants. The notion of the former is not even required for most properties, since a constant energy does not affect the dynamics as demonstrated in the next section (Section 2.2.2). The elastic constants themselves are generally not independent of each other as they have to obey the lattice symmetries. Furthermore, the elastic constants decrease with the distance of the interacting nuclei and can be truncated beyond one or a few coordination spheres.

Finally, it should be mentioned that some properties intrinsically require an anharmonic theory even for qualitative explanations. An important example in thermal equilibrium is the thermal expansion. In the harmonic approximation, the nuclei vibrate about their equilibrium positions (as discussed in Section 2.2.2); the amplitude of which is temperature dependent. The equilibrium positions themselves do not depend on temperature, hence, there is no thermal expansion (cf. Section 2.2.3). Concerning transport properties, the solid would have an infinite heat conductivity without anharmonic terms or electron-phonon interactions [32].

2.2.2 Classical Equations of Motion

The previous two sections have laid the groundwork for the study of the lattice dynamics, for which I present first a classical solution based on Newtonian mechanics in this section. While I have briefly discussed the ground state of the nuclei – the lattice – in the previous section, here I consider their *excitations*. Specifically, the dispersion relation of the excitations can be obtained classically, which determines not only spectroscopic properties, but also affects macroscopic properties in thermal equilibrium at finite temperatures. However, to obtain the correct low-temperature behavior, the quantum nature cannot be neglected. Nonetheless, the classical solution can be used as a basis for the quantum theory of the nuclear dynamics. The classical approach to lattice dynamics presented below is covered in several textbooks like Refs. [2, 26, 28, 32, 33].

⁵Classically, there is always a regime in which the mean square displacement is arbitrarily small if the temperature is decreased. In solids with strong quantum fluctuations, this assumption breaks down even at very low temperature, which requires a more complex theory [32].

General solution

The equations of motion for the displacements follow from NEWTON's second law, which states that the force \mathbf{F}_{im} acting on a particular i -th nucleus in the m -th unit cell is related to its acceleration by $\mathbf{F}_{im} = M_i \frac{\partial^2 \mathbf{u}_{im}}{\partial t^2}$. In general, the masses M_i may depend on the sublattice i for polyatomic compounds, but not on the unit cell. For the conservative force results from a potential energy, $\mathbf{F}_{im} = -\hat{\nabla}_{\mathbf{R}_{im}} \mathcal{W}$, a system of coupled second-order differential equations is obtained:

$$M_i \frac{\partial^2 u_{im}^\alpha}{\partial t^2} + \sum_{jn\beta} C_{i\alpha}^{j\beta}(\mathbf{R}_n - \mathbf{R}_m) u_{jn}^\beta = 0. \quad (2.20)$$

This system comprises a differential equation for each unit cell m , each sublattice i , and each component of vibration α ; hence, it encompasses $\mathcal{N}_{\text{vib}} \mathcal{N}_{\text{sl}} \mathcal{N}_{\text{uc}}$ equations, where \mathcal{N}_{sl} is the number of sublattices, \mathcal{N}_{uc} is the number of unit cells, and \mathcal{N}_{vib} is the number of spatial dimensions of the vibration (usually $\mathcal{N}_{\text{vib}} = 3$ for $\alpha = x, y, z$). Although this number of coupled equations would overexert any computer for macroscopic systems, a drastic simplification results from the ansatz⁶

$$u_{im}^\alpha = \text{Re} \frac{1}{\sqrt{M_i}} \epsilon_{\mathbf{k}}^{i\alpha} e^{i(\mathbf{k} \cdot \mathbf{R}_{im} - \omega_{\mathbf{k}} t)}, \quad (2.21)$$

which exploits translational invariance to transform the $\mathcal{N}_{\text{vib}} \mathcal{N}_{\text{sl}} \mathcal{N}_{\text{uc}}$ coupled differential equations to \mathcal{N}_{uc} decoupled systems of $\mathcal{N}_{\text{vib}} \mathcal{N}_{\text{sl}}$ coupled algebraic equations of motion:⁷

$$-\omega_{\mathbf{k}}^2 \epsilon_{\mathbf{k}}^{i\alpha} + \sum_{jn\beta} \frac{1}{\sqrt{M_i M_j}} C_{i\alpha}^{j\beta}(\mathbf{R}_n - \mathbf{R}_m) e^{i\mathbf{k} \cdot (\mathbf{R}_{jn} - \mathbf{R}_{im})} \epsilon_{\mathbf{k}}^{j\beta} = 0. \quad (2.22)$$

Here, the problem consists of solving for $\epsilon_{\mathbf{k}}^{i\alpha}$, where \mathbf{k} is a fixed parameter. The complex phonon polarization vector $\epsilon_{\mathbf{k}}^{i\alpha}$ determines the direction, amplitude, and phase of the vibration for all nuclei. Since it does not depend on the unit cell, the summation over n in the second term can be put into the definition of the *dynamical matrix*

$$\mathcal{D}_{i\alpha}^{j\beta}(\mathbf{k}) := \frac{e^{i\mathbf{k} \cdot (\mathbf{b}_j - \mathbf{b}_i)}}{\sqrt{M_i M_j}} \sum_n e^{i\mathbf{k} \cdot \mathbf{R}_n} C_{i\alpha}^{j\beta}(\mathbf{R}_n), \quad (2.23)$$

which is related to the FOURIER transform of the elastic constants. Although it has 4 indices, it can be rearranged as a $\mathcal{N}_p \times \mathcal{N}_p$ matrix with complex entries, where $\mathcal{N}_p = \mathcal{N}_{\text{vib}} \mathcal{N}_{\text{sl}}$. Using the dynamical matrix, Eq. (2.22) can be recast into

$$\sum_{j\beta} \mathcal{D}_{i\alpha}^{j\beta}(\mathbf{k}) \epsilon_{\lambda\mathbf{k}}^{j\beta} = \omega_{\lambda\mathbf{k}}^2 \epsilon_{\lambda\mathbf{k}}^{i\alpha}. \quad (2.24)$$

Therefore, the system of differential equations has become an eigenvalue problem of the dynamical matrix with eigenvalues $\omega_{\lambda\mathbf{k}}^2$ and eigenvectors $\epsilon_{\lambda\mathbf{k}}^{i\alpha}$, which can be labeled by a

⁶Here, the real part is taken to account for the fact that the left-hand side is real. However, the imaginary part or any linear combination of real or imaginary part are valid choices too.

⁷Note that the real part was truncated. If the solution of the complex equation exists so that the left-hand side is zero, then the real part of the solution is a solution as well.

quantum number $\lambda = 1, \dots, \mathcal{N}_p$. Importantly, the angular frequencies $\omega_{\lambda\mathbf{k}}$ cannot be chosen freely, but depend on \mathbf{k} . This functional dependence is known as *dispersion relation* or *band structure*. Hence, with the correct angular frequencies and phonon eigenvectors, the ansatz of Eq. (2.21) is indeed a solution of the system of differential equations [Eq. (2.20)].

Physically, the solutions are lattice vibration plane waves. The nuclei collectively oscillate about their equilibrium positions with the same angular frequency $\omega_{\lambda\mathbf{k}}$. Different unit cells that are displaced along the wave vector \mathbf{k} differ in their phases, while those displaced perpendicular to \mathbf{k} oscillate in phase. The phase differences between nuclei within the same unit cells are given by the relative phases of $\epsilon_{\lambda\mathbf{k}}^{i\alpha}$, while their absolute values govern the oscillation amplitudes of the various sublattices.⁸

Before turning to an example, one should be concerned with the mathematical properties of the solution of the eigenvalue problem [Eq. (2.24)]. One has to question whether the eigenvalues of $\mathcal{D}_{i\alpha}^{j\beta}(\mathbf{k})$ are real and, if so, whether they are nonnegative, since *negative* values would imply imaginary angular frequencies $\omega_{\lambda\mathbf{k}}$, i.e., decaying or self-amplifying waves depending on its sign. Such solutions would violate the conservation of energy.

Two general properties of the dynamical matrix can be proven. First, since the elastic constants must be real, the dynamical matrix needs to satisfy $\mathcal{D}_{i\alpha}^{j\beta}(\mathbf{k}) = [\mathcal{D}_{i\alpha}^{j\beta}(-\mathbf{k})]^*$. Second, the symmetry property Eq. (2.19) requires $\mathcal{D}_{i\alpha}^{j\beta}(\mathbf{k}) = \mathcal{D}_{j\beta}^{i\alpha}(-\mathbf{k})$.

With those two general properties of the dynamical matrix, it directly follows that it is Hermitian and, therefore, has real eigenvalues. Consequently, the eigenvectors of the dynamical matrix must be orthogonal,⁹ can be normalized

$$\sum_{i\alpha} (\epsilon_{\lambda\mathbf{k}}^{i\alpha})^* \epsilon_{\sigma\mathbf{k}}^{i\alpha} = \delta_{\lambda\sigma}, \quad (2.25)$$

and must be complete.

For the proof of $\omega_{\lambda\mathbf{k}} \in \mathbb{R}$, let $A_{i\alpha}$ be the components of an arbitrary vector with complex entries. One has to check whether the sesquilinear form

$$\sum_{i\alpha} \sum_{j\beta} A_{i\alpha}^* \mathcal{D}_{i\alpha}^{j\beta}(\mathbf{k}) A_{j\beta} \quad (2.26)$$

is positive semidefinite in $A_{i\alpha} \in \mathbb{C}$ for an arbitrary, but fixed \mathbf{k} . This is readily proven by recalling that the bilinear form

$$\sum_{mn} \sum_{ij} \sum_{\alpha\beta} C_{i\alpha}^{j\beta}(\mathbf{R}_n - \mathbf{R}_m) u_{im}^\alpha u_{jn}^\beta \quad (2.27)$$

is positive semidefinite in $u_{im}^\alpha \in \mathbb{R}$ because it corresponds to the change in energy $\mathcal{W}(\mathbf{R})$ when displacing the nuclei from their equilibrium positions [cf. Eq. (2.17)]. Using these arguments, one proves that the dynamical matrix is positive semidefinite and, thus, has nonnegative eigenvalues so that $\omega_{\lambda\mathbf{k}}$ are real.

In principle, there are two admissible choices for the angular frequencies (if nonzero) because the eigenvalues of the dynamical matrix define their absolute values but not their signs. However, the negative-frequency solutions are contained in the positive-frequency

⁸Note that there is also a factor $1/\sqrt{M_i}$ in the amplitudes.

⁹If the eigenvalues are not degenerate. Otherwise, the eigenvectors can be chosen orthogonal.

solutions, which I exclusively consider for the rest of this thesis. For the proof, rewrite the ansatz Eq. (2.21), using the trivial identity $\operatorname{Re} z = \operatorname{Re} z^*$ for any $z \in \mathbb{C}$, as¹⁰

$$u_{im}^\alpha = \operatorname{Re} \frac{1}{\sqrt{M_i}} (\epsilon_{\lambda\mathbf{k}}^{i\alpha})^* e^{i(-\mathbf{k} \cdot \mathbf{R}_{im} + \omega_{\mathbf{k}} t)}. \quad (2.28)$$

For $\omega_{\lambda\mathbf{k}} > 0$, this has the structure of a negative-frequency solution $\tilde{\omega}_{\lambda(-\mathbf{k})} := -\omega_{\lambda\mathbf{k}} < 0$. To demonstrate that this is indeed a solution, one needs to show that $\tilde{\epsilon}_{\lambda(-\mathbf{k})}^{i\alpha} := (\epsilon_{\lambda\mathbf{k}}^{i\alpha})^*$ is an eigenvector of the dynamical matrix at $-\mathbf{k}$ with eigenvalue $\tilde{\omega}_{\lambda(-\mathbf{k})}^2$ provided that $\omega_{\lambda\mathbf{k}}$ and $\epsilon_{\lambda\mathbf{k}}^{i\alpha}$ are eigenvalues and eigenvectors at \mathbf{k} .

Because of the property $\mathcal{D}_{i\alpha}^{j\beta}(\mathbf{k}) = [\mathcal{D}_{i\alpha}^{j\beta}(-\mathbf{k})]^*$ the solutions of the eigenvalue problem

$$\sum_{j\beta} \mathcal{D}_{i\alpha}^{j\beta}(-\mathbf{k}) (\epsilon_{\lambda\mathbf{k}}^{j\beta})^* = \omega_{\lambda\mathbf{k}}^2 (\epsilon_{\lambda\mathbf{k}}^{i\alpha})^* \quad (2.29)$$

at $-\mathbf{k}$ are obtained by complex conjugation of Eq. (2.24). Consequently, the eigenvectors at \mathbf{k} and $-\mathbf{k}$ are related by complex conjugation (up to an arbitrary phase) and the eigenvalues $\omega_{\lambda\mathbf{k}}^2 = \omega_{\lambda(-\mathbf{k})}^2$ are symmetric. This property is a consequence of the time-reversal symmetry of the lattice dynamics, which is why it suffices to consider positive-frequency solutions.

Another property of the solutions is the periodicity in \mathbf{k} . Let $\mathbf{G} \in \mathbb{R}^3$ be a reciprocal lattice vector so that $\mathbf{G} \cdot \mathbf{R}_m = 2\pi p$ with $p \in \mathbb{Z}$ for any lattice vector \mathbf{R}_m . Then, the dynamical matrix at $\mathbf{k} + \mathbf{G}$ fulfills the property

$$\mathcal{D}_{i\alpha}^{j\beta}(\mathbf{k} + \mathbf{G}) = e^{i\mathbf{G} \cdot (\mathbf{b}_j - \mathbf{b}_i)} \mathcal{D}_{i\alpha}^{j\beta}(\mathbf{k}), \quad (2.30)$$

i.e., it is identical to itself at \mathbf{k} up to a unitary transformation. Consequently, $\omega_{\lambda, \mathbf{k} + \mathbf{G}} = \omega_{\lambda\mathbf{k}}$ and $\epsilon_{\lambda, \mathbf{k} + \mathbf{G}}^{i\alpha} = e^{-i\mathbf{G} \cdot \mathbf{b}_i} \epsilon_{\lambda\mathbf{k}}^{i\alpha}$ (up to a gauge transformation).

Elastic Chain with Two-Atomic Basis

It is instructive to apply the general theory to a simple example that gives some physical insight. In the following, I consider a chain of two different types of atoms that have masses M_A and M_B . I assume that the positions of the first (second) type of atoms are $R_{An} = 2na$ ($R_{Bn} = R_{An} + a$), where $n \in \mathbb{Z}$ and $a \in \mathbb{R}$ so that they are equidistantly placed on the chain. The coupling between nearest neighbors is described by the potential energy

$$\mathcal{W} = \frac{C}{4} \sum_n [(u_{An} - u_{Bn})^2 + (u_{Bn} - u_{A, n+1})^2]. \quad (2.31)$$

The vibrations are assumed to be restricted to only one dimension, which allows to suppress the third, spatial index for u .

By computing the forces, two coupled equations of motion

$$M_A \frac{\partial^2 u_{An}}{\partial t^2} = \frac{C}{2} (u_{Bn} + u_{B, n-1} - 2u_{An}), \quad (2.32a)$$

$$M_B \frac{\partial^2 u_{Bn}}{\partial t^2} = \frac{C}{2} (u_{An} + u_{A, n+1} - 2u_{Bn}) \quad (2.32b)$$

¹⁰If I had defined u_{im}^α using the imaginary part, there would be an additional minus sign, which just corresponds to a global phase that can be compensated by redefining $\epsilon_{\lambda\mathbf{k}}^{i\alpha}$.

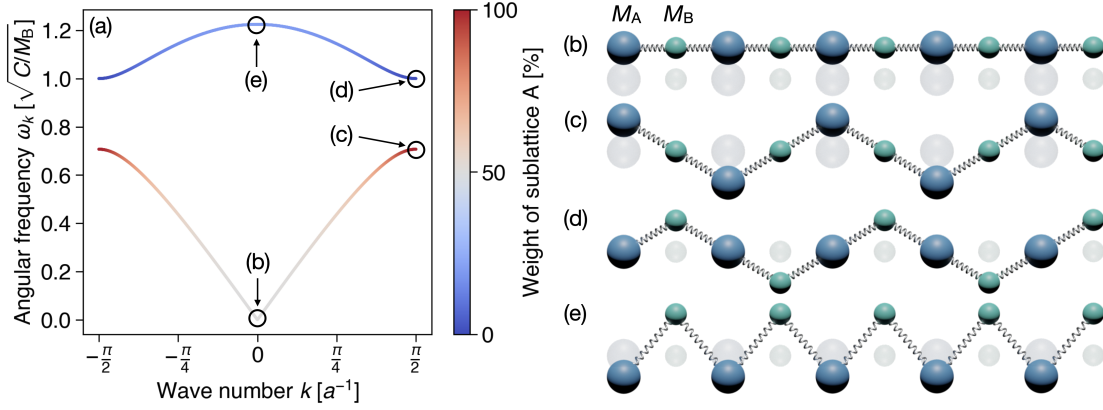


Figure 2.1: Phonon spectrum and selected normal modes. (a) Phonon band structure of a one-dimensional chain with acoustic and optical branches. Color represents the normalized squared amplitudes $|A_{\lambda k}^A|^2 = 1 - |A_{\lambda k}^B|^2$ of the modes with band index λ and wave number k on sublattice A. (b–e) Snapshots of elastic waves representing amplitudes and phases of selected phonon modes [cf. panel (a)]. Big (small) spheres represent atoms on first (second) sublattice. Faint spheres in the background show their equilibrium positions. Shown phonon modes correspond to (b, c) acoustic and (d, e) optical branches at the (b, e) BRILLOUIN zone center and (c, d) the BRILLOUIN zone edge. Here, the masses of the sublattices have been set as $M_A = 2M_B$.

arise. In analogy to Eq. (2.21) the ansatz

$$u_{in} = \text{Re} \frac{1}{\sqrt{M_i}} \epsilon_k^i e^{i(kR_{in} - \omega_k t)} \quad (2.33)$$

($i = A, B$) transforms the two differential equations for $u_{in}(t)$ to algebraic equations

$$\left(\frac{C}{M_A} - \omega_k^2 \right) \epsilon_k^A = \frac{C}{2\sqrt{M_A M_B}} \left(e^{ika} + e^{-ika} \right) \epsilon_k^B, \quad (2.34a)$$

$$\left(\frac{C}{M_B} - \omega_k^2 \right) \epsilon_k^B = \frac{C}{2\sqrt{M_A M_B}} \left(e^{ika} + e^{-ika} \right) \epsilon_k^A \quad (2.34b)$$

for ϵ_k^i . Multiplying both sides of Eq. (2.34a) by $\frac{C \cos(ka)}{\sqrt{M_A M_B}}$ and Eq. (2.34b) by $\frac{C}{M_A} - \omega_k^2$ and eliminating ϵ_k^A yields

$$\left[\left(\frac{C}{M_A} - \omega_k^2 \right) \left(\frac{C}{M_B} - \omega_k^2 \right) - \frac{C^2 \cos^2(ka)}{M_A M_B} \right] \epsilon_k^B = 0. \quad (2.35)$$

For the nontrivial solutions, the first factor has to vanish, which is the case if

$$\omega_{1/2,k}^2 = \frac{C}{2} \left(\frac{1}{M_A} + \frac{1}{M_B} \right) \mp C \sqrt{\frac{1}{4} \left(\frac{1}{M_A} + \frac{1}{M_B} \right)^2 - \frac{\sin^2(ka)}{M_A M_B}}. \quad (2.36)$$

As expected, two (positive-frequency) solutions are obtained because of $\mathcal{N}_{\text{sl}} = 2$ and $\mathcal{N}_{\text{vib}} = 1$. In the long-wavelength limit ($k \ll a$), the angular frequencies of the two

branches can be approximated by

$$\omega_{1k}^2 \approx \frac{C(ka)^2}{M_A + M_B}, \quad (2.37a)$$

$$\omega_{2k}^2 \approx \left(\frac{C}{M_A} + \frac{C}{M_B} \right) - \frac{C(ka)^2}{M_A + M_B}. \quad (2.37b)$$

The ratio of the (phase-comprising) vibrational amplitudes $A_{\lambda k}^i = \epsilon_{\lambda k}^i / \sqrt{M_i}$ of both sublattices i at $k = 0$ is exactly obtained as

$$\left. \frac{A_{1k}^A}{A_{1k}^B} \right|_{k=0} = 1, \quad (2.38a)$$

$$\left. \frac{A_{2k}^A}{A_{2k}^B} \right|_{k=0} = -\frac{M_B}{M_A} \quad (2.38b)$$

for the two branches. In the lower branch, the energies are linear in the long-wavelength limit and become zero for $k = 0$ [cf. Fig. 2.1(a)]. Precisely at $k = 0$, all nuclei oscillate in phase with the same amplitudes [cf. Fig. 2.1(b)], which corresponds to a rigid translation of the entire solid that leaves the energy constant [cf. Eq. (2.31)]. At $k = \pi/2a$, the sublattice with the lower mass (in this case M_B) is at rest, while the larger masses vibrate with a phase shift of 180° between neighboring atoms [cf. Fig. 2.1(c)]. In the upper branch, on the contrary, only the atoms on the B sublattice oscillate in antiphase and those on the A sublattice remain at rest [cf. Fig. 2.1(d)]. The upper branch at $k = 0$ features oscillations of both sublattices with a phase shift of 180° *between* the sublattices, while *within* the sublattices all atoms oscillate in phase [cf. Fig. 2.1(e)].

The zero-energy mode at $k = 0$ is a consequence of the GOLDSTONE theorem, which states that there is a zero-energy excitation¹¹ for each generator of a spontaneously broken continuous symmetry of the ground state [34–37].¹² Here, the system is homogeneous in space and the Hamiltonian is invariant under arbitrary translations $u_{in} \rightarrow u_{in} + r$ ($r \in \mathbb{R}$). However, by definition, the ground state fixes $u_{in} = 0$. As a consequence of this arbitrary choice, there is a GOLDSTONE mode.

The lower branch with the linear dispersion in the long-wavelength limit, which encompasses the GOLDSTONE mode, is also known as the “acoustic branch.” The upper branch is denoted “optical branch,” as those oscillations induce electric dipole moments in an ionic crystal, which affects its optical properties.

So far, the vibrations were confined to one dimension, but I did not make an assumption of whether the elongations take place parallel or perpendicular to the chain. Generally there is an acoustic and an optical branch for each dimension with different elastic constants. If the oscillation occurs parallel to the chain (or, in higher dimension, parallel to the propagation direction defined by the wave vector \mathbf{k}), those modes are called “longitudinal phonons,” while the perpendicular motion is characteristic for “transversal

¹¹Although the GOLDSTONE mode has the same energy as the ground state and, thus, corresponds to a ground state itself, it is called “excitation” because the chosen ground state is assumed to be dynamically stable in the low-temperature regime. Thus, the usage of the terms “ground state” and “excitation” in this context refers to the density matrix rather than the Hamiltonian.

¹²Actually, this statement covers a special case, which is not entirely general, as it ignores a subtlety that is addressed in Section 2.3.3.

phonons.” The bands of longitudinal phonons generally have a greater slope (i.e., larger sound velocities) than the transversal ones [38].

The emergence of additional acoustic modes is in agreement with the GOLDSTONE theorem because there exists a generator of translation for each dimension, each of which contributes a GOLDSTONE mode as part of an acoustic branch. In general, there are \mathcal{N}_{vib} acoustic and $\mathcal{N}_{\text{sl}}(\mathcal{N}_{\text{sl}} - 1)$ optical branches.

2.2.3 Second Quantization

The classical theory of the lattice dynamics is expedient to give an intuition about the structure of the solutions, the symmetries of the underlying equations of motion and how these affect the symmetry of the solutions. Hereafter, I reformulate the classical theory into a quantum theory that is not only required to reproduce the correct low-temperature behavior of thermodynamic quantities like the heat capacity [2], but it also allows treating different kinds of excitations on equal footing. This lays the groundwork for magnon polarons in Section 2.4.

I will start by a brief reminder on the algebraic solution of the harmonic oscillator, which can be found in standard textbooks like [2, 39–41]. It is based on the construction of creation and annihilation operators that generate orthogonal eigenstates of the Hamiltonian. From a single wave function, e.g., that of the ground state, the complete eigenbasis of the Hamiltonian can be generated. However, it turns out that the energy spectrum and expectation values can be computed without the notion of the real-space representation of the wave functions.

The same idea can be applied to lattice waves, which exhibit a similar Hamiltonian, but require a more complex construction. Indeed, the final Hamiltonian resembles that of an ensemble of noninteracting harmonic oscillators with generally distinct frequencies. I present two constructions. While the first construction is found in text books like Refs. [1, 2, 30, 33, 40] and employs the classical solution obtained from the diagonalization of the dynamical matrix to directly define creation and annihilation operators for the normal modes, the second construction is a local mapping, which does not define creation and annihilation operators for uncoupled normal modes, but maps to coupled harmonic oscillators. The second construction avoids some complications that become apparent in Section 2.4 and Chapter 3. This construction has not been published by other authors to my knowledge.

The Hamiltonian of the harmonic oscillator

$$\hat{\mathcal{H}} = \frac{\hat{p}^2}{2m} + \frac{m\omega^2 \hat{x}^2}{2} \quad (2.39)$$

in first quantization is written in terms of the conjugate variables position \hat{x} and momentum \hat{p} , which satisfy the commutation relation $[\hat{x}, \hat{p}] = i\hbar$. One could solve the SCHRÖDINGER equation in first quantization and obtain the Hermite polynomials as solutions. Alternatively, the Hamiltonian can be rewritten in second quantization.

The Hamiltonian is a sum of the squares of two operators, \hat{x} and \hat{p} . It can be factorized in analogy to a complex variant of the binomial formula $(a + ib)(a - ib) = a^2 + b^2$ for

$a, b \in \mathbb{R}$. This is achieved by defining the creation, annihilation operators

$$\hat{a} = \sqrt{\frac{m\omega}{2\hbar}} \hat{x} + i\sqrt{\frac{1}{2\hbar m\omega}} \hat{p}, \quad (2.40a)$$

$$\hat{a}^\dagger = \sqrt{\frac{m\omega}{2\hbar}} \hat{x} - i\sqrt{\frac{1}{2\hbar m\omega}} \hat{p}, \quad (2.40b)$$

respectively. The inverse transformation is

$$\hat{x} = \sqrt{\frac{\hbar}{2m\omega}} (\hat{a}^\dagger + \hat{a}), \quad (2.41a)$$

$$\hat{p} = i\sqrt{\frac{\hbar m\omega}{2}} (\hat{a}^\dagger - \hat{a}). \quad (2.41b)$$

The newly defined operators fulfill the commutation relation of bosons: $[\hat{a}, \hat{a}^\dagger] = 1$. Contrary to the numbers in the binomial formula, \hat{x} and \hat{p} do not commute so that the Hamiltonian

$$\hat{\mathcal{H}} = \hbar\omega \left(\hat{a}^\dagger \hat{a} + \frac{1}{2} \right) \quad (2.42)$$

has an extra constant of $\hbar\omega/2$.

The eigenvalue problem of $\hat{\mathcal{H}}$ has been reformulated into an eigenvalue problem of the particle number operator $\hat{n} = \hat{a}^\dagger \hat{a}$. To solve its eigenvalue problem, let $|n\rangle$ be a normalized eigenstate of \hat{n} with eigenvalue n . Then, $\hat{a}^\dagger |n\rangle$ is an eigenstate with eigenvalue $n+1$ and $\hat{a} |n\rangle$ is an eigenstate with eigenvalue n as seen from the application of the commutation relation:

$$\hat{n} \hat{a}^\dagger |n\rangle = (n+1) \hat{a}^\dagger |n\rangle, \quad (2.43a)$$

$$\hat{n} \hat{a} |n\rangle = (n-1) \hat{a} |n\rangle. \quad (2.43b)$$

Therefore, one can write $|n+1\rangle = z_1 \hat{a}^\dagger |n\rangle$ and $|n-1\rangle = z_2 \hat{a} |n\rangle$ with coefficients $z_1, z_2 \in \mathbb{C}$ that ensure the normalization of the eigenstates

$$\langle n+1 | n+1 \rangle = |z_1|^2 \langle n | \hat{a} \hat{a}^\dagger | n \rangle = |z_1|^2 (n+1) \stackrel{!}{=} 1, \quad (2.44a)$$

$$\langle n-1 | n-1 \rangle = |z_2|^2 \langle n | \hat{a}^\dagger \hat{a} | n \rangle = |z_2|^2 n \stackrel{!}{=} 1. \quad (2.44b)$$

Since the phases of the eigenstates are arbitrary, z_1 and z_2 are not uniquely defined. Customary, the eigenstates of \hat{n} are defined so that the action of the creation and annihilation operators can be expressed as

$$\hat{a} |n\rangle = \sqrt{n} |n-1\rangle, \quad (2.45a)$$

$$\hat{a}^\dagger |n\rangle = \sqrt{n+1} |n+1\rangle. \quad (2.45b)$$

Because the Hamiltonian has to be bounded below, the eigenvalues n must be natural numbers including 0, i.e., $n \in \mathbb{N}_0$ with $\mathbb{N}_0 = \{0, 1, 2, \dots\}$.¹³ Hence, $|0\rangle$ represents the

¹³By requiring that $\hat{\mathcal{H}}$ is bounded below for it has a ground state, there has to be a smallest eigenvalue $n_0 \in \mathbb{R}$ so that $\hat{a} |n_0\rangle = 0$, which is the case for $n_0 = 0$. Hence, the eigenvalues n must be natural numbers including 0. If there was an eigenvalue $\tilde{n} \notin \mathbb{N}_0$, then successive application of \hat{a} onto $|\tilde{n}\rangle$ could generate eigenstates with negative eigenvalues. This contradicts the finding that 0 is the lowest eigenvalue.

ground state of the harmonic oscillator and excited states can be constructed as

$$|n\rangle = \frac{(\hat{a}^\dagger)^n}{\sqrt{n!}} |0\rangle \quad (n \in \mathbb{N}_0) \quad (2.46)$$

and the energy eigenvalues read $\hat{\mathcal{H}}|n\rangle = \hbar\omega(n + \frac{1}{2})|n\rangle$. The explicit real-space representation of the wave functions can be incrementally constructed from the ground state, which is obtained as the solution of $\hat{a}|0\rangle = 0$, where the definition of \hat{a} [Eq. (2.40a)] has to be inserted.

The excitation spectrum of a Hamiltonian in the form of Eq. (2.42) can immediately be stated without knowledge of the real-space representation of the eigenfunctions. Instead of solving the differential equation for a particular Hamiltonian by constructing wave functions, the Hamiltonian itself can be mapped onto a bosonic Hamiltonian, where the eigenvalues are known.

This pertains to expectation values and matrix elements of \hat{x} and \hat{p} as well. It is possible to compute the moments of the position operator, e.g.,

$$\langle n|\hat{x}|n\rangle = \sqrt{\frac{\hbar}{2m\omega}} \langle n|\hat{a}^\dagger + \hat{a}|n\rangle = 0, \quad (2.47a)$$

$$\langle n|\hat{x}^2|n\rangle = \frac{\hbar}{2m\omega} \langle n|(\hat{a}^\dagger + \hat{a})^2|n\rangle = \frac{\hbar(2n+1)}{2m\omega}, \quad (2.47b)$$

without having to integrate the probability amplitude, i.e., the square of the absolute value of the wave function. This significantly reduces the complexity of the calculations. Note that Eq. (2.47a) justifies the previous statement that thermal expansion requires anharmonic potentials.

For the lattice dynamics, one has to bosonize the Hamiltonian

$$\hat{\mathcal{H}}_p = \sum_{im} \frac{\hat{\mathbf{P}}_{im}^2}{2M_i} + \sum_{mn} \sum_{ij} \sum_{\alpha\beta} C_{i\alpha}^{j\beta}(\mathbf{R}_n - \mathbf{R}_m) \hat{u}_{im}^\alpha \hat{u}_{jn}^\beta, \quad (2.48)$$

where $\hat{\mathbf{P}}$ is the momentum operator and M is the mass of the nuclei. The summation indices m and n , i and j , α and β represent unit cell indices, sublattice indices, components of displacement, respectively.

As a first step, I define the FOURIER transforms¹⁴

$$\hat{u}_{i\mathbf{k}}^\alpha = \frac{1}{\sqrt{\mathcal{N}_{\text{uc}}}} \sum_m e^{-i\mathbf{k}\cdot\mathbf{R}_{im}} \hat{u}_{im}^\alpha, \quad \hat{u}_{im}^\alpha = \frac{1}{\sqrt{\mathcal{N}_{\text{uc}}}} \sum_m e^{i\mathbf{k}\cdot\mathbf{R}_{im}} \hat{u}_{i\mathbf{k}}^\alpha, \quad (2.49a)$$

$$\hat{P}_{i\mathbf{k}}^\alpha = \frac{1}{\sqrt{\mathcal{N}_{\text{uc}}}} \sum_m e^{i\mathbf{k}\cdot\mathbf{R}_{im}} \hat{P}_{im}^\alpha, \quad \hat{P}_{im}^\alpha = \frac{1}{\sqrt{\mathcal{N}_{\text{uc}}}} \sum_m e^{-i\mathbf{k}\cdot\mathbf{R}_{im}} \hat{P}_{i\mathbf{k}}^\alpha \quad (2.49b)$$

of the momentum and displacement operators. These operators are not Hermitian and, instead, satisfy $(\hat{u}_{i\mathbf{k}}^\alpha)^\dagger = \hat{u}_{i(-\mathbf{k})}^\alpha$ and $(\hat{P}_{i\mathbf{k}}^\alpha)^\dagger = \hat{P}_{i(-\mathbf{k})}^\alpha$. Their commutation relation reads

$$\left[\hat{u}_{i\mathbf{k}}^\alpha, \hat{P}_{j\mathbf{k}'}^\beta \right] = i\hbar \delta_{\mathbf{k}\mathbf{k}'} \delta_{ij} \delta_{\alpha\beta}.$$

¹⁴The sign of the exponent is opposite in the FOURIER transform to guarantee that the Fourier components of the momentum and the position operators at different wave vectors commute. Sometimes, the same phase factor is used in the FOURIER transformation irrespective of the operator. In that case, the commutation relation is modified to $\left[\hat{u}_{i\mathbf{k}}^\alpha, \hat{P}_{j\mathbf{k}'}^\beta \right] = i\hbar \delta_{\mathbf{k}(-\mathbf{k}')} \delta_{ij} \delta_{\alpha\beta}$.

The Hamiltonian can be cast into the form

$$\hat{\mathcal{H}}_p = \sum_{\mathbf{k}} \left[\sum_i \sum_{\alpha} \frac{\hat{P}_{i(-\mathbf{k})}^{\alpha} \hat{P}_{i\mathbf{k}}^{\alpha}}{2M_i} + \frac{1}{2} \sum_{ij} \sum_{\alpha\beta} \sqrt{M_i M_j} \mathcal{D}_{i\alpha}^{j\beta}(\mathbf{k}) \hat{u}_{i(-\mathbf{k})}^{\alpha} \hat{u}_{j\mathbf{k}}^{\beta} \right]. \quad (2.50)$$

Here, the dynamical matrix $\mathcal{D}_{i\alpha}^{j\beta}(\mathbf{k})$ reappears in the quantum formulation that I have introduced in the solution of the classical equation of motion (cf. Section 2.2.2).

The Hamiltonian [Eq. (2.50)] has almost the form of that of the harmonic oscillator [Eq. (2.39)] with two important differences. (i) Instead of the squares of the momentum and the position operators, products of their FOURIER transform at \mathbf{k} and $-\mathbf{k}$ appear. (ii) The potential energy is nondiagonal in the sublattice and the displacement components if the dynamical matrix is nondiagonal. As a result, the mapping must include its eigenvectors, which are the polarization vectors $\epsilon_{\lambda\mathbf{k}}^{i\alpha}$.

One can check that the creation and annihilation operators defined as

$$\hat{\alpha}_{\lambda\mathbf{k}} = \sum_{i\alpha} \sqrt{\frac{1}{2\hbar M_i \omega_{\lambda\mathbf{k}}}} \left(M_i \omega_{\lambda\mathbf{k}} \epsilon_{\lambda(-\mathbf{k})}^{i\alpha} \hat{u}_{i\mathbf{k}}^{\alpha} + i \epsilon_{\lambda\mathbf{k}}^{i\alpha} \hat{P}_{i(-\mathbf{k})}^{\alpha} \right), \quad (2.51a)$$

$$\hat{\alpha}_{\lambda\mathbf{k}}^{\dagger} = \sum_{i\alpha} \sqrt{\frac{1}{2\hbar M_i \omega_{\lambda\mathbf{k}}}} \left(M_i \omega_{\lambda\mathbf{k}} \epsilon_{\lambda\mathbf{k}}^{i\alpha} \hat{u}_{i(-\mathbf{k})}^{\alpha} - i \epsilon_{\lambda(-\mathbf{k})}^{i\alpha} \hat{P}_{i\mathbf{k}}^{\alpha} \right) \quad (2.51b)$$

satisfy the bosonic commutation relations

$$\left[\hat{\alpha}_{\lambda\mathbf{k}}, \hat{\alpha}_{\sigma\mathbf{k}'}^{\dagger} \right] = \delta_{\mathbf{k}\mathbf{k}'} \delta_{\lambda\sigma}, \quad \left[\hat{\alpha}_{\lambda\mathbf{k}}, \hat{\alpha}_{\sigma\mathbf{k}'} \right] = \left[\hat{\alpha}_{\lambda\mathbf{k}}^{\dagger}, \hat{\alpha}_{\sigma\mathbf{k}'}^{\dagger} \right] = 0. \quad (2.52)$$

The angular frequencies $\omega_{\lambda\mathbf{k}}$ are obtained from the eigenvalues of the dynamical matrix [cf. Eq. (2.24)]. The inverse transformation

$$\hat{u}_{i\mathbf{k}}^{\alpha} = \sum_{\lambda} \sqrt{\frac{\hbar}{2M_i \omega_{\lambda\mathbf{k}}}} \epsilon_{\lambda\mathbf{k}}^{i\alpha} \left(\hat{\alpha}_{\lambda\mathbf{k}} + \hat{\alpha}_{\lambda(-\mathbf{k})}^{\dagger} \right), \quad (2.53a)$$

$$\hat{P}_{i\mathbf{k}}^{\alpha} = i \sum_{\lambda} \sqrt{\frac{\hbar M_i \omega_{\lambda\mathbf{k}}}{2}} \epsilon_{\lambda\mathbf{k}}^{i\alpha} \left(\hat{\alpha}_{\lambda\mathbf{k}}^{\dagger} - \hat{\alpha}_{\lambda(-\mathbf{k})} \right) \quad (2.53b)$$

can be applied to diagonalize the Hamiltonian [Eq. (2.50)]:

$$\hat{\mathcal{H}}_p = \sum_{\lambda\mathbf{k}} \hbar \omega_{\lambda\mathbf{k}} \left(\hat{\alpha}_{\lambda\mathbf{k}}^{\dagger} \hat{\alpha}_{\lambda\mathbf{k}} + \frac{1}{2} \right). \quad (2.54)$$

The Hamiltonian has been converted into that of an ensemble of noninteracting harmonic oscillators [cf. Eq. (2.42)]. For each mode characterized by the band index λ and the wave vector \mathbf{k} , the excitation spectrum is that of a harmonic oscillator with angular frequency $\omega_{\lambda\mathbf{k}}$. The eigenstates of the total Hamiltonian $|\{n_{\lambda\mathbf{k}}\}\rangle$ are therefore product states of the eigenstates with quantum numbers $n_{\lambda\mathbf{k}}$ of isolated harmonic oscillators.

In Section 2.2.2, the solution of the nuclear dynamics were plane waves of lattice vibrations. In the quantum theory, the solutions are quantized in terms of $n_{\lambda\mathbf{k}}$, which can be conceived as the number of quasiparticles per mode. As the ground state does not

comprise any quasiparticles, it corresponds to the quasiparticle vacuum. Adding quasiparticles to the system requires an energy of $\hbar\omega_{\lambda\mathbf{k}}$. These bosonic quasiparticles, which represent the collective lattice vibrations, are called *phonons*. The quantization of the lattice excitations on the one hand and their delocalized, wave-like nature on the other hand are manifestations of the particle-wave duality.

The second construction is based on a particular decomposition $\hat{\mathcal{H}}_{\text{p}} = \hat{\mathcal{H}}_{\text{intra}} + \hat{\mathcal{H}}_{\text{inter}}$ of the Hamiltonian. Consider the *isolated* one-dimensional vibrations along $\alpha \in \{x, y, z\}$ of the nuclei in the m -th unit cell on the i -th sublattice. Neglecting the interaction $\hat{\mathcal{H}}_{\text{inter}}$ between them, the intra-oscillator Hamiltonian

$$\hat{\mathcal{H}}_{\text{intra}} = \sum_{im\alpha} \left[\frac{(\hat{P}_{im}^\alpha)^2}{2M_i} + \frac{C_{i\alpha}^{i\alpha}(\mathbf{0})}{2} (\hat{u}_{im}^\alpha)^2 \right] = \sum_{im\alpha} \hbar\omega_{i\alpha} \left(\hat{a}_{i\alpha}^\dagger \hat{a}_{i\alpha} + \frac{1}{2} \right) \quad (2.55)$$

has the structure of uncoupled harmonic oscillators with angular frequencies $\omega_{i\alpha} = \sqrt{\frac{C_{i\alpha}^{i\alpha}(\mathbf{0})}{M_i}}$ so that local oscillator modes

$$\hat{a}_{i\alpha m} = \sqrt{\frac{1}{2\hbar M_i \omega_{i\alpha}}} \left(M_i \omega_{i\alpha} \hat{u}_{im}^\alpha + i \hat{P}_{im}^\alpha \right), \quad (2.56a)$$

$$\hat{a}_{i\alpha m}^\dagger = \sqrt{\frac{1}{2\hbar M_i \omega_{i\alpha}}} \left(M_i \omega_{i\alpha} \hat{u}_{im}^\alpha - i \hat{P}_{im}^\alpha \right) \quad (2.56b)$$

can be defined. The remaining inter-oscillator terms

$$\hat{\mathcal{H}}_{\text{inter}} = \sum_{mn} \sum_{ij} \sum_{\alpha\beta} (1 - \delta_{mn} \delta_{ij} \delta_{\alpha\beta}) C_{i\alpha}^{j\beta}(\mathbf{R}_n - \mathbf{R}_m) \hat{u}_{im}^\alpha \hat{u}_{jn}^\beta \quad (2.57)$$

couple the local one-dimensional oscillators to each other.

In the following, I will use a combined index μ (ν) for the sublattice index i (j) and the direction of vibration α (β). Furthermore, I define a modified dynamical matrix as

$$\tilde{\mathcal{D}}_{i\alpha}^{j\beta}(\mathbf{k}) = \frac{e^{i\mathbf{k}\cdot(\mathbf{b}_j - \mathbf{b}_i)}}{\sqrt{M_i M_j \omega_{i\alpha} \omega_{j\beta}}} \sum_n e^{i\mathbf{k}\cdot\mathbf{R}_n} C_{i\alpha}^{j\beta}(\mathbf{R}_n). \quad (2.58)$$

Then, the Hamiltonian can be compactly written as

$$\hat{\mathcal{H}}_{\text{p}} = \frac{1}{2} \sum_{\mathbf{k}} \hat{\phi}_{\mathbf{k}}^\dagger \mathbf{H}_{\text{p},\mathbf{k}} \hat{\phi}_{\mathbf{k}}, \quad (2.59)$$

where

$$\hat{\phi}_{\mathbf{k}}^\dagger = \left(\hat{a}_{1\mathbf{k}}^\dagger \quad \cdots \quad \hat{a}_{N_{\text{p}}\mathbf{k}}^\dagger \quad \hat{a}_{1(-\mathbf{k})} \quad \cdots \quad \hat{a}_{N_{\text{p}}(-\mathbf{k})} \right) \quad (2.60)$$

and

$$\mathbf{H}_{\text{p},\mathbf{k}} = \begin{pmatrix} \mathbf{A}_{\text{p},\mathbf{k}} & \mathbf{B}_{\text{p},\mathbf{k}} \\ \mathbf{B}_{\text{p},\mathbf{k}} & \mathbf{A}_{\text{p},\mathbf{k}} \end{pmatrix}, \quad (2.61a)$$

$$(\mathbf{A}_{\text{p},\mathbf{k}})_{\mu\nu} = \frac{\hbar}{2} \left[\tilde{\mathcal{D}}_{\mu}^{\nu}(\mathbf{k}) + \delta_{\mu\nu} \omega_{\mu} \right], \quad (2.61b)$$

$$(\mathbf{B}_{\text{p},\mathbf{k}})_{\mu\nu} = \frac{\hbar}{2} \left[\tilde{\mathcal{D}}_{\mu}^{\nu}(\mathbf{k}) - \delta_{\mu\nu} \omega_{\mu} \right]. \quad (2.61c)$$

As the local oscillator modes are no eigenmodes, the Hamiltonian couples different local modes. Consequently, the Hamilton matrix $\mathbf{H}_{\mathbf{p},\mathbf{k}} \in \mathbb{C}^{2\mathcal{N}_{\mathbf{p}} \times 2\mathcal{N}_{\mathbf{p}}}$ is nondiagonal. To obtain the normal modes and install a form like in Eq. (2.54), it has to be diagonalized and the normal modes have to be constructed as superpositions of the local oscillator modes. This is achieved by the so-called *BOGOLIUBOV diagonalization*, which is discussed in Section 2.3.4.

2.3 Theory of Spin Excitations: Magnons

Up to now, the electron dynamics has been neglected for the description of the lattice dynamics, which is justified by the adiabatic approximation (cf. Section 2.1). In the following, I address the electron dynamics disregarding the phonons. In particular, the aim of this section is to motivate the origin of magnetism and to present a formalism for the quantum-mechanical description of the magnetic ground state and the excitations. Analogous to the quantized, bosonic excitations of the *structural* order – the phonons –, a type of bosonic quasiparticle for the excitation of the *magnetic* order – the magnons – is introduced. Before I discuss any details, a general overview over the field of magnetism is given following Ref. [42].

Magnetic order can come in many forms and classes. Generally, one distinguishes between collinear and noncollinear magnetism [43]. Among the former, there exist ferromagnetism, ferrimagnetism, antiferromagnetism, and, discovered more recently, altermagnetism [43–45]. The latter includes coplanar magnetic phases such as helimagnets and noncoplanar phases such as skyrmions [43, 46]. All these forms of magnetism have in common that they rely on permanent magnetic moments in the absence of external magnetic fields. Generally, there is an ordering temperature, below which the symmetries of the Hamiltonian are spontaneously broken by the respective order parameters. The various forms differ by the order parameter, which depends on the collective orientations of the microscopic magnetic moments. They are contrasted by *paramagnetism* and *diamagnetism*, where permanent magnetic moments only exist in the presence of external magnetic fields [42].

While phenomena as diamagnetism and paramagnetism do not necessarily require interactions between magnetic moments, magnetic order does not exist without these. Owing to the variety of magnetic states, there exists no unified theory of magnetism.

In *magnetic insulators*, the electrons are localized in partially filled *d* or *f* orbitals and can be described by the HEISENBERG model [47], which is discussed in more detail in this Chapter. In contrast, magnetic metals feature delocalized electrons, which may or may not be responsible for magnetism.

For *band magnetism*, the delocalized electrons are responsible both for the magnetic properties and the electrical conduction. Figuratively speaking, the spin-up and spin-down bands, which are degenerate in the paramagnetic phase without external magnetic field, are shifted by the exchange interaction so that the electrons preferably occupy one band over the other. The HUBBARD model [48] is paradigmatic for that class. It treats the COULOMB interaction as a short-ranged, intra-atomic repulsion due to screening by mobile electrons – known as the HUBBARD interaction, which brings about spin-split energy bands. A special case is the STONER model [49, 50], where the spin-split bands result from a mean-field description of the HUBBARD interaction.

Localized magnetism refers to magnetic metals, in which the magnetic moments are generated by localized electrons and the transport properties are governed by itinerant electrons. The delocalized electrons' spins interact with the local magnetic moments and mediate an effective interaction between the localized permanent magnetic moments. This situation is captured in the KONDO-lattice model, also known as the *s-d* or *s-f* model [51–53].

This work focuses on magnetic insulators. First, the HEISENBERG Hamiltonian is motivated by a two-electron system, which provides an effective description of the many-body electron Hamiltonian in certain types of magnets by mapping the electron degrees of freedom onto spin degrees of freedom (cf. Section 2.3.1). The microscopic mechanisms, which give rise to a HEISENBERG Hamiltonian, and their applicability are briefly described. Moreover, extensions beyond the HEISENBERG Hamiltonian are discussed in Section 2.3.2. Second, a particular spin-to-boson mapping that allows to expand the spin Hamiltonian as series of bosonic Hamiltonians distinct in orders of $1/S$, where S is the length of the local spins, is introduced in Section 2.3.3. Finally, Section 2.3.4 is dedicated to the diagonalization of the resulting truncated bilinear Hamiltonian.

2.3.1 Heisenberg Model

The HEISENBERG model, as postulated by WERNER HEISENBERG in 1926 [47, 54], consists of an effective spin Hamiltonian¹⁵

$$\hat{\mathcal{H}}_s = \frac{1}{2\hbar^2} \sum_{ij} J_{ij} \hat{\mathbf{S}}_i \cdot \hat{\mathbf{S}}_j \quad (2.62)$$

that reproduces the low-energy spectrum of the original electron Hamiltonian, which does not (necessarily) depend on the spin degrees of freedom. It can be applied to molecules, magnetic insulators, and metals with localized magnetic moments if one is only interested in the effective interaction between them [42]. Depending on the concrete situation one wishes to describe, there are multiple microscopic theories such as the HEITLER-LONDON method, the RUDERMAN-KITTEL-KASUYA-YOSIDA interaction, and superexchange that give rise to a Hamiltonian like Eq. (2.62), although the interpretation of the exchange constant J changes [42]. However, one often treats J as a parameter so that the magnetic properties, e.g., magnetic order, magnon band structure, or magnetic phase transitions, can be used to determine the parameters of the spin Hamiltonian.

Instead of a microscopic theory, I present the general idea of the mapping for a two-electron Hamiltonian

$$\hat{\mathcal{H}} = \frac{\hat{\mathbf{p}}_1^2}{2m} + \frac{\hat{\mathbf{p}}_2^2}{2m} + \mathcal{V}(\mathbf{r}_1, \mathbf{r}_2) \quad (2.63)$$

following Refs. [2, 42, 55, 56]. The first two terms represent the kinetic energies of the electrons with momentum operator $\hat{\mathbf{p}}_i$ and electron mass m . $\mathcal{V}(\mathbf{r}_1, \mathbf{r}_2)$ represents the potential energy that includes the electron-electron repulsion.

¹⁵In order to define exchange constants J_{ij} in units of energy, the coefficient comprises a factor \hbar^2 to compensate the unit of angular momentum. This is merely a convention and can be avoided if one sets $\hbar = 1$. The factor $1/2$ accounts for double counting. Furthermore, the exchange constant is sometimes also defined with the opposite sign.

Since the two electrons are identical, they cannot be distinguished in a quantum-mechanical theory, where there is no notion of trajectories. It follows that the permutation operator $\hat{\mathcal{P}}_{12}$, which transforms position and momentum operators as

$$\hat{\mathcal{P}}_{12}\mathbf{r}_{1/2}\hat{\mathcal{P}}_{12} = \mathbf{r}_{2/1}, \quad (2.64a)$$

$$\hat{\mathcal{P}}_{12}\hat{\mathbf{p}}_{1/2}\hat{\mathcal{P}}_{12} = \hat{\mathbf{p}}_{2/1}, \quad (2.64b)$$

commutes with the Hamiltonian:

$$\left[\hat{\mathcal{H}}, \hat{\mathcal{P}}_{12}\right] = \left[\frac{\hat{\mathbf{p}}_1^2}{2m} + \frac{\hat{\mathbf{p}}_2^2}{2m}, \hat{\mathcal{P}}_{12}\right] + \left[\mathcal{V}(\mathbf{r}_1, \mathbf{r}_2), \hat{\mathcal{P}}_{12}\right] = 0. \quad (2.65)$$

According to the *symmetry postulate*, the HILBERT space of a system of identical particles contains either *only symmetric* or *only antisymmetric* wave functions [30]. The *spin-statistics theorem* relates the particles with the former symmetry to integer and those with the latter to half-odd integer spins [57]. Symmetric wave functions are eigenfunctions of $\hat{\mathcal{P}}_{12}$ with eigenvalue $+1$, while the antisymmetric wave function exhibit eigenvalue -1 . The special case of the symmetry postulate for electrons is known as the PAULI exclusion principle, which states that the many-electron wave function is antisymmetric.

The HILBERT space of the electrons is composed of a spatial and a spin subspace. Only the former is relevant for the energies of Eq. (2.63), as the Hamiltonian does not act in the spin space.¹⁶ It is therefore possible to construct the total wave function

$$|\Psi\rangle = |\psi\rangle^{(\pm)} |\chi\rangle^{(\mp)} \quad (2.66)$$

as a product of the spatial $|\psi\rangle^{(\pm)}$ and the spin wave functions $|\chi\rangle^{(\mp)}$. The superscript $+$ ($-$) signals the eigenvalue $+1$ (-1) under particle permutation. As the total wave function $|\Psi\rangle$ needs to be antisymmetric, the symmetric spatial part $|\psi\rangle^{(+)}$ is multiplied by the antisymmetric spin part $|\chi\rangle^{(-)}$ or vice versa.

While the spin wave function can be arbitrary for $|\Psi\rangle$ to be an eigenfunction of the two-electron Hamiltonian, the spatial part has to satisfy

$$\hat{\mathcal{H}}|\psi\rangle^{(\pm)} = \varepsilon_{\pm}|\psi\rangle^{(\pm)}, \quad (2.67)$$

where the energies ε_{\pm} are assumed to be the two lowest energies of the symmetric and antisymmetric eigenfunctions, respectively. The goal is to find an alternative Hamiltonian that acts on the spin but not on the spatial subspace and reproduces the same energy spectrum and the same corresponding spin wave functions:

$$\hat{\mathcal{H}}_s|\chi\rangle^{(\pm)} = \varepsilon_{\mp}|\chi\rangle^{(\pm)}. \quad (2.68)$$

Without the PAULI principle that relates the symmetries of spatial and spin wave functions, this attempt would be bound to fail because the original Hamiltonian [Eq. (2.63)] is spin degenerate and any spin wave function would be an eigenfunction. It is the PAULI principle that excludes combinations of certain spin states and energies leading to an effective spin splitting even in the absence of a magnetic field.

¹⁶Formally, it acts as an identity operator in the spin subspace.

The symmetric and antisymmetric spin wave functions

$$|\chi\rangle^{(+)} = |1, m\rangle, \quad m \in \{-1, 0, 1\}, \quad (2.69a)$$

$$|\chi\rangle^{(-)} = |0, 0\rangle \quad (2.69b)$$

can be constructed as the common eigenfunctions $|S, m\rangle$ of $\hat{\mathbf{S}}^2$ and \hat{S}_z , where $\hat{\mathbf{S}} = \hat{\mathbf{s}}_1 + \hat{\mathbf{s}}_2$ is the two-electron spin operator and $\hat{\mathbf{s}}_{1/2}$ are the two single-electron spin operators. Importantly, the triplet states $|1, m\rangle$ and the singlet states $|0, 0\rangle$ are symmetric and antisymmetric, respectively. Hence, the two-electron spin quantum number S discriminates between symmetric and antisymmetric *spin* wave functions, thereby it discriminates also between symmetric and antisymmetric *spatial* wave functions and their energies ε_{\pm} .

The spin quantum number is related to the eigenvalues of the operator $\hat{\mathbf{S}}^2$ by

$$\hat{\mathbf{S}}^2 |S, m\rangle = \hbar^2 S(S+1) |S, m\rangle. \quad (2.70)$$

Therefore, it can be used to define the effective Hamiltonian

$$\hat{\mathcal{H}}_s = \frac{\varepsilon_- - \varepsilon_+}{2\hbar^2} \hat{\mathbf{S}}^2 + \varepsilon_+, \quad (2.71)$$

which indeed satisfies Eq. (2.68). It is common to express the spin Hamiltonian in terms of single-electron spin rather than many-electron spin operators. Using its definition, one finds $\hat{\mathbf{S}}^2 = \hat{\mathbf{s}}_1^2 + \hat{\mathbf{s}}_2^2 + 2\hat{\mathbf{s}}_1 \cdot \hat{\mathbf{s}}_2$. Because electrons are spin-1/2 particles, $\hat{\mathbf{s}}_{1/2}^2$ can be replaced by $\frac{3\hbar^2}{4}$ and the effective Hamiltonian becomes

$$\hat{\mathcal{H}}_s = \frac{J}{\hbar^2} \hat{\mathbf{s}}_1 \cdot \hat{\mathbf{s}}_2 + \frac{3\varepsilon_- + \varepsilon_+}{4}, \quad (2.72)$$

where the exchange constant is $J = \varepsilon_- - \varepsilon_+$. This motivates the generalization of the HEISENBERG model to a lattice [cf. Eq. (2.62)], where $\hat{\mathbf{S}}_i$ do not represent spin operators of single electrons, but the collective spin of the electrons localized at the lattice site i . The constant energy term can be truncated as it corresponds to a gauge transformation of the potential energy, which is only defined up to a constant.

If $\varepsilon_+ \neq \varepsilon_-$, parallel ($S = 1$) and antiparallel alignment ($S = 0$) are energetically inequivalent, which is a necessity for magnetic order. Ferromagnetism is promoted by a negative J , which is the case if $\varepsilon_+ > \varepsilon_-$, i.e., the antisymmetric spatial part of the two-electron wave function needs to be energetically favorable, while antiferromagnetism is brought about by lower energies of the symmetric solution.

Although it is intuitively evident that without (electrostatic) electron-electron interactions, the electrons' spins would not "talk" to each other, I did not have to make statements about the potential energy $\mathcal{V}(\mathbf{r}_1, \mathbf{r}_2)$. However, only the genuine many-body terms in \mathcal{V} lift the degeneracy between symmetric and antisymmetric states and, thus, admit a nonzero J . To substantiate this crucial fact, I assume there were no interactions, allowing me to write $\mathcal{V}(\mathbf{r}_1, \mathbf{r}_2) = \mathcal{U}(\mathbf{r}_1) + \mathcal{U}(\mathbf{r}_2)$. Then, the two-electron Hamiltonian [Eq. (2.63)] would fragment into a sum of single-electron Hamiltonians and the eigenfunctions would be any product state of single-electron eigenfunctions $|\psi_{a/b}\rangle^{(1/2)}$, where a, b are quantum numbers of the single-electron Hamiltonians and 1/2 symbolize the two

single-electron HILBERT vectors/spaces.¹⁷ Then, the symmetric and antisymmetric wave functions $|\psi\rangle^{(\pm)} = |\psi_a\rangle^{(1)} |\psi_b\rangle^{(2)} \pm |\psi_b\rangle^{(1)} |\psi_a\rangle^{(2)}$ would be degenerate.

Considering the situation of two electrons in an atom as an example, the COULOMB repulsion between the electrons is minimized by an antisymmetric spatial wave function (i.e., $\varepsilon_+ > \varepsilon_-$) because it vanishes at $\mathbf{r}_1 = \mathbf{r}_2$. Hence, ferromagnetic order ($S = 1$) is favorable.¹⁸ This is known in the context of electronic configurations of atoms as the second HUND's rule, which states that electrons tend to maximize their total spin in unoccupied shells [58–60]. On the other hand, in a two-center system like a hydrogen molecule in the HEITLER-LONDON approximation, there is not only the mutual repulsion between the electrons, but also the attraction between electrons and protons, which leads to antiferromagnetic coupling [42, 56]. Therefore, different theories can lead to different expressions and magnitudes of the exchange constant J . Usually, J is treated as a parameter that can be fitted to theoretical or experimental results, e.g., the spin structure factor in inelastic neutron scattering measurements [23, 61].

2.3.2 Extended Heisenberg Model

The HEISENBERG model motivated above is isotropic in the spin degrees of freedom and, thus, does not couple the spins to the lattice. Realistic models of magnets must include other terms that may be derived from spin-orbit coupling or dipole-dipole interactions. Therefore, the spin Hamiltonian has to be generalized.

In general, the bilinear spin-spin interactions can be subsumed as [62–64]

$$\hat{\mathcal{H}}_s = \frac{1}{2\hbar^2} \sum_{ij} \hat{\mathbf{S}}_i^\top \mathbf{J}_{ij} \hat{\mathbf{S}}_j. \quad (2.73)$$

Here, the interaction parameters are given as entries of the interaction matrix $\mathbf{J}_{ij} = \mathbf{J}_{ji}^\top$. For $\mathbf{J}_{ij} = J_{ij} \mathbf{I}$, where $\mathbf{I} \in \mathbb{R}^{3 \times 3}$ is the identity matrix, the isotropic HEISENBERG model [Eq. (2.62)] is retrieved. Below, some other special types of interactions are discussed similarly to Ref. [65].

Anisotropic Interactions

There are two common types of anisotropic interaction, which break the continuous rotational symmetry of the isotropic HEISENBERG model. The single-ion anisotropy (or magnetocrystalline anisotropy) [42, 66]

$$\hat{\mathcal{H}}_{\text{si}} = \frac{A}{\hbar^2} \sum_i (\mathbf{e}_i \cdot \hat{\mathbf{S}}_i)^2, \quad (2.74)$$

can appear in the form of an easy-axis ($A < 0$) or an easy-plane anisotropy ($A > 0$), where the spins tend to align (anti-)parallel or in the plane perpendicular to the unit vector \mathbf{e}_i . This interaction is only relevant to spins with spin quantum numbers $S_i > 1/2$, because it becomes a constant for the case of spin $1/2$ rendering the interaction isotropic.

¹⁷Because of the indistinguishability of both electrons, the two single-particle Hamiltonians and HILBERT spaces are identical.

¹⁸If the energy corresponding to the quantum number a is sufficiently lower than that of b , it is energetically favorable to occupy a symmetric two-electron wave function $|\psi\rangle^{(+)} = |\psi_a\rangle^{(1)} |\psi_a\rangle^{(2)}$, which is associated with the singlet ($S = 0$) spin state. Such a state appears in the spectrum of parahelium [58].

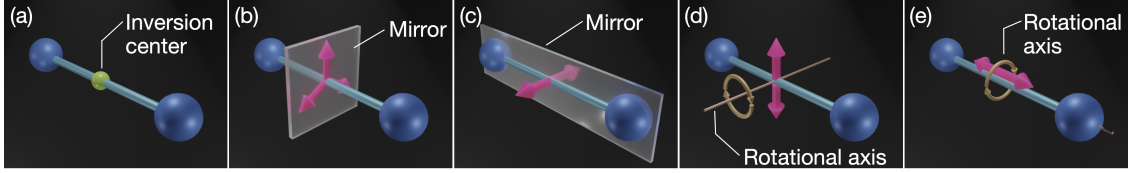


Figure 2.2: (a-e) The five MORIYA rules showing the possible orientations of the DZYALOSHINSKII-MORIYA vector (magenta arrows) between two magnetic sites (blue spheres) in the presence of (a) an inversion center, (b, c) mirror planes, and (d, e) rotational axes. In (a) the vector is zero.

In the Hamiltonian of the two-ion anisotropy [42]

$$\hat{\mathcal{H}}_{\text{ti}} = \frac{1}{2\hbar^2} \sum_{\substack{ij \\ i \neq j}} A_{ij} (\mathbf{e}_{ij} \cdot \hat{\mathbf{S}}_i) (\mathbf{e}_{ij} \cdot \hat{\mathbf{S}}_j), \quad (2.75)$$

spins at *different* sites are projected onto a unit vector \mathbf{e}_{ij} . This interaction resembles the ISING model if \mathbf{e}_{ij} is fixed [67]. Moreover, it has similarities to the anisotropic part of the dipolar interaction, which is why it is also known as the *pseudo-dipolar* interaction.

Dzyaloshinskii-Moriya Interaction

The antisymmetric interaction, parameterized as the nonzero elements of

$$\mathbf{J}_{ij} - \mathbf{J}_{ij}^\top = 2 \begin{pmatrix} 0 & D_{ij}^z & -D_{ij}^y \\ -D_{ij}^z & 0 & D_{ij}^x \\ D_{ij}^y & -D_{ij}^x & 0 \end{pmatrix}, \quad (2.76)$$

is known as the DZYALOSHINSKII-MORIYA interaction [68, 69]

$$\hat{\mathcal{H}}_{\text{DMI}} = \frac{1}{2\hbar^2} \sum_{ij} \mathbf{D}_{ij} \cdot (\hat{\mathbf{S}}_i \times \hat{\mathbf{S}}_j). \quad (2.77)$$

Classically, the interaction prefers canted spins in the plane perpendicular to $\mathbf{D}_{ij} = -\mathbf{D}_{ji}$ and was historically predicted in 1958 by IGOR E. DZYALOSHINSKII to explain the weak ferromagnetism found in antiferromagnets based on symmetry considerations [68]. In 1960, this interaction was microscopically derived and ascribed to spin-orbit coupling by TÔRU MORIYA [69].

The existence and the directions of the axial vector \mathbf{D}_{ij} are restricted by the symmetry of the lattice as summarized by the *MORIYA rules* that are visualized in Fig. 2.2. Let A be the position of site i , B that of site j , and C the location of the center between A and B . Then, the MORIYA rules read [69]

1. If a center of inversion is located at C , $\mathbf{D}_{ij} = \mathbf{0}$.
2. If a mirror plane perpendicular to AB passes through C , $\mathbf{D}_{ij} \perp AB$.
3. If a mirror plane including A and B exists, $\mathbf{D}_{ij} \perp$ mirror plane.

4. If a two-fold rotation axis \mathbf{n} perpendicular to AB passes through C , $\mathbf{D}_{ij} \perp \mathbf{n}$.
5. If there is an n -fold axis ($n \geq 2$) along AB , $\mathbf{D}_{ij} \parallel AB$.

These rules can be derived using the transformation properties of axial vectors. Axial vectors are by definition even under inversion. If a symmetry operation interchanges i and j , \mathbf{D}_{ij} must be chosen to change sign. Whenever this can not be achieved (rule 1), it has to vanish.

Special Interactions In Honeycomb Lattices

The honeycomb lattice is a bipartite, two-dimensional lattice with hexagonal symmetry and two sites per primitive unit cell. Each site is connected with three different neighbors by bonds that pairwise include an angle of 120° .

The DZHALOSHINSKII-MORIYA interaction is forbidden between nearest neighbors because of an inversion center at the midpoint of the bond (rule 1). However, an out-of-plane \mathbf{D}_{ij} is allowed between next-nearest neighbors (rule 3).

An important spin-spin interaction derived from spin-orbit coupling in honeycomb lattices is the KITAEV interaction [70]

$$\hat{\mathcal{H}}_K = \frac{K}{2\hbar^2} \sum_{\langle ij \rangle_\gamma} \hat{S}_i^\gamma \hat{S}_j^\gamma, \quad (2.78)$$

where the sum runs over nearest-neighbor sites $\langle ij \rangle$. Here, for each of the three bonds, mutually orthogonal spin components $\gamma = x, y, z$ are considered. Furthermore, the KITAEV interaction is commonly accompanied by the Gamma

$$\hat{\mathcal{H}}_\Gamma = \frac{\Gamma}{2\hbar^2} \sum_{\langle ij \rangle_\gamma} \left(\hat{S}_i^\alpha \hat{S}_j^\beta + \hat{S}_i^\beta \hat{S}_j^\alpha \right), \quad (2.79)$$

and the Gamma' interaction

$$\hat{\mathcal{H}}_{\Gamma'} = \frac{\Gamma'}{2\hbar^2} \sum_{\langle ij \rangle_\gamma} \left(\hat{S}_i^\gamma \hat{S}_j^\alpha + \hat{S}_i^\alpha \hat{S}_j^\beta + \hat{S}_i^\beta \hat{S}_j^\gamma + \hat{S}_i^\gamma \hat{S}_j^\beta \right), \quad (2.80)$$

where the α and β refer to the remaining components orthogonal to γ [71–74].

Magnetostatic Interactions

The action of an external magnetic field is commonly described by the ZEEMAN Hamiltonian [42]

$$\hat{\mathcal{H}}_Z = \frac{g\mu_B}{\hbar} \mathbf{B} \cdot \sum_i \hat{\mathbf{S}}_i, \quad (2.81)$$

where g is the gyromagnetic factor, and μ_B is the BOHR magneton. This interaction can be understood by classical physics as every spin $\hat{\mathbf{S}}_i$ encompasses an antiparallel magnetic moment $\hat{\mathbf{m}}_i = -\frac{g\mu_B}{\hbar} \hat{\mathbf{S}}_i$ that is aligned by the magnetic field.

Furthermore, classical dipole-dipole interactions

$$\hat{\mathcal{H}}_{\text{dd}} = \frac{g\mu_{\text{B}}}{\hbar} \sum_{\substack{ij \\ i \neq j}} \hat{\mathbf{S}}_i \cdot \hat{\mathbf{B}}_j(\mathbf{r}_i - \mathbf{r}_j) \quad (2.82)$$

can be included by substituting \mathbf{B} in $\hat{\mathcal{H}}_Z$ by the magnetic dipole field

$$\hat{\mathbf{B}}_j(\mathbf{r}) = \frac{\mu_0}{4\pi} \frac{3\mathbf{r}(\mathbf{r} \cdot \hat{\mathbf{m}}_j) - |\mathbf{r}|^2 \hat{\mathbf{m}}_j}{|\mathbf{r}|^5} \quad (2.83)$$

generated by the surrounding spins j [42, 75, 76]. Since the energy scale is in the order of μeV and, thus, around three orders of magnitude smaller than the typical exchange interaction, it is neglected in this work.

2.3.3 Second Quantization

Previously, it was motivated that the low-energy many-body electronic degrees of freedom in a magnetic insulator can be effectively mapped onto the spin degrees of freedom by introducing a (spin) Hamiltonian that only acts on the spin but no longer on the spatial part of the wave function. In other words, the problem of electron dynamics has been transformed into a problem of spin dynamics.

There are several approaches to solve the spin dynamics. Atomistic spin dynamics simulations [63, 65] involve deriving the equations of motion of the classical spin variables, the LANDAU-LIFSHITZ-GILBERT equation [77, 78], which can be numerically integrated. To describe thermal effects, LANGEVIN dynamics is employed, which involves randomly fluctuating magnetic fields whose variance increases with temperature [79–82]. As an advantage, the interaction between the spins, as given by the Hamiltonian, can be treated without approximations. The disadvantage is, however, that the classical results do not apply at low temperatures, where quantum effects become essential.

In this work, a transformation mapping spin operators to bosonic operators, as done for phonons in Section 2.2.3, is presented. This approach is usually suited in the low-temperature regime with magnetic order and can capture quantum effects. The theory is introduced in text books such as Refs. [42, 54, 61] and a more general situation is considered in Ref. [64].

General Theory

Published in 1940, THEODORE HOLSTEIN and HENRY PRIMAKOFF introduced the transformation [11]

$$\frac{\hat{S}_i^+}{\hbar} = \sqrt{2S - \hat{b}_i^\dagger \hat{b}_i} \hat{b}_i, \quad \frac{\hat{S}_i^-}{\hbar} = \hat{b}_i^\dagger \sqrt{2S - \hat{b}_i^\dagger \hat{b}_i}, \quad \frac{\hat{S}_i^z}{\hbar} = S - \hat{b}_i^\dagger \hat{b}_i, \quad (2.84)$$

that maps the local spin operators $\hat{S}_i^\pm = \hat{S}_i^x \pm i\hat{S}_i^y$ and \hat{S}_i^z of the i -th site onto local bosonic creation and annihilation operators \hat{b}_i^\dagger and \hat{b}_i , hence, they fulfill the commutation relations $[\hat{b}_i, \hat{b}_j] = [\hat{b}_i^\dagger, \hat{b}_j^\dagger] = 0$ and $[\hat{b}_i, \hat{b}_j^\dagger] = \delta_{ij}$. The action of the newly defined bosonic operators can be understood in the common eigenbasis $|S, m\rangle$ of $\hat{\mathbf{S}}_i^2$ and \hat{S}_i^z , onto which the spin

ladder operators act as $\hat{S}_i^\pm |S, m\rangle = \sqrt{S(S+1) - m(m \pm 1)} |S, m \pm 1\rangle$ [54]. Ignoring the square roots in Eq. (2.84), \hat{b}_i^\dagger is related to \hat{S}_i^- , while \hat{b}_i appears in \hat{S}_i^+ . Furthermore, the number operator $\hat{n}_i = \hat{b}_i^\dagger \hat{b}_i$ measures the deviations of the z component $\hbar m$ from its fully polarized state $S = m$. Therefore, the bosonic quasiparticles correspond to local spin flips of the fully-polarized (ground) state.

The transformation Eq. (2.84) is only a special case that applies to ferromagnets with magnetization along z . It can be generalized to describe antiferromagnetic or noncollinear ground states as well. First, one needs to ascertain the classical ground state by treating the spin operators $\hat{\mathbf{S}}_i \rightarrow S_i \mathbf{z}_i$ as classical vectors of length S_i and direction \mathbf{z}_i and minimize the classical spin HAMILTON function corresponding to $\hat{\mathcal{H}}_s$ with respect to $\{\mathbf{z}_i\}$. Then, one chooses arbitrary orthogonal axes \mathbf{x}_i and \mathbf{y}_i that form a tripod with \mathbf{z}_i . With the local quantization axis defined by \mathbf{z}_i , the general HOLSTEIN-PRIMAKOFF transformation reads [64]

$$\frac{\hat{\mathbf{S}}_i}{\hbar} = \sqrt{\frac{S_i}{2}} \left(\mathbf{e}_i^+ \hat{b}_i^\dagger \hat{f}_i + \mathbf{e}_i^- \hat{f}_i \hat{b}_i \right) + \mathbf{z}_i \left(S_i - \hat{b}_i^\dagger \hat{b}_i \right), \quad (2.85)$$

where S_i is the spin quantum number of the i -th spin and $\mathbf{e}_i^\pm = \mathbf{x}_i \pm i\mathbf{y}_i$. The operator

$$\hat{f}_i = \sqrt{1 - \frac{\hat{b}_i^\dagger \hat{b}_i}{2S_i}} \quad (2.86)$$

is defined by the series expansion $\sqrt{1-x} = 1 - \frac{x}{2} - \frac{x^2}{8} - \frac{x^3}{16} + \mathcal{O}(x^4)$ of the square root.

Therefore, any *spin* Hamiltonian

$$\hat{\mathcal{H}}_s = \sum_{r=0}^{\infty} \hat{\mathcal{H}}_b^{(r)} \quad (2.87)$$

can be written as a sum of *bosonic* Hamiltonians, which is an expansion in powers of creation and annihilation operators. Here, $\hat{\mathcal{H}}_b^{(r)}$ comprises products of r creation or annihilation operators.¹⁹

In the *harmonic approximation* the expansion is truncated beyond $r = 2$ so that only two nonzero terms remain. $\hat{\mathcal{H}}_b^{(0)}$ is the classical ground state energy proportional to S^2 (assuming uniform spin lengths) that is obtained from the spin HAMILTON function, which in turn is minimized by $\{\mathbf{z}_i\}$. Furthermore, $\hat{\mathcal{H}}_b^{(2)}$ represents the excitations above the ground state (and the quantum corrections of the ground state) that can be mapped onto the harmonic oscillator, as demonstrated below. Note that $\hat{\mathcal{H}}_b^{(1)}$ corresponding to the spontaneous creation or annihilation of spin deflections from the quantization axes has to vanish for the correct classical magnetic ground state.

Instead of representing each spin by a site index, henceforth, the notation of, e.g., the local spin operators is changed to $\hat{\mathbf{S}}_{im}$, where the first index i distinguishes the sublattices and the second one m represents the unit cell. Then, the FOURIER transformed creation

¹⁹Note that the number of creation and annihilation operators for a fixed expression depends on the order. Consider the expression $\hat{b}^\dagger \hat{b}$, which can also be written as $\hat{b} \hat{b}^\dagger - 1$. It is expedient to perform a *normal-ordered series expansion*, where all creation operators are written left of all annihilation operators.

and annihilation operators are introduced as

$$\hat{b}_{i\mathbf{k}} = \frac{1}{\sqrt{\mathcal{N}_{\text{uc}}}} \sum_m e^{-i\mathbf{k}\cdot\mathbf{R}_{im}} \hat{b}_{im}, \quad \hat{b}_{im} = \frac{1}{\sqrt{\mathcal{N}_{\text{uc}}}} \sum_m e^{i\mathbf{k}\cdot\mathbf{R}_{im}} \hat{b}_{i\mathbf{k}}, \quad (2.88a)$$

$$\hat{b}_{i\mathbf{k}}^\dagger = \frac{1}{\sqrt{\mathcal{N}_{\text{uc}}}} \sum_m e^{i\mathbf{k}\cdot\mathbf{R}_{im}} \hat{b}_{im}^\dagger, \quad \hat{b}_{im}^\dagger = \frac{1}{\sqrt{\mathcal{N}_{\text{uc}}}} \sum_m e^{-i\mathbf{k}\cdot\mathbf{R}_{im}} \hat{b}_{i\mathbf{k}}^\dagger, \quad (2.88b)$$

which allows representing

$$\hat{\mathcal{H}}_{\text{b}}^{(2)} = \frac{1}{2} \sum_{\mathbf{k}} \hat{\psi}_{\mathbf{k}}^\dagger \mathbf{H}_{\mathbf{m},\mathbf{k}} \hat{\psi}_{\mathbf{k}} + \text{const} \quad (2.89)$$

as a BOGOLIUBOV-DE GENNES Hamiltonian that involves the NAMBU spinors

$$\hat{\psi}_{\mathbf{k}}^\dagger = \left(\hat{b}_{1\mathbf{k}}^\dagger \quad \cdots \quad \hat{b}_{\mathcal{N}_m\mathbf{k}}^\dagger \quad \hat{b}_{1(-\mathbf{k})} \quad \cdots \quad \hat{b}_{\mathcal{N}_m(-\mathbf{k})} \right) \quad (2.90)$$

and the HAMILTON matrix $\mathbf{H}_{\mathbf{m},\mathbf{k}} \in \mathbb{C}^{2\mathcal{N}_m \times 2\mathcal{N}_m}$. $\mathcal{N}_m = \mathcal{N}_{\text{sl}}$ is the number of magnon bands.

This form accounts for anomalous magnon pairing terms $\hat{b}_{i\mathbf{k}} \hat{b}_{j\mathbf{k}'}$ and $\hat{b}_{i\mathbf{k}}^\dagger \hat{b}_{j\mathbf{k}'}^\dagger$ in the Hamiltonian that break the magnon number conservation. These terms, which also appear in the BARDEEN-COOPER-SCHRIEFFER theory of superconductivity [2], can be elegantly represented in an extended, redundant basis $\hat{\psi}_{\mathbf{k}}$. Here, each mode characterized by a sublattice index i and wave vector \mathbf{k} exists as a particle-like $\hat{\psi}_{i\mathbf{k}}^\dagger = \hat{b}_{i\mathbf{k}}^\dagger$ and a hole-like state $\hat{\psi}_{i+\mathcal{N}_m,\mathbf{k}}^\dagger = \hat{b}_{i(-\mathbf{k})}$.

General explicit expressions for $\mathbf{H}_{\mathbf{m},\mathbf{k}}$ can be given by considering the generic spin Hamiltonian

$$\hat{\mathcal{H}}_{\text{s}} = \frac{1}{2\hbar^2} \sum_{mn} \sum_{ij} \hat{\mathbf{S}}_{im}^\top \mathbf{J}_{ij}(\mathbf{R}_n - \mathbf{R}_m) \hat{\mathbf{S}}_{jn} + \frac{g\mu_{\text{B}}}{\hbar} \mathbf{B} \cdot \sum_{im} \hat{\mathbf{S}}_{im}. \quad (2.91)$$

In the following, I assume without loss of generality that the contingent symmetry $\mathbf{J}_{ij}(\mathbf{R}) = \mathbf{J}_{ji}^\top(-\mathbf{R})$ is installed in the definition of the bilinear spin-spin interaction matrix \mathbf{J} . By defining the magnonic analogue to the dynamical matrix

$$\mathcal{J}_{ij}(\mathbf{k}) = \sum_m e^{i\mathbf{k}\cdot(\mathbf{R}_m + \mathbf{b}_j - \mathbf{b}_i)} \mathbf{J}_{ij}(\mathbf{R}_m) \quad (2.92)$$

as the FOURIER transform of $\mathbf{J}_{ij}(\mathbf{R}_n - \mathbf{R}_m)$, the magnon HAMILTON matrix can be compactly expressed as

$$\mathbf{H}_{\mathbf{m},\mathbf{k}} = \begin{pmatrix} \mathbf{A}_{\mathbf{m},\mathbf{k}} & \mathbf{B}_{\mathbf{m},\mathbf{k}} \\ \mathbf{B}_{\mathbf{m},-\mathbf{k}}^\top & \mathbf{A}_{\mathbf{m},-\mathbf{k}}^\top \end{pmatrix}, \quad (2.93a)$$

$$(\mathbf{A}_{\mathbf{m},\mathbf{k}})_{ij} = (A_{\mathbf{m},\mathbf{k}}^{+-})_{ij} + (A_{\mathbf{m},\mathbf{k}}^{zz})_{ij} + (A_{\mathbf{m},\mathbf{k}}^Z)_{ij}, \quad (2.93b)$$

$$(A_{\mathbf{m},\mathbf{k}}^{+-})_{ij} = \frac{\sqrt{S_i S_j}}{2} (\mathbf{e}_i^+)^\top \mathcal{J}_{ij}(\mathbf{k}) \mathbf{e}_j^-, \quad (2.93c)$$

$$(A_{\mathbf{m},\mathbf{k}}^{zz})_{ij} = \delta_{ij} \sum_l S_l \mathbf{z}_i^\top \mathcal{J}_{il}(\mathbf{0}) \mathbf{z}_l, \quad (2.93d)$$

$$(A_{\mathbf{m},\mathbf{k}}^Z)_{ij} = \delta_{ij} g\mu_{\text{B}} \mathbf{B} \cdot \mathbf{z}_i, \quad (2.93e)$$

$$(\mathbf{B}_{\mathbf{m},\mathbf{k}})_{ij} = \frac{\sqrt{S_i S_j}}{2} (\mathbf{e}_i^+)^\top \mathcal{J}_{ij}(\mathbf{k}) \mathbf{e}_j^+. \quad (2.93f)$$

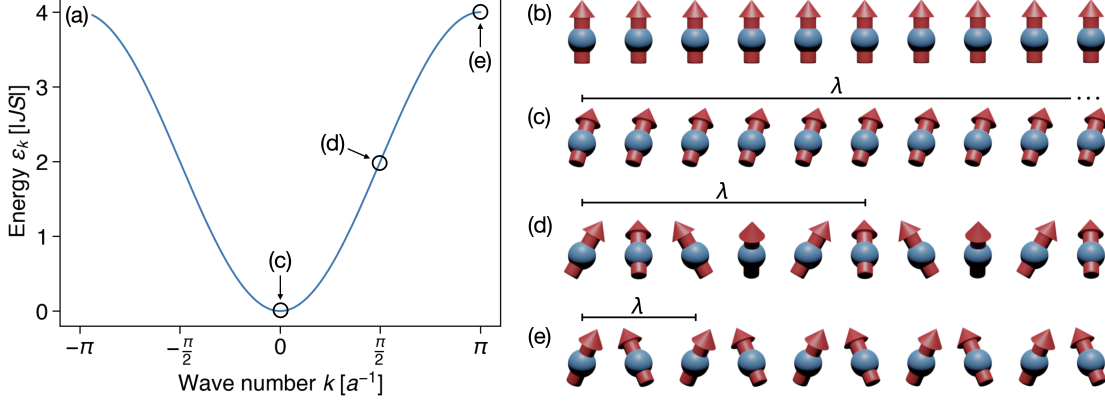


Figure 2.3: Magnon spectrum and selected magnon modes of one-dimensional HEISENBERG ferromagnet. (a) Magnon band structure featuring one band. (b) Collinear spin texture of the ferromagnetic ground state. (c–e) Snapshots of spin waves of different wave numbers (c) $k = 0$, (d) $k = \pi/2a$, and (e) $k = \pi/a$ [cf. panel (a)].

Note that $\mathbf{A}_{\mathbf{m},\mathbf{k}}$ is Hermitian and $\mathbf{B}_{\mathbf{m},\mathbf{k}} = \mathbf{B}_{\mathbf{m},-\mathbf{k}}^*$ so that $\mathbf{H}_{\mathbf{m},\mathbf{k}}$ is Hermitian.

Ferromagnetic Heisenberg Chain

The Hamiltonian of the one-dimensional HEISENBERG ferromagnet

$$\hat{\mathcal{H}}_s = \frac{J}{\hbar^2} \sum_i \hat{\mathbf{S}}_i \cdot \hat{\mathbf{S}}_{i+1} \quad (2.94)$$

only comprises ferromagnetic exchange interaction ($J < 0$) between nearest neighbors, wherefore the spins are mutually parallel in the classical ground state, e.g., $\mathbf{z}_i \parallel \mathbf{z}$.²⁰ Employing the HOLSTEIN-PRIMAKOFF transformation [Eq. (2.84)], the Hamiltonian in the harmonic approximation reads

$$\hat{\mathcal{H}}_m = J \sum_i \left[S^2 - 2S\hat{b}_i^\dagger \hat{b}_i + S\hat{b}_i^\dagger \hat{b}_{i+1} + S\hat{b}_{i+1}^\dagger \hat{b}_i \right], \quad (2.95)$$

which can be transformed into

$$\hat{\mathcal{H}}_m = JS^2\mathcal{N}_{uc} + \sum_k \varepsilon_{\mathbf{m},k} \hat{b}_k^\dagger \hat{b}_k, \quad \varepsilon_{\mathbf{m},k} = -4JS \sin^2 \frac{ka}{2} \quad (2.96)$$

with the FOURIER transformation of the creation and annihilation operators [Eq. (2.88)]. Here, a is the lattice constant and $\varepsilon_{\mathbf{m},k}$ describes the dispersion relation of the spin waves [cf. Fig. 2.3(a)].

The transformed Hamiltonian assumes the same shape as that of the harmonic oscillator [Eq. (2.42)] and that of quantized phonons [Eq. (2.54)]. Note, however, that the quantum fluctuations that correct the ground state energy by $\varepsilon_{\mathbf{m},k}/2$ are absent, as the ground state

²⁰Since the Hamiltonian is isotropic, there is a continuous degeneracy of the ground state manifold. By making the explicit choice $\mathbf{z}_i \parallel \mathbf{z}$, the symmetry is spontaneously broken.

is exact. Pictorially, the normal modes are spin waves, in which each localized atomic spin precesses about its ground state orientation \mathbf{z} [depicted in Fig. 2.3(b)] with an angular frequency $\varepsilon_{m,k}/\hbar$. Depending on the wave number k , the spins precess in phase for $k = 0$ [Fig. 2.3(c)], with a phase shift of 90° between neighbors for $k = \pi/2a$ [Fig. 2.3(d)], in antiphase for $k = \pi/a$ [Fig. 2.3(e)] or anything in between. In the quantum theory, the spin waves are described by the bosonic quasiparticles created and annihilated by \hat{b}_k^\dagger and \hat{b}_k called *magnons*.

In the long wavelength limit, $k \rightarrow 0$, the magnon energy $\varepsilon_{m,k} \propto k^2$ is quadratic in k [cf. Fig. 2.3(a)], which is unlike the linear dispersion of acoustic phonons [cf. Eq. (2.37a)], and vanishes for infinite wavelength. This is another example of the GOLDSTONE theorem, which guarantees the zero-energy mode based on the symmetry of the Hamiltonian. The original spin Hamiltonian [Eq. (2.94)] respects isotropy with respect to the global spin axes. In other words, the global quantization axis is not unique. By fixing a classical ground state direction, two of three spin rotation axes are broken. However, there is only one GOLDSTONE mode.

To understand this discrepancy, two types of such modes have to be distinguished. Type-I (type-II) modes are those that have dispersion relations with odd (even) powers of their momenta [35, 37, 83]. The number of type-I (n_I) and type-II modes (n_{II}) is related to the number of broken generators n_{bg} as [35–37]

$$n_I + 2n_{II} = n_{bg}. \quad (2.97)$$

Applied to the present case, $n_{bg} = 2$ so that $n_{II} = 1$. On the contrary, the zero-energy states in the acoustic phonon branches correspond to type-I modes, which is why their number equals the number of broken symmetry generators.

2.3.4 Bogoliubov Transformation

The previous example of the HEISENBERG ferromagnet was a special case that was diagonalized by FOURIER transformation. In general, however, one deals with systems that are not described by BRAVAIS lattices because they have a structural basis or the magnetic unit cell is increased by the magnetic superstructure. In these cases, the HOLSTEIN-PRIMAKOFF transformation leads to a Hamiltonian like Eq. (2.89). Such a Hamiltonian requires a particular diagonalization procedure. Here, the general and mathematical framework of Ref. [84] is transferred to the magnon theory and the idea is exemplified by a HEISENBERG antiferromagnet afterwards.

General Theory

Because of the nondiagonal structure of the BOGOLIUBOV-DE GENNES Hamiltonian $\hat{\mathcal{H}}_b^{(2)}$ [Eq. (2.89)] and the pairing terms, the normal modes $\hat{\beta}_k^\dagger \propto \hat{b}_k^\dagger + \hat{b}_{-k}$ are superpositions of particle- and hole-like excitations. In the NAMBU notation, the creation and annihilation operators of the normal modes can be subsumed in the spinor

$$\hat{\Psi}_k^\dagger = \left(\hat{\beta}_{1k}^\dagger \quad \cdots \quad \hat{\beta}_{\mathcal{N}_m k}^\dagger \quad \hat{\beta}_{1(-k)} \quad \cdots \quad \hat{\beta}_{\mathcal{N}_m(-k)} \right), \quad (2.98)$$

which is constructed as a linear combination

$$\hat{\Psi}_k = \mathbf{T}_k^{-1} \hat{\psi}_k \quad (2.99)$$

of the HOLSTEIN-PRIMAKOFF modes $\hat{\psi}_{\mathbf{k}}$.

Two conditions have to be satisfied by the operators $\hat{\beta}_{m\mathbf{k}}$ and $\hat{\beta}_{m\mathbf{k}}^\dagger$: (i) they have to fulfill the bosonic commutation relations and (ii) they have to be the normal modes of the bilinear part of the bosonic Hamiltonian $\hat{\mathcal{H}}_b^{(2)}$.

Condition (i) implies $[\hat{\Psi}_{m\mathbf{k}}, \hat{\Psi}_{n\mathbf{k}'}] = [\hat{\Psi}_{m\mathbf{k}}, \hat{\Psi}_{n\mathbf{k}'}^\dagger] = 0$ and $[\hat{\Psi}_{m\mathbf{k}}, \hat{\Psi}_{n\mathbf{k}'}^\dagger] = \delta_{\mathbf{k}\mathbf{k}'}(\sigma_3)_{mn}$. Here, $\sigma_3 = \text{diag}(1 \ \cdots \ 1 \ -1 \ \cdots \ -1) \in \mathbb{R}^{2\mathcal{N}_m \times 2\mathcal{N}_m}$ is the bosonic metric. Consequently,

$$\mathbf{T}_{\mathbf{k}}^\dagger \sigma_3 \mathbf{T}_{\mathbf{k}} = \sigma_3, \quad \text{or} \quad \mathbf{T}_{\mathbf{k}} \sigma_3 \mathbf{T}_{\mathbf{k}}^\dagger = \sigma_3, \quad \text{or} \quad \mathbf{T}_{\mathbf{k}}^\dagger \sigma_3 = \sigma_3 \mathbf{T}_{\mathbf{k}}^{-1}, \quad (2.100)$$

must be fulfilled. Matrices with this property are called *paraunitary*.

Condition (ii) implies that the bilinear Hamiltonian can be expressed as

$$\hat{\mathcal{H}}_b^{(2)} = \sum_{\mathbf{k}} \sum_{\lambda} \varepsilon_{m,\lambda\mathbf{k}} \hat{\beta}_{\lambda\mathbf{k}}^\dagger \hat{\beta}_{\lambda\mathbf{k}} + \text{const}, \quad (2.101)$$

which is achieved by requiring

$$\mathbf{T}_{\mathbf{k}}^\dagger \mathbf{H}_{m,\mathbf{k}} \mathbf{T}_{\mathbf{k}} = \mathcal{E}_{\mathbf{k}} = \text{diag}(\varepsilon_{m,1\mathbf{k}} \ \cdots \ \varepsilon_{m,\mathcal{N}_m\mathbf{k}} \ \varepsilon_{m,1(-\mathbf{k})} \ \cdots \ \varepsilon_{m,\mathcal{N}_m(-\mathbf{k})}). \quad (2.102)$$

Assume that such a matrix $\mathbf{T}_{\mathbf{k}}$ exists and let $\mathbf{t}_{m\mathbf{k}}$ denote its column vectors. Using the conditions (i) and (ii), one derives the eigenvalue problem

$$(\sigma_3 \mathbf{H}_{m,\mathbf{k}} - (\sigma_3)_{mm} \varepsilon_{m,m\mathbf{k}}) \mathbf{t}_{m\mathbf{k}} = 0. \quad (2.103)$$

Therefore, the magnon energies and eigenvectors are obtained from the eigenvalue problem of the non-Hermitian matrix $\sigma_3 \mathbf{H}_{m,\mathbf{k}}$. This evokes several questions. (i) Are the eigenvalues of the non-Hermitian matrix $\sigma_3 \mathbf{H}_{m,\mathbf{k}}$ real? (ii) Does the paraunitary matrix $\mathbf{T}_{\mathbf{k}}$ with $\mathbf{t}_{m\mathbf{k}}$ as its column vectors exist? (iii) How can the magnon eigenvectors and eigenvalues be obtained in practice?

The answer of the first and partly the second question is given by the following theorem: *A $2m$ -dimensional Hermitian matrix \mathbf{A} can be paraunitarily diagonalized into a matrix with positive diagonal elements if and only if \mathbf{A} is positive definite.*

The restriction to positive definite matrices ensures that the magnon energies are indeed positive. Although it ensures the stability of the magnetic ground state, the theorem does not cover the case of zero-energy modes as forced by the GOLDSTONE theorem. In the below example, it is demonstrated that the theorem cannot be generalized to positive semidefinite matrices.

The third question is answered by a construction algorithm for $\mathbf{T}_{\mathbf{k}}$ that involves the following 4 steps.

1. Decompose the $2\mathcal{N}_m$ square positive definite Hermitian matrix $\mathbf{H}_{m,\mathbf{k}}$ as $\mathbf{H}_{m,\mathbf{k}} = \mathbf{K}_{\mathbf{k}}^\dagger \mathbf{K}_{\mathbf{k}}$ by employing, e.g., the CHOLESKY decomposition.
2. Diagonalize the Hermitian matrix $\mathbf{K}_{\mathbf{k}} \sigma_3 \mathbf{K}_{\mathbf{k}}^\dagger$ by means of the unitary matrix $\mathbf{U}_{\mathbf{k}}$ resulting in the diagonal matrix $\mathbf{L}_{\mathbf{k}}$.
3. The eigenvalues are given as $\mathcal{E}_{\mathbf{k}} = \sigma_3 \mathbf{L}_{\mathbf{k}}$.
4. The eigenvectors are obtained from $\mathbf{U}_{\mathbf{k}} \mathcal{E}_{\mathbf{k}}^{\frac{1}{2}} = \mathbf{K}_{\mathbf{k}} \mathbf{T}_{\mathbf{k}}$, where the square root of the matrix $\mathcal{E}_{\mathbf{k}}$ is the matrix of the square roots of the elements of $\mathcal{E}_{\mathbf{k}}$.

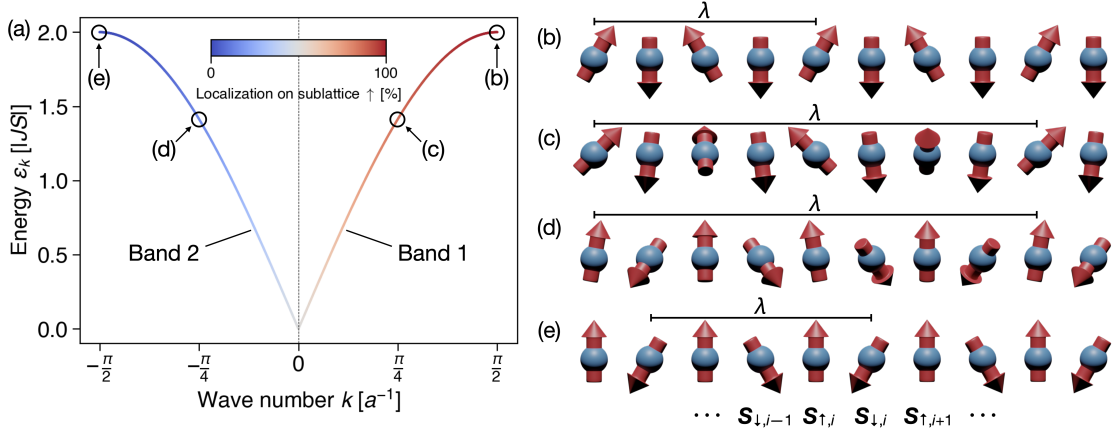


Figure 2.4: Magnon spectrum and selected magnon modes of in a one-dimensional HEISENBERG antiferromagnet. (a) Magnon band structure featuring the two degenerate bands. Color indicates localization of the modes on sublattice \uparrow . For $k > 0$ ($k < 0$), band 1 (band 2) is shown. (b–e) Snapshots of spin waves of (b, c) band 1 and (d, e) band 2 with (b, e) $k = \pm\pi/2a$ and (c, d) $k = \pm\pi/4a$ [cf. panel (a)]. Band 1 (band 2) generally features larger precession amplitudes on sublattice \uparrow (sublattice \downarrow). As $|k| \rightarrow 0$, the amplitudes of the precessions of both sublattices diverge to ∞ for both bands.

Antiferromagnetic Heisenberg Chain

Although the HEISENBERG ferromagnet and antiferromagnet share the same Hamiltonian

$$\hat{\mathcal{H}}_s = \frac{J}{\hbar^2} \sum_i \left(\hat{\mathbf{S}}_{\uparrow,i} \cdot \hat{\mathbf{S}}_{\downarrow,i} + \hat{\mathbf{S}}_{\downarrow,i} \cdot \hat{\mathbf{S}}_{\uparrow,i+1} \right), \quad (2.104)$$

the ferromagnet exhibits only one sublattice and is diagonalized by FOURIER transformation of the HOLSTEIN-PRIMAKOFF operators. In contrast, the antiferromagnet has two sublattices \uparrow and \downarrow because the antiferromagnetic order favored by $J > 0$ breaks translational symmetry and doubles the unit cell, which has the size $2a$ if the spins are separated by a distance a .

After the HOLSTEIN-PRIMAKOFF transformation [Eq. (2.85)] and the FOURIER transformation [Eq. (2.88)], one obtains the HAMILTON matrix

$$\mathbf{H}_{m,\mathbf{k}} = \begin{pmatrix} \xi & & \eta_k \\ & \xi & \eta_k \\ \eta_k & \eta_k & \xi \\ & & & \xi \end{pmatrix}, \quad (2.105)$$

where $\xi = 2JS$ and $\eta_k = -2JS \cos(ka)$. Except at the edge of the first BRILLOUIN zone, $k = \pm\frac{\pi}{2a}$, where $\eta_k = 0$, the Hamiltonian contains anomalous pairing terms like $\eta_k \hat{b}_{\downarrow,-k} \hat{b}_{\uparrow,k}$, which require the normal modes to be a superposition of particle- and hole-like modes.

Instead of applying the general algorithm, I solve the eigenvalue problem [Eq. (2.103)] and check afterwards if a paraunitary matrix $\mathbf{T}_{\mathbf{k}}$ can be constructed from the eigenvectors $\mathbf{t}_{m\mathbf{k}}$.

As a first step, one computes the roots of the characteristic polynomial of $\sigma_3 \mathbf{H}_{\mathbf{m},\mathbf{k}}$, which read

$$\lambda_{1/2,k} = \sqrt{\xi^2 - \eta_k^2}, \quad \lambda_{3/4,k} = -\sqrt{\xi^2 - \eta_k^2}. \quad (2.106)$$

Because these are directly related to the magnon energies as $\varepsilon_{\mathbf{m},m\mathbf{k}} = (\sigma_3)_{mm} \lambda_{m\mathbf{k}}$, the dispersion relation in HEISENBERG antiferromagnets reads

$$\varepsilon_{\mathbf{m},1/2\mathbf{k}} = \varepsilon_{\mathbf{m},\mathbf{k}} = 2JS|\sin(ka)|. \quad (2.107)$$

Thus, the antiferromagnet hosts two bands, shown in Fig. 2.4(a), which are doubly degenerate because the antiferromagnet effectively restores time-reversal symmetry by combining the time-reversal operation with inversion that interchanges the spins of both sublattices. This effective time-reversal symmetry implements an analog of the KRAMERS theorem. The number of spontaneously broken symmetry generators is, again, $n_{\text{bg}} = 2$. Because of the effective KRAMERS degeneracy, there must be an even number of GOLDSTONE modes. Hence, one can conclude from Eq. (2.97) that there *must* be two type-I modes with linear dispersion relations in a collinear antiferromagnet without any calculations. The linear dispersion affects the magnons' group velocities, which are crucial for transport, as well as the density of states and, therefore, the low-temperature behavior of thermodynamic properties like heat capacity or magnetization. Because of the linear dispersion, the energy of the magnons in an antiferromagnet increases more rapidly than in a ferromagnet. Therefore, the average number of magnons increases slower with temperature and thermodynamic quantities generally display a weaker dependence on temperature compared to ferromagnets [10, 85, 86].

Reverting to the diagonalization of $\mathbf{H}_{\mathbf{m},\mathbf{k}}$, the eigenvectors of $\sigma_3 \mathbf{H}_{\mathbf{m},\mathbf{k}}$ are given as

$$\mathbf{t}_{m\mathbf{k}} = \zeta_{m\mathbf{k}} (\xi + \lambda_{m\mathbf{k}} \quad 0 \quad 0 \quad -\eta_k)^\top, \quad \mathbf{t}_{m+1,\mathbf{k}} = \zeta_{m+1,\mathbf{k}} (0 \quad \xi + \lambda_{m\mathbf{k}} \quad -\eta_k \quad 0)^\top \quad (2.108)$$

for $m = 1, 3$. The coefficients $\zeta_{m\mathbf{k}}$ are chosen so that

$$\mathbf{t}_{m\mathbf{k}}^\dagger \sigma_3 \mathbf{t}_{m\mathbf{k}} = 2|\zeta_{m\mathbf{k}}|^2 \lambda_{m\mathbf{k}} (\xi + \lambda_{m\mathbf{k}}) \stackrel{!}{=} (\sigma_3)_{mm} \quad (2.109)$$

according to Eq. (2.100). Apparently, the phase of $\zeta_{m\mathbf{k}}$ is not defined and can be chosen freely. By choosing $\zeta_{m\mathbf{k}} = \sqrt{2|\lambda_{m\mathbf{k}}|(\xi + \lambda_{m\mathbf{k}})}$ the eigenvectors can be indeed “paranormalized” so that the Bogoliubov transformation mediated by

$$\mathbf{T}_k = \begin{pmatrix} \sqrt{\frac{\xi + \varepsilon_{\mathbf{m},\mathbf{k}}}{2\varepsilon_{\mathbf{m},\mathbf{k}}}} & 0 & \sqrt{\frac{\xi - \varepsilon_{\mathbf{m},\mathbf{k}}}{2\varepsilon_{\mathbf{m},\mathbf{k}}}} & 0 \\ 0 & \sqrt{\frac{\xi + \varepsilon_{\mathbf{m},\mathbf{k}}}{2\varepsilon_{\mathbf{m},\mathbf{k}}}} & 0 & \sqrt{\frac{\xi - \varepsilon_{\mathbf{m},\mathbf{k}}}{2\varepsilon_{\mathbf{m},\mathbf{k}}}} \\ 0 & -\sqrt{\frac{\xi - \varepsilon_{\mathbf{m},\mathbf{k}}}{2\varepsilon_{\mathbf{m},\mathbf{k}}}} & 0 & -\sqrt{\frac{\xi + \varepsilon_{\mathbf{m},\mathbf{k}}}{2\varepsilon_{\mathbf{m},\mathbf{k}}}} \\ -\sqrt{\frac{\xi - \varepsilon_{\mathbf{m},\mathbf{k}}}{2\varepsilon_{\mathbf{m},\mathbf{k}}}} & 0 & -\sqrt{\frac{\xi + \varepsilon_{\mathbf{m},\mathbf{k}}}{2\varepsilon_{\mathbf{m},\mathbf{k}}}} & 0 \end{pmatrix} \quad (2.110)$$

exists.

There are two special cases, (i) $k = 0$ and (ii) $k = \pm \frac{\pi}{2a}$. In case (ii) the Hamiltonian is diagonal, since the pairing terms proportional to η_k disappear. Then, the normal modes do not encompass hole excitations because \mathbf{T}_k becomes block diagonal. For case (i), \mathbf{T}_k is ill-defined because the magnon energies vanish. In this case, the BOGOLIUBOV

transformation does not exist, which is not in contradiction to the general theorem above because the eigenvalues of $\mathbf{H}_{\mathbf{m},k}$, $\xi \pm \eta_k$, are not exclusively positive anymore rendering it positive semidefinite at $k = 0$. Hence, the HEISENBERG antiferromagnet is a counterexample, which demonstrates that the theorem cannot be extended to positive semidefinite matrices (without additional constraints).

For better illustration snapshots of 4 selected modes are shown in Fig. 2.4(b–e). While band 1 features modes with larger precession amplitudes on sublattice \uparrow , band 2 behaves oppositely. At $k = \pm\pi/2a$, only one of the two sublattices is excited for each band. Because the precession reduces the sublattice magnetization, the magnons of band 1 (band 2) carry a spin down (spin up) of magnitude \hbar .²¹ As $k \rightarrow 0$, the amplitudes increase on both sublattices and diverge at $k = 0$, which explains the singularity in the BOGOLIUBOV transformation. Even as the amplitudes on both sublattices increase, it is ensured that the component of the total spin parallel to the Néel vector changes by exactly \hbar .

It should be noted that the MERMIN-WAGNER theorem forbids the spontaneous breaking of continuous symmetries at nonzero temperatures in one and two dimensions [42, 88]. Assuming antiferromagnetic order in the present model violates the theorem. However, this can be easily remedied by an easy-axis anisotropy, which invalidates the applicability of both the MERMIN-WAGNER and the GOLDSTONE theorem. This additional interaction would enter as a constant in ξ and shift the entire magnon spectrum. By removing the zero-energy mode, the BOGOLIUBOV transformation can be performed for all k .

2.4 Theory of Spin-Lattice Excitations: Magnon Polarons

Founded on the BORN-OPPENHEIMER approximation, the nuclear and electronic dynamics have been studied independently in Sections 2.2 and 2.3 under conditions that apply to crystalline magnetic insulators. In both cases, different kinds of bosonic quasiparticles emerged from the quantum-mechanical treatment of the problems. The nuclear dynamics brings about lattice waves that are quantized in terms of phonons and describe the collective vibration of the lattice. The low-energy electronic dynamics was shown to map onto spin degrees of freedom, the excited states of which, the spin waves, i.e., collective precessions of the localized spins, are quantized in terms of magnons.

In this part, the coupling between electrons and nuclei dynamics is effectively reintroduced as an interaction between phonons and magnons, the spin-lattice coupling (cf. Section 2.4.1), which goes beyond the BORN-OPPENHEIMER approximation. As a consequence of this interaction, the normal modes are neither magnons nor phonons and a new kind of quasiparticle emerges by their hybridization, which is discussed in Section 2.4.2.

2.4.1 Spin-Lattice Coupling

A simple argument readily demonstrates the origin and the omnipresence of spin-lattice coupling without invoking the many-body Hamiltonian or the BORN-OPPENHEIMER approximation. Consider a pair of interacting spins $\hat{\mathbf{S}}_1$ and $\hat{\mathbf{S}}_2$, whose interaction is given by

²¹This is a consequence of spin conservation. Since the Hamiltonian does not comprise spin-orbit coupling, the total spin must be conserved. Hence, the Hamiltonian and the total spin possess a common eigenbasis, to which the states of band 1 and 2 belong to. Because the spin eigenvalues are quantized as multiples of \hbar , the one-magnon wave function may only alter the total spin by \hbar [87].

the HEISENBERG exchange interaction $J\hat{\mathbf{S}}_1 \cdot \hat{\mathbf{S}}_2$. It is intuitive to assume that the strength of the interaction depends on the distance between both spins, i.e., $J = J(\mathbf{R}_2 - \mathbf{R}_1)$.²² In the BORN-OPPENHEIMER approximation, the distance is considered fixed but arbitrary for the electronic dynamics. At low temperatures, however, only the vicinity of the equilibrium positions $\mathbf{R}_i^{(0)}$ ($i = 1, 2$) are of interest, where the exchange constants can be approximated as

$$J(\mathbf{R}_2 - \mathbf{R}_1) \approx J\left(\mathbf{R}_2^{(0)} - \mathbf{R}_1^{(0)}\right) + \hat{\nabla}_{\mathbf{R}} J(\mathbf{R}) \cdot (\mathbf{u}_2 - \mathbf{u}_1) \Big|_{\mathbf{R}_2^{(0)} - \mathbf{R}_1^{(0)}}. \quad (2.111)$$

This expansion installs a coupling between the displacements of the nuclei $\mathbf{u}_i = \mathbf{R}_i - \mathbf{R}_i^{(0)}$ from their equilibrium positions on the lattice and the spins $\hat{\mathbf{S}}_1$ and $\hat{\mathbf{S}}_2$. In the following, \mathbf{R} represent the equilibrium positions and \mathbf{u} the deviations from it.

This argument can be generalized for any spin-spin interaction that depends on the distance of the involved interacting spins. Abstractly, different mechanisms of spin-lattice couplings can be captured to the lowest order by the Hamiltonian

$$\hat{\mathcal{H}}_{\text{slic}} = \frac{1}{2\hbar^2} \sum_{uvw} \sum_{pqr} \sum_{\alpha\beta\gamma} I_{pqr}^{\alpha\beta\gamma}(\mathbf{R}_u - \mathbf{R}_w, \mathbf{R}_v - \mathbf{R}_w) \hat{S}_{pu}^{\alpha} \hat{S}_{qv}^{\beta} u_{rw}^{\gamma}, \quad (2.112)$$

where the first three sums (u, v, w) run over unit cells, the second (p, q, r) over all sublattices, and the third (α, β, γ) over all Cartesian components. By relabeling the indices, one shows that the symmetry $I_{pqr}^{\alpha\beta\gamma}(\mathbf{R}_u - \mathbf{R}_w, \mathbf{R}_v - \mathbf{R}_w) = I_{pqr}^{\beta\alpha\gamma}(\mathbf{R}_v - \mathbf{R}_w, \mathbf{R}_u - \mathbf{R}_w)$ can be installed by definition without loss of generality.

This expression for the spin-lattice coupling is very general so that $I_{pqr}^{\alpha\beta\gamma}(\mathbf{R}_u - \mathbf{R}_w, \mathbf{R}_v - \mathbf{R}_w)$ may comprise contributions from different mechanisms like exchange magnetostriction [89–92], dipolar interactions [93], single-ion anisotropies [94–102], DZYALOSHINSKII-MORIYA interaction [102–108], two-ion anisotropies [109, 110], among which the KITAEV interaction [91, 92, 111], the Gamma [92, 111], and Gamma' interactions [92] are special cases.

It should be noted that through indirect exchange, which is mediated by nonmagnetic ions, the spins of the magnetic ions may also be coupled to the displacement of nonmagnetic ions [91], which is in principle included in Eq. (2.112).²³ The expression does not comprise the spin-lattice coupling originating from the ZEEMAN interaction in an inhomogeneous magnetic field [112], and higher orders of spin-spin (e.g., biquadratic) interactions, or interactions that are of higher orders in the displacement [113, 114].

2.4.2 Hybridization of Phonons and Magnons

The spin-lattice coupling Hamiltonian [Eq. (2.112)] can be used to reintroduce the dynamics of the lattice by treating the (so far) static displacement as a dynamic operator $u_{rw}^{\gamma} \rightarrow \hat{u}_{rw}^{\gamma}$, thereby going beyond the BORN-OPPENHEIMER approximation. Hence, the spin HILBERT space is now augmented with the nuclear or lattice HILBERT space. This

²²This assumption was implicitly employed in the previous models by restricting the spin-spin interactions to nearest neighbors. In many realistic models, the spin-spin interactions are short-ranged and can be truncated beyond a few coordination shells.

²³The only difference is that the sublattice index r runs over a larger set including both magnetic and nonmagnetic sublattices, while p and q are restricted to magnetic sublattices.

is, however, different to the original many-body Hamiltonian [Eq. (2.2)] because the interactions between electrons, nuclei, and their mutual interactions are treated effectively by the aforementioned approximations.

First, I discuss how the harmonic approximation of the spin-lattice coupling leads to a hybridization of magnons and phonons that brings about a new kind of quasiparticle – the magnon polaron. A general theory is presented that formulates a bosonic Hamiltonian in the extended HILBERT space of magnetoelastic excitations. Afterwards, the perturbative solution of a ferromagnetic and elastic chain serves as an instructive example to illustrate the physics of magnon polarons.

General Theory

In order to account for spin-lattice coupling, the Hamiltonian of Eq. (2.112) is transformed into a bosonic Hamiltonian that mixes annihilation and creation operators of magnons and phonons. The spin operators are mapped onto the magnon operators by means of the HOLSTEIN-PRIMAKOFF transformation introduced in Section 2.3.3, while the displacement operator is mapped onto local oscillator modes as described in Section 2.2.3.

As the spin Hamiltonian, the spin-lattice Hamiltonian can be expanded in terms of the number of bosonic creation or annihilation operators. The leading order that affects the mutual dynamics of phonon and magnons is the bilinear term, where one magnon is converted into one phonon or vice versa. Other terms are henceforth neglected, which is a good approximation if the spin quantum number S is large and the fluctuations are small.

To bilinear order, $\hat{\mathcal{H}}_{\text{slc}}$ [Eq. (2.112)] amounts to

$$\hat{\mathcal{H}}_{\text{mp}}^{(2)} = \frac{\sqrt{\hbar}}{2} \sum_{pqr} \sum_{\alpha\beta\gamma} \sum_{\mathbf{k}} \sqrt{S_p^2 S_q z_{p\alpha}} \left[\mathcal{I}_{pqr}^{\alpha\beta\gamma}(\mathbf{k}) e_{q\beta}^+ \hat{b}_{q\mathbf{k}}^\dagger \frac{\hat{a}_{r\gamma\mathbf{k}} + \hat{a}_{r\gamma(-\mathbf{k})}^\dagger}{\sqrt{M_r \omega_{r\gamma}}} + \text{h.c.} \right], \quad (2.113)$$

where

$$\mathcal{I}_{pqr}^{\alpha\beta\gamma}(\mathbf{k}) = \sum_{uv} e^{-i\mathbf{k}\cdot(\mathbf{R}_v + \mathbf{b}_q - \mathbf{b}_r)} I_{pqr}^{\alpha\beta\gamma}(\mathbf{R}_u, \mathbf{R}_v) \quad (2.114)$$

is the FOURIER transform of the spin-lattice coupling tensor [Eq. (2.112)], $z_{p\alpha}$ and $e_{p\alpha}^+$ are the α components of the vectors \mathbf{z}_p and \mathbf{e}_p^+ defined in Section 2.3.3 as the local spin coordinate system, and h.c. refers to the Hermitian conjugate.

Because the displacement operator is a linear combination of creation and annihilation operators, the number of bosons is no longer a conserved quantity (if $\hat{\mathcal{H}}_{\text{mp}}^{(2)}$ is nonzero). As a consequence, the magnon-phonon NAMBU spinor $\hat{\chi}_{\mathbf{k}}^\dagger = \begin{pmatrix} \hat{\psi}_{\mathbf{k}}^\dagger & \hat{\phi}_{\mathbf{k}}^\dagger \end{pmatrix}$ encompassing both magnon $\hat{\psi}_{\mathbf{k}}^\dagger$ [defined in Eq. (2.90)] and phonon degrees of freedoms $\hat{\phi}_{\mathbf{k}}^\dagger$ [defined in Eq. (2.60)] are necessary to represent the BOGOLIUBOV-DE GENNES Hamiltonian of the

spin-lattice coupling,

$$\hat{\mathcal{H}}_{\text{mp}}^{(2)} = \frac{1}{2} \sum_{\mathbf{k}} \hat{\chi}_{\mathbf{k}}^\dagger \mathcal{H}_{\text{mp},\mathbf{k}} \hat{\chi}_{\mathbf{k}}, \quad (2.115\text{a})$$

$$\mathcal{H}_{\text{mp},\mathbf{k}} = \begin{pmatrix} \mathbf{0}_{2\mathcal{N}_m \times 2\mathcal{N}_m} & \mathbf{H}_{\text{mp},\mathbf{k}} \\ \mathbf{H}_{\text{mp},\mathbf{k}}^\dagger & \mathbf{0}_{2\mathcal{N}_p \times 2\mathcal{N}_p} \end{pmatrix}, \quad (2.115\text{b})$$

$$\mathbf{H}_{\text{mp},\mathbf{k}} = \begin{pmatrix} \mathbf{A}_{\text{mp},\mathbf{k}} & \mathbf{A}_{\text{mp},\mathbf{k}} \\ \mathbf{A}_{\text{mp},-\mathbf{k}}^* & \mathbf{A}_{\text{mp},-\mathbf{k}}^* \end{pmatrix}, \quad (2.115\text{c})$$

$$(A_{\text{mp},\mathbf{k}})_{ij} = \sum_h \sum_{\alpha\beta} \sqrt{\frac{\hbar S_h^2 S_i}{M_j \omega_j}} \mathcal{I}_{hij}^{\alpha\beta}(\mathbf{k}) z_{h\alpha} e_{i\beta}^+, \quad (2.115\text{d})$$

where $\mathcal{H}_{\text{mp},\mathbf{k}} \in \mathbb{C}^{2\mathcal{N}_{\text{mp}} \times 2\mathcal{N}_{\text{mp}}}$, $\mathbf{H}_{\text{mp},\mathbf{k}} \in \mathbb{C}^{2\mathcal{N}_m \times 2\mathcal{N}_p}$, $\mathbf{A}_{\text{mp},\mathbf{k}} \in \mathbb{C}^{\mathcal{N}_m \times \mathcal{N}_p}$ with the abbreviation $\mathcal{N}_{\text{mp}} = \mathcal{N}_m + \mathcal{N}_p$. In Eq. (2.115d), I introduced a multi-index notation for the phonon sublattice r and displacement components γ that are subsumed in the joint index j , for which the details of the mapping do not matter. The index h runs over all magnetic sublattices.

The matrix representation $\mathcal{H}_{\mathbf{k}}$ of the full Hamiltonian $\hat{\mathcal{H}} = \hat{\mathcal{H}}_s + \hat{\mathcal{H}}_p + \hat{\mathcal{H}}_{\text{slc}}$ would be obtained by replacing $\mathbf{0}_{2\mathcal{N}_m \times 2\mathcal{N}_m}$ by $\mathbf{H}_{\text{m},\mathbf{k}}$ [cf. Eq. (2.93)] and $\mathbf{0}_{2\mathcal{N}_p \times 2\mathcal{N}_p}$ by $\mathbf{H}_{\text{p},\mathbf{k}}$ [cf. Eq. (2.61)] in the expression of $\mathcal{H}_{\text{mp},\mathbf{k}}$ [cf. Eq. (2.115b)]. Without spin-lattice coupling ($\mathcal{H}_{\text{mp},\mathbf{k}} = \mathbf{0}_{2\mathcal{N}_{\text{mp}} \times 2\mathcal{N}_{\text{mp}}}$), $\mathcal{H}_{\mathbf{k}}$ would be block diagonal and the eigenvalues and eigenvectors would be identical to the separate solutions of $\hat{\mathcal{H}}_s$ and $\hat{\mathcal{H}}_p$. In other words, magnons and phonons would exist independently of each other. In the presence of spin-lattice coupling, however, one would need to perform a BOGOLIUBOV transformation diagonalizing the full matrix $\mathcal{H}_{\mathbf{k}}$ by applying the same formalism as outlined in Section 2.3.4.²⁴ Then, the new eigenmodes would be superpositions of magnons and phonons – magnon polarons. To gain a better understanding of their formation and their properties, a simple example is given below.

Elastic Ferromagnetic Chain

To exemplify the formation of magnon polarons, I choose a one-dimensional system, whose Hamiltonian

$$\hat{\mathcal{H}} = \hat{\mathcal{H}}_s + \hat{\mathcal{H}}_p + \hat{\mathcal{H}}_{\text{slc}} \quad (2.116)$$

comprises ferromagnetic HEISENBERG exchange interaction

$$\hat{\mathcal{H}}_s = \frac{J}{\hbar^2} \sum_i \hat{\mathbf{S}}_i \cdot \hat{\mathbf{S}}_{i+1}, \quad (2.117)$$

²⁴It should be noted that the chosen arrangement of the creation and annihilation operators for magnons and phonons in the NAMBU spinors $\hat{\chi}_{\mathbf{k}}^\dagger$ and $\hat{\chi}_{\mathbf{k}}$ entails a changed bosonic metric. It can be beneficial to perform a unitary transformation so that the creation operators of both phonons and magnons precede the annihilation operators in $\hat{\chi}_{\mathbf{k}}^\dagger$ (and vice versa for $\hat{\chi}_{\mathbf{k}}$). Then, the bosonic metric remains unchanged (except in the number of bands).

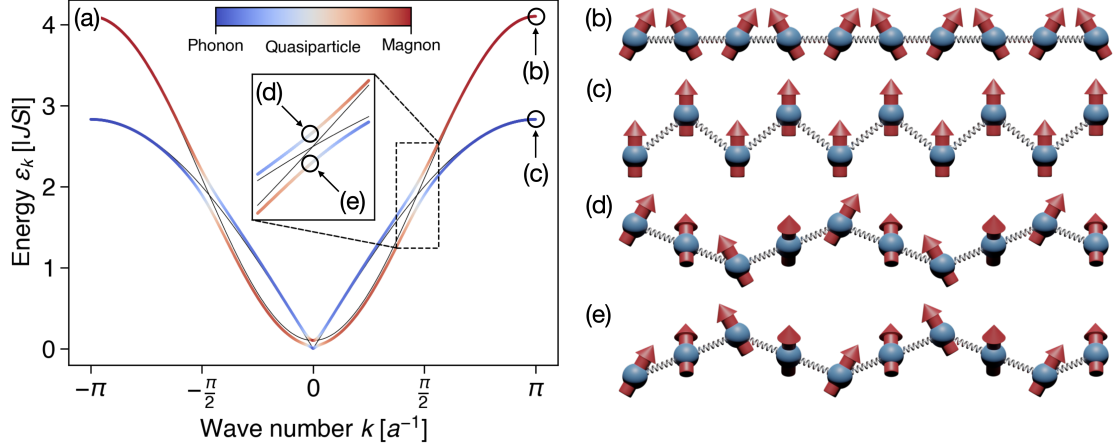


Figure 2.5: Magnon polaron spectrum and selected normal modes. (a) Magnon polaron band structure of one-dimensional elastic HEISENBERG ferromagnet with two branches. Red/blue/gray color represents magnon-like/phonon-like/hybrid character of quasiparticles (see color bar). Inset: zoom into the area of the avoided crossing. Thin black lines indicate bands without spin-lattice coupling. (b–e) Snapshots of magnetoelastic waves of selected magnon polaron modes [cf. panel (a)]. In (d) [(e)], the elastic wave has a phase shift of 90° [-90°] with respect to the spin wave. The parameters have been specified as $\hbar = 1$, $J = -1$, $S = 1$, $M = 1$, $C = 2$, $\kappa_{\text{mc}} = 0.2$. The magnon branch has been shifted by $0.1JS$ to avoid a ground state instability in the presence of spin-lattice coupling.

($J < 0$), harmonic lattice dynamics

$$\hat{\mathcal{H}}_{\text{p}} = \sum_i \frac{\hat{P}_i^2}{2M} + \frac{C}{4} \sum_i (\hat{u}_i - \hat{u}_{i+1})^2 \quad (2.118)$$

along one dimension, for instance the transversal one, and spin-lattice coupling $\hat{\mathcal{H}}_{\text{slc}}$. Disregarding $\hat{\mathcal{H}}_{\text{slc}}$ for the moment, the results for $\hat{\mathcal{H}}_{\text{s}}$ in Section 2.3.3 can be carried over, where it was approximated by

$$\hat{\mathcal{H}}_{\text{m}} = JS^2 \mathcal{N}_{\text{uc}} + \sum_k \varepsilon_{\text{m},k} \hat{b}_k^\dagger \hat{b}_k, \quad \varepsilon_{\text{m},k} = -4JS \sin^2 \frac{ka}{2}. \quad (2.96 \text{ revisited})$$

Concerning $\hat{\mathcal{H}}_{\text{p}}$, the results of Section 2.2.2 can be carried over by setting $M = M_1 = M_2$. Because the translational periodicity changes from $2a$ to a , the first BRILLOUIN zone is doubled and the acoustic and optical branch can be merged into one branch $\varepsilon_{\text{p},k}$, which for $|k| \leq \frac{\pi}{2a}$ describes the energies of the acoustic and for $\frac{\pi}{2a} \leq |k| \leq \frac{\pi}{a}$ those of the optical branch. Since the energy approaches zero for $k \rightarrow 0$ and disperses linearly in the vicinity of $k = 0$, the former two branches are unified by a single *acoustic* branch. By quantizing lattice waves by means of the transformation in Eq. (2.53b), the phonon Hamiltonian

$$\hat{\mathcal{H}}_{\text{p}} = \sum_k \varepsilon_{\text{p},k} \left(\hat{\alpha}_k^\dagger \hat{\alpha}_k + \frac{1}{2} \right), \quad \varepsilon_{\text{p},k} = \hbar \sqrt{\frac{2C}{M}} \left| \sin \frac{ka}{2} \right| \quad (2.119)$$

is obtained.

It is now instructive to study the effect of $\hat{\mathcal{H}}_{\text{sfc}}$ perturbatively. The obvious choice would be to study the effect of exchange magnetostriction

$$\hat{\mathcal{H}}_{\text{sfc}} = \frac{\kappa_J}{\hbar^2} \sum_i \hat{\mathbf{S}}_i \cdot \hat{\mathbf{S}}_{i+1} (\hat{u}_i - \hat{u}_{i+1}), \quad (2.120)$$

where $\kappa_J = \left. \frac{dJ(R)}{dR} \right|_a$. However, the scalar product $\hat{\mathbf{S}}_i \cdot \hat{\mathbf{S}}_{i+1}$ does only produce products of \hat{b} and \hat{b}^\dagger that are even so that the leading order of $\hat{\mathcal{H}}_{\text{sfc}}$ would encompass terms of the form $\hat{b}^\dagger \hat{b} (\hat{\alpha} + \hat{\alpha}^\dagger)$, which are not bilinear. Exchange magnetostriction gives rise to bilinear terms only in noncollinear magnets [90].

Instead, consider the magnetocrystalline spin-lattice coupling

$$\hat{\mathcal{H}}_{\text{sfc}} = \frac{\kappa_{\text{mc}}}{\hbar^2} \sum_i \sum_{\zeta=\pm 1} \zeta \hat{S}_i^z \hat{S}_i^x (\hat{u}_i - \hat{u}_{i+\zeta}), \quad (2.121)$$

in which the z and x components of the local spins are coupled. Indeed, this gives rise to a bilinear magnon-phonon coupling, which reads

$$\hat{\mathcal{H}}_{\text{mp}}^{(2)} = i\hbar\kappa_{\text{mc}} \sqrt{\frac{S^3}{M}} \sum_k \frac{\sin ka}{\sqrt{\varepsilon_{\text{p},k}}} (\hat{b}_k + \hat{b}_{-k}^\dagger) (\hat{\alpha}_{-k} + \hat{\alpha}_k^\dagger). \quad (2.122)$$

Usually the spin-lattice coupling is weak compared to pure spin or elastic interactions. Therefore, to good approximation, one obtains the renormalized energies and wave functions with time-independent perturbation theory. Let $|m, k\rangle$ and $|p, k\rangle$ be nondegenerate and unperturbed magnon and phonon states with wave vector k , respectively. To first order, their energy is renormalized as [115]

$$\Delta\varepsilon_{m,k}^{(1)} = \langle m, k | \hat{\mathcal{H}}_{\text{mp}}^{(2)} | m, k \rangle = 0 = \langle p, k | \hat{\mathcal{H}}_{\text{mp}}^{(2)} | p, k \rangle = \Delta\varepsilon_{p,k}^{(1)}. \quad (2.123)$$

The reason is that $\hat{\mathcal{H}}_{\text{mp}}^{(2)}$ converts a phonon into a magnon and vice versa. Since phonon and magnon states are orthogonal, their overlap and, with it, the first-order energy corrections $\Delta\varepsilon_{m,k}^{(1)}$ and $\Delta\varepsilon_{p,k}^{(1)}$ vanish.

To second order, the correction of the magnon, phonon energy is given as [115]

$$\Delta\varepsilon_{m,k}^{(2)} = -\Delta\varepsilon_{p,k}^{(2)} = \frac{|\langle m, k | \hat{\mathcal{H}}_{\text{mp}}^{(2)} | p, k \rangle|^2}{\varepsilon_{m,k} - \varepsilon_{p,k}}, \quad (2.124)$$

where the matrix element evaluates to $\eta_k := \langle m, k | \hat{\mathcal{H}}_{\text{mp}}^{(2)} | p, k \rangle = -i\kappa_{\text{mc}}\hbar \sqrt{\frac{S^3}{M}} \frac{\sin ka}{\sqrt{\varepsilon_{\text{p},k}}}$.

In case of a degeneracy, the perturbation theory diverges. Then, one can approximate the energies by neglecting the pairing terms in $\hat{\mathcal{H}}_{\text{mp}}^{(2)}$ and diagonalize the Hamilton matrix

$$\mathcal{H}_k = \begin{pmatrix} \varepsilon_{m,k} & \eta_k \\ \eta_k^* & \varepsilon_{p,k} \end{pmatrix} \quad (2.125)$$

in the basis $\{|m, k\rangle, |p, k\rangle\}$. The corrected energies are

$$\varepsilon_{1/2k} = \frac{\varepsilon_{m,k} + \varepsilon_{p,k}}{2} \mp \sqrt{\left(\frac{\varepsilon_{m,k} - \varepsilon_{p,k}}{2}\right)^2 + |\eta_k|^2} \quad (2.126)$$

and the eigenvectors for $\eta_k \neq 0$ are

$$\mathbf{v}_{1k} \propto (\varepsilon_{1k} - \varepsilon_{p,k} \quad \eta_k^*)^\top, \quad \mathbf{v}_{2k} \propto (\eta_k \quad \varepsilon_{2k} - \varepsilon_{m,k})^\top \quad (2.127)$$

up to a normalization factor.

Consider the case that the magnon and phonon bands cross at some k , i.e., $\varepsilon_{m,k} = \varepsilon_{p,k}$. Due to spin-lattice coupling, the degeneracies are lifted, $\varepsilon_{1/2k} = \varepsilon_{m,k} \mp |\eta_k|$, and the new eigenstates

$$|\text{mp}, 1, k\rangle = \frac{1}{\sqrt{2}} [|m, k\rangle - e^{-i \arg \eta_k} |p, k\rangle], \quad (2.128a)$$

$$|\text{mp}, 2, k\rangle = \frac{1}{\sqrt{2}} [|m, k\rangle + e^{-i \arg \eta_k} |p, k\rangle] \quad (2.128b)$$

are uniform superpositions of magnon and phonon modes. Hence, magnons and phonons cease to exist in the presence of spin-lattice coupling and, instead, merge into magnon polarons that account for the coupled spin and lattice dynamics. An excitation of the lattice entails an excitation of spins and vice versa. Far away from such a degeneracy, the magnon polaron wave functions exhibit either strong magnon or phonon character so that the notion of magnons and phonons remains approximately intact.

These findings are supported by the numerical calculations: At the edge of the first BRILLOUIN zone, where the energies of magnons and phonons are far apart (for the chosen parameters), the renormalization by spin-lattice coupling is minute [Fig. 2.5(a)]. The wave functions either correspond to that of a spin wave [Fig. 2.5(b)] or to that of an elastic wave [Fig. 2.5(c)]. At the crossing between magnon and phonon bands [black line in Fig. 2.5(a)], a gap is opened by spin-lattice coupling. The wave functions of the hybridized states comprise spin and elastic excitations with equal amplitudes and phase differences of $\pm 90^\circ$ [Fig. 2.5(d, e)].

In Fig. 2.5(a), the magnon branch has been shifted by $0.1JS$ mimicking an easy-axis anisotropy or a magnetic field. Both kinds of interactions stabilize the ground state and install a spin-wave excitation gap. This is necessary because the hybridization shifts the low-energy modes to even lower energies so that the energies would become negative otherwise, rendering \mathcal{H}_k indefinite. Equivalently, the plotted eigenvalues of $\sigma_3 \mathcal{H}_k$ would acquire an imaginary part close to $k = 0$. The (real part of the) magnon band close to $k = 0$ would be deformed from a parabolic to a flat dispersion by the spin-lattice coupling. These indications signal a ground state instability, which can be avoided by an easy-axis anisotropy or a magnetic field as long as the hybridization gap is sufficiently small compared to the spin-wave gap. For the above arguments, a stable ferromagnetic ground state was presumed.

BAND TOPOLOGY OF BOSONIC QUASIPARTICLES

3.1 Adiabatic Time Evolution

The BORN-OPPENHEIMER approximation delineated in Section 2.1 resulted in an electronic Hamiltonian that parametrically depends on the nuclear positions. Since the dynamics of the electrons is much faster than that of the nuclei, the electronic wave function instantaneously follows the time evolution of the nuclear positions without any electronic transitions (within the approximation). There, a term was arising in the electronic wave function, which is discussed in a more general framework here.

Imagine that a system can be described by a time-independent Hamiltonian $\hat{\mathcal{H}}(\mathbf{X})$ and is prepared in a stationary state, i.e., in an eigenstate of the Hamiltonian. Taking the dynamic phase factor into account, the stationary state is a solution of the time-dependent SCHRÖDINGER equation so that the system remains in this state (hence the name stationary). What happens if the system does depend on an external parameter \mathbf{X} that is slowly varied? Does the system remain in the respective eigenstate of $\hat{\mathcal{H}}(\mathbf{X}(t))$ for each time t ? These questions are answered by the *adiabatic theorem*, which is presented in the following.

3.1.1 Derivation of the Adiabatic Theorem

MICHAEL VICTOR BERRY considered these questions in his 1983 paper, where he showcased how the adiabatic evolution of a parameter-dependent system alters the wave function [116]. Here, I follow his approach as well as Refs. [41, 117].

First, for any value \mathbf{X} of the parameter, one can solve the eigenvalue equation of the Hamiltonian

$$\hat{\mathcal{H}}(\mathbf{X}) |n(\mathbf{X})\rangle = E_n(\mathbf{X}) |n(\mathbf{X})\rangle, \quad (3.1)$$

which, however, does not solve the time-dependent SCHRÖDINGER equation

$$i\hbar \frac{\partial |\psi(t)\rangle}{\partial t} = \hat{\mathcal{H}}(\mathbf{X}(t)) |\psi(t)\rangle, \quad (3.2)$$

where the time evolution of \mathbf{X} is implied. This partial differential equation can be reformulated as a system of ordinary differential equations by expanding $|\psi\rangle$ in terms of eigenfunctions:

$$|\psi(t)\rangle = \sum_n c_n(t) |n(\mathbf{X}(t))\rangle. \quad (3.3)$$

This is possible because the eigenfunctions $|n(\mathbf{X})\rangle$ span the entire HILBERT space for each $\mathbf{X}(t)$. Note that for each t , $|\psi\rangle$ is represented in a different basis, which is assumed to be discrete.

Plugging Eq. (3.3) into Eq. (3.2), one obtains the differential equation

$$\frac{\partial c_m(t)}{\partial t} = -\frac{i}{\hbar} E_m(\mathbf{X}(t)) c_m(t) - \sum_n \frac{\partial \mathbf{X}(t)}{\partial t} \cdot \langle m(\mathbf{X}) | \nabla_{\mathbf{X}} n(\mathbf{X}) \rangle c_n(t) \quad (3.4)$$

under the condition that the eigenfunctions $|n(\mathbf{X})\rangle$ have a locally differentiable gauge with respect to the parameter \mathbf{X} . This would not be necessary because they are only required to fulfill the eigenvalue problem Eq. (3.1). This is a weak requirement because the eigenfunction has a $U(1)$ symmetry. The gauge transformation $|n(\mathbf{X})\rangle \rightarrow e^{i\varphi(\mathbf{X})} |n(\mathbf{X})\rangle$ maps a normalized eigenfunction to an equivalent normalized eigenfunction of $\hat{\mathcal{H}}(\mathbf{X})$. It is a general feature of quantum mechanics that the global phase of the wave function is not observable. Once \mathbf{X} is treated as time dependent, it does no longer correspond to a global (constant) phase because the time-dependent wave function, as a solution of Eq. (3.2), has to be analytic in time. In order for the expansion coefficients $c_m(t)$ to be analytic, a locally analytic gauge has to be chosen.

In Eq. (3.4), it is the last term on the right-hand side that mutually couples the ordinary differential equations. So far, no approximations have been made. In the following, I argue that the terms¹

$$\langle m | \nabla_{\mathbf{X}} n \rangle = \frac{\langle m | \nabla_{\mathbf{X}} \hat{\mathcal{H}}(\mathbf{X}) | n \rangle}{E_n(\mathbf{X}) - E_m(\mathbf{X})} \quad (3.5)$$

for $m \neq n$ are negligible if the corresponding energies differences $|E_m(\mathbf{X}) - E_n(\mathbf{X})|$ are large compared to the dynamics of $\mathbf{X}(t)$. In that case, the adiabatic dynamics of \mathbf{X} is insufficient to cause transitions between different states n and m . Thus, the sum in Eq. (3.4) can be restricted to $n = m$ so that one obtains a decoupled system of differential equations, whose solution is

$$c_m(t) = e^{-\frac{i}{\hbar} \int_{t'}^t d\tau E_m(\mathbf{X}(\tau))} e^{i\gamma_m(\mathcal{C})}, \quad (3.6)$$

where t' is chosen so that $c_m(t') = 1$ without loss of generality. The first factor in the right-hand side is the dynamical phase that is reminiscent of the stationary problem, where the time dependence only corresponds to an oscillation with an angular frequency $E_m(\mathbf{X})/\hbar$. The second factor is the so-called *BERRY phase*

$$\gamma_m(\mathcal{C}) = \int_{\mathcal{C}} d\mathbf{X} \cdot \mathbf{A}_m(\mathbf{X}), \quad \mathbf{A}_m(\mathbf{X}) = i \langle m(\mathbf{X}) | \nabla_{\mathbf{X}} m(\mathbf{X}) \rangle, \quad (3.7)$$

which is obtained by a line integral of the *BERRY connection* \mathbf{A}_m over the contour \mathcal{C} in parameter space traced by $\mathbf{X}(t)$.

By decoupling of the system of differential equations, the *adiabatic theorem* has been proven. It states that the time evolution of the parameter does not cause interband transitions in the time-dependent wave function $|\psi(t)\rangle$. Prepared in a stationary state $|m(\mathbf{X})\rangle$, the system always remains in its respective stationary state at each point in time, while $\mathbf{X}(t)$ follows a path in parameter space. The wave function can be written as $|\psi(t)\rangle = |m(\mathbf{X}(t))\rangle$ except for two phase factors. First, the wave function picks up the dynamical phase even if the parameter is not changed, in which case it only is a

¹This identity is proven below.

harmonic oscillation in time. Second, there is a *geometric phase* that does not depend on the dynamics, but only on the geometry of the parameter space. It is similar to the parallel transport of a tangential vector along a loop on a curved surface like a sphere. Upon returning to its initial position, the vector after the transport has rotated within the tangential space by the solid angle of the surface on the sphere enclosed by the loop [118], while parallel transport *on a plane* does not cause a change in its orientation. As an example, the FOUCAULT pendulum changes its direction after one full rotation of the earth. Parallel transport is an example of *anholonomy*, which designates the phenomenon, where some variables do not assume their original values when other variables are evolved on a loop [119].

The conditions used to derive the adiabatic theorem is that the spectrum is nondegenerate within the parameter subspace of interest, and that the parameter is changed adiabatically, i.e., $\hbar \left| \left\langle m(\mathbf{X}(t)) \left| \frac{\partial m(\mathbf{X}(t))}{\partial t} \right\rangle \right| \ll |E_m(\mathbf{X}) - E_n(\mathbf{X})|$ [120].

3.1.2 Observability of the Geometric Phase

At this point, the question arises, whether the geometric phase is observable. First, one needs to ensure that the phase is indeed real. This can be readily seen from the normalization of the wave function $\langle m(\mathbf{X}) | m(\mathbf{X}) \rangle = 1$. By taking the derivative with respect to \mathbf{X} , one shows $\langle m | \nabla_{\mathbf{X}} m \rangle = -\langle \nabla_{\mathbf{X}} m | m \rangle = -\langle m | \nabla_{\mathbf{X}} m \rangle^*$, hence \mathbf{A}_m and γ_m are real. Second, the behavior under gauge transformations has to be considered as any physical observable needs to respect *gauge invariance*. Let $|m'(\mathbf{X})\rangle = e^{i\varphi(\mathbf{X})} |m(\mathbf{X})\rangle$ be the stationary wave function in a different gauge and $\varphi(\mathbf{X})$ a differentiable gauge phase. Then, the BERRY connection in the new gauge is $\mathbf{A}_{m'} = \mathbf{A}_m - \nabla_{\mathbf{X}}\varphi$. Thus, the BERRY connection and generally even the BERRY phase are gauge dependent. However, if \mathcal{C} corresponds to a closed path in parameter space, the integral over $\nabla_{\mathbf{X}}\varphi$ vanishes and $\gamma_m(\mathcal{C})$ is observable. Note that in general the BERRY phase is *nonintegrable* because the BERRY connection cannot be written as a gradient of a scalar field so that $\gamma_m(\mathcal{C}) \neq 2\pi l$ with $l \in \mathbb{Z}$ for a closed contour \mathcal{C} .

Another way to construct a gauge-independent quantity relies on STOKES' theorem. From now on, I assume that $\mathbf{X} \in \mathbb{R}^3$. If the contour $\mathcal{C} = \partial\mathcal{S}$ is closed, it demarcates a surface \mathcal{S} in parameter space so that the integral Eq. (3.7) can be rewritten as

$$\gamma_m(\mathcal{S}) = \int_{\mathcal{S}} d\mathbf{S}_{\mathbf{X}} \cdot \boldsymbol{\Omega}_m(\mathbf{X}), \quad (3.8)$$

where $\boldsymbol{\Omega}_m(\mathbf{X}) = \nabla_{\mathbf{X}} \times \mathbf{A}_m(\mathbf{X})$ is the *BERRY curvature*. Because it is defined as the curl of the BERRY connection, which is determined up to a gradient of a gauge phase, the BERRY curvature is gauge invariant. There is a close analogy to electrodynamics, where the vector potential, which is analogous to the BERRY connection, is a gauge dependent quantity and the magnetic field, defined as the curl of the vector potential, is not modified under gauge transformations similar to the BERRY curvature.

3.1.3 Alternative Expressions for Geometric Quantities

The BERRY curvature is an important quantity for transversal transport coefficients as corroborated in Chapter 4. It can be difficult to compute $|\nabla_{\mathbf{X}} m\rangle$ because usually the eigenstates are not known analytically so that the derivative has to be approximated

by finite differences numerically. On the other hand, the Hamiltonian is often known analytically, and its derivative can easily be obtained.

It is possible to compute the BERRY curvature with only the matrix elements of $\nabla_{\mathbf{X}}\hat{\mathcal{H}}(\mathbf{X})$. To do so, one takes the derivative of Eq. (3.1) on both sides:

$$\left[\nabla_{\mathbf{X}}\hat{\mathcal{H}}\right]|n\rangle + \hat{\mathcal{H}}|\nabla_{\mathbf{X}}n\rangle = [\nabla_{\mathbf{X}}E_n]|n\rangle + E_n|\nabla_{\mathbf{X}}n\rangle. \quad (3.9)$$

Since the stationary states are orthogonal to each other, one obtains

$$\langle m|\nabla_{\mathbf{X}}\hat{\mathcal{H}}|n\rangle - \delta_{mn}\nabla_{\mathbf{X}}E_n = [E_n - E_m]\langle m|\nabla_{\mathbf{X}}n\rangle \quad (3.10)$$

after scalar multiplication with $|m\rangle$. For $m = n$, the right-hand side vanishes and, thus, one cannot express the BERRY connection as the matrix elements of $\nabla_{\mathbf{X}}\hat{\mathcal{H}}$. This is a reflection of the gauge dependence of the BERRY connection, which is incompatible with any gauge-invariant quantity. On the other hand, the BERRY curvature

$$\Omega_n = i\nabla_{\mathbf{X}} \times \langle n|\nabla_{\mathbf{X}}n\rangle = i\langle \nabla_{\mathbf{X}}n|\times|\nabla_{\mathbf{X}}n\rangle = i\sum_m \langle \nabla_{\mathbf{X}}n|m\rangle \times \langle m|\nabla_{\mathbf{X}}n\rangle \quad (3.11)$$

is a gauge-invariant quantity. For the last identity the completeness relation has been inserted. For the completeness, the sum for m runs over all states including n . However, because $\langle n|\nabla_{\mathbf{X}}n\rangle = -\langle \nabla_{\mathbf{X}}n|n\rangle$, the cross product vanishes for $m = n$ so that the sum may be written to exclude n . By inserting Eq. (3.10) into Eq. (3.11), the BERRY curvature

$$\Omega_n(\mathbf{X}) = i\sum_{\substack{m \\ m \neq n}} \frac{\langle n(\mathbf{X})|\nabla_{\mathbf{X}}\hat{\mathcal{H}}(\mathbf{X})|m(\mathbf{X})\rangle \times \langle m(\mathbf{X})|\nabla_{\mathbf{X}}\hat{\mathcal{H}}(\mathbf{X})|n(\mathbf{X})\rangle}{[E_n(\mathbf{X}) - E_m(\mathbf{X})]^2} \quad (3.12)$$

is expressed via the matrix elements of $\nabla_{\mathbf{X}}\hat{\mathcal{H}}$. The summand in Eq. (3.12) is antisymmetric under exchange of quantum numbers $m \leftrightarrow n$. Using this observation, one shows that the BERRY curvatures of all states mutually cancel:

$$\sum_n \Omega_n(\mathbf{X}) = 0. \quad (3.13)$$

3.2 Geometric Concepts in Band Structure Theory

The general arguments of the previous sections did not specify the nature of the parameter that the Hamiltonian depends on. Consequently, the BERRY curvature is not a priori a fixed quantity, but comes in different forms. Reverting to the BORN-OPPENHEIMER approximation of Section 2.1, the key ingredient for the decoupling of the electronic and nuclear dynamics is the slowness of the latter compared to the former. For the electrons, the motion of the nuclei can be described by treating the nuclear positions as adiabatically evolving parameters in the electronic Hamiltonian. Hence, a close trajectory in the high-dimensional parameter space of nuclear coordinates encompasses a BERRY phase, which has been implicitly identified in Eq. (2.13), where the derivative of the electronic wave function with respect to the nuclear coordinates is taken. This corresponds to the general definition of the BERRY connection [Eq. (3.7)].

Here, another kind of BERRY phase, connection, and curvature is studied, which arises from the single-electron wave functions in a periodic potential. Based on the structure of the solution of the problem, a new parameter-dependent Hamiltonian is derived, which is *based on a quantum number*. This situation is different from the BORN-OPPENHEIMER approximation because a quantum number has no time evolution *in equilibrium*. However, it can be anticipated that a perturbation of the equilibrium with a Hamiltonian breaking the essential symmetries invalidates the quantum number and the nonequilibrium state may be described by a time-dependent quantum number, which may seem paradox at the beginning, but turns out to be useful in linear response theory. I will corroborate this aspect more in the subsequent Section 3.2.1.

Lattice-periodic Hamiltonians are not restricted to electrons, but also comprise spin lattices. Magnon, phonon, and magnon polaron Hamiltonians, for instance, abide by translational invariance as well and may be subject to external perturbations breaking this symmetry and causing to a time evolution of certain quantum numbers. The formal definitions are similar to those for electrons, but special attention has to be paid to the nonconserving nature of (bosonic) BOGOLIUBOV-DE GENNES Hamiltonians. Since these kinds of Hamiltonians are of particular relevance for this work, a separate section is dedicated to them (cf. Section 3.2.2).

3.2.1 Application to Bloch Electrons

In 1989, JOSHUA ZAK published a paper that highlights the role of the BERRY phase in the band theory of solids when subjected to an electric field [121]. Here, I focus mostly on the application of the previously presented general theory (Section 3.1) similar to Refs. [120–122] and mention the connection to the nonequilibrium physics, which is extensively discussed in Chapter 4.

The Hamiltonian under consideration

$$\hat{\mathcal{H}}\psi(\mathbf{r}) = E\psi(\mathbf{r}), \quad \hat{\mathcal{H}} = \frac{\hat{\mathbf{p}}^2}{2m} + \mathcal{U}(\mathbf{r}) \quad (3.14)$$

describes a single electron in a periodic potential $\mathcal{U}(\mathbf{r} + \mathbf{R}) = \mathcal{U}(\mathbf{r})$, where $\mathbf{R} = n_1\mathbf{a}_1 + n_2\mathbf{a}_2 + n_3\mathbf{a}_3$ is an arbitrary lattice vector represented as a linear combination of primitive lattice vectors \mathbf{a}_i with integer coefficients $n_i \in \mathbb{Z}$ ($i = 1, 2, 3$). This Hamiltonian appears in the description of electrons in the solids after the BORN-OPPENHEIMER approximation, if the electron-electron interactions are treated effectively.² Due to the discrete translational invariance of $\mathcal{U}(\mathbf{r})$, the translation operators $\hat{T}_{\mathbf{R}}$ that translate the wave function $\hat{T}_{\mathbf{R}}\psi(\mathbf{r}) = \psi(\mathbf{r} + \mathbf{R})$ by a lattice vector commute with the Hamiltonian and mutually commute for different lattice vectors. Thus, both the Hamiltonian and the set of all lattice translation operators must possess a common eigensystem.

The eigenvalue problem of the unitary translation operators reads

$$\hat{T}_{\mathbf{R}}\psi_{\mathbf{k}}(\mathbf{r}) = \psi_{\mathbf{k}}(\mathbf{r} + \mathbf{R}) = e^{i\mathbf{k}\cdot\mathbf{R}}\psi_{\mathbf{k}}(\mathbf{r}), \quad (3.15)$$

where the BLOCH vector $\mathbf{k} \in \mathbb{R}^3$ comprises the quantum numbers that are related to the complex eigenvalues of the translation operators. The BLOCH vector is defined as

²The many-electron problem can be (approximately) transformed onto a single-electron Hamiltonian by neglecting the electron-electron interactions, by the HARTREE approximation [123–125], or by considering the KOHN-SHAM equation [126].

3 Band Topology of Bosonic Quasiparticles

a continuous quantum number, which is only defined modulo reciprocal lattice vectors $\mathbf{G} = n_1 \mathbf{a}_1^* + n_2 \mathbf{a}_2^* + n_3 \mathbf{a}_3^*$, where $\mathbf{a}_i \cdot \mathbf{a}_j^* = 2\pi\delta_{ij}$, because the eigenfunctions of all lattice translation operators exhibit the same eigenvalue for \mathbf{k} and $\mathbf{k} + \mathbf{G}$ for any $n_i \in \mathbb{Z}$ ($i = 1, 2, 3$).

As a consequence of Eq. (3.15), the wave functions exhibit the structure of BLOCH functions

$$\psi_{n\mathbf{k}}(\mathbf{r}) = e^{i\mathbf{k}\cdot\mathbf{r}} u_{n\mathbf{k}}(\mathbf{r}), \quad (3.16)$$

where $u_{n\mathbf{k}}(\mathbf{r} + \mathbf{R}) = u_{n\mathbf{k}}(\mathbf{r})$ is a cell-periodic wave function. This is the famous BLOCH theorem [127]. Since the common eigenfunctions of the translation operators and the Hamiltonian could have the same translation eigenvalues while being orthogonal, it is expedient to introduce an additional quantum number n , which is the *band index*.

Now, the Hamiltonian for the periodic part of the BLOCH function reads

$$\hat{\mathcal{H}}_{\mathbf{k}} := e^{-i\mathbf{k}\cdot\mathbf{r}} \hat{\mathcal{H}} e^{i\mathbf{k}\cdot\mathbf{r}} = \frac{(\hat{\mathbf{p}} + \hbar\mathbf{k})^2}{2m} + \mathcal{U}(\mathbf{r}), \quad (3.17)$$

so that the SCHRÖDINGER equation becomes

$$\hat{\mathcal{H}}_{\mathbf{k}} u_{n\mathbf{k}}(\mathbf{r}) = E_{n\mathbf{k}} u_{n\mathbf{k}}(\mathbf{r}). \quad (3.18)$$

At this point, the BLOCH vector \mathbf{k} has entered the Hamiltonian $\hat{\mathcal{H}}_{\mathbf{k}}$ as a parameter. The original Hamiltonian respects the translational symmetry that conserves \mathbf{k} so that no BERRY phase arises. The situation changes if a perturbation emerges which causes an adiabatic dynamics of \mathbf{k} . Such a perturbation has to be described by a Hamiltonian that breaks the discrete translational symmetry, i.e., it must not commute with $\hat{T}_{\mathbf{R}}$. The corresponding momentum-space BERRY connection

$$\mathbf{A}_n(\mathbf{k}) = i \langle u_{n\mathbf{k}} | \nabla_{\mathbf{k}} u_{n\mathbf{k}} \rangle \quad (3.19)$$

and the BERRY curvature

$$\boldsymbol{\Omega}_n(\mathbf{k}) = i \langle \nabla_{\mathbf{k}} u_{n\mathbf{k}} | \times | \nabla_{\mathbf{k}} u_{n\mathbf{k}} \rangle \quad (3.20)$$

are defined with respect to $u_{n\mathbf{k}}$. Since $\boldsymbol{\Omega}_n$ only depends on the wave function $u_{n\mathbf{k}}$ and not on its gauge, it is an intrinsic property of the band structure. Alternatively, the BERRY curvature

$$\boldsymbol{\Omega}_n(\mathbf{k}) = i \langle \nabla_{\mathbf{k}} \psi_{n\mathbf{k}} | \times | \nabla_{\mathbf{k}} \psi_{n\mathbf{k}} \rangle + \nabla_{\mathbf{k}} \times \langle \psi_{n\mathbf{k}} | \mathbf{r} | \psi_{n\mathbf{k}} \rangle \quad (3.21)$$

recast in terms of the BLOCH function [Eq. (3.16)] encompasses both the gradient (first term on right-hand side) and the dipole contributions (second term).

The existence and the structure of the BERRY curvature depends on the symmetry of the system. Because the BERRY curvature is an axial vector, it is symmetric in centrosymmetric systems: $\boldsymbol{\Omega}_n(\mathbf{k}) = \boldsymbol{\Omega}_n(-\mathbf{k})$. On the other hand, the BERRY curvature is odd in time-reversal symmetric systems: $\boldsymbol{\Omega}_n(\mathbf{k}) = -\boldsymbol{\Omega}_n(-\mathbf{k})$. In other words, if the material is nonmagnetic or does not have an external field, $\boldsymbol{\Omega}_n(\mathbf{k})$ is antisymmetric. Both symmetries combined would lead to a cancelation of the BERRY curvature.

The importance of *translational* symmetry breaking is evident in the semiclassical description of electrons. Consider an electron wave packet localized around \mathbf{r}_c with mean BLOCH vector \mathbf{k}_c constructed of BLOCH functions of band n . In the presence of electric or magnetic fields, both position and BLOCH vector follow the dynamics [128, 129]

$$\frac{\partial \mathbf{r}_c}{\partial t} = \frac{1}{\hbar} \nabla_{\mathbf{k}} E_{n\mathbf{k}} - \frac{\partial \mathbf{k}_c}{\partial t} \times \boldsymbol{\Omega}_n(\mathbf{k}), \quad (3.22a)$$

$$\frac{\partial \mathbf{k}_c}{\partial t} = -\frac{e}{\hbar} \left(\mathbf{E} + \frac{\partial \mathbf{r}_c}{\partial t} \times \mathbf{B} \right). \quad (3.22b)$$

Obviously, in the presence of electric or magnetic fields, the BLOCH vector is no conserved quantity anymore [cf. Eq. (3.22b)] and the wave function picks up the momentum-space BERRY phase. As a result, the real-space motion of the wave packet is no longer exclusively determined by the group velocity [first term on right-hand side of Eq. (3.22a)], but co-affected by the *anomalous velocity* [second term in Eq. (3.22a)], which is perpendicular to the BERRY curvature and the electric field.

In Section 4.3, I show that the influence of the temperature gradient indeed introduces a term that breaks the momentum conservation so that the momentum-space BERRY curvature plays a pivotal role in the thermally induced transverse transport.

3.2.2 Application to Bosonic Bogoliubov-de Gennes Hamiltonians

Having introduced the momentum-space BERRY curvature in Section 3.2.1, it remains to transfer the theory to bosons like magnons or magnon polarons. Compared to the previous section, the wave function is not explicit, but hidden in the creation and annihilation operators. Furthermore, the Hamiltonian might not be particle number conserving, which introduces artificial additional bands and changes the normalization of the eigenvectors. Ref. [15, 130, 131] present different, but equivalent expressions for the BERRY curvature for magnons, which I cover below. Since the phonons have been quantized as bosons in a local basis similar to magnons in the second method delineated in Section 2.2.3, they can be regarded as “additional spin sublattices” so that the same equations are valid in the presence of phonon bands.³

I start with a general bosonic Hamiltonian in reciprocal space

$$\hat{\mathcal{H}} = \frac{1}{2} \sum_{\mathbf{k}} \hat{\boldsymbol{\psi}}_{\mathbf{k}}^\dagger \mathbf{H}_{\mathbf{k}} \hat{\boldsymbol{\psi}}_{\mathbf{k}}, \quad (3.23)$$

where the NAMBU spinors

$$\hat{\boldsymbol{\psi}}_{\mathbf{k}}^\dagger = \left(\hat{c}_{1\mathbf{k}}^\dagger \quad \cdots \quad \hat{c}_{\mathcal{N}\mathbf{k}}^\dagger \quad \hat{c}_{1(-\mathbf{k})} \quad \cdots \quad \hat{c}_{\mathcal{N}(-\mathbf{k})} \right) \quad (3.24)$$

comprise \mathcal{N} independent operators corresponding to the degrees of freedom within a unit cell (e.g., sublattices). The operators depend on the BLOCH vector as a result of the

³In the bosonic basis, the information about the physical interpretation of the quantized excitation is no longer relevant, but hidden in the particular mapping that was used to formulate the bosonic Hamiltonian in the first place. This includes spin-to-boson mappings like the HOLSTEIN-PRIMAKOFF transformation (cf. Section 2.3.3) or the phonon quantization (cf. Section 2.2.3). Hence, phonon and magnons (as well as other bosonic quasiparticles) can be treated on equal footing.

FOURIER transformation

$$\hat{c}_{i\mathbf{k}} = \frac{1}{\sqrt{\mathcal{N}_{\text{uc}}}} \sum_m e^{-i\mathbf{k}\cdot\mathbf{R}_{im}} \hat{c}_{im}, \quad \hat{c}_{im} = \frac{1}{\sqrt{\mathcal{N}_{\text{uc}}}} \sum_{\mathbf{k}} e^{i\mathbf{k}\cdot\mathbf{R}_{im}} \hat{c}_{i\mathbf{k}}, \quad (3.25a)$$

$$\hat{c}_{i\mathbf{k}}^\dagger = \frac{1}{\sqrt{\mathcal{N}_{\text{uc}}}} \sum_m e^{i\mathbf{k}\cdot\mathbf{R}_{im}} \hat{c}_{im}^\dagger, \quad \hat{c}_{im}^\dagger = \frac{1}{\sqrt{\mathcal{N}_{\text{uc}}}} \sum_{\mathbf{k}} e^{-i\mathbf{k}\cdot\mathbf{R}_{im}} \hat{c}_{i\mathbf{k}}^\dagger. \quad (3.25b)$$

Here, the positions $\mathbf{R}_{im} = \mathbf{R}_m + \mathbf{b}_i$ include both unit cell (m) and sublattice (i) position vectors. Because I include the sublattice position vectors, $\mathbf{H}_{\mathbf{k}}$ may not be periodic in reciprocal space if multiple sites belong to one unit cell. This is consistent with the transformed Hamiltonian for the cell-periodic wave function that might also not be translationally invariant [cf. Eq. (3.17)]. Because a translation $\mathbf{k} \rightarrow \mathbf{k} + \mathbf{G}$ by a reciprocal lattice vector \mathbf{G} results only in a unitary transformation of the matrix $\mathbf{H}_{\mathbf{k}}$, the eigenvalues $\varepsilon_{n\mathbf{k}} = \varepsilon_{n,\mathbf{k}+\mathbf{G}}$ are periodic. Excluding the sublattice vector in the phase factors in Eq. (3.25) would result in a Hamiltonian and eigenvectors inappropriate for computing the BERRY curvature using the expressions given below [132].

The eigenmodes are obtained by the BOGOLIUBOV transformation

$$\hat{\Psi}_{\mathbf{k}} = \mathbf{T}_{\mathbf{k}}^{-1} \hat{\psi}_{\mathbf{k}} = \left(\hat{\gamma}_{1\mathbf{k}} \quad \cdots \quad \hat{\gamma}_{\mathcal{N}\mathbf{k}} \quad \hat{\gamma}_{1(-\mathbf{k})}^\dagger \quad \cdots \quad \hat{\gamma}_{\mathcal{N}(-\mathbf{k})}^\dagger \right)^\top \quad (3.26)$$

comprising the creation and annihilation operators of the eigenmodes with band indices n and Bloch vector \mathbf{k} corresponding to the energies $\varepsilon_{n\mathbf{k}}$ ($n = 1, \dots, 2\mathcal{N}$), where $\varepsilon_{n\mathbf{k}} = \varepsilon_{n+\mathcal{N},-\mathbf{k}}$ for $n = 1, \dots, \mathcal{N}$. The details of the BOGOLIUBOV transformation are explained in Section 2.3.4.

For electrons, it is possible to transfer the expression Eq. (3.21) into the language of second quantization by identifying $\psi_{n\mathbf{k}}$ with $\hat{\gamma}_{n\mathbf{k}}^\dagger |0\rangle$, where $|0\rangle$ is the ground state of the system. For bosons, the bosonic metric σ_3 needs to be included in the definition of the scalar product because the eigenvectors given by $\mathbf{T}_{\mathbf{k}}^{-1}$ are not normalized in general. One finds for component λ of the bosonic BERRY curvature [130]

$$\Omega_{\lambda,n}(\mathbf{k}) = i \sum_{\mu\nu} \epsilon_{\lambda\mu\nu} \left(\sigma_3 \frac{\partial \mathbf{T}_{\mathbf{k}}^\dagger}{\partial k_\mu} \sigma_3 \frac{\partial \mathbf{T}_{\mathbf{k}}}{\partial k_\nu} \right)_{nn}. \quad (3.27)$$

The vector product is written in component notation using the LEVI-CIVITA symbol $\epsilon_{\lambda\mu\nu}$. Without σ_3 , one would obtain the result for electronic momentum space BERRY curvature. Because of the particle-hole symmetry, which relates the energies and the wave functions of bands with indices $n \leq \mathcal{N}$ and $n > \mathcal{N}$, the Berry curvature satisfies $\Omega_n(\mathbf{k}) = -\Omega_{n+\mathcal{N}}(-\mathbf{k})$ for $n \leq \mathcal{N}$. As for electrons, the sum of the BERRY curvature over all bands vanishes. This, however, includes the ‘‘hole’’ bands ($n > \mathcal{N}$) so that the sum over the ‘‘particle’’ bands ($n \leq \mathcal{N}$) does not vanish, but instead obeys

$$\sum_{n=1}^{\mathcal{N}} \Omega_n(\mathbf{k}) = \sum_{n=1}^{\mathcal{N}} \Omega_n(-\mathbf{k}). \quad (3.28)$$

Hence, if the system is inversion symmetric, which implies a symmetric BERRY curvature, there is no additional constraint.

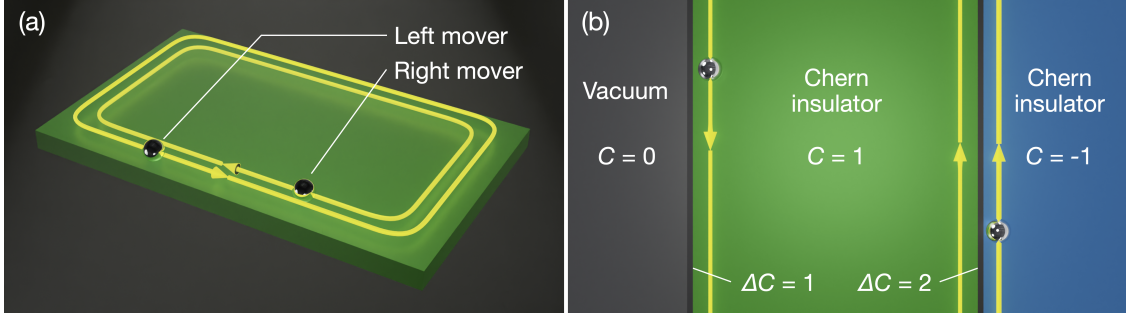


Figure 3.1: Topological chiral edge states and bulk-boundary correspondence. (a) Two-dimensional system hosting edge states. Left and right movers propagate in opposite directions. (b) Edge states at interfaces between vacuum and two CHERN insulators with different CHERN numbers C . The number and the chirality of the edge states for a given interface depends on the change of the CHERN numbers ΔC across the interface.

Using Eqs. (2.100) and (2.102), one proves the identity

$$\left(\mathbf{T}_{\mathbf{k}}^\dagger \sigma_3 \frac{\partial \mathbf{T}_{\mathbf{k}}}{\partial k_\mu} \right)_{mn} = \frac{\left(\mathbf{T}_{\mathbf{k}}^\dagger \frac{\partial \mathbf{H}_{\mathbf{k}}}{\partial k_\mu} \mathbf{T}_{\mathbf{k}} \right)_{mn}}{(\sigma_3 \mathcal{E}_{\mathbf{k}})_{mm} - (\sigma_3 \mathcal{E}_{\mathbf{k}})_{nn}} \quad (3.29)$$

for $m \neq n$ that allows to rewrite the BERRY curvature as [131]

$$\Omega_{\lambda,m}(\mathbf{k}) = i\epsilon_{\lambda\mu\nu} \sum_{\substack{m,n=1 \\ m \neq n}}^{2\mathcal{N}} \frac{\left(\sigma_3 \mathbf{T}_{\mathbf{k}}^\dagger \frac{\partial \mathbf{H}_{\mathbf{k}}}{\partial k_\mu} \mathbf{T}_{\mathbf{k}} \right)_{mn} \left(\sigma_3 \mathbf{T}_{\mathbf{k}}^\dagger \frac{\partial \mathbf{H}_{\mathbf{k}}}{\partial k_\nu} \mathbf{T}_{\mathbf{k}} \right)_{nm}}{[(\sigma_3 \mathcal{E}_{\mathbf{k}})_{mm} - (\sigma_3 \mathcal{E}_{\mathbf{k}})_{nn}]^2}. \quad (3.30)$$

Here, $\mathcal{E}_{\mathbf{k}}$ is the diagonal matrix with $\varepsilon_{m\mathbf{k}}$ as its entries. This formulation of the BERRY curvature is useful for calculations as the Hamilton matrix $\mathbf{H}_{\mathbf{k}}$ can be analytically derived. In this work, its entries have been explicitly derived for phonons (cf. Section 2.2.3), magnons (cf. Section 2.3.3), and magnon polarons (cf. Section 2.4.2). Therefore, the calculation of the BERRY curvature for \mathbf{k} only requires (numerical) diagonalization locally, instead of approximating the derivatives by finite differences.

Alternatively, one may compute the BERRY curvature based on the overlap of the wave functions at nearby wave vectors as described in Ref. [133].

3.3 Chern Insulators and Chiral Edge States

The BERRY curvature that I introduced in the previous sections plays an important role in the field of band topology, in particular for so-called CHERN insulators. In the field of topology, materials are classified by topological invariants, which do not depend on details of the system and are robust under certain conditions. For the CHERN insulator, the corresponding topological invariant is the CHERN number⁴ [7, 14, 15, 117, 134]

$$C_n = -\frac{1}{2\pi} \int d^2\mathbf{k} \Omega_n(\mathbf{k}), \quad (3.31)$$

⁴The sign of the CHERN numbers is not consistent throughout the literature. Some authors define it with the reversed sign, e.g., Refs. [2, 14–16, 120, 130].

where the system is two-dimensional and $\Omega_n(\mathbf{k})$ is the z component of BERRY curvature if the system is translationally invariant in the xy plane.⁵ The CHERN number is an integer number that is protected by the splitting of the n -th band to the remaining bands. In order for it to change, the band gap must be closed and reopened again. The band gap provides a topological protection of the CHERN number against small perturbations [117].

If one now places two systems with different CHERN numbers next to each other, the CHERN number has to interpolate from one to the other. Because it is integer-valued, it cannot smoothly vary across the interface and the band gap has to close. As a result, edge states appear that bridge the gap between the bulk bands, allowing the CHERN number to change [2]. Two types of edge states exist that are distinguished by their propagation direction. Left movers circle counterclockwise, while right movers revolve clockwise around the sample (cf. Fig. 3.1) [70]. Deformations at the edge may alter the wave function of these edge states, but they cannot be destroyed as long as there is a bulk band gap. The edge states also occur in systems with a nonzero CHERN number that have a boundary, i.e., an interface to the vacuum. Conversely, if the CHERN numbers vanish, there are not necessarily edge states.⁶ In an electronic system with a FERMI energy in a bulk band gap and an interface to the vacuum, the CHERN number is related to the number of left- and right-moving edge states as [3, 70]

$$C := \sum_{n \in \text{occ}} C_n = N_L - N_R. \quad (3.32)$$

N_L (N_R) is the number of left (right) movers and the sum runs over all occupied bands. This is the *bulk-boundary correspondence* because it relates a bulk property (left-hand side) to an edge property (right-hand side). If $C \neq 0$, there is a preponderance of left over right movers or vice versa. In this case, the edge states are said to be *chiral*, and the system is *topologically nontrivial*. If one considers the interface between two insulators, one would need to replace the left-hand side of Eq. (3.32) by the difference ΔC of C of both insulators on either side of the interface [3]. Hence, the number of chiral edge states depends on “how much” the topological invariants change from one to the other system that form the interface [cf. Fig. 3.1(b)].

ZHANG *et al.* [14] and SHINDOU *et al.* [15] were the first to predict that CHERN insulators also exist for magnons, where they are commonly referred to as “topological magnon insulators.” Although magnons do not feature a FERMI level, their bands may be gapped and possess nonzero CHERN numbers. Then, the gap above the n -th bulk band hosts at least

$$N_L(n) - N_R(n) = \sum_{m \leq n} C_m \quad (3.33)$$

edge modes [8, 9]. Contrary to electrons, the edge states of magnons are necessarily *excitations* above the ground state. This means that either nonzero temperature or a preparation of a nonequilibrium state are required to observe them. Since there are

⁵Note that the components of the BERRY curvature parallel to the plane are not defined because a two-dimensional system displays no translational invariance along the out-of-plane component and, hence, the BLOCH vector does not have an out-of-plane component.

⁶There may be *trivial* edge states that are not robust and whose energies depend on the details of the edges. The topologically protected edge states are guaranteed within the bulk band gap for topological insulators irrespective of the details.

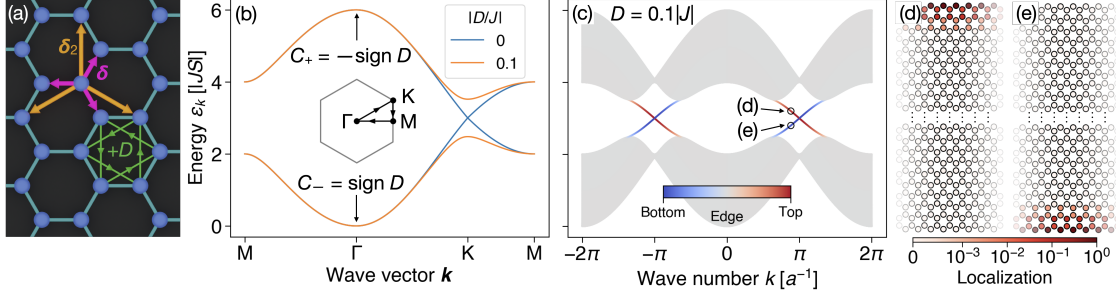


Figure 3.2: Magnonic HALDANE model. (a) Honeycomb lattice with nearest (δ) and next-nearest neighbor bonds (δ_2). Green arrows indicate counterclockwise next-nearest neighbor bonds, for which $D_{ij} = +D$. (b) Bulk magnon spectrum with and without DZYALOSHINSKII-MORIYA interaction (see legend). Inset: High-symmetry path in the first BRILLOUIN zone. (c) Nanoribbon magnon spectrum with zigzag terminations for $D = 0.1|J|$. Gray/blue/red color of the bands indicate bulk/bottom edge/top edge modes (see color bar). (d, e) Amplitudes of two magnon wave functions in a zigzag nanoribbon localized at the top/bottom edge, respectively [cf. panel (c)]. The color represents the logarithmically scaled squares of the wave functions' amplitudes (see color bar). The ribbon is finite (infinite) in the vertical (horizontal) direction.

no topological chiral edge states below the lowest bulk band, they are higher-energy excitations. This is one of the main problems that exacerbates their detection as discussed in the Publications [RN2, RN4] (cf. Sections 6.2.1 and 6.3).

3.3.1 Magnonic Haldane Model

In the following, the theoretical existence of chiral topological magnons is demonstrated by the magnonic analogue of the famous HALDANE model, by which FREDERICK DUNCAN MICHAEL HALDANE showcased the existence of a CHERN insulating phase in the absence of an external magnetic field in 1988 [135]. It has been rediscovered for magnons in Refs. [18, 19].

The magnonic HALDANE model describes a ferromagnet on a two-dimensional honeycomb lattice [cf. Fig. 3.2(a)], which has two sublattices A and B. The localized spins are oriented along the out-of-plane directions ($\mathbf{z}_i \parallel \mathbf{z}$, $i = A, B$) and their interactions are given by [18, 19, 136]

$$\hat{\mathcal{H}}_s = \frac{J}{2\hbar^2} \sum_{\langle ij \rangle} \hat{\mathbf{S}}_i \cdot \hat{\mathbf{S}}_j + \frac{1}{2\hbar^2} \sum_{\langle\langle ij \rangle\rangle} \mathbf{D}_{ij} \cdot (\hat{\mathbf{S}}_i \times \hat{\mathbf{S}}_j). \quad (3.34)$$

Here, the first term is the HEISENBERG exchange interaction $J < 0$ between the three nearest neighbors of each spin, and the second one corresponds to the DZYALOSHINSKII-MORIYA interaction between the six next-nearest neighbors per spin. The vector $\mathbf{D}_{ij} = -\mathbf{D}_{ji} = D_{ij}\mathbf{z}$ with $D_{ij} = \pm D$ is oriented perpendicular to the honeycomb plane and has the same sign for all bonds connecting the sites by counterclockwise loops [cf. Fig. 3.2(a)]. By employing the HOLSTEIN-PRIMAKOFF transformation (Section 2.3.3),

one obtains for the bilinear bosonic Hamiltonian

$$\hat{\mathcal{H}}_b^{(2)} = -3JS \sum_i \hat{b}_i^\dagger \hat{b}_i + JS \sum_{\langle ij \rangle} \hat{b}_i^\dagger \hat{b}_j - iS \sum_{\langle\langle ij \rangle\rangle} D_{ij} \hat{b}_i^\dagger \hat{b}_j. \quad (3.35)$$

The first term corresponds to an on-site potential for the magnons that shifts their energy, the second term accounts for real hopping between nearest neighbors, and the last one describes the complex hopping between second-nearest neighbors. After FOURIER transformation, one obtains a 2×2 matrix that can be readily diagonalized yielding the magnon energies [19]

$$\varepsilon_{m,\pm\mathbf{k}} = 3JS \pm |\mathbf{h}_{\mathbf{k}}|, \quad \mathbf{h}_{\mathbf{k}} = \begin{pmatrix} JS \sum_{\delta} \cos \mathbf{k} \cdot \delta \\ -JS \sum_{\delta} \sin \mathbf{k} \cdot \delta \\ 2DS \sum_{\delta_2} \sin \mathbf{k} \cdot \delta_2 \end{pmatrix}, \quad (3.36)$$

where δ and δ_2 denote nearest and three of the six next-nearest neighbor bonds, respectively [cf. Fig. 3.2(a)].⁷

The magnon band structure features two bands, which touch at the K point if $D = 0$ forming a DIRAC point with linearly dispersing magnon bands [cf. Fig. 3.2(b)]. In the presence of the DZYLOSHINSKII-MORIYA interaction ($D \neq 0$), a gap is opened, which does not depend on the sign of D .

In a two-level system, the BERRY curvature can conveniently be expressed as [19, 137, 138]

$$\Omega_{\pm}(\mathbf{k}) = \mp \frac{\mathbf{h}_{\mathbf{k}}}{2|\mathbf{h}_{\mathbf{k}}|^3} \cdot \left(\frac{\partial \mathbf{h}_{\mathbf{k}}}{\partial k_x} \times \frac{\partial \mathbf{h}_{\mathbf{k}}}{\partial k_y} \right), \quad (3.37)$$

which, for $D \neq 0$, becomes nonzero giving rise to the CHERN numbers $C_{\pm} = \mp \text{sign } D$. Only if $D \neq 0$ the CHERN numbers are well-defined and their signs are governed by the sign of D . Alternatively, to reverse the CHERN numbers, one could also reverse the ground state direction. This is a general consequence of the symmetry properties of the BERRY curvature, which leads to a reversal of the CHERN numbers under time reversal (cf. Section 3.2.1).

As a consequence of the formed gap between the topologically nontrivial bulk bands, in-gap edge modes appear in nanoribbons, which are infinite along one and finite along the other direction.⁸ For zigzag terminations and $D = 0.1|J|$, the in-gap modes connect the projected gapped DIRAC points of the bulk bands [cf. Fig. 3.2(c)]. For other terminations, the dispersion of the edge modes can be changed, but their existence is guaranteed by the topological bulk band gap. Here, the gray colored bulk continuum results from the projection of the two-dimensional band structure [Fig. 3.2(b)] onto the zigzag edges. The two red and blue colored bands are edge modes at opposite sites of the nanoribbon, which have opposite group velocities due to the opposite slopes of their bands. Because $C_- = +1$, the two bands correspond to a left mover as visualized in Fig. 3.1(a) in agreement with Eq. (3.33).

⁷The vectors δ_2 are defined as those three next-nearest bond vectors connecting sites i and j on sublattice A so that $D_{ij} = +D$.

⁸Alternatively, they are finite in both directions, but periodic boundary conditions are applied to one direction, whereas the other is subject to open boundary conditions.

To get an impression of the degree of localization, I plot the squared amplitudes of the magnon wave functions for the two selected modes highlighted in Fig. 3.2(c) in Fig. 3.2(d, e) on the zigzag nanoribbon. Here, they are visualized on a logarithmic scale. Both modes are strongly localized at opposite edges and rapidly decay into the bulk. Those modes whose energies approach those of the bulk bands have higher localization lengths, eventually interpolating to the bulk modes that are delocalized (not shown).

LINEAR RESPONSE THEORY

This thesis is not only concerned with the microscopic description and phenomena that are predicted by quantum mechanics and topology, but also their observable macroscopic consequences. A straight-forward example would be the relation between the microscopic magnetic moment of a magnon, which is related to the macroscopic magnetization of the sample. These two can be related by the density operator [139]

$$\hat{\rho}_0 = \frac{e^{-\beta(\hat{\mathcal{H}}_0 - \mu\hat{N})}}{Z}, \quad (4.1)$$

which, loosely speaking, weights each microstate with a probability amplitude $\langle n|\hat{\rho}_0|n\rangle$ to obtain a temporal average of an observable by an ensemble average over all possible microstates $|n\rangle$.¹ This is known as the *ergodic hypothesis*, which states that the phase space trajectory of the microstate samples every point of the phase space during the observation time so that temporal averages are identical to ensemble averages [139].² Here, I am working with the grand canonical ensemble, where $\beta = (k_B T)^{-1}$ is the thermodynamic beta, k_B is the BOLTZMANN constant, T is the temperature, $\hat{\mathcal{H}}_0$ is a time-independent Hamiltonian, μ is the chemical potential, \hat{N} is the particle number operator, and $Z = \text{Tr} e^{-\beta(\hat{\mathcal{H}}_0 - \mu\hat{N})}$ is the partition function. More rigorously, if \hat{O} is an operator that is defined for each microstate, its statistical expectation value is given as [40]

$$\langle \hat{O} \rangle_0 := \text{Tr} \hat{\rho}_0 \hat{O} = \sum_n \frac{e^{-\beta(E_n - \mu N_n)}}{Z} \langle n|\hat{O}|n\rangle, \quad (4.2)$$

with the energy E_n and the particle number N_n of the microstate n . The second equation holds for the eigenbasis of $\hat{\mathcal{H}}_0$.

Assume the total Hamiltonian

$$\hat{\mathcal{H}}(t) = \hat{\mathcal{H}}_0 + \hat{V}(t) \quad (4.3)$$

is time-dependent and the system is coupled to a heat bath. Now, the question arises how the associated density operator $\hat{\rho}(t)$ is modified in presence of this perturbation $\hat{V}(t)$. Is it sufficient to replace $\hat{\mathcal{H}}_0$ by $\hat{\mathcal{H}}(t)$ in Eq. (4.1)? This seems unlikely because the bath is not expected to follow the temporal oscillations [39]. Then, how can the thermal expectation values of operators be expressed? These questions are addressed in Section 4.1 in a general framework. In order to describe diffusion processes, which are driven by statistical forces like thermal gradients or gradients in the chemical potential, the LUTTINGER method is introduced in Section 4.2. With the general theory established, the last section (Section 4.3) is concerned with the thermal transport.

¹This statement is correct as long as the microstate is defined as an eigenstate of both $\hat{\mathcal{H}}_0$ and \hat{N} so that $\hat{\rho}_0$ is diagonal in that basis. Otherwise, it does not merely weight the microstates, but its matrix elements mix with the matrix element of the observable.

²A relaxed version only assumes that every trajectory except a null set is approaching every point in phase space with arbitrarily small distance [139].

4.1 General Kubo Formula

Published in 1957, RYOGO KUBO developed a general quantum statistical theory for the linear response of quantities to external perturbations by linearizing and subsequently solving the equation of motion for the nonequilibrium density operator $\hat{\rho}$ [140]. The quintessential idea, succinctly known as the *fluctuation-dissipation theorem*, is that the response of a system to a small external perturbation is related to its *equilibrium fluctuations*. In equilibrium, all variables fluctuate about their mean with a certain standard deviation. If there is a deviation from the mean, the system has the tendency to return to its mean value, otherwise it would not be at equilibrium. According to the fluctuation-dissipation theorem, the noise of thermodynamic variables in equilibrium and the response of a system to an external perturbation are caused by a common microscopic origin [141]. This fundamental abstract relation applies to many different contexts, e.g., the relation between voltage fluctuations and electrical impedance known as the NYQUIST relation, or between Brownian motion and viscous drag of fluids on moving bodies [142]. The mathematical framework presented here follows the original article [140] and the textbooks [39, 40].

Kubo Formula in Time Domain

The nonequilibrium density operator obeys the VON NEUMANN equation

$$i\hbar \frac{\partial \hat{\rho}(t)}{\partial t} = [\hat{\mathcal{H}}(t), \hat{\rho}(t)] \quad (4.4)$$

that one solves for $\hat{\rho}(t) = \hat{\rho}_0 + \hat{\rho}_V(t)$. After linearization, the VON NEUMANN equation becomes

$$i\hbar \frac{\partial \hat{\rho}_V(t)}{\partial t} = [\hat{V}(t), \hat{\rho}_0] + [\hat{\mathcal{H}}_0, \hat{\rho}_V(t)], \quad (4.5)$$

whose solution reads

$$\hat{\rho}_V(t) = -\frac{i}{\hbar} e^{\frac{i}{\hbar} t \hat{\mathcal{H}}_0} \int_{t_0}^t dt' [\hat{V}_D(t'), \hat{\rho}_0] e^{-\frac{i}{\hbar} t' \hat{\mathcal{H}}_0}. \quad (4.6)$$

I have assumed that $\hat{V}(t)$ vanishes before t_0 and is adiabatically switched on at t_0 . Before t_0 , the density matrix is given as $\hat{\rho} = \hat{\rho}_0$. A new notation for operators has been introduced. Let $\hat{X}(t)$ be an operator in the SCHRÖDINGER picture, then

$$\hat{X}_D(t) = e^{\frac{i}{\hbar} \hat{\mathcal{H}}_0 t} \hat{X}(t) e^{-\frac{i}{\hbar} \hat{\mathcal{H}}_0 t} \quad (4.7)$$

is the same operator in the DIRAC picture.

Having obtained the nonequilibrium density matrix to first order in the perturbation \hat{V} , statistical expectation values of arbitrary operators $\hat{O}(t)$ can be computed as $\langle \hat{O}(t) \rangle = \langle \hat{O}(t) \rangle_0 + \Delta \langle \hat{O}(t) \rangle$ with

$$\Delta \langle \hat{O}(t) \rangle = \int_{t_0}^{\infty} dt' C_{\hat{O}\hat{V}}^R(t, t') e^{-\eta(t-t')}, \quad (4.8)$$

where the retarded correlation function is integrated over time. For arbitrary operators \hat{X} and \hat{Y} , the retarded correlation function is defined as

$$C_{\hat{X}\hat{Y}}^{\text{R}}(t, t') = -\frac{i}{\hbar}\theta(t-t') \left\langle \left[\hat{X}_{\text{D}}(t), \hat{Y}_{\text{D}}(t') \right] \right\rangle_0, \quad (4.9)$$

which vanishes for $t < t'$ due to the HEAVISIDE function $\theta(t-t')$. Equation (4.8) is the famous KUBO formula that relates the change of an expectation value to the retarded correlation function of that operator with the perturbation. The exponential factor $e^{-\eta(t-t')}$ was artificially added to bestow a finite memory upon the system. It ensures that the response at time t to the perturbation at time t' decays over time. After the evaluation of the integral, one takes the limit $\eta \rightarrow 0^+$.

Kubo Formula in Frequency Domain

In the remainder of this section, I show how to rewrite the KUBO formula in frequency domain and how to express the retarded correlation functions as MATSUBARA correlation functions. The FOURIER transform \hat{V}_ω of

$$\hat{V}(t) = \int_{-\infty}^{\infty} \frac{d\omega}{2\pi} e^{-i\omega t} \hat{V}_\omega \quad (4.10)$$

no longer depends on time in the SCHRÖDINGER picture. Therefore, the retarded correlation function

$$C_{\hat{O}\hat{V}_\omega}^{\text{R}}(t-t') = -\frac{i}{\hbar}\theta(t-t') \left\langle \left[\hat{O}_{\text{D}}(t-t'), \hat{V}_\omega \right] \right\rangle_0 \quad (4.11)$$

is homogeneous in time since the time dependence of the DIRAC picture can be carried over to $\hat{O}_{\text{D}}(t) \rightarrow \hat{O}_{\text{D}}(t-t')$ because of the commutativity of operators under the trace. It is related to the correlation function in the KUBO formula [Eq. (4.8)] as

$$C_{\hat{O}\hat{V}}^{\text{R}}(t, t') = \int_{-\infty}^{\infty} \frac{d\omega}{2\pi} e^{-i\omega t'} C_{\hat{O}\hat{V}_\omega}^{\text{R}}(t-t'). \quad (4.12)$$

Inserting this relation in the KUBO formula [Eq. (4.8)] and taking the limit $t_0 \rightarrow -\infty$, one obtains

$$\Delta \left\langle \hat{O}(t) \right\rangle = \int_{-\infty}^{\infty} \frac{d\omega}{2\pi} e^{-i\omega t} C_{\hat{O}\hat{V}_\omega}^{\text{R}}(\omega). \quad (4.13)$$

Here, the retarded correlation function has been defined in frequency domain as

$$C_{\hat{O}\hat{V}_\omega}^{\text{R}}(\omega) = \int_{-\infty}^{\infty} d\tau e^{i\omega\tau} e^{-\eta\tau} C_{\hat{O}\hat{V}_\omega}^{\text{R}}(\tau). \quad (4.14)$$

The left-hand side of Eq. (4.13) is written in the time-domain, while the right-hand side involves the frequency-domain correlation function that is transformed to the time domain. Recasting the expression to frequency domain gives a concise formulation of the KUBO formula:

$$\Delta \left\langle \hat{O}_\omega \right\rangle = C_{\hat{O}\hat{V}_\omega}^{\text{R}}(\omega). \quad (4.15)$$

Hence, the FOURIER transform of the nonequilibrium contribution to the expectation value of \hat{O} is equal to the FOURIER transform of the retarded correlation function between \hat{O} and the FOURIER transform of the time-dependent part of the Hamiltonian.

In some cases it is more convenient to compute the correlation function with the time derivative of \hat{V} rather than \hat{V} itself. As an example, consider an electric field, which couples to the electric polarization $\hat{V} = -V\hat{\mathbf{P}} \cdot \mathbf{E}$ with the total volume of the system denoted as V . Rather than computing the correlation function with the electric polarization, one may consider its time derivative, which is the charge current density [140].³

First, I assume that \hat{O} is time-independent in its SCHRÖDINGER representation. Then, the time derivative of the retarded correlation function reads

$$\frac{\partial C_{\hat{O}\hat{V}_\omega}^{\text{R}}(t)}{\partial t} = -\frac{i}{\hbar}\delta(t)\left\langle\left[\hat{O}, \hat{V}_{\omega, \text{D}}(-t)\right]\right\rangle_0 + \frac{i}{\hbar}\theta(t)\left\langle\left[\hat{O}, \frac{\partial \hat{V}_{\omega, \text{D}}(-t)}{\partial(-t)}\right]\right\rangle_0, \quad (4.16)$$

where I exploited the identity $\frac{\partial \theta(t)}{\partial t} = \delta(t)$. By partial integration of Eq. (4.14) and insertion of Eq. (4.16), one obtains

$$C_{\hat{O}\hat{V}_\omega}^{\text{R}}(\omega) = \frac{C_{\hat{O}\frac{\partial \hat{V}_\omega}{\partial t}}^{\text{R}}(\omega) - C_{\hat{O}\frac{\partial \hat{V}_\omega}{\partial t}}^{\text{R}}(0)}{i\omega}, \quad (4.17)$$

where the limit $\eta \rightarrow 0^+$ has been taken. The operator $\frac{\partial \hat{V}_\omega}{\partial t}$ is an abbreviation for the operator $\frac{i}{\hbar}[\hat{\mathcal{H}}_0, \hat{V}_\omega]$, which is the time derivative of $\hat{V}_{\omega, \text{D}}(t)$ before it has been transformed back to its SCHRÖDINGER representation. Note that the explicit time dependence of $\hat{V}(t)$ is not included here because it has been eliminated in the FOURIER transform \hat{V}_ω .

Matsubara Correlation Functions

Besides retarded correlation functions, there is another important kind of correlation functions, which are related to the former. In the context of this thesis, the MATSUBARA correlation functions, named after TAKEO MATSUBARA, defined for arbitrary operators \hat{X} and \hat{Y} as

$$C_{\hat{X}\hat{Y}}(t, t') = -\left\langle\hat{T}\hat{X}_{\text{D}}(t)\hat{Y}_{\text{D}}(t')\right\rangle_0 \quad (4.18)$$

plays an important role because they can be employed for obtaining the corresponding retarded correlation functions. Here, the DIRAC picture has been introduced for imaginary “times” as $\hat{X}_{\text{D}}(t) := \hat{X}_{\text{D}}(-i\hbar t)$ (and analogue for \hat{Y}). The time-ordering operator \hat{T} acts on the operators $\hat{X}_{\text{D}}(t)$ and $\hat{Y}_{\text{D}}(t')$ such that it reorders their product as

$$\hat{T}\hat{X}_{\text{D}}(t)\hat{Y}_{\text{D}}(t') = \theta(t - t')\hat{X}_{\text{D}}(t)\hat{Y}_{\text{D}}(t') \pm \theta(t' - t)\hat{Y}_{\text{D}}(t')\hat{X}_{\text{D}}(t), \quad (4.19)$$

where the upper (lower) sign applies to bosons (fermions). In the following, \hat{X} and \hat{Y} are assumed to be time independent.

³In the SCHRÖDINGER picture, $\hat{\mathbf{P}}$ does not depend on time. However, in its DIRAC picture, the time derivative is given by the commutator with $\hat{\mathcal{H}}_0$. Hence, whenever I loosely refer to the time derivative of a time-independent operator \hat{X} , the actual operator I am referring to is $\frac{i}{\hbar}[\hat{\mathcal{H}}_0, \hat{X}]$.

The MATSUBARA correlation function can be shown to depend only on the time difference $t - t'$ and is only well-defined in the interval $-\beta < t - t' < \beta$. Furthermore, it satisfies $C_{\hat{X}\hat{Y}}(\tau) = \pm C_{\hat{X}\hat{Y}}(\tau + \beta)$ depending on whether it describes a bosonic (+) or fermionic (-) system. These properties allow for a representation of the MATSUBARA correlation functions as a FOURIER series with coefficients

$$C_{\hat{X}\hat{Y}}(i\omega_l) = \int_0^\beta d\tau e^{i\hbar\omega_l\tau} C_{\hat{X}\hat{Y}}(\tau). \quad (4.20)$$

The so-called MATSUBARA frequencies take the discrete values $\omega_l = \frac{2l\pi}{\beta\hbar}$ for bosons or $\omega_l = \frac{(2l+1)\pi}{\beta\hbar}$ for fermions ($l \in \mathbb{Z}$).

The importance of the MATSUBARA correlation functions in the context of linear response theory becomes apparent upon revealing their connection to the retarded correlation functions. Usually, it is much easier to compute the MATSUBARA correlation functions in frequency space. After the integral has been computed, the retarded correlation function is simply obtained by analytic continuation to the real axis:

$$C_{\hat{X}\hat{Y}}^R(\omega) = C_{\hat{X}\hat{Y}}(i\omega_l \rightarrow \omega + i0^+). \quad (4.21)$$

This provides yet another way of computing the linear response.

4.2 Statistical Forces

The KUBO formula in the last section quantifies the reaction of a system to an external stimulus. Two main assumptions have been made. Firstly, the stimulus must be sufficiently weak so that the linear order provides a good approximation to the response. Secondly, the perturbation must be expressible as a Hamiltonian. The latter condition represents a severe restriction to the applicability to statistical forces such as gradients in temperature or chemical potential. These quantities are not defined on the level of the Hamiltonian, but they are introduced in the statistical-mechanical description, i.e., in the equilibrium density operator.

Temperature is a measure of the mean energy of a system. Gradients in temperature lead to a compensating current that tries to balance the inhomogeneity. In order to describe a disturbance of the homogeneous temperature or the mean energy, a conjugated external field has to be applied that controls the perturbation. In 1964, JOAQUIN MAZDAK LUTTINGER proposed introducing a gravitational potential that couples to the energy density to mimic the temperature gradient at the level of the Hamiltonian [143]. This installs a force proportional to the energy of the particles. Hence, at the core of the LUTTINGER method, a dynamical force – the pseudogravitational potential – is employed to incorporate a statistical force – the temperature gradient, where the former acts on individual particles and the latter affects their dynamics via the distribution function [130]. The following presentation of the LUTTINGER method is guided by Refs. [130, 143–146].

To further motivate the use of a pseudogravitational potential, recall that the temperature enters the BOLTZMANN factor $e^{-\hat{H}_0/(k_B T)}$, where the temperature gradient enters $T(\mathbf{r}) = T_0[1 - \chi(\mathbf{r})]$. T_0 is the mean temperature and χ governs the spatial inhomogeneity. To linear order in χ , the BOLTZMANN factor can be rewritten as $e^{-(1+\chi)\hat{H}_0/(k_B T_0)}$ so that $\hat{V} = \chi\hat{H}_0$ can be considered as the Hamiltonian of the perturbation. Assuming a linear temperature profile, the temperature gradient enters as $\chi(\mathbf{r}) = -\mathbf{r} \cdot \hat{\nabla}_{\mathbf{r}} T/T_0$.

4 Linear Response Theory

First, the equilibrium Hamiltonian

$$\hat{\mathcal{H}}_0 = \frac{1}{2} \int d^d \mathbf{r} \hat{\psi}^\dagger(\mathbf{r}) \hat{\mathbf{H}}_0 \hat{\psi}(\mathbf{r}) \quad (4.22)$$

is defined in terms of a Hamiltonian density $\hat{\mathbf{H}}_0 \in \text{Mat}(2\mathcal{N}, 2\mathcal{N})$, which should be interpreted as a matrix superoperator acting on the NAMBU spinors

$$\hat{\psi}^\dagger(\mathbf{r}) = \left(\hat{c}_1^\dagger(\mathbf{r}) \quad \cdots \quad \hat{c}_N^\dagger(\mathbf{r}) \quad \hat{c}_1(\mathbf{r}) \quad \cdots \quad \hat{c}_N(\mathbf{r}) \right) \quad (4.23)$$

of bosonic creation and annihilation operators. Although the derivation applies to lattices, they are herein described by a continuum theory, where the creation operators $\hat{c}_i^\dagger(\mathbf{r})$ depend on the sublattice i and the position \mathbf{r} of the unit cell (as for annihilation operators). The commutation relation in the continuum limit becomes $[\hat{c}_i(\mathbf{r}_1), \hat{c}_j^\dagger(\mathbf{r}_2)] = \delta_{ij} \delta(\mathbf{r}_1 - \mathbf{r}_2)$, where $\delta(\mathbf{r})$ is the delta distribution. Other combinations of bosonic operators commute. Even though the Hamiltonian [Eq. (4.22)] *seems* diagonal in \mathbf{r} , $\hat{\mathbf{H}}_0 = \sum_{\delta} \mathbf{H}_{\delta} e^{\delta \cdot \hat{\nabla}_{\mathbf{r}}}$ generally acts on $\hat{\psi}(\mathbf{r}) \rightarrow \hat{\psi}(\mathbf{r} + \delta)$ and translates it [145].

Having introduced the continuum notation, it is now possible to express the perturbation as

$$\hat{V} = \frac{1}{4} \int d^d \mathbf{r} \hat{\psi}^\dagger(\mathbf{r}) \left(\hat{\mathbf{H}}_0(\mathbf{r}) \chi(\mathbf{r}) + \chi(\mathbf{r}) \hat{\mathbf{H}}_0(\mathbf{r}) \right) \hat{\psi}(\mathbf{r}). \quad (4.24)$$

Here, the energy density comprising χ had to be symmetrized in order to render \hat{V} Hermitian. Since χ is assumed to be small, the total Hamiltonian

$$\hat{\mathcal{H}} = \frac{1}{2} \int d^d \mathbf{r} \left(1 + \frac{\chi(\mathbf{r})}{2} \right) \hat{\psi}^\dagger(\mathbf{r}) \hat{\mathbf{H}}_0(\mathbf{r}) \left(1 + \frac{\chi(\mathbf{r})}{2} \right) \hat{\psi}(\mathbf{r}) \quad (4.25)$$

is obtained by rescaling the creation operators $\hat{\psi}^\dagger(\mathbf{r}) \rightarrow \left(1 + \frac{\chi(\mathbf{r})}{2} \right) \hat{\psi}^\dagger(\mathbf{r})$ [and analogous for $\hat{\psi}(\mathbf{r})$] in the expression of the equilibrium Hamiltonian [Eq. (4.22)].

Now, a Hamiltonian for the temperature gradient has been provided that can be tackled with the KUBO formula. As a result of the pseudogravitational potential, the total Hamiltonian has changed. This affects the dynamics of operators that are governed by their commutation with the *total* Hamiltonian according to the HEISENBERG equation of motion [30, 39, 40]

$$\frac{\partial \hat{X}_H(t)}{\partial t} = \frac{i}{\hbar} \left[\hat{\mathcal{H}}, \hat{X}_H(t) \right], \quad (4.26)$$

where $\hat{X}_H(t) = e^{\frac{i}{\hbar} t \hat{\mathcal{H}}} \hat{X} e^{-\frac{i}{\hbar} t \hat{\mathcal{H}}}$ is the HEISENBERG representation of a time-independent operator \hat{X} in the SCHRÖDINGER picture.⁴ The time evolution of \hat{X}_H is already considered in the KUBO formula by the solution of the VON NEUMANN equation. On the other hand, if a current for \hat{X} is defined from a continuity equation, the definition of the current itself will change under \hat{V} . Therefore, there are two contributions to the linear response of a current: one arising from the KUBO formula and one from the modification of the continuity equation that alters the definition of the current operator. This is elaborated in the next section for the example of thermal currents.

⁴In the most general case, the HEISENBERG picture of an operator $\hat{X}(t)$ would be defined as $\hat{X}_H(t) = \hat{U}^\dagger(t) \hat{X}(t) \hat{U}(t)$, where $\hat{U}(t)$ is the time-evolution operator [30]. Only in the case of an explicitly time-independent Hamiltonian $\hat{\mathcal{H}}$, the time-evolution operator can be expressed as $\hat{U}(t) = e^{-\frac{i}{\hbar} t \hat{\mathcal{H}}}$. Here, $\hat{\mathcal{H}}$ expressed in Eq. (4.25) is time-independent.

4.3 Intrinsic Thermal Hall Conductivity

The thermal HALL effect, named after EDWIN HALL, also known as the RIGHI-LEDUC effect, named after AUGUSTO RIGHI and SYLVESTRE ANATOLE LEDUC, refers to the appearance of a *transverse* heat current induced by a *longitudinal* temperature gradient (cf. Fig. 1.1). It is the complementary transport effect to FOURIER's law, named after JEAN-BAPTISTE JOSEPH FOURIER, which denotes the longitudinal flow of heat in response to a longitudinal temperature gradient. While the thermal HALL effect of electrons in nonmagnetic metals in an external magnetic field is driven by the LORENTZ force, the thermal HALL effect in magnetic insulators without disorder studied in this work is driven by the BERRY curvature, as demonstrated below. The following derivations provide the basis for the Publications [RN2, RN3] of this thesis.

In general, heat transport in the linear response regime is governed by the heat conductivity κ that mediates between heat current

$$\langle \hat{\mathbf{J}} \rangle = \kappa (-\hat{\nabla}_{\mathbf{r}} T) \quad (4.27)$$

and thermal gradient $\hat{\nabla}_{\mathbf{r}} T$. The thermal Hall conductivity $\kappa_{\mu\nu}^{\text{H}} = (\kappa_{\mu\nu} - \kappa_{\nu\mu})/2$ ($\mu \neq \nu$) is associated with the antisymmetric part of κ and quantifies the thermal HALL effect. The thermal Hall conductivity is time-reversal odd, i.e., it changes sign upon reversal of the external magnetic field and the magnetic order. Consequently, it vanishes without magnetic field and magnetism. On the other hand, the symmetric part $(\kappa_{\mu\nu} + \kappa_{\nu\mu})/2$ is even under time reversal and associated with the so-called planar HALL effect. The planar HALL effects sensitively depend on the geometry because the corresponding transverse current changes its magnitude depending on the direction of the temperature gradient. It even can be suppressed along certain crystallographic directions, which can be found by diagonalizing the symmetric part of κ . In contrast, the thermal HALL effect is robust and exists independently of the direction of the temperature gradient.⁵ In this section, the derivation of the thermal HALL effect by MATSUMOTO *et al.* is sketched [130].

The heat current operator can be derived from the continuity equation⁶

$$\frac{\partial \hat{h}_{\text{H}}}{\partial t} + \nabla \cdot \hat{\mathbf{j}}_{\text{H}} = 0 \quad (4.28)$$

for the total energy density operator $\hat{h} = \frac{1}{2}(1 + \frac{\chi}{2})\hat{\psi}^\dagger(\mathbf{r})\hat{H}_0(1 + \frac{\chi}{2})\hat{\psi}(\mathbf{r})$ [cf. Eq. (4.25)] in its HEISENBERG representation \hat{h}_{H} .⁷ Since in transport experiments one measures the average heat current rather than the local heat current densities, the latter are averaged across the sample as $\hat{\mathbf{J}} = \frac{1}{V} \int d^d \mathbf{r} \hat{\mathbf{j}}(\mathbf{r})$ (V is the total volume of the system) so that the former does not depend on \mathbf{r} .

⁵In higher dimensions, the thermal HALL effect appears in certain planes in which the temperature gradient can be freely rotated and the transverse heat current by the antisymmetric part will follow without changing its magnitude. If the temperature gradient is tilted out-of-plane, only the in-plane component generates the thermal HALL current. In three dimensions, there are three independent thermal HALL conductivities associated with the three orthogonal planes.

⁶Here, the HEISENBERG picture is used to write the continuity equation as an operator equation and to derive an expression for the current density in the HEISENBERG picture, which then can be translated back to the SCHRÖDINGER picture. In the SCHRÖDINGER picture, the continuity equation would be an equation for the expectation values since the dynamics is included in the wave functions.

⁷Note that the heat current density defined this way is only determined up to a curl [144].

The first term in Eq. (4.28) is computed by $\frac{\partial \hat{h}_H}{\partial t} = \frac{i}{\hbar} [\hat{\mathcal{H}}, \hat{h}_H]$. The local current density $\hat{\mathbf{j}} = \hat{\mathbf{j}}_0 + \hat{\mathbf{j}}_1$ consists of an equilibrium and nonequilibrium part:⁸

$$\hat{j}_{0,\mu} = \frac{1}{4} \hat{\psi}^\dagger(\mathbf{r}) \left(\hat{\mathbf{V}}_\mu \sigma_3 \hat{\mathbf{H}}_0 + \hat{\mathbf{H}}_0 \sigma_3 \hat{\mathbf{V}}_\mu \right) \hat{\psi}(\mathbf{r}), \quad (4.29a)$$

$$\begin{aligned} \hat{j}_{1,\mu} = & -\frac{i}{8} \frac{\partial \chi}{\partial r_\nu} \hat{\psi}^\dagger(\mathbf{r}) \left(\hat{\mathbf{V}}_\mu \sigma_3 \hat{\mathbf{V}}_\nu - \hat{\mathbf{V}}_\nu \sigma_3 \hat{\mathbf{V}}_\mu \right) \hat{\psi}(\mathbf{r}) \\ & + \frac{1}{8} \frac{\partial \chi}{\partial r_\nu} \hat{\psi}^\dagger(\mathbf{r}) \left(r_\nu \hat{\mathbf{V}}_\mu \sigma_3 + 3 \hat{\mathbf{V}}_\mu \sigma_3 r_\nu \right) \hat{\mathbf{H}}_0 \hat{\psi}(\mathbf{r}) \\ & + \frac{1}{8} \frac{\partial \chi}{\partial r_\nu} \hat{\psi}^\dagger(\mathbf{r}) \hat{\mathbf{H}}_0 \left(3 r_\nu \sigma_3 \hat{\mathbf{V}}_\mu + \sigma_3 \hat{\mathbf{V}}_\mu r_\nu \right) \hat{\psi}(\mathbf{r}), \end{aligned} \quad (4.29b)$$

where the velocity operator $\hat{\mathbf{V}}_\mu = \frac{i}{\hbar} [\hat{\mathbf{H}}_0, r_\mu]$ is introduced. This follows from the observation that $\hat{\mathbf{j}}_0$ is independent of $\hat{\nabla}_r \chi$, while $\hat{\mathbf{j}}_1$ comprises the linear-in- $\hat{\nabla}_r \chi$ terms. Higher order terms are neglected. The nonequilibrium part $\hat{\mathbf{j}}_1$ corresponds to a circulating heat current that may exist in the presence of time-reversal symmetry breaking. This circulating heat current (also called magnetization current) associated with the so-called ‘‘energy magnetization’’ has to be subtracted for the transport current as it is not observable [144, 147, 148].

The average heat current density

$$\langle \hat{\mathbf{J}} \rangle = \langle \hat{\mathbf{J}}_0 \rangle + \langle \hat{\mathbf{J}}_1 \rangle, \quad (4.30a)$$

$$\langle \hat{J}_{0,\mu} \rangle = S_{\mu\nu} \left(-\frac{\partial \chi}{\partial r_\nu} \right) \quad (4.30b)$$

$$\langle \hat{J}_{1,\mu} \rangle = M_{\mu\nu} \left(-\frac{\partial \chi}{\partial r_\nu} \right) \quad (4.30c)$$

can therefore be obtained up to linear order by taking the thermal and quantum-mechanical expectation value, where the expectation value of $\hat{\mathbf{J}}_0$ vanishes in equilibrium⁹ and one evaluates $\Delta \langle \hat{\mathbf{J}}_0 \rangle$ using the KUBO formula. This part is contained in \mathbf{S} . $\hat{\mathbf{J}}_1$ on the other hand is already linear in the perturbation and, hence, should be evaluated using the equilibrium density operator $\hat{\rho}_0$ to compute the linear response tensor \mathbf{M} . Then, the heat conductivity is obtained as $\boldsymbol{\kappa} = (\mathbf{S} + \mathbf{M})/T$.

Basis Transformation

In order to compute the relevant correlation functions appearing in the KUBO formula for heat currents, which involves the DIRAC picture of the creation and annihilation operators, it is expedient to transform to the eigenbasis of $\hat{\mathcal{H}}_0$. First, the FOURIER transformation of Eq. (4.22) installs a familiar form that has been considered before:

$$\hat{\mathcal{H}}_0 = \frac{1}{2} \sum_{\mathbf{k}} \hat{\psi}_{\mathbf{k}}^\dagger \mathbf{H}_{0,\mathbf{k}} \hat{\psi}_{\mathbf{k}}, \quad (4.31)$$

⁸The EINSTEIN convention is employed for $\nu = x, y, z$ in Eq. (4.29).

⁹According to the BLOCH theorem for persistent currents, any system of electrons or bosons in its ground state or thermal equilibrium must not exhibit finite charge or heat currents in the thermodynamic limit. This statement holds very generally for one-dimensional or gapped systems [149–154].

where the NAMBU spinors have been introduced as

$$\hat{\psi}_{\mathbf{k}}^\dagger = \left(\hat{c}_{1\mathbf{k}}^\dagger \quad \cdots \quad \hat{c}_{\mathcal{N}\mathbf{k}}^\dagger \quad \hat{c}_{1(-\mathbf{k})} \quad \cdots \quad \hat{c}_{\mathcal{N}(-\mathbf{k})} \right). \quad (4.32)$$

The FOURIER transformations of $\hat{c}_i^\dagger(\mathbf{r})$ and $\hat{c}_i(\mathbf{r})$ have been performed in analogy to Eq. (2.88). Importantly, the FOURIER-transformed Hamilton density

$$(H_{0,\mathbf{k}})_{ij} = \sum_{\delta} (H_{\delta})_{ij} e^{i\mathbf{k} \cdot (\delta + \mathbf{b}_j - \mathbf{b}_i)} \quad (4.33)$$

is no longer a superoperator that acts on the creation and annihilation operators because of translational invariance. As in Section 2.3.4, a BOGOLIUBOV transformation

$$\hat{\Psi}_{\mathbf{k}} = \mathbf{T}_{\mathbf{k}}^{-1} \hat{\psi}_{\mathbf{k}} = \left(\hat{\gamma}_{1\mathbf{k}} \quad \cdots \quad \hat{\gamma}_{\mathcal{N}\mathbf{k}} \quad \hat{\gamma}_{1(-\mathbf{k})}^\dagger \quad \cdots \quad \hat{\gamma}_{\mathcal{N}(-\mathbf{k})}^\dagger \right)^\top \quad (4.34)$$

is employed to diagonalize $\hat{\mathcal{H}}_0$, the eigenvalues of which are $\varepsilon_{m\mathbf{k}}$ ($m = 1, \dots, 2\mathcal{N}$), where $\varepsilon_{m+\mathcal{N},\mathbf{k}} = \varepsilon_{m(-\mathbf{k})}$ for $m = 1, \dots, \mathcal{N}$.

Within the eigenbasis, equilibrium expectation values can be conveniently evaluated as

$$\left\langle \hat{\Psi}_{m\mathbf{k}}^\dagger \hat{\Psi}_{n\mathbf{k}'} \right\rangle_0 = \delta_{\mathbf{k}\mathbf{k}'} (\sigma_3)_{mn} \rho(\tilde{\varepsilon}_{m\mathbf{k}}), \quad (4.35a)$$

$$\left\langle \hat{\Psi}_{m\mathbf{k}} \hat{\Psi}_{n\mathbf{k}'}^\dagger \right\rangle_0 = -\delta_{\mathbf{k}\mathbf{k}'} (\sigma_3)_{mn} \rho(-\tilde{\varepsilon}_{m\mathbf{k}}), \quad (4.35b)$$

$$\left\langle \hat{\Psi}_{m\mathbf{k}} \hat{\Psi}_{n\mathbf{k}'} \right\rangle_0 = -\delta_{\mathbf{k}(-\mathbf{k}')} (\sigma_3)_{mm} \Sigma_{mn}^x \rho(-\tilde{\varepsilon}_{m\mathbf{k}}), \quad (4.35c)$$

$$\left\langle \hat{\Psi}_{m\mathbf{k}}^\dagger \hat{\Psi}_{n\mathbf{k}'}^\dagger \right\rangle_0 = \delta_{\mathbf{k}(-\mathbf{k}')} (\sigma_3)_{mm} \Sigma_{mn}^x \rho(\tilde{\varepsilon}_{m\mathbf{k}}), \quad (4.35d)$$

where $\rho(x) = [e^{\beta x} - 1]^{-1}$ is the BOSE-EINSTEIN distribution function, which has the property $\rho(x) = -[1 + \rho(-x)]$, $\tilde{\varepsilon}_{m\mathbf{k}} = (\sigma_3)_{mm} \varepsilon_{m\mathbf{k}}$ are the signed energies, and

$$\Sigma^x = \begin{pmatrix} \mathbf{0} & \mathbf{I} \\ \mathbf{I} & \mathbf{0} \end{pmatrix} \in \mathbb{Z}^{2\mathcal{N} \times 2\mathcal{N}}. \quad (4.36)$$

Furthermore, the DIRAC and SCHRÖDINGER pictures of the creation and annihilation operators can be easily related as

$$\hat{\Psi}_{\text{D},m\mathbf{k}}(\tau) = e^{\tilde{\omega}_{m\mathbf{k}}\tau} \hat{\Psi}_{m\mathbf{k}}, \quad (4.37a)$$

$$\hat{\Psi}_{\text{D},m\mathbf{k}}^\dagger(\tau) = e^{-\tilde{\omega}_{m\mathbf{k}}\tau} \hat{\Psi}_{m\mathbf{k}}^\dagger, \quad (4.37b)$$

where $\tilde{\omega}_{m\mathbf{k}} = \tilde{\varepsilon}_{m\mathbf{k}}/\hbar$.

Computation of S

For $\hat{\mathbf{J}}_0$ is independent of $\hat{\nabla}_{\mathbf{r}}\chi$, its linear-response contribution is directly given by the KUBO formula. There are two possibilities to compute the statistical and quantum-mechanical average, which involve different correlation functions. On the one hand, one could compute the correlation function between $\hat{\mathbf{J}}_0$ and \hat{V} according to Eq. (4.8). On the other hand, one could consider the correlation function between $\hat{\mathbf{J}}_0$ and $\frac{\partial \hat{Y}}{\partial t} \equiv \frac{i}{\hbar} [\hat{\mathcal{H}}_0, \hat{V}] =$

4 Linear Response Theory

$\hat{J}_{0,\mu} \frac{\partial \chi}{\partial r_\mu}$, which is proportional to the autocorrelation function of \hat{J}_0 . Hence, the first contribution to the thermal conductivity reads

$$S_{\mu\nu} = - \lim_{\omega \rightarrow 0} \frac{C_{\hat{J}_{0,\mu} \hat{J}_{0,\nu}}^R(\omega) - C_{\hat{J}_{0,\mu} \hat{J}_{0,\nu}}^R(0)}{i\omega} \quad (4.38)$$

according to Eq. (4.17). The equilibrium part of the current operator

$$\hat{J}_{0,\mu} = \frac{1}{4} \sum_{\mathbf{k}} \hat{\psi}_{\mathbf{k}}^\dagger (\mathbf{V}_{\mu,\mathbf{k}} \sigma_3 \mathbf{H}_{0,\mathbf{k}} + \mathbf{H}_{0,\mathbf{k}} \sigma_3 \mathbf{V}_{\mu,\mathbf{k}}) \hat{\psi}_{\mathbf{k}} \quad (4.39)$$

can be expressed within reciprocal space defining the FOURIER-transformed velocity density as $\mathbf{V}_{\mu,\mathbf{k}} = \frac{1}{\hbar} \frac{\partial \mathbf{H}_{0,\mathbf{k}}}{\partial k_\mu}$. Those matrix elements enter the MATSUBARA autocorrelation function

$$C_{\hat{J}_{0,\mu} \hat{J}_{0,\nu}}(i\omega_l) = - \int_0^\beta d\lambda e^{i\hbar\omega_l\lambda} \left\langle \hat{T} \hat{J}_{\bar{D},0,\mu}(\lambda) \hat{J}_{\bar{D},0,\nu}(0) \right\rangle_0, \quad (4.40)$$

which is computed by inserting the expression for \hat{J}_0 [Eq. (4.39)], transforming it into the eigenbasis of $\hat{\mathcal{H}}_0$ by Eq. (4.34), and applying the identities Eqs. (4.35) and (4.37), which leads to

$$S_{\mu\nu} = -\frac{i}{8} \sum_{m,n=1}^{2\mathcal{N}} \sum_{\mathbf{k}} \frac{\rho(\tilde{\varepsilon}_{m\mathbf{k}}) - \rho(\tilde{\varepsilon}_{n\mathbf{k}})}{(\tilde{\varepsilon}_{m\mathbf{k}} - \tilde{\varepsilon}_{n\mathbf{k}})^2} (\tilde{\varepsilon}_{m\mathbf{k}} + \tilde{\varepsilon}_{n\mathbf{k}})^2 \left(\mathbf{T}_{\mathbf{k}}^\dagger \mathbf{V}_{\mu,\mathbf{k}} \mathbf{T}_{\mathbf{k}} \right)_{mn} \left(\mathbf{T}_{\mathbf{k}}^\dagger \mathbf{V}_{\nu,\mathbf{k}} \mathbf{T}_{\mathbf{k}} \right)_{nm} \quad (4.41)$$

Computation of M

The second contribution is derived from the nonequilibrium part \hat{J}_1 of the current operator, whose statistical and quantum-mechanical expectation value is computed in equilibrium within linear response theory. With the definition of the nonequilibrium part of the local heat current density [Eq. (4.29b)], one finds

$$\begin{aligned} \hat{J}_{1,\mu} &= -\frac{i}{8} \frac{\partial \chi}{\partial r_\nu} \sum_{\mathbf{k}} \hat{\psi}_{\mathbf{k}}^\dagger (\mathbf{V}_{\mu,\mathbf{k}} \sigma_3 \mathbf{V}_{\nu,\mathbf{k}} - \mathbf{V}_{\nu,\mathbf{k}} \sigma_3 \mathbf{V}_{\mu,\mathbf{k}}) \hat{\psi}_{\mathbf{k}} \\ &\quad + \frac{1}{8} \frac{\partial \chi}{\partial r_\nu} \sum_{\mathbf{k}} \hat{\psi}_{\mathbf{k}}^\dagger (\hat{r}_\nu \mathbf{V}_{\mu,\mathbf{k}} \sigma_3 + 3\mathbf{V}_{\mu,\mathbf{k}} \sigma_3 \hat{r}_\nu) \mathbf{H}_{0,\mathbf{k}} \hat{\psi}_{\mathbf{k}} \\ &\quad + \frac{1}{8} \frac{\partial \chi}{\partial r_\nu} \sum_{\mathbf{k}} \hat{\psi}_{\mathbf{k}}^\dagger \mathbf{H}_{0,\mathbf{k}} (3\hat{r}_\nu \sigma_3 \mathbf{V}_{\mu,\mathbf{k}} + \sigma_3 \mathbf{V}_{\mu,\mathbf{k}} \hat{r}_\nu) \hat{\psi}_{\mathbf{k}} \end{aligned} \quad (4.42)$$

in the FOURIER basis. By taking the trace over $\hat{\rho}_0 \hat{J}_{1,\mu}$, one identifies

$$\begin{aligned} M_{\mu\nu} &= \frac{i}{8} \sum_{\mathbf{k}} \sum_{m,n=1}^{2\mathcal{N}} \rho(\tilde{\varepsilon}_{m\mathbf{k}}) (\sigma_3)_{mm} (\sigma_3)_{nn} (\mathcal{V}_{\mu,\mathbf{k}})_{mn} (\mathcal{V}_{\nu,\mathbf{k}})_{nm} - (\mu \leftrightarrow \nu) \\ &\quad - \frac{1}{2} \sum_{\mathbf{k}} \sum_{m=1}^{2\mathcal{N}} \varepsilon_{m\mathbf{k}} \rho(\tilde{\varepsilon}_{m\mathbf{k}}) \left[\mathbf{T}_{\mathbf{k}}^\dagger (\hat{r}_\nu \mathbf{V}_{\mu,\mathbf{k}} + \mathbf{V}_{\mu,\mathbf{k}} \hat{r}_\nu) \mathbf{T}_{\mathbf{k}} \right]_{mm}, \end{aligned} \quad (4.43)$$

where $\mathcal{V}_{\mu,\mathbf{k}} = \mathbf{T}_{\mathbf{k}}^\dagger \mathbf{V}_{\mu,\mathbf{k}} \mathbf{T}_{\mathbf{k}}$ are the matrix elements of the velocity operator along μ in the eigenbasis of $\hat{\mathcal{H}}_0$.

Thermal Hall Conductivity

The following steps of the derivation involve a particular separation of the terms in $S_{\mu\nu}$ and $M_{\mu\nu}$ so that some of them cancel, while the remaining terms are transformed so that they involve derivatives of $\mathbf{T}_{\mathbf{k}}$. I skip these steps here and directly focus on the thermal HALL conductivity, which is obtained as

$$\kappa_{\mu\nu}^{\text{H}} = \frac{S_{\mu\nu} + M_{\mu\nu} - (\mu \leftrightarrow \nu)}{2T} = \sum_{\lambda} \epsilon_{\lambda\mu\nu} \frac{k_{\text{B}}^2 T}{\hbar V} \sum_{\mathbf{k}} \sum_{m=1}^{\mathcal{N}} c_2[\rho(\varepsilon_{m\mathbf{k}})] \Omega_{\lambda,m\mathbf{k}}, \quad (4.44)$$

where $\epsilon_{\lambda\mu\nu}$ is the totally antisymmetric LEVI-CIVITA symbol, $c_2(x) = (1+x) \ln^2 \frac{1+x}{x} - \ln^2 x - 2\text{Li}_2(-x)$ with the dilogarithm $\text{Li}_2(x) = -\int_0^x dt \frac{\ln(1-t)}{t}$ and the BERRY curvature

$$\Omega_{\lambda,m\mathbf{k}} = \text{i} \sum_{\mu\nu} \epsilon_{\lambda\mu\nu} \left[\boldsymbol{\sigma}_3 \frac{\partial \mathbf{T}_{\mathbf{k}}^\dagger}{\partial k_\mu} \boldsymbol{\sigma}_3 \frac{\partial \mathbf{T}_{\mathbf{k}}}{\partial k_\nu} \right]_{mm}, \quad (4.45)$$

where $m = 1, \dots, 2\mathcal{N}$. As discussed in Section 3.2.1, the BERRY curvature endows the bosons with an *anomalous velocity* that is transverse to the applied temperature gradient similar to how the LORENTZ force would be oriented to an applied electric field. Each boson contributes an energy $\varepsilon_{m\mathbf{k}}$ to the heat current. However, the higher the energy, the smaller the number of bosons in that state. Consequently, the BERRY curvature is weighted with the temperature-dependent function $c_2[\rho(\varepsilon)]$ that decreases monotonously with ε . Its maximum at $\varepsilon = 0$ is $\frac{\pi^2}{3}$, while it approaches 0 for $\varepsilon \rightarrow \infty$.

MAGNETOELECTRIC EFFECTS

The electrons in a solid generally interact with external electric or magnetic fields, which can induce an internal electric polarization or a magnetization depending on the electric or magnetic susceptibility, respectively. The magnetoelectric effect refers to the cross-coupling between electric and magnetic properties in solids. For example, a magnetization may be induced by an external electric field or an electric polarization can be caused by an external magnetic field. The strength of the cross-response is determined by the magnetoelectric susceptibility [155, 156].

Materials with both ferroelectric and ferromagnetic order tend to have a strong magnetoelectric effect. Such materials are called multiferroics.¹ In a multiferroic, the magnetoelectric coupling manifests in the cross-control of domain walls by external fields. While an external magnetic field causes a magnetic domain wall motion that changes the magnetization forming a hysteresis loop in ferromagnets, the same field additionally causes a motion of the *electric* domain walls changing the electric polarization in a hysteretic fashion [155].

One distinguishes two types of multiferroics [157]. Type-I multiferroics owe their ferroelectric and ferromagnetic order to independent origins and both merely coexist. They are characterized by different transition temperatures, where the magnetic ordering temperature usually lies below the electric one. One example is BiFeO_3 , which has a ferroelectric ordering temperature of 1100 K and a NÉEL temperature of 643 K [157]. In type-II multiferroics, magnetism is the origin of ferroelectricity. Therefore, both magnetic and electrical order are stable up to the same ordering temperature. The onset of the ferroelectric phase in the type-II TbMnO_3 is explained by the simultaneous transition from a sinusoidal to helical magnetic phase at 28 K [158, 159]. Typically, type-I systems have a larger ferroelectric polarization at the expense of a smaller magnetoelectric effect than type-II materials [157].

Importantly, although the magnetoelectric effect and multiferroicity are closely related, the former can exist independently of the latter [160]. In multiferroics and materials with a nonzero static magnetoelectric susceptibility both inversion and time reversal symmetries are broken [156]. On the other hand, the localized electrons responsible for magnetism carry a charge and interact with electric fields even if the ground state is not ferroelectric. It can give rise to magnetoelectric coupling, where the charge dynamics of the electron is affected on the energy scale of the magnons far below of the insulating gap of the electrons [160]. Such a coupling can exist even in the absence of symmetry breaking, although lower symmetries allow for additional coupling mechanisms [155, 161].

Phenomenologically, one can expand the local electric polarization operator in terms

¹Depending on the context, the requirement of ferromagnetic order for the definition of a multiferroic is relaxed in favor of long-range magnetic order including antiferromagnetic, ferrimagnetic, helimagnetic ones [155].

of spin operators as [22, 162]

$$\hat{P}_\lambda = \sum_i \sum_{\mu=x,y,z} \alpha_{i\mu}^{(1),\lambda} \hat{S}_i^\mu + \sum_{ij} \sum_{\mu,\nu=x,y,z} \alpha_{ij\mu\nu}^{(2),\lambda} \hat{S}_i^\mu \hat{S}_j^\nu + \dots, \quad (5.1)$$

where the shape of the spin-polarization coupling tensors $\alpha^{(l)}$ ($l = 1, 2$) can be derived from symmetry. For example, the linear spin-polarization coupling $\alpha_{i\mu}^{(1),\lambda}$ requires that the site i is no inversion center [22, 162].

The magnetoelectric coupling mediates an interaction between external electric fields and the spins, which generally affects both the ground state and the excited states, i.e., the magnons. Certain magnon modes become electrically active as they can be excited by alternating electrical fields. Those ‘‘electromagnons’’ have been first experimentally identified in the dielectric function of TbMnO₃ and GdMnO₃ [163].

The electromagnons are the motivation to introduce the magnetoelectric effects in this work. In Publication [RN4], the implications of magnetoelectric effects for topological magnons are explored (cf. Section 3.2.1). In the following, I will discuss four common mechanisms that give rise to a spin-dependent polarization. The vacuum magnetoelectric effect is a material-independent effect that is mainly discussed for its simplicity and plays a role in Publication [RN4]. Afterwards, the three commonly discussed magnetoelectric effects of solids, one of which – the spin current mechanism – is also employed in Publication [RN4], are presented. All three can be related to different components of $\alpha^{(2)}$ [cf. Eq. (5.1)]. I will focus mainly on the physical pictures to give an idea of the underlying ideas and refrain from lengthy derivations.

5.1 Vacuum Magnetoelectric Effect

The vacuum magnetoelectric effect refers to the electric dipole created by a moving magnetic dipole. It is a fundamental consequence of the LORENTZ invariance of electromagnetism that is covered in many text books such as Ref. [76].

Let \mathcal{S} be an inertial system with respect to which the coordinate origin of another inertial system $\bar{\mathcal{S}}$ moves along the x axis with velocity v . If (x, y, z, t) are the coordinates of an event in \mathcal{S} , then the coordinates of the same event in $\bar{\mathcal{S}}$

$$\bar{x} = \gamma(x - vt), \quad (5.2a)$$

$$\bar{y} = y, \quad (5.2b)$$

$$\bar{z} = z, \quad (5.2c)$$

$$\bar{t} = \gamma\left(t - \frac{xv}{c^2}\right) \quad (5.2d)$$

are obtained by LORENTZ transformation [76]. Here, c is the speed of light and $\gamma = (1 - v^2/c^2)^{-1/2}$. Assume that there is a magnetic dipole located at the origin of $\bar{\mathcal{S}}$, which generates a magnetic dipole field [76]

$$\bar{\mathbf{B}} = \nabla_{\bar{\mathbf{r}}} \times \bar{\mathbf{A}}, \quad \bar{\mathbf{A}} = \frac{\mu_0}{4\pi} \frac{\bar{\mathbf{m}} \times \bar{\mathbf{r}}}{|\bar{\mathbf{r}}|^5} \quad (5.3)$$

and is moving with a velocity v in \mathcal{S} . What is the structure of the electromagnetic fields observed by \mathcal{S} ? To answer this question one needs to understand how electromagnetic fields transform going from one to the other inertial system.

The scalar and vector potentials are summarized as the four potential and transform like any four vector [76]

$$\bar{A}_x = \gamma \left(A_x - \frac{v\phi}{c^2} \right), \quad (5.4a)$$

$$\bar{A}_y = A_y, \quad (5.4b)$$

$$\bar{A}_z = A_z, \quad (5.4c)$$

$$\bar{\phi} = \gamma(\phi - vA_x). \quad (5.4d)$$

The transformation of the scalar and vector potentials from $\bar{\mathcal{S}}$ to \mathcal{S} is obtained by inverting the sign of v . According to (5.4d), the scalar potential $\phi = \mathbf{v} \cdot \bar{\mathbf{A}}$ in \mathcal{S} is solely given by the component of the vector potential in $\bar{\mathcal{S}}$ parallel to the velocity if $\bar{\phi} = 0$. Therefore, in the nonrelativistic limit, the scalar potential

$$\phi = \frac{\mathbf{p} \cdot (\mathbf{r} - \mathbf{r}_0)}{4\pi\epsilon_0 |\mathbf{r} - \mathbf{r}_0|^3} \quad (5.5)$$

in \mathcal{S} represents that of a dipole field of an electric dipole $\mathbf{p} = \frac{\mathbf{v} \times \bar{\mathbf{m}}}{c^2}$ located at $\mathbf{r}_0 = \mathbf{v}t$.

A magnon possesses both a magnetic moment of magnitude $g\mu_B$ due to its spin of \hbar and a group velocity $\mathbf{v}_{n\mathbf{k}} = \nabla_{\mathbf{k}} \epsilon_{m,n\mathbf{k}} / \hbar$.² Because of the vacuum magnetoelectric effect, the magnon has an electric dipole perpendicular to its spin direction, given by the quantization axis in a ferromagnet, and its group velocity. The electric dipole allows the magnon to interact with electric fields. In an electric field gradient, a transversal force analogous to the magnetic LORENTZ force for charged particles acts on the magnons. This has led to the prediction of transversal transport effects for magnons in full analogy to the ordinary HALL effect for electrons [164]. The vacuum magnetoelectric effect represents the conceptual starting point for Publication [RN4].

5.2 Exchange Striction Model

The exchange striction mechanism produces an electric polarization by the symmetric interaction between spins. Suppose the ions in Fig. 5.1(a) have opposite charges. Depending on the spin orientations of the interacting magnetic ions, the bond might be stretched or compressed along a certain crystallographic direction to minimize the energy of the interacting spins [Fig. 5.1(b)]. Because of the opposite charges, the lattice displacement is concurrently linked to the electric polarization. The exchange striction mechanism is related to the nonrelativistic symmetric exchange interaction and, thus, does not require spin-orbit coupling [155].

Mathematically, the electric dipole by exchange striction for one bond reads [155]

$$\hat{\mathbf{p}}_{ij} = \mathbf{\Pi}_{ij} \left(\hat{\mathbf{S}}_i \cdot \hat{\mathbf{S}}_j \right), \quad (5.6)$$

where i and j are the sites of the magnetic ions. The direction of the electric dipole given by $\mathbf{\Pi}_{ij}$ is restricted by the lattice symmetries. If the bond center between i and j represents an inversion center, $\mathbf{\Pi}_{ij} = \mathbf{0}$. Importantly, the inversion symmetry needs

²The spin of a magnon can deviate from \hbar if the spin is not conserved or the ground state is not ferromagnetic [87].

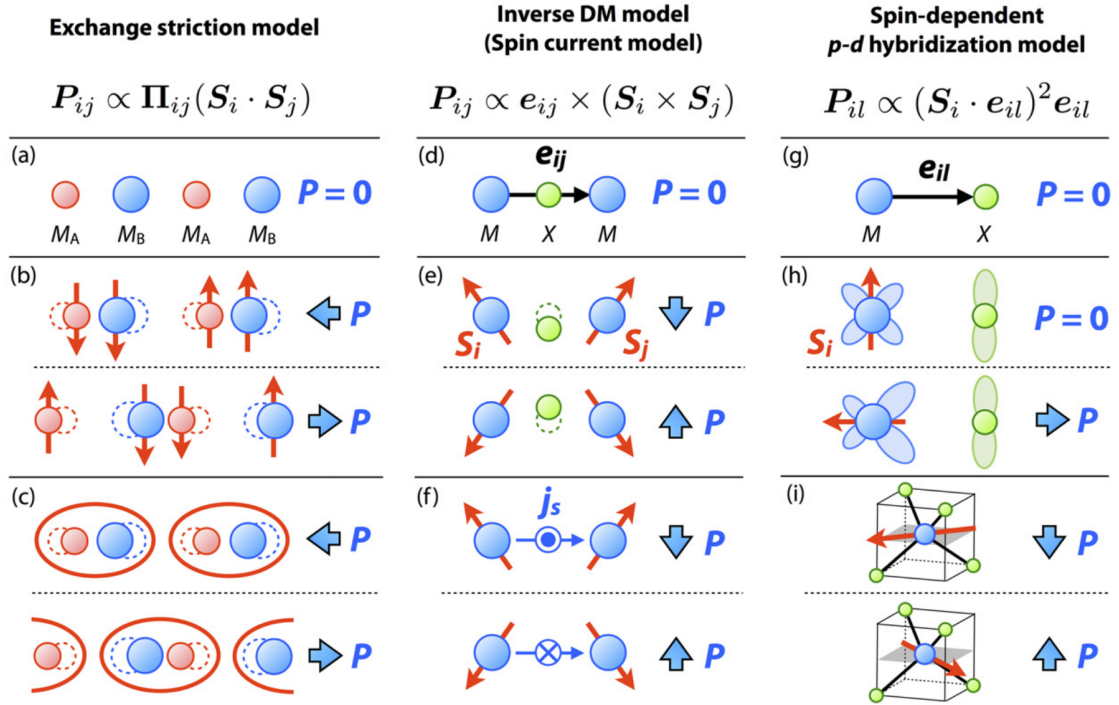


Figure 5.1: Three types of magnetoelectric effects. (a–c) Exchange striction mechanism from symmetric spin exchange interaction. (d–f) Spin current model, inverse DZHALO-SHINSKII-MORIYA model, or KATSURA-NAGAOSA-BALATSKY effect from antisymmetric spin exchange interaction. (g–i) Spin-dependent *p-d* hybridization model from single-ion anisotropy. *M* and *X* indicate magnetic and ligand ions, respectively. (a) Array of inequivalent sites M_A and M_B . (b, c) Emergence of electric polarization along the bonds due to (b) symmetry-breaking spin order or (c) dimer-singlet formation. (d) Cluster of *M-X-M* ions with structural inversion symmetry. (e, f) Formation of electric polarization normal to the bond direction due to (e) displacement of *X* or (f) spin currents with spin polarization $\hat{\mathbf{S}}_i \times \hat{\mathbf{S}}_j$ between the magnetic sites caused by spin canting. (g) Pair of *M* and *X* sites. (h) Electric polarization along the bond due to asymmetric charge density by spin-dependent hybridization of magnetic *d* orbitals and ligand *p* orbitals. (i) Cancellation of the electric polarization is avoided in specific lattice geometries such as MX_4 tetrahedra. Reprinted figure from Y. Tokura, S. Seki, and N. Nagaosa, Reports on Progress in Physics **77**, 076501 (2014); Ref. [155]; <http://dx.doi.org/10.1088/0034-4885/77/7/076501>. Copyright (2014) IOP Publishing. Reproduced with permission. All rights reserved.

to be broken on the structural level. Therefore, this mechanism can only be present in materials with a sufficiently low symmetry. In a BRAVAIS lattice, for example, it cannot exist.

Even if the structural inversion symmetry between the magnetic ions is locally broken, in order to generate a net polarization, the spin texture needs to both break inversion symmetry on a global level and has to be commensurate with the lattice so that the local electric dipole moments do not cancel. A collinear ferromagnet or antiferromagnet would have compensated dipoles because they exhibit an inversion center at a magnetic site. A spin order such as $\downarrow\downarrow\uparrow\uparrow$ breaks inversion symmetry and admits a net polarization [cf. Fig. 5.1(b)].

Instead of long-range magnetic ordering, spin-singlet dimerization represents an alternative route for realizing an electric polarization [cf. Fig. 5.1(c)]. Consider the Hamiltonian

$$\hat{\mathcal{H}} = \sum_i J_{i,i+1} \hat{\mathbf{S}}_i \cdot \hat{\mathbf{S}}_{i+1} \quad (5.7)$$

of a one-dimensional chain of ions with different valences, in which the antiferromagnetic exchange coupling is modified by the displacements u_i of the ions as [155]

$$J_{i,i+1} = J_0 + g(u_i - u_{i+1}). \quad (5.8)$$

The staggered dimerization $u_i = (-1)^i u$ reduces the energy of the spin singlet. This is the spin-PEIERLS instability, which corresponds to a transition to a phase of a periodic array of spin-singlet pairs.

The exchange striction model has been identified as the key ingredient for the electromagnons in the rare earth manganites [165]. In these orthorhombic compounds, the exchange interaction between nearest neighbors is mediated by oxygen ions. Since the electric field shifts the oxygen ions, the exchange constants are modified. This induces a coupling between the electric field and the magnons, i.e., electromagnons. As a side note, this coupling is linear in the magnon creation and annihilation operators in noncollinear magnets and, thus, enables so-called one-magnon processes [162, 165, 166]. The features of one- and two-magnon processes are further discussed in Publication [RN4].

5.3 Spin Current Model

The spin current model, which is also known as inverse DZHALOSHINSKII-MORIYA interaction or KATSURA-NAGAOSA-BALATSKY effect, has been microscopically derived by KATSURA *et al.* [161] and phenomenologically discovered by MOSTOVOY [159]. Here, the polarization originates from the antisymmetric spin interaction and is generated by the inversion symmetry breaking due to spin canting. The electric dipole moment associated to two (noncollinear) spins connected by a bond vector $\boldsymbol{\delta}_{ij}$ reads [155, 161]

$$\hat{\mathbf{p}}_{ij} = q_{\text{eff}} \boldsymbol{\delta}_{ij} \times (\hat{\mathbf{S}}_i \times \hat{\mathbf{S}}_j), \quad (5.9)$$

where q_{eff} is the effective charge that quantifies the magnitude of the electric dipole. To understand its origin, it is useful to illustrate the analogy to the DZHALOSHINSKII-MORIYA interaction.

Assume that there is a ligand ion located between the magnetic ions [cf. Fig. 5.1(d)]. If the ligand ion is displaced by a vector \mathbf{u} from the bond center, it generates a local electric field along its displacement that breaks the inversion symmetry and mediates a DZHALOSHINSKII-MORIYA interaction

$$\hat{\mathcal{H}} = \mathbf{D}_{ij} \cdot (\hat{\mathbf{S}}_i \times \hat{\mathbf{S}}_j) \quad (5.10)$$

between the two spins. This interaction promotes their canting in the plane perpendicular to \mathbf{D}_{ij} . The vector \mathbf{D}_{ij} needs to be parallel to $\boldsymbol{\delta}_{ij} \times \mathbf{u}$ according to the MORIYA rules (cf. Section 2.3.2).³

Instead of a local electric field inducing spin canting, the spin canting also can induce an electric field. Without the canting, the ligand ion is located at the inversion center between both spins [cf. Fig. 5.1(e)]. In the presence of spin canting, the displacement of the ligand ion is energetically favored, which generates a local electric dipole moment.⁴ The direction of the dipole moment, i.e., the displacement of the ligand, is perpendicular to $\boldsymbol{\delta}_{ij}$ and $\hat{\mathbf{S}}_i \times \hat{\mathbf{S}}_j$. This is the lattice contribution to the spin current model [167].

Besides the lattice contribution, there is also an electronic contribution [161]. The spin canting generates a spin current flowing between the two magnetic ions [cf. Fig. 5.1(f)]. Its spin polarization points along $\hat{\mathbf{S}}_i \times \hat{\mathbf{S}}_j$. Similar to the spin HALL effect, the spin current results in an electric dipole that is perpendicular to both the spin current and the spin polarization direction.

In contrast to the DZHALOSHINSKII-MORIYA interaction, the spin current model is ubiquitous because it does not rely on structural symmetry breaking. Instead, the symmetry is purely broken by the spin texture. This property distinguishes it from the exchange striction and spin-dependent p - d hybridization model and renders its study relevant beyond multiferroics [160]. Even in a ferromagnet, where the inversion symmetry is not broken by the ground state spin texture, the magnons can give rise to dynamical canting and induce local electric dipole moments. Furthermore, it couples magnons to alternating electric fields as studied in Publication [RN4].

Turning to multiferroics, the mechanism promotes ferroelectricity in materials with noncollinear spin textures. Importantly, the local electric dipoles must not cancel each other to give rise to a net electric polarization. In contrast to the exchange striction mechanism, both commensurate and incommensurate spin textures can lead to the net polarization. This mechanism successfully explains the multiferroicity of helimagnets such as TbMnO_3 [159, 168], a representative of the family of rare earth manganites. Interestingly, the electromagnons in this material could not be explained by the spin current model, but by the exchange striction model [165, 166]. Thus, different types of

³The displacement breaks inversion symmetry, which is a necessary condition according to the first rule. It preserves the mirror plane perpendicular to the bond, which requires \mathbf{D}_{ij} to lie inside the plane according to the second rule. Moreover, it preserves the rotational axis passing through the ligand, which bound \mathbf{D}_{ij} to the plane perpendicular to the displacement vector. Taking the intersection of both planes only the axis along $\boldsymbol{\delta}_{ij} \times \mathbf{u}$ remains.

⁴Spin canting implies noncollinearity. Technically, the inversion symmetry can be broken by a collinear arrangement: the NÉEL order. This collinear antiferromagnetic configuration is insufficient for generating the spin polarization. Even though it breaks inversion symmetry, it preserves the combined inversion and time-reversal symmetry. Since time reversal does not affect the electric dipole, the symmetry is equivalent to the pure inversion symmetry. The noncollinearity ensures that the spins cannot be mapped onto each other by a reversal of the spins.

magnetolectric couplings are generally necessary to explain static and dynamic coupling phenomena within the same material.

5.4 Spin-Dependent p - d Hybridization Model

The spin-dependent p - d hybridization mechanism generates an electric dipole [155]

$$\hat{\mathbf{p}}_i \propto \mathbf{\Lambda}_i \left(\hat{\mathbf{S}}_i \cdot \mathbf{\Lambda}_i \right)^2 \quad (5.11)$$

which is analogous to the single-ion anisotropic spin interaction (cf. Section 2.3.2). The physical origin of the hybridization model is spin-orbit coupling that alters the orbital part of the electronic wave function depending on the spin orientation of the electron. If a magnetic ion is located near a ligand ion [cf. Fig. 5.1(g)], the d orbitals of the former hybridize with the p orbitals of the latter. In the presence of spin-orbit coupling, the strength of the hybridization depends on whether the spin is parallel to the bond $\boldsymbol{\delta}_{il}$ connecting both ions or perpendicular. The hybridization causes an antisymmetric charge distribution and, hence, an electric dipole along $\mathbf{\Lambda}_i = \boldsymbol{\delta}_{il}$ [155] as indicated in Fig. 5.1(h). If there was a second ligand placed symmetrically next to the magnetic ion, the hybridization would take place with the p orbitals of both ligands similarly (not shown in Fig. 5.1). Although the charge distribution would be altered, it would be symmetric cancelling out the electric dipole. Thus, the spin-dependent p - d hybridization causes magnetolectric coupling only in materials with low on-site symmetry for example with tetrahedral structures as displayed in Fig. 5.1(i).

While for the exchange striction mechanism, inversion symmetry has to be locally broken at the bond center, a necessary condition for the hybridization model is breaking of local inversion symmetry at the site of the respective magnetic ion i . Hence, one has to distinguish between inter- and on-site inversion symmetry breaking. A honeycomb lattice possesses on-site local (and global) inversion symmetry, but does not feature inter-site local inversion symmetry between second-nearest neighbors. This precludes the hybridization model in kagome and pyrochlore lattices, which underlie the models of Publication [RN1], and honeycomb magnets [22], which are the basis for the models of the Publications [RN2, RN3, RN4].

PUBLICATIONS

In this chapter, the four publications of this thesis are presented. The first Publication [RN1] predicts a previously undiscovered contribution to the magnon's magnetic moment and highlights its significance for the magnetization in coplanar antiferromagnets and the transport of magnetic moment in response to thermal gradients. In Publication [RN2], the thermal HALL effect of magnons is considered in a collinear antiferromagnet that undergoes magnetic and topological phase transitions driven by external magnetic fields. The two kinds of phase transitions both imprint specific signatures onto the heat transport signal. Thereafter, the magnon transport theory is applied to the experimental data for the thermal HALL effect in the collinear antiferromagnet $\text{Na}_2\text{Co}_2\text{TeO}_6$ (Publication [RN3]). It is demonstrated that magnons themselves fail to account for the measured transport signal, while a theory that includes magnon polarons capture important qualitative features. Lastly, an electric dipole moment of (topological) magnons is predicted in Publication [RN4], which gives rise to an electric polarization in equilibrium and an absorption of alternating electric fields in nonequilibrium. The one-magnon processes discussed in that publication give rise to in-gap peaks at frequencies that match the energies of topological magnons. A complete list of publications is given in Chapter 8.

6.1 Orbital Magnetic Moment of Magnons

When a magnon is excited from an ordered ground state, the accompanying precession of the local spins effectively reduces the size of the ordered moments. In a ferromagnet the magnetization of the ground state is maximal and decreases with the number of excited magnons that increases with temperature. The spin of a magnon is defined by [87]

$$\mathbf{s}_{n\mathbf{k}} = \langle n\mathbf{k} | \hat{\mathbf{S}}_{\text{tot}} | n\mathbf{k} \rangle - \langle 0 | \hat{\mathbf{S}}_{\text{tot}} | 0 \rangle, \quad (6.1)$$

which corresponds to the difference of the expectation values of the total spin operator $\hat{\mathbf{S}}_{\text{tot}} = \sum_i \hat{\mathbf{S}}_i$ in the excited state $|n\mathbf{k}\rangle$ compared to the ground state $|0\rangle$. Technically, the creation of a magnon is linked to the spin ladder operators \hat{S}_i^- that reduce the spin quantum number by one \hbar (cf. Section 2.3.3). Thus, in a ferromagnet, $\mathbf{s}_{n\mathbf{k}}$ conventionally has a magnitude of \hbar and is antiparallel to the ground state spin directions [cf. Fig. 6.1(a)].¹

This implies several severe restrictions to the macroscopic properties of a magnetic insulator because the magnetic ground state, which often has different symmetries than the Hamiltonian, determines the orientation of the magnon spin. A coplanar antiferromagnet, which has an in-plane ground state spin texture as in Fig. 6.1(b), can be compatible with an out-of-plane magnetization. The compatibility can be achieved by nonmagnetic ions that lower the symmetry. However, due to frustration, the classical ground state accidentally does not exhibit a net magnetization. Because magnons can only have spins

¹The magnon spin may deviate from \hbar if spin-orbit interaction breaks the conservation of the total spin operator $\hat{\mathbf{S}}_{\text{tot}}$ along the quantization axis.

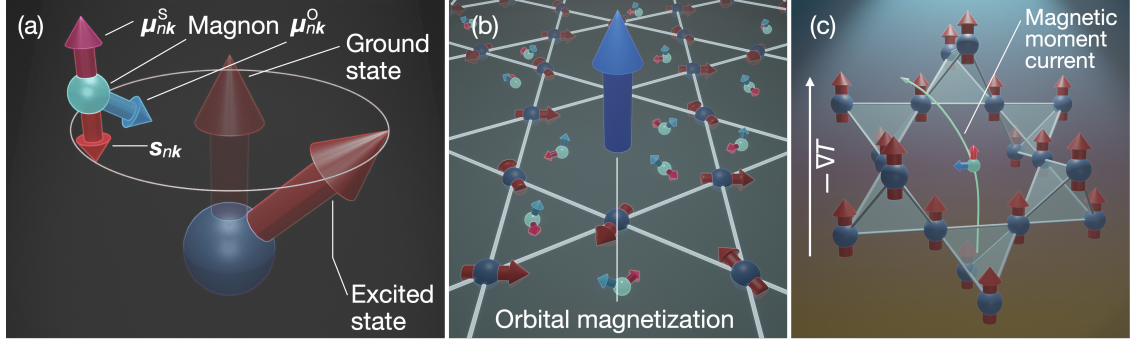


Figure 6.1: The orbital magnetic moment of magnons and its macroscopic consequences. (a) The magnon spin $\mathbf{s}_{n\mathbf{k}}$ defined as the difference between the excited and ground state total spin is antiparallel to the magnetization, while the spin magnetic moment $\boldsymbol{\mu}_{n\mathbf{k}}^{\text{S}}$ is antiparallel to $\mathbf{s}_{n\mathbf{k}}$. The direction of $\boldsymbol{\mu}_{n\mathbf{k}}^{\text{O}}$ is not restricted by the ground state spin texture. (b) Magnons in a coplanar kagome antiferromagnet. $\boldsymbol{\mu}_{n\mathbf{k}}^{\text{S}}$ is in-plane, while $\boldsymbol{\mu}_{n\mathbf{k}}^{\text{O}}$ features out-of-plane components, which give rise to an out-of-plane orbital magnetization. (c) Magnon transport in a pyrochlore ferromagnet subjected to a temperature gradient. $\boldsymbol{\mu}_{n\mathbf{k}}^{\text{S}}$ is parallel to the quantization axis, while $\boldsymbol{\mu}_{n\mathbf{k}}^{\text{O}}$ is perpendicular leading to an orbital NERNST effect.

along the directions offered by the ground state, the accidental symmetry of the ground state inhibits the magnons to feature an out-of-plane spin.

The restriction of the magnon spin also affects the spin transport in pyrochlore ferromagnets. For electrons, it is established that the spin HALL effect can exist in *any* material irrespective of its symmetries [169, RN6]. In materials with high symmetries, the spin current is generated perpendicular to the electric field with spin polarization perpendicular to both current and field. The spin NERNST effect, where the transverse spin current is generated by a temperature gradient, has the same symmetry requirements as the spin HALL effect and, thus, is also ubiquitous. In contrast, the spin currents carried by magnons may only feature a spin polarization along the quantization axis defined by the ground state, fundamentally changing the symmetry of the magnonic spin NERNST effect.

In this paper, the magnon spin, which encompasses a spin magnetic moment $\boldsymbol{\mu}_{n\mathbf{k}}^{\text{S}} = -\frac{g\mu_{\text{B}}}{\hbar}\mathbf{s}_{n\mathbf{k}}$ parallel to the magnons' spins, is contrasted by the total magnetic moment

$$\boldsymbol{\mu}_{n\mathbf{k}} = -\frac{\partial \varepsilon_{m,n\mathbf{k}}}{\partial \mathbf{B}} \quad (6.2)$$

identified as the derivative of the magnon energies $\varepsilon_{m,n\mathbf{k}}$ with respect to the magnetic field \mathbf{B} . It is demonstrated that $\boldsymbol{\mu}_{n\mathbf{k}}^{\text{S}}$ does not fully account for the total magnetic moment. Instead, there is an additional contribution $\boldsymbol{\mu}_{n\mathbf{k}}^{\text{O}} = \boldsymbol{\mu}_{n\mathbf{k}} - \boldsymbol{\mu}_{n\mathbf{k}}^{\text{S}}$, which is attributed to the orbital magnetic moment of magnons.

To understand the discrepancy of total and spin magnetic moment, one needs to consider the Hamiltonian in the presence of a magnetic field, which typically comprises the spin-spin interactions $\hat{\mathcal{H}}_{\text{spin}}$ and a ZEEMAN term $\hat{\mathcal{H}}_{\text{Zee}} = \frac{g\mu_{\text{B}}}{\hbar}\mathbf{B} \cdot \hat{\mathbf{S}}_{\text{tot}}$ (cf. Section 2.3.2). The latter causes the magnetic field dependence of the magnon energies that gives rise to $\boldsymbol{\mu}_{n\mathbf{k}}^{\text{S}}$ by virtue of Eq. (6.2). This definition of $\boldsymbol{\mu}_{n\mathbf{k}}^{\text{S}}$ is fully consistent with the quantum-

mechanical definition of $\mathbf{s}_{n\mathbf{k}}$ [Eq. (6.1)]. However, all other magnetic field dependencies of $\varepsilon_{\mathbf{m},n\mathbf{k}}$ are not accounted for.

Herein, an additional contribution $\boldsymbol{\mu}_{n\mathbf{k}}^{\text{O}}$ arising from the dependence of the magnetic ground state on the magnetic field is considered. Typically, a magnetic field distorts the spin texture of the magnetic ground state by canting all spins in the direction of the magnetic field. Since the magnon band structure clearly depends on the magnetic ground state, the field dependence of the ground state manifests as an additional field dependence of $\varepsilon_{\mathbf{m},n\mathbf{k}}$. The resulting $\boldsymbol{\mu}_{n\mathbf{k}}^{\text{O}}$ has fewer restrictions than $\boldsymbol{\mu}_{n\mathbf{k}}^{\text{S}}$.

The macroscopic consequences of this additional contribution to the magnon's magnetic moment encompass both equilibrium and nonequilibrium properties. Firstly, we demonstrate that the coplanar antiferromagnet develops an orbital magnetization perpendicular to the kagome plane due to $\boldsymbol{\mu}_{n\mathbf{k}}^{\text{O}}$ [cf. Fig. 6.1(b)]. Although the spin texture is in-plane, the magnons realize a weak ferromagnetism at zero and nonzero temperatures by quantum and thermal fluctuations, respectively. Importantly, the weak ferromagnetism does not rely on a canting of the classical spin texture. Secondly, it is shown that the currents of magnetic moment arising in the pyrochlore ferromagnet are nonzero in all geometries, which admit these currents according to the symmetry of the system. In particular, magnetic moment perpendicular to the ferromagnetic quantization axis can be transported, in which case the magnetic moment only comprises the orbital contribution. Therefore, an orbital NERNST effect is realized [cf. Fig. 6.1(c)].


Reprinted article from R. R. Neumann, A. Mook, J. Henk, and I. Mertig, *Physical Review Letters* **125**, 117209 (2020); Ref. [RN1]; <http://dx.doi.org/10.1103/PhysRevLett.125.117209>. Copyright (2020) American Physical Society. Reproduced with permission. All rights reserved.

Orbital Magnetic Moment of Magnons

Robin R. Neumann¹, Alexander Mook^{1,2}, Jürgen Henk¹, and Ingrid Mertig¹

¹*Institut für Physik, Martin-Luther-Universität Halle-Wittenberg, D-06099 Halle (Saale), Germany*

²*Department of Physics, University of Basel, Klingelbergstrasse 82, CH-4056 Basel, Switzerland*

 (Received 19 June 2020; accepted 23 July 2020; published 10 September 2020)

In experiments and their interpretation usually the spin magnetic moment of magnons is considered. In this Letter, we identify a complementing *orbital* magnetic moment of magnons brought about by spin-orbit coupling. Our microscopic theory uncovers that spin magnetization \mathbf{M}^S and orbital magnetization \mathbf{M}^O are independent quantities; they are not necessarily collinear. Even when the total spin moment is compensated due to antiferromagnetism, \mathbf{M}^O may be nonzero. This scenario of orbital weak ferromagnetism is realized in paradigmatic kagome antiferromagnets with Dzyaloshinskii-Moriya interaction. We demonstrate that magnets exhibiting a magnonic orbital moment are omnipresent and propose transport experiments for probing it.

DOI: 10.1103/PhysRevLett.125.117209

Introduction.—Textbooks on magnetism introduce spin waves as collective excitations of a magnetically ordered ground state, as epitomized by ferromagnets (Ref. [1], among others). The quanta of spin waves—the magnons—are typically viewed as local deviations from the ordered state [2,3]. Within this picture, it appears natural that the magnetic moment carried by magnons has only spatial components that are offered by the ground-state spin texture, because the latter defines the directions relative to which a deviation can occur [4]. This implies in particular that collinear magnets feature only magnons whose magnetic moment is along the collinear axis. Likewise the magnetic moments of magnons of coplanar magnets lie within that plane. This reasoning is widely accepted and adopted for a plethora of transport phenomena that involve the magnon magnetic moment, such as the spin Seebeck [5], spin Nernst [6–14], and magnon Edelstein effect [15,16] in ferromagnets [17] and in both collinear [18–20] and noncollinear [13,14,21–23] antiferromagnets.

In this Letter, we challenge this paradigm by revealing an additional magnonic property: their orbital magnetic moment. Overall, the magnetic moment,

$$\boldsymbol{\mu}_{n,k} = -\frac{\partial \varepsilon_{n,k}}{\partial \mathbf{B}} = \boldsymbol{\mu}_{n,k}^S + \boldsymbol{\mu}_{n,k}^O, \quad (1)$$

of a magnon in band n and with momentum $\hbar\mathbf{k}$ decomposes into two contributions. These are derived from the explicit and implicit dependence of the magnon energy $\varepsilon_{n,k}$ with respect to the magnetic field \mathbf{B} . The first contribution,

$$\boldsymbol{\mu}_{n,k}^S \propto -\mathbf{s}_{n,k}, \quad (2)$$

is the spin magnetic moment (SMM) which is proportional to the magnon spin $\mathbf{s}_{n,k}$ [4,16]. As mentioned above, this is the contribution conventionally referred to as the magnetic

moment of magnons. The second contribution $\boldsymbol{\mu}_{n,k}^O$ —the *orbital* magnetic moment (OMM)—captures the difference of Eqs. (1) and (2) and is the main object of interest in this Letter. It is associated with an *implicit* dependence of $\varepsilon_{n,k}$ on \mathbf{B} , which arises from the field-dependent relative orientation of the magnetic texture to the structural lattice [24] and, hence, requires spin-orbit coupling (SOC). The SMM and the OMM result in macroscopic spin and orbital magnetizations, \mathbf{M}^S and \mathbf{M}^O , respectively. These independent quantities can be disentangled clearly in the situation of magnonic orbital weak ferromagnetism, in which $\mathbf{M}^S = \mathbf{0}$ but $\mathbf{M}^O \neq \mathbf{0}$. Importantly, even if $\mathbf{M}^O = \mathbf{0}$ in equilibrium, the OMM may be addressed by an orbital Nernst effect of magnons in nonequilibrium. As a consequence, the complete set of magnonic degrees of freedom may be utilized for insulator spintronics.

Identification of the orbital magnetic moment.—We start with a generic spin Hamiltonian $\hat{H} = \hat{H}_{\text{spin}} + \hat{H}_{\text{Zee}}$; \hat{H}_{spin} and $\hat{H}_{\text{Zee}} = \hbar^{-1} \mu_B \sum_i \mathbf{B} \cdot \mathbf{g}_i \hat{\mathbf{S}}_i$ describe the spin-spin interactions (where the magnetic field \mathbf{B} does not enter) and the coupling to the magnetic field (Zeeman term; \hbar reduced Planck constant, μ_B Bohr's magneton), respectively. \mathbf{g}_i is the g tensor of the spin operator $\hat{\mathbf{S}}_i$ at site i . Assuming an ordered ground state with N spins per magnetic unit cell pointing along $\hat{\mathbf{z}}_n$ ($n = 1, \dots, N$), we perform a truncated Holstein-Primakoff (HP) transformation [25] from spin operators to bosonic operators $\hat{a}_i^{(\dagger)}$, yielding $\hat{H} \approx E_0 + \hat{H}_2$. Here, E_0 is the classical ground state energy and \hat{H}_2 describes noninteracting magnons. After a transformation to magnonic normal modes $\hat{\alpha}_{n,k}^{(\dagger)}$ in reciprocal space, we obtain $\hat{H} \approx E_0 + \Delta E_0 + \sum_k \sum_{n=1}^N \varepsilon_{n,k} \hat{\alpha}_{n,k}^\dagger \hat{\alpha}_{n,k}$. The harmonic zero-point quantum fluctuations, $\Delta E_0 = \Delta E_0^{(1)} + \Delta E_0^{(2)}$, with $\Delta E_0^{(1)} = -\frac{1}{4} \sum_k \text{Tr} \mathbf{H}_k$, and

$\Delta E_0^{(2)} = \frac{1}{2} \sum_k \sum_{n=1}^N \varepsilon_{n,k}$, provide a correction to E_0 ; \mathbf{H}_k is the Hamilton matrix. See the Supplemental Material [26], Sec. I, for details.

When considering effective spin Hamiltonians, usually the spin magnetization ([26], Sec. II),

$$\begin{aligned} \mathbf{M}^S(T) &= -\frac{\mu_B}{V} \sum_k \sum_{n=1}^N \mathbf{g}_n \hat{z}_n (S_n - \langle \hat{a}_{n,k}^\dagger \hat{a}_{n,k} \rangle) \\ &= \underbrace{-\frac{\mu_B}{V_{\text{uc}}} \sum_{n=1}^N S_n \mathbf{g}_n \hat{z}_n}_{\mathbf{M}_0^S} - \underbrace{\frac{\mu_B}{2V_{\text{uc}}} \sum_{n=1}^N \mathbf{g}_n \hat{z}_n}_{\Delta \mathbf{M}_0^{S,(1)}} + \underbrace{\frac{1}{2V} \sum_{n=1}^N \sum_k \boldsymbol{\mu}_{n,k}^S}_{\Delta \mathbf{M}_0^{S,(2)}} + \underbrace{\frac{1}{V} \sum_{n=1}^N \sum_k \boldsymbol{\mu}_{n,k}^S \rho(\varepsilon_{n,k}, T)}_{\mathbf{M}_2^S(T)}, \end{aligned} \quad (3)$$

is addressed (V sample volume, V_{uc} volume of a unit cell, $\langle \cdot \rangle$ thermodynamic average). S_n and \mathbf{g}_n are the length and the g tensor of the n th spin in the unit cell, respectively. Although \mathbf{g}_n already incorporates SOC, we denote \mathbf{M}^S as a ‘‘spin’’ magnetization, because the set $\{\mathbf{g}_n\}$ merely transforms the directions \hat{z}_n . The above sum is decomposed into the classical ground state spin magnetization \mathbf{M}_0^S , its quantum corrections

$\Delta \mathbf{M}_0^S = \Delta \mathbf{M}_0^{S,(1)} + \Delta \mathbf{M}_0^{S,(2)}$, and into $\mathbf{M}_2^S(T)$, which is due to the thermal population of magnons [$\rho(\varepsilon_{n,k}, T) = (e^{\beta \varepsilon_{n,k}} - 1)^{-1}$ Bose-Einstein distribution function at temperature $T = (k_B \beta)^{-1}$]. Eventually, $\boldsymbol{\mu}_{n,k}^S$ is the SMM of magnons in band n with momentum \mathbf{k} ([26], Sec. II).

$\mathbf{M}^S(T)$ does not coincide with the thermodynamical definition of magnetization ([26], Sec. III)

$$\mathbf{M}(T) = -\frac{1}{V} \frac{\partial \Omega}{\partial \mathbf{B}} = \underbrace{-\frac{1}{V} \frac{\partial E_0}{\partial \mathbf{B}}}_{\mathbf{M}_0} + \underbrace{\frac{1}{4V} \sum_k \frac{\partial \text{Tr} \mathbf{H}_k}{\partial \mathbf{B}}}_{\Delta \mathbf{M}_0^{(1)} = -\frac{1}{V} \frac{\partial \Delta E_0^{(1)}}{\partial \mathbf{B}}} + \underbrace{\frac{1}{2V} \sum_k \sum_{n=1}^N \boldsymbol{\mu}_{n,k}}_{\Delta \mathbf{M}_0^{(2)} = -\frac{1}{V} \frac{\partial \Delta E_0^{(2)}}{\partial \mathbf{B}}} + \underbrace{\frac{1}{V} \sum_{n=1}^N \sum_k \boldsymbol{\mu}_{n,k} \rho(\varepsilon_{n,k}, T)}_{\mathbf{M}_2(T)} \quad (4)$$

(Ω grand potential). $\boldsymbol{\mu}_{n,k}$ is the full magnonic magnetic moment defined in Eq. (1). The constituents of \mathbf{M} are defined in analogy to those of \mathbf{M}^S .

To verify briefly that $\mathbf{M}^S \neq \mathbf{M}$ replace the g tensor by a scalar ($\mathbf{g}_n \rightarrow g_n$). \mathbf{M}^S is then restricted to those spatial components offered by the \hat{z}_n s; however, \mathbf{M} and $\boldsymbol{\mu}_{n,k}$ are not, because the \hat{z}_n s themselves depend on \mathbf{B} . Thus, even if all \hat{z}_n s are collinear (or coplanar), $\boldsymbol{\mu}_{n,k}$ may have an orthogonal component whose integral is nonzero; hence, $\mathbf{M} \nparallel \mathbf{M}^S$.

The observation $\mathbf{M}_0 = \mathbf{M}_0^S$ ([26], Sec. IV) allows us to trace the difference of \mathbf{M} and \mathbf{M}^S back to the difference between $\boldsymbol{\mu}_{n,k}$ and $\boldsymbol{\mu}_{n,k}^S$. More precisely, one obtains $\boldsymbol{\mu}_{n,k} = \boldsymbol{\mu}_{n,k}^S + \boldsymbol{\mu}_{n,k}^O$, in which the SMM is derived from the explicit \mathbf{B} dependence of the Zeeman energy and the OMM ([26], Sec. V)

$$\boldsymbol{\mu}_{n,k}^O = -\sum_{m=1}^N \sum_{\alpha=x,y,z} \frac{\partial \varepsilon_{n,k}}{\partial \hat{\alpha}_m} \cdot \frac{\partial \hat{\alpha}_m}{\partial \mathbf{B}} \quad (5)$$

from the implicit \mathbf{B} dependence of the local coordinate system $\{\hat{x}_n, \hat{y}_n, \hat{z}_n\}$ [32]. Such a dependence has to result from SOC (or SOC-like interactions), which couples spins

and lattice and therefore motivates the term ‘‘orbital’’ moment. The orbital magnetization,

$$\begin{aligned} \mathbf{M}^O(T) &= \Delta \mathbf{M}_0^{O,(1)} \\ &+ \underbrace{\frac{1}{2V} \sum_k \sum_{n=1}^N \boldsymbol{\mu}_{n,k}^O}_{\Delta \mathbf{M}_0^{O,(2)}} + \underbrace{\frac{1}{V} \sum_{n=1}^N \sum_k \boldsymbol{\mu}_{n,k}^O \rho(\varepsilon_{n,k}, T)}_{\mathbf{M}_2^O(T)}, \end{aligned} \quad (6)$$

is absent in the classical ground state, since it is exclusively due to quantum ($\Delta \mathbf{M}_0^{O,(1)} + \Delta \mathbf{M}_0^{O,(2)}$) and thermal fluctuations [$\mathbf{M}_2^O(T)$].

In what follows, we assume scalar g factors and include SOC exclusively via spin-spin interactions.

Orbital magnetic moments in equilibrium.—First, we demonstrate how OMM can be probed in equilibrium as a contribution to weak ferromagnetism. This phenomenon is usually described at the level of classically antiferromagnetic spin textures that exhibit a small canting, e.g., due to a Dzyaloshinskii-Moryia interaction (DMI) [34,35] ($\mathbf{M}_0^S \neq \mathbf{0}$). Here, we predict pure *orbital* weak ferromagnetism: $\mathbf{M}_0^S = \mathbf{0}$ but $\mathbf{M}^O \neq \mathbf{0}$. A system of choice is a kagome antiferromagnet [Fig. 1(a)] with the spin Hamiltonian

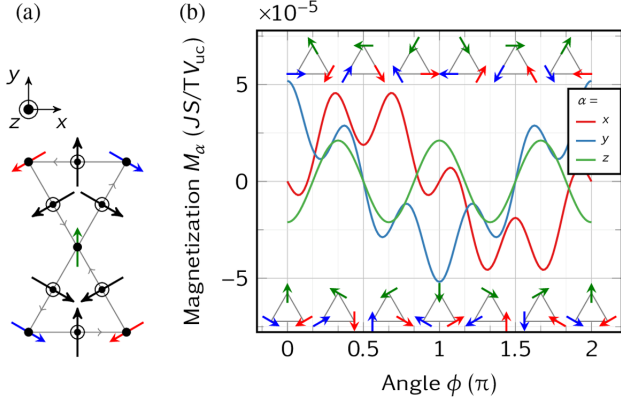


FIG. 1. Weak ferromagnetism due to quantum fluctuations in the NVC phase on the kagome lattice. (a) Structural lattice with \hat{z}_n ($n = 1, 2, 3$) indicated by colored arrows and DMI vectors by black arrows. (b) Magnetization components M_α ($\alpha = x, y, z$) at zero temperature in dependence on ϕ . Since $|\mathbf{M}| \neq 0$, quantum weak ferromagnetism is omnipresent; the out-of-plane magnetization $M_z = M_z^O$ is attributed to an orbital moment. Parameters used $J = 3.18$ meV, $S = 5/2$, $D_z = 0.062J$, $D_{||} = 1$ meV.

$$\hat{H} = \frac{1}{2\hbar^2} \sum_{\langle ij \rangle} (-J \hat{S}_i \cdot \hat{S}_j + \mathbf{D}_{ij} \cdot \hat{S}_i \times \hat{S}_j) + \frac{g\mu_B}{\hbar} \mathbf{B} \cdot \sum_i \hat{S}_i, \quad (7)$$

whose classical phase diagram was derived in Ref. [36]. Each spin interacts with its four neighbors via antiferromagnetic exchange $J < 0$ and SOC-induced DMI. The DMI vectors \mathbf{D}_{ij} are orthogonal to the respective bond [black arrows in Fig. 1(a)] and have both an in-plane ($D_{||}$) and an out-of-plane component (D_z). For $D_z > 0$ and $|D_{||}|$ below a critical value, the classical magnetic ground state is an antiferromagnetic *coplanar* texture with negative vector chirality (NVC) [36] [colored arrows in Fig. 1(a)]. The classical spin magnetization vanishes ($\mathbf{M}_0^S = \mathbf{0}$). For E_0 exhibits an accidental degeneracy under global in-plane rotation of all spins, we perform an order-by-disorder study with respect to the rotation angle ϕ [insets in Fig. 1(b)]. Both quantum and thermal fluctuations select the $\phi = 0$ texture [Fig. 1(a)] and its $\pi/3$ rotations over any other rotated texture ([26], Sec. IV). Nonetheless, we proceed with studying all textures.

For the discussion we single out the phases for $\phi = 0$ with magnetic point group $2'/m'$ (the prime indicates additional time reversal) and $\phi = \pi/2$ with $2/m$ [37]. In both cases the twofold rotation axis is along the x direction and the mirror plane coincides with the yz plane. Both groups are compatible with ferromagnetism (Table I). Besides an in-plane magnetization, the $\phi = 0$ phase is also compatible with a nonzero M_z . Since $\hat{z}_{n,z} = 0$ by construction, any nonzero $M_z = M_z^O$ must be attributed to an orbital moment.

This symmetry analysis is fully confirmed by the magnetization calculated from Eq. (4) [Fig. 1(b)]. Although

TABLE I. Magnetic point group and symmetry-imposed shape of \mathbf{M} for NVC phases with $\phi = 0$ and $\phi = \pi/2$.

Angle ϕ	0	$\pi/2$
Magnetic point group	$2'/m'$	$2/m$
Compatible magnetization	$(0 M_y M_z)$	$(M_x 0 0)$

$\mathbf{M}_0(\phi) = \mathbf{M}_0^S(\phi) = \mathbf{0}$ for all ϕ , the quantum-corrected magnetization is never compensated: $|\Delta \mathbf{M}_0(\phi)| \neq 0$. Hence, the quantum fluctuations cause the weak ferromagnetism, of both spin and orbital origin for M_x and M_y but of pure orbital origin for M_z . This finding complements classical analyses of kagome antiferromagnets [36] and shows that even the NVC phase exhibits weak ferromagnetism without the need of higher-order anisotropies beyond DMI [38]. It is also a counterexample to the common belief that quantum fluctuations only reduce the magnitude of the ordered moment.

The microscopic origin of $M_z \neq 0$ can be studied on the basis of the OMM $\mu_{1,k,z} = \mu_{1,k,z}^O$ of the lowest magnon band ($n = 1$) for both phases (top row of Fig. 2; recall $\mu_{1,k,z}^S = 0$). Already an ‘‘ocular integration’’ over the Brillouin zone reveals that $M_z(T) = M_z^O(T)$ from Eq. (6) must be either nonzero ($\phi = 0$) or zero ($\phi = \pi/2$), an observation confirmed by numerical integration (bottom row of Fig. 2). For the $\phi = 0$ phase $|M_z(T)|$ increases in absolute value with temperature, showing that thermal fluctuations enhance the quantum mechanical weak moment (the T dependence of M_x and M_y is detailed in the Supplemental Material [26], Sec. VI).

That SOC is causing the orbital moment is supported by noting that $\mu_{n,k,z}, M_z(T) \rightarrow 0$ as $D_{||} \rightarrow 0$ (not shown). If $D_{||} = 0$ the kagome plane is an m' plane, which renders M_z zero by symmetry. Hence, in the absence of SOC-induced spin-spin interactions, the orbital magnetization vanishes.

Orbital magnetic moments in nonequilibrium.—Having established signatures of OMMs at equilibrium, we now focus on nonequilibrium and consider as an example transport of magnetic moment—rather than spin—in the pyrochlore ferromagnet $\text{Lu}_2\text{V}_2\text{O}_7$. The spin Hamiltonian [42]

$$\hat{H} = \frac{1}{2\hbar^2} \sum_{\langle ij \rangle} (-J \hat{S}_i \cdot \hat{S}_j + \mathbf{D}_{ij} \cdot \hat{S}_i \times \hat{S}_j) + \frac{g\mu_B}{\hbar} \mathbf{B} \cdot \sum_i \hat{S}_i, \quad (8)$$

includes DMI vectors $\mathbf{D}_{ij} = D \hat{n}_{ij} \times \hat{e}_{ij}$ that are perpendicular to both the bonds \hat{e}_{ij} and the normal \hat{n}_{ij} of the cube that surrounds that tetrahedron the bond belongs to [43]. For $J > 0$, collinear ferromagnetism is found, $\hat{z}_n = -\hat{\mathbf{b}} = -\mathbf{B}/B$ ($n = 1, \dots, 4$), and quantum fluctuations are absent, $\Delta \mathbf{M}_0 = \mathbf{0}$.

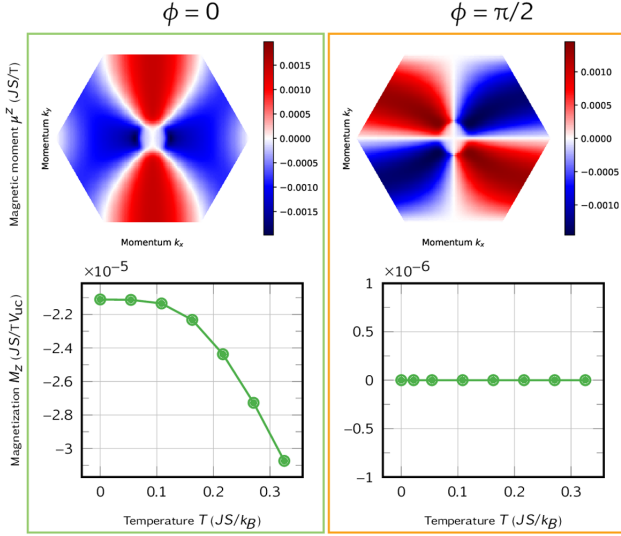


FIG. 2. Top: momentum-dependent OMM $\mu_{1,k,z}$ of the lowest magnon band ($n=1$) in the Brillouin zone of the kagome antiferromagnet in the NVC phase for $\phi=0$ (left) and $\phi=\pi/2$ (right). Bottom: temperature dependence of the orbital magnetization M_z . Parameters as in Fig. 1.

The application of a magnetic field $\mathbf{B} = (0, 0, B_z)$ [44] results in $\mu_{n,k,z} = \mu_{n,k,z}^S = g\mu_B$ and $\mu_{n,k,\alpha} = \mu_{n,k,\alpha}^O = O(D)$ for $\alpha = x, y$. Hence, the constant z component of $\boldsymbol{\mu}_{n,k}$ is a SMM. The x and y components are OMMs, however, which for positive (negative) k_z resembles a source-like (sink-like) vector field, as depicted in Fig. 3.

In equilibrium, the OMM integrates to zero, $\mathbf{M}_2^O(T) = \mathbf{0}$. However, in nonequilibrium, it is transported in transverse direction to a temperature gradient ∇T . In other words, this is a Nernst effect (NE) for magnetic moment rather than for spin. Its analysis focuses on the response tensor Υ^γ which relates the nonequilibrium current density of the magnetization with the temperature gradient: $\langle j_\alpha^i \rangle = \Upsilon_{\alpha\beta}^\gamma (-\nabla_\beta T)$ with $\alpha, \beta, \gamma = x, y, z$.

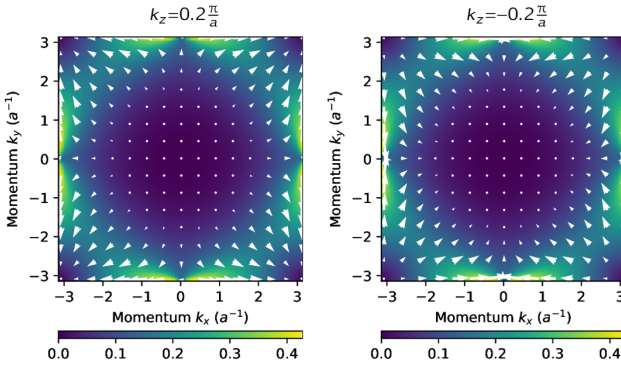


FIG. 3. Orbital magnetic moments $\mu_{k,x}$ and $\mu_{k,y}$ of the lowest magnon band of the pyrochlore ferromagnet $\text{Lu}_2\text{V}_2\text{O}_7$. The color scale represents $\sqrt{\mu_{k,x}^2 + \mu_{k,y}^2}$ (in units of μ_B) in two selected $k_x - k_y$ planes: $k_z = 0.2\pi/a$ (left) and $k_z = -0.2\pi/a$ (right); a is the lattice constant.

TABLE II. Shape of response tensors Υ^γ ($\gamma = x, y, z$) for the magnetic point group $4/m\bar{m}'m'$. A subscript “ e ” (“ o ”) indicates elements that are even (odd) under magnetization reversal.

Υ^x	Υ^y	Υ^z
$\begin{pmatrix} 0 & 0 & \Upsilon_o \\ 0 & 0 & -\Upsilon_e \\ \Upsilon'_o & -\Upsilon'_e & 0 \end{pmatrix}$	$\begin{pmatrix} 0 & 0 & \Upsilon_e \\ 0 & 0 & \Upsilon_o \\ \Upsilon'_e & \Upsilon'_o & 0 \end{pmatrix}$	$\begin{pmatrix} \tilde{\Upsilon}_o & \tilde{\Upsilon}_e & 0 \\ -\tilde{\Upsilon}_e & \tilde{\Upsilon}_o & 0 \\ 0 & 0 & \tilde{\Upsilon}'_o \end{pmatrix}$

Pyrochlore ferromagnets magnetized in z direction belong to the magnetic point group $4/m\bar{m}'m'$, which dictates the shape of Υ^γ (Table II). Tensor elements that are even upon magnetization reversal (subscript “ e ”) are associated with intrinsic contributions to the transport, whereas odd elements (subscript “ o ”) are associated with extrinsic contributions [13,45].

The elements $\tilde{\Upsilon}_o$ and $\tilde{\Upsilon}'_o$ of Υ^z comprise a spin Seebeck effect, while $\tilde{\Upsilon}_e$ indicates an anomalous spin Nernst effect (SNE) which is associated with spin-polarized transverse particle currents caused by the Berry curvature [12,37,42,46–50].

Besides transport of the z component, symmetry admits transport of x and y components as well (Υ^x and Υ^y in Table II). Υ_e (Υ'_e) comprises an anomalous SNE with mutual orthogonality of force, current, and moment directions, whereas Υ_o (Υ'_o) indicates a magnetic SNE [14]. Since the x and y components are OMMs, the respective SNEs could be termed “magnonic orbital Nernst effects.”

The above symmetry analysis suggests straightaway an experimental setup for probing OMMs. In a finite pyrochlore sample with $-\nabla T \parallel \mathbf{M} \parallel \hat{z}$, OMM accumulates at the surfaces parallel to \mathbf{M} (xz and yz surfaces). The resulting surface-located nonequilibrium tilt on \mathbf{M} , conceivably measured by magneto-optical Kerr microscopy, would clearly indicate transport of magnonic orbital magnetization.

We support the above analysis by calculating numerically all 27 elements of Υ^γ within Kubo transport theory (Fig. 4; [26], Sec. VII). Vanishing elements (marked by yellow background) agree with the zeroes in Table II; and so does the either intrinsic (blue, “ e ”) or extrinsic (red, “ o ”) character. Except for the diagonal elements of Υ^z , all elements scale with the strength D of the DMI, because DMI causes either a nonzero Berry curvature ($\tilde{\Upsilon}_e$) or OMMs ($\Upsilon_e, \Upsilon'_e, \Upsilon_o, \Upsilon'_o$). With an orbital Nernst conductivity $\Upsilon_{xz}^x \approx -0.4$ mJ/(TKms) at $T = 20$ K and $\nabla_z T = 25$ K/mm, we find $\langle j_x^x \rangle \approx 10$ J/(Tm²s) (in units of spin, this corresponds to $\hbar \langle j_x^x \rangle / \mu_B \sim 10^{-10}$ J/m²).

Another class of magnets lends itself support for non-trivial magnonic OMMs: chiral magnets, like Cu_2OSeO_3 , which hold a prominent place in skyrmion research [52]. Their DMI-induced magnonic OMM $\boldsymbol{\mu}_k^O$ is nonzero, but integrates to $\mathbf{M}^O = \mathbf{0}$ in equilibrium. Due to broken centrosymmetry, however, a magnon current caused by

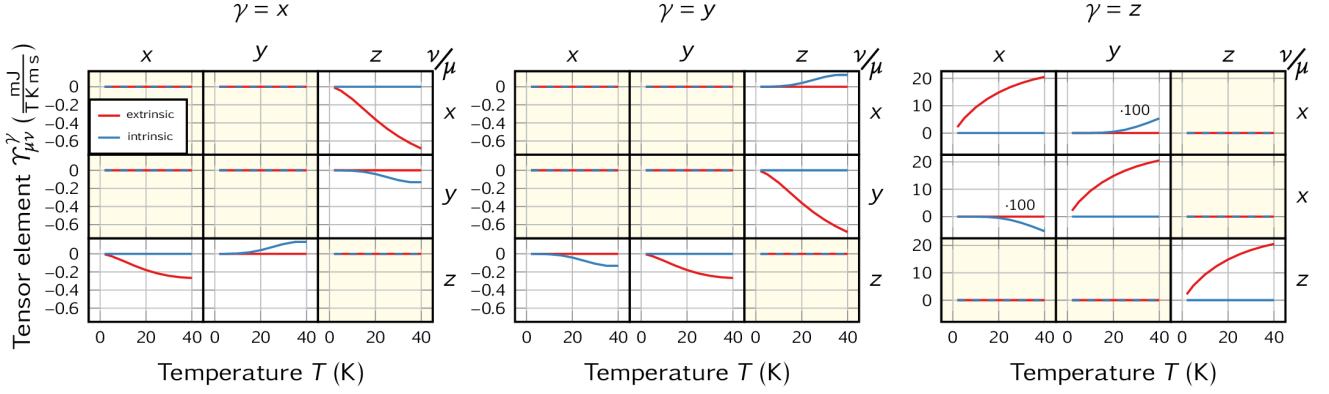


FIG. 4. Transport of magnetic moment in the pyrochlore ferromagnet $\text{Lu}_2\text{V}_2\text{O}_7$. The temperature dependence of all 27 elements of the response tensors Υ^γ are depicted: $\gamma = x$ (left), $\gamma = y$ (center), and $\gamma = z$ (right). In each of the three-by-three subfigures, rows (columns) represent the current direction μ (direction ν of the temperature gradient). The yellow background highlights vanishing elements. For the extrinsic contributions (red lines), a transport relaxation time $\tau_{nk} = \hbar/(\alpha\varepsilon_{nk})$ with $\alpha = 0.05$ is assumed. Intrinsic contributions (blue lines) are calculated in the so-called clean limit. Parameters read $J = -7.99$ meV, $S = 1/2$, $D = 0.5659$ meV, $a = 2.49$ Å [42,51], and $B_z = -0.69$ T. The ordering temperature of $\text{Lu}_2\text{V}_2\text{O}_7$ is 70 K [42].

$-\nabla T$ exerts a torque on \mathbf{M} [8,53], an effect that can be explained as an orbital version of the magnon Edelstein effect proposed in Ref. [16]; see the Supplemental Material [26], Sec. VIII.

Dipolar interactions couple spins to the lattice as well. A magnonic OMM—or better: dipolar magnetic moment—could be identified as follows. Magnons with $\mathbf{k} \nparallel \mathbf{M}$ carry nonzero $\boldsymbol{\mu}_k^O \perp \mathbf{M}$. Again, $\mathbf{M}^O = \mathbf{0}$ in equilibrium, but a dipolar-driven “orbital” Nernst effect should show up for symmetry reasons, for example in yttrium iron garnet (YIG); see the Supplemental Material [26], Sec. IX.

Synopsis.—We introduced the orbital magnetic moment of magnons and proposed two experimental signatures: (i) weak ferromagnetic orbital moment in equilibrium and (ii) accumulation of orbital magnetic moment in nonequilibrium due to a magnonic orbital Nernst effect. Since the latter has the same symmetry as the spin Hall effect [54], it should occur in *any* magnet with large enough SOC or dipolar interactions. Hence, our results pave a way for an all-insulator magnonic spin-orbit torque.

This work is supported by CRC/TRR 227 of Deutsche Forschungsgemeinschaft (DFG).

Note added.—The magnonic OMM defined as the difference between total moment and SMM applies to any spin Hamiltonian. For the Hamiltonians discussed in this Letter, it can be traced back to the dependence of the local coordinate axes on the magnetic field as written in Eq. (5). The “topological orbital moment” and the resulting orbital Nernst effect of magnons discussed in Ref. [33], both of which rely on a special type of spin interaction, namely three-spin ring exchange, is also captured by Eq. (1) and would appear as an additional contribution

in Eq. (5). However, in the frame of this Letter, we confined ourselves to bilinear spin-spin interactions.

- [1] N. W. Ashcroft and N. D. Mermin, *Solid State Physics* (Saunders College, Philadelphia, 1976).
- [2] F. Bloch, Zur Theorie des Ferromagnetismus, *Z. Phys.* **61**, 206 (1930).
- [3] F. Bloch, Zur Theorie des Austauschproblems und der Remanenzerscheinung der Ferromagnetika, *Z. Phys.* **74**, 295 (1932).
- [4] N. Okuma, Magnon Spin-Momentum Locking: Various Spin Vortices and Dirac Magnons in Noncollinear Antiferromagnets, *Phys. Rev. Lett.* **119**, 107205 (2017).
- [5] K. Uchida, J. Xiao, H. Adachi, J. Ohe, S. Takahashi, J. Ieda, T. Ota, Y. Kajiwara, H. Umezawa, H. Kawai *et al.*, Spin Seebeck insulator, *Nat. Mater.* **9**, 894 (2010).
- [6] J. H. Han and H. Lee, Spin chirality and Hall-like transport phenomena of spin excitations, *J. Phys. Soc. Jpn.* **86**, 011007 (2017).
- [7] R. Cheng, S. Okamoto, and D. Xiao, Spin Nernst Effect of Magnons in Collinear Antiferromagnets, *Phys. Rev. Lett.* **117**, 217202 (2016).
- [8] A. A. Kovalev and V. Zyuzin, Spin torque and Nernst effects in Dzyaloshinskii-Moriya ferromagnets, *Phys. Rev. B* **93**, 161106(R) (2016).
- [9] A. Mook, J. Henk, and I. Mertig, Spin dynamics simulations of topological magnon insulators: From transverse current correlation functions to the family of magnon Hall effects, *Phys. Rev. B* **94**, 174444 (2016).
- [10] Y. Shiomi, R. Takashima, and E. Saitoh, Experimental evidence consistent with a magnon Nernst effect in the antiferromagnetic insulator MnPS_3 , *Phys. Rev. B* **96**, 134425 (2017).
- [11] X. S. Wang and X. R. Wang, Anomalous magnon Nernst effect of topological magnonic materials, *J. Phys. D* **51**, 194001 (2018).

- [12] A. Mook, B. Göbel, J. Henk, and I. Mertig, Taking an electron-magnon duality shortcut from electron to magnon transport, *Phys. Rev. B* **97**, 140401(R) (2018).
- [13] A. Mook, R. R. Neumann, J. Henk, and I. Mertig, Spin Seebeck and spin Nernst effects of magnons in noncollinear antiferromagnetic insulators, *Phys. Rev. B* **100**, 100401(R) (2019).
- [14] A. Mook, R. R. Neumann, A. Johansson, J. Henk, and I. Mertig, Origin of the magnetic spin Hall effect: Spin current vorticity in the Fermi sea, *Phys. Rev. Research* **2**, 023065 (2020).
- [15] A. Shitade and Y. Yanase, Magnon gravitomagnetolectric effect in noncentrosymmetric antiferromagnetic insulators, *Phys. Rev. B* **100**, 224416 (2019).
- [16] B. Li, A. Mook, A. Raeliarijaona, and A. A. Kovalev, Magnonic analog of the Edelstein effect in antiferromagnetic insulators, *Phys. Rev. B* **101**, 024427 (2020).
- [17] J. Cramer, E.-J. Guo, S. Geprägs, A. Kehlberger, Y. P. Ivanov, K. Ganzhorn, F. Della Coletta, M. Althammer, H. Huebl, R. Gross, J. Kosel, M. Kläui, and S. T. B. Goennenwein, Magnon mode selective spin transport in compensated ferrimagnets, *Nano Lett.* **17**, 3334 (2017).
- [18] S. Seki, T. Ideue, M. Kubota, Y. Kozuka, R. Takagi, M. Nakamura, Y. Kaneko, M. Kawasaki, and Y. Tokura, Thermal Generation of Spin Current in an Antiferromagnet, *Phys. Rev. Lett.* **115**, 266601 (2015).
- [19] S. M. Wu, W. Zhang, A. KC, P. Borisov, J. E. Pearson, J. S. Jiang, D. Lederman, A. Hoffmann, and A. Bhattacharya, Antiferromagnetic Spin Seebeck Effect, *Phys. Rev. Lett.* **116**, 097204 (2016).
- [20] R. Lebrun, A. Ross, S. A. Bender, A. Qaiumzadeh, L. Baldrati, J. Cramer, A. Brataas, R. A. Duine, and M. Kläui, Tunable long-distance spin transport in a crystalline antiferromagnetic iron oxide, *Nature (London)* **561**, 222 (2018).
- [21] A. Mook, B. Göbel, J. Henk, and I. Mertig, Magnon transport in noncollinear spin textures: Anisotropies and topological magnon Hall effects, *Phys. Rev. B* **95**, 020401(R) (2017).
- [22] B. Flebus, Y. Tserkovnyak, and G. A. Fiete, Interfacial spin Seebeck effect in noncollinear magnetic systems, *Phys. Rev. B* **99**, 224410 (2019).
- [23] B. Li, S. Sandhoefner, and A. A. Kovalev, Intrinsic spin Nernst effect of magnons in a noncollinear antiferromagnet, *Phys. Rev. Research* **2**, 013079 (2020).
- [24] We implicitly assume that the usual Zeeman term is the only field-dependent term in the spin Hamiltonian.
- [25] T. Holstein and H. Primakoff, Field dependence of the intrinsic domain magnetization of a ferromagnet, *Phys. Rev.* **58**, 1098 (1940).
- [26] See the Supplemental Material at <http://link.aps.org/supplemental/10.1103/PhysRevLett.125.117209>, which contains a detailed derivation of linear spin-wave theory (Sec. I) and of the spin, orbital, and full magnetization (Secs. II–V). Extra information on the order-by-disorder study in kagome antiferromagnets and temperature dependence of the in-plane magnetization components is provided (Sec. VI). Moreover, we outline the linear spin-wave theory for pyrochlore ferromagnets and the basics of the transport calculations (Sec. VII). Finally, we address the magnonic orbital moment both in chiral (Sec. VIII) and dipolar ferromagnets (Sec. IX). Additional reference to Refs. [27–31] is provided.
- [27] S. Toth and B. Lake, Linear spin wave theory for single- q incommensurate magnetic structures, *J. Phys. Condens. Matter* **27**, 166002 (2015).
- [28] A. L. Chernyshev and P. A. Maksimov, Damped Topological Magnons in the Kagome-Lattice Ferromagnets, *Phys. Rev. Lett.* **117**, 187203 (2016).
- [29] N. Su, F. Li, Y. Jiao, Z. Liu, J. Sun, B. Wang, Y. Sui, H. Zhou, G. Chen, and J. Cheng, Asymmetric ferromagnetic criticality in pyrochlore ferromagnet $\text{Lu}_2\text{V}_2\text{O}_7$, *Science Bull.* **64**, 1222 (2019).
- [30] M. Mena, R. S. Perry, T. G. Perring, M. D. Le, S. Guerrero, M. Stormi, D. T. Adroja, Ch. Rüegg, and D. F. McMorrow, Spin-Wave Spectrum of the Quantum Ferromagnet on the Pyrochlore Lattice $\text{Lu}_2\text{V}_2\text{O}_7$, *Phys. Rev. Lett.* **113**, 047202 (2014).
- [31] B. Flebus, K. Shen, T. Kikkawa, K.-I. Uchida, Z. Qiu, E. Saitoh, R. A. Duine, and G. E. W. Bauer, Magnon-polaron transport in magnetic insulators, *Phys. Rev. B* **95**, 144420 (2017).
- [32] Field-dependent terms in the spin Hamiltonian beyond the Zeeman term, e.g., ring exchange [33], yield additional contributions. For a general definition and more details, see the Supplemental Material [26].
- [33] L. C. Zhang, F. R. Lux, J.-P. Hanke, P. M. Buhl, S. Grytsiuk, S. Blgel, and Y. Mokrousov, Orbital Nernst effect of magnons, [arXiv:1910.03317](https://arxiv.org/abs/1910.03317).
- [34] I. Dzyaloshinsky, A thermodynamic theory of “weak” ferromagnetism of antiferromagnetics, *J. Phys. Chem. Solids* **4**, 241 (1958).
- [35] T. Moriya, Anisotropic superexchange interaction and weak ferromagnetism, *Phys. Rev.* **120**, 91 (1960).
- [36] M. Elhajal, B. Canals, and C. Lacroix, Symmetry breaking due to Dzyaloshinsky-Moriya interactions in the kagomé lattice, *Phys. Rev. B* **66**, 014422 (2002).
- [37] A. Mook, J. Henk, and I. Mertig, Thermal Hall effect in noncollinear coplanar insulating antiferromagnets, *Phys. Rev. B* **99**, 014427 (2019).
- [38] For parameters of $\text{CdCu}_3(\text{OH})_6(\text{NO}_3)_2 \cdot \text{H}_2\text{O}$ —we used $S = 1/2$, $g = 2.1$, $D_{\parallel} = D_z = 0.1J$, and $J = 3.87$ meV and $\phi = \pi/2$ —we find that the weak moment accounts for $\lesssim 1\%$ of the experimentally found $7.93 \times 10^{-2} \mu_B/\text{Cu}$ [39]. Similar estimates may apply to Ca-kapellasite [40] and $\text{YCu}_3(\text{OH})_6\text{Cl}_3$ [41].
- [39] R. Okuma, T. Yajima, D. Nishio-Hamane, T. Okubo, and Z. Hiroi, Weak ferromagnetic order breaking the threefold rotational symmetry of the underlying kagome lattice in $\text{CdCu}_3(\text{OH})_6(\text{NO}_3)_2 \cdot \text{H}_2\text{O}$, *Phys. Rev. B* **95**, 094427 (2017).
- [40] Y. Ihara, H. Yoshida, K. Arashima, M. Hirata, and T. Sasaki, Anisotropic magnetic excitations from single-chirality antiferromagnetic state in Ca-kapellasite, *Phys. Rev. Research* **2**, 023269 (2020).
- [41] A. Zorko, M. Pregelj, M. Gomilšek, M. Klanjšek, O. Zaharko, W. Sun, and J.-X. Mi, Negative-vector-chirality 120° spin structure in the defect- and distortion-free quantum kagome antiferromagnet $\text{YCu}_3(\text{OH})_6\text{Cl}_3$, *Phys. Rev. B* **100**, 144420 (2019).

- [42] Y. Onose, T. Ideue, H. Katsura, Y. Shiomi, N. Nagaosa, and Y. Tokura, Observation of the magnon Hall effect, *Science* **329**, 297 (2010).
- [43] M. Elhajal, B. Canals, R. Sunyer, and C. Lacroix, Ordering in the pyrochlore antiferromagnet due to Dzyaloshinsky-Moriya interactions, *Phys. Rev. B* **71**, 094420 (2005).
- [44] This field models an anisotropy; see the Supplemental Material [26], Sec. VII, for details.
- [45] J. Železný, Y. Zhang, C. Felser, and B. Yan, Spin-Polarized Current in Noncollinear Antiferromagnets, *Phys. Rev. Lett.* **119**, 187204 (2017).
- [46] H. Katsura, N. Nagaosa, and P. A. Lee, Theory of the Thermal Hall Effect in Quantum Magnets, *Phys. Rev. Lett.* **104**, 066403 (2010).
- [47] R. Matsumoto and S. Murakami, Rotational motion of magnons and the thermal Hall effect, *Phys. Rev. B* **84**, 184406 (2011).
- [48] R. Matsumoto and S. Murakami, Theoretical Prediction of a Rotating Magnon Wave Packet in Ferromagnets, *Phys. Rev. Lett.* **106**, 197202 (2011).
- [49] R. Matsumoto, R. Shindou, and S. Murakami, Thermal Hall effect of magnons in magnets with dipolar interaction, *Phys. Rev. B* **89**, 054420 (2014).
- [50] A. Mook, J. Henk, and I. Mertig, Magnon Hall effect and topology in kagome lattices: A theoretical investigation, *Phys. Rev. B* **89**, 134409 (2014).
- [51] K. Riedl, D. Guterding, H. O. Jeschke, M. J. P. Gingras, and R. Valentí, *Ab initio* determination of spin hamiltonians with anisotropic exchange interactions: The case of the pyrochlore ferromagnet $\text{Lu}_2\text{V}_2\text{O}_7$, *Phys. Rev. B* **94**, 014410 (2016).
- [52] S. Seki, X. Z. Yu, S. Ishiwata, and Y. Tokura, Observation of skyrmions in a multiferroic material, *Science* **336**, 198 (2012).
- [53] A. Manchon, P. B. Ndiaye, J.-H. Moon, H.-W. Lee, and K.-J. Lee, Magnon-mediated Dzyaloshinskii-Moriya torque in homogeneous ferromagnets, *Phys. Rev. B* **90**, 224403 (2014).
- [54] J. Sinova, S. O. Valenzuela, J. Wunderlich, C. H. Back, and T. Jungwirth, Spin Hall effects, *Rev. Mod. Phys.* **87**, 1213 (2015).

6.2 Thermal Hall Effect in Magnetic Insulators

The thermal HALL effect is an important probe for the BERRY curvature of charge neutral quasiparticles. In Section 4.3, I delineated the derivation of the intrinsic thermal HALL conductivity, which depends on the BERRY curvature. The BERRY curvature also plays a central role in topology (cf. Section 3.3). Measuring the transversal heat transport is therefore one possible approach for identifying topological states of bosons in analogy to the anomalous HALL effect, which universally indicates topological electronic phases. However, the analogy has limitations for topological magnons.

The following two papers both study the thermal HALL effect in collinear antiferromagnets in the presence of an external magnetic field. The magnetic field competes with the antiferromagnetic order and drives the magnet across two magnetic phase transitions. The spin-flop transition describes the change from the collinear antiferromagnetic phase to a noncollinear spin-flop phase, where the spins partly align to the external field to reduce their ZEEMAN energy and partly maintain their antiparallel orientation depending on the magnitude of the field. When the spins have fully rotated parallel to the external field, the spin texture is that of a ferromagnet and the system has entered the field-polarized phase.

Both kinds of magnetic phase transitions can be expected to drastically affect the thermal HALL conductivity. While the first publication considers the pure magnon transport, the second publication addresses the role of hybridization of magnons and phonons in the transversal heat transport. Both works reveal a significant effect of the magnetic phase transitions on the transport properties.

6.2.1 Magnon Thermal Hall Effect

While the anomalous HALL effect can be quantized at zero temperature if the FERMI level is located in the topological gap (quantum anomalous HALL effect), which is a direct experimental signature of topological insulators for electrons, the quantization of the thermal HALL effect fails to materialize for two main reasons. First, any heat transport vanishes at zero temperature and, thus, must be small at low temperature. It is therefore no ground state property and, hence, can only be observed at finite temperatures.

Second, magnons in general and topological magnons in particular are *excitations* of the ground state. Even if the thermal HALL conductivity was finite at zero temperature, no magnon states would be thermally populated and therefore the signal would be independent of (topological) magnons. Topological magnons in particular are not the lowest-energy excitations, since they “live” between two bulk bands (cf. Section 3.3.1). Because lower-energy states are preferably occupied by the BOSE distribution, both bulk and edge magnons contribute to the thermal transport. Hence, there is no universal signature of topological magnon phases in the thermal transport properties.

This insight has motivated the study of topological phase *transitions*. Besides the magnetic phase transitions, topological phase transitions must appear in a collinear antiferromagnet. The antiferromagnetic phase is effectively time-reversal symmetric, which excludes a topologically nontrivial band topology. This is because the CHERN numbers vanish in the presence of time-reversal symmetry (cf. Section 3.3) The field-polarized phase on the other hand directly maps onto the HALDANE model, which is known to feature topological phases (cf. Section 3.3.1). Consequently, topological phase transitions

have to exist in between.

By calculating the thermal HALL conductivity across the magnetic and topological phase transitions driven by an external magnetic field, signatures of the phase transitions can be identified. These signatures encompass jumps, peaks, and sign changes in the thermal HALL conductivity. We quantify the impact of the phase transitions onto the transport signal by defining the thermal HALL magnetoconductivity as a figure of merit. While the impact of the spin-flop transition on the signal decreases with temperature with the thermal HALL magnetoconductivity reaching up to almost 100 % at low temperatures, the topological phase transition has a larger impact at higher temperatures. Since the temperature provides the tunability of the sensitivity to either type of phase transition, they can be distinguished in the thermal HALL conductivity.

The sensitivity of the thermal HALL conductivity to topological phase transitions distinguishes it from other macroscopic quantities that exclusively indicate magnetic phase transitions. As an example, we have considered the heat capacity of the magnons, which display distinct peaks at the magnetic phase transitions, but no traces of the topological ones.² A combination of thermal HALL and heat capacity measurements can thus identify topological phase transitions and discern them from magnetic ones.

Reprinted article from R. R. Neumann, A. Mook, J. Henk, and I. Mertig, *Physical Review Letters* **128**, 117201 (2022); Ref. [RN2]; <http://dx.doi.org/10.1103/PhysRevLett.128.117201>. Copyright (2022) American Physical Society. Reproduced with permission. All rights reserved.

²The results are part of the Supplemental Material of Publication [RN2].

Thermal Hall Effect of Magnons in Collinear Antiferromagnetic Insulators: Signatures of Magnetic and Topological Phase Transitions

Robin R. Neumann¹, Alexander Mook², Jürgen Henk¹ and Ingrid Mertig¹

¹*Institut für Physik, Martin-Luther-Universität Halle-Wittenberg, D-06099 Halle (Saale), Germany*

²*Department of Physics, University of Basel, Klingelbergstrasse 82, CH-4056 Basel, Switzerland*



(Received 1 September 2021; accepted 21 January 2022; published 14 March 2022)

We demonstrate theoretically that the thermal Hall effect of magnons in collinear antiferromagnetic insulators is an indicator of magnetic and topological phase transitions in the magnon spectrum. The transversal heat current of magnons caused by a thermal gradient is calculated for an antiferromagnet on a honeycomb lattice. An applied magnetic field drives the system from the antiferromagnetic phase via a spin-flop phase into the field-polarized phase. In addition to these magnetic phase transitions, we find topological phase transitions within the spin-flop phase. Both types of transitions manifest themselves in prominent and distinguishing features in the thermal conductivity, which changes by several orders of magnitude. The variation of temperature provides a tool to discern experimentally the two types of phase transitions. We include numerical results for the van der Waals magnet MnPS₃.

DOI: 10.1103/PhysRevLett.128.117201

Introduction.—In electronic systems, details of the electronic structure and the magnetic configuration manifest themselves in the transport properties. As an example, the quantum anomalous Hall effect, in which the transversal transport coefficient is quantized, is a clear signature of a topologically nontrivial phase. Moreover, topological phases of the electronic states can be clearly identified spectroscopically, e.g., in topological insulators [1–5].

The field of topology is not restricted to fermions, but also applies to bosons. The topological features of phonons [6–13], photons [14–18], and magnetic excitations [19–27], however, are more subtle due to the lack of the Pauli exclusion principle and quantized transport. In this Letter, we focus on magnons because they are easily manipulated by external magnetic fields. The identification of magnon edge states, the hallmarks of a nontrivial system, is notoriously difficult. On the one hand, angle-resolved photoelectron spectroscopy cannot be applied at all and spin-polarized scanning tunneling spectroscopy has severe restrictions [28–33]. On the other hand, inelastic neutron scattering succeeds in detecting gapped bulk spectra, but fails in resolving edge modes [34]. These apparent shortcomings call for identifying clear signatures of magnetic and topological phase transitions.

In this Letter, we aim at bridging the apparent gap sketched in the preceding paragraph. For this purpose, we investigate theoretically an antiferromagnet that exhibits spin-split, nonreciprocal magnon bands and both magnetic and topological phase transitions induced by an applied magnetic field. These phase transitions show up as clear characteristic signatures in the field and temperature dependence of the thermal Hall conductivity, which are explained by the magnonic band structure and the Berry

curvature. In order to convey the strong tunability and sensitivity of the thermal Hall effect, we calculate the thermal Hall magnetoconductivity at two selected phase transitions. Our findings suggest a means for identifying magnetic and topological phases via transport measurements, which could be especially attractive in two-dimensional materials, for which other methods are impractical (e.g., neutron scattering due to low signal intensities). Conversely, they insinuate a way to externally control the thermal Hall effect due to the significant changes across the phase transitions. The numerical results for MnPS₃, which is known for its nontrivial magnon transport [35], ask for comparison with experimental data.

Previous reports addressed thermal Hall effects in collinear ferromagnets with Dzyaloshinskii-Moriya interaction (DMI) and dipolar interactions [19,20,24,36–61], in weak ferromagnets with scalar spin chirality or due to magnetic fields [62–76], in noncollinear antiferromagnets [77], or in paramagnets [13,42,45,62,78–83]. Here, we present a thermal Hall effect in collinear antiferromagnets without DMI, which may even be present without external fields. While noncollinear antiferromagnets rely exclusively on their magnetic order to break an effective time-reversal symmetry (which is a prerequisite for the thermal Hall effect), collinear antiferromagnets additionally rely on the symmetry-breaking effect of the crystal, e.g., due to nonmagnetic atoms. The underlying mechanism is the magnonic analog of the Hall effect reported in Ref. [84].

Model and methods.—We consider a magnet on a two-dimensional (2D) honeycomb lattice (in the xy plane; depicted in Fig. 1). In the ground state without a magnetic field, the spins of sublattice A (B) point in the $+z$ ($-z$) direction.

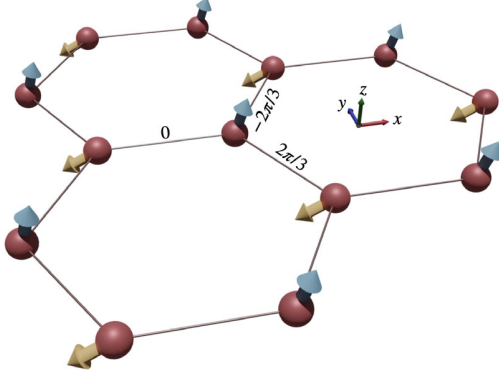


FIG. 1. Honeycomb lattice with antiferromagnetically coupled spins on sublattices A (blue) and B (orange). The spin configuration shown here is paradigmatic for the spin-flop phase with $A \neq 0$ and a magnetic field applied along $-z$.

The spin Hamiltonian

$$\mathcal{H} = \mathcal{H}_{\text{NN}} + \mathcal{H}_{\text{on}} + \mathcal{H}_B \quad (1)$$

comprises the coupling of nearest-neighbor spins,

$$\mathcal{H}_{\text{NN}} = \frac{1}{2\hbar^2} \sum_{\langle ij \rangle} \mathbf{S}_i^T \begin{pmatrix} J + J_a \cos \theta_{ij} & -J_a \sin \theta_{ij} & 0 \\ -J_a \sin \theta_{ij} & J - J_a \cos \theta_{ij} & 0 \\ 0 & 0 & J_z \end{pmatrix} \mathbf{S}_j \quad (2)$$

(\hbar reduced Planck constant). Both in- and out-of-plane spin components are coupled antiferromagnetically, but with different strengths ($J_z > J > 0$). The traceless and symmetric coupling, introduced by J_a , originates from spin-orbit coupling [85]. It is related to the nearest-neighbor bonds $\langle ij \rangle$ by the bond-dependent angles $\theta_{ij} = 0, 2\pi/3$, and $-2\pi/3$ (cf. angles near bonds in Fig. 1). The classical collinear configuration favored by J and J_z is maintained as long as J_a is sufficiently small.

This model was proposed for manganese thiophosphate MnPS_3 in Ref. [85] and it produces a nonreciprocal magnon spectrum. Wildes *et al.* did not find signatures of an asymmetric band structure in MnPS_3 and ruled out the presence of DMI [86], another source of nonreciprocity [87]. However, bond-dependent exchange interaction J_a is allowed by symmetry [85], consistent with results from neutron resonance spin echo spectroscopy [88], and cannot be excluded due to the limited experimental resolution in Ref. [86]. Nevertheless, further insights into the spin-spin interactions are desirable, for example, by comparing experimental results with our predictions for the transport properties.

We extend the model of Ref. [85] by considering an on-site anisotropy

$$\mathcal{H}_{\text{on}} = -\frac{A}{\hbar^2} \sum_{i \in A} (S_i^z)^2 \quad (3)$$

for the spins on sublattice A, which breaks the inversion symmetry on the level of the Hamiltonian. It may be brought about by placing the sample on a substrate or in a heterostructure (e.g., on a transition-metal dichalcogenide), thereby producing local environments of the atoms that differ for the two sublattices [89]. The anisotropy translates into a sublattice-dependent on-site potential of the magnons.

The Zeeman Hamiltonian

$$\mathcal{H}_B = \frac{g\mu_B B_z}{\hbar} \sum_i S_i^z \quad (4)$$

(g is g -factor, μ_B is Bohr magneton) accounts for an out-of-plane magnetic field that destabilizes the antiferromagnetic (AFM) order and induces magnetic phase transitions. Below the critical magnetic field $B_1^{(m)}$, defined by

$$g\mu_B B_1^{(m)}/S = \sqrt{(3J_z + A)^2 - 9J^2} - A, \quad (5)$$

the classical ground state is a collinear antiferromagnet with a Néel vector pointing in the z direction. Between $B_1^{(m)}$ and $B_2^{(m)}$,

$$g\mu_B B_2^{(m)}/S = 3J_z + \sqrt{9J^2 + A^2} - A, \quad (6)$$

the system is in a coplanar spin-flop (SF) phase, and in the field-polarized (FP) phase (fields larger than $B_2^{(m)}$) all spins point along $+z$. The ground state's spin configuration has been obtained by analytical and numerical methods; for details see the Supplemental Material [90].

For the thermal Hall conductivity [38]

$$\kappa_{xy} = -\frac{k_B^2 T}{\hbar V} \sum_{\mathbf{k}} \sum_{n=1}^N c_2[\rho(\varepsilon_{n,\mathbf{k}})] \Omega_{n,\mathbf{k}}, \quad (7)$$

(T temperature, k_B Boltzmann's constant, V volume), a large Berry curvature $\Omega_{n,\mathbf{k}}$ at low energies $\varepsilon_{n,\mathbf{k}}$, which enter the weight function $c_2[\rho(\varepsilon)]$, are relevant. More details can be found in the Supplemental Material [90].

We continue with MnPS_3 : $J_z = 1.541$ meV, $J = 1.54$ meV, $J_a = 0.02$ meV, and $S = 5/2$ [86,94]. Regarding the on-site anisotropy A , we consider two cases. First, the bulk properties of MnPS_3 are modeled by setting $A = 0$. Second, we account for a substrate by setting $A = 0.1$ meV, which is a realistic value in the range of predictions by *ab initio* calculations for other van der Waals magnets [89]. Our choice for A renders the respective calculations semiquantitative, since the precise numerical value of A depends on the selected substrate.

Below, we describe and explain the field-dependent Hall conductivity $\kappa_{xy}(B_z)$ for increasing field starting at zero. Magnetic (m) and topological (t) phase transitions occur at $B_1 < B_2^{(t)} < B_3^{(t)} < B_2^{(m)}$. If a topological and a magnetic phase transition coincide (e.g., at B_1), the notation $B^{(m)}$ and $B^{(t)}$ becomes redundant. Changes in κ_{xy} are traced back to the evolution of the magnon spectrum and the Berry curvature. In addition to the descriptions and figures provided here, animations are available in the Supplemental Material [90].

Discussion of results for bulk MnPS₃.—For $A = 0$ and zero magnetic field, the AFM phase is invariant under simultaneous space inversion P and time reversal T , which causes $\Omega_{n\mathbf{k}} = 0$ and, thus, $\kappa_{xy} = 0$. The otherwise degenerate magnon bands are spin-orbit split by $J_a \neq 0$, with the exception of the Γ and K' points in the Brillouin zone (BZ) [85].

A small magnetic field breaks PT symmetry and lifts the band degeneracies at Γ and K' , which brings about Berry curvature of opposite sign [$\Omega_{1\mathbf{k}} > 0$ at Γ , $\Omega_{1\mathbf{k}} < 0$ at K' as displayed in Fig. 3(a)]. The higher thermal occupation of the states around Γ and the minus sign in Eq. (7) explain that κ_{xy} is negative. The higher the temperature, the larger the occupation at Γ and the larger $|\kappa_{xy}|$.

As the field strength increases, the positive Berry curvature around Γ is gradually redistributed toward the K points and the negative Berry curvature at K' extends toward Γ (cf. Supplemental Material, Video 1 [90]), which explains the nonmonotonic behavior of κ_{xy} .

At the first-order AFM-SF phase transition at $g\mu_B B_1^{(m)} = 0.416$ meV, also identified by a diverging susceptibility, both A and B spins are abruptly rotated into the xy plane but obtain a small (ferromagnetic) component parallel to the magnetic field. In Fig. 2(a), this redirection is seen in the angles θ_A and θ_B between the xy plane and the spins (inset: A blue, B orange) and in the jump of the magnetization from zero to negative values. The experimentally measured critical field in the range of $g\mu_B B_1 = 0.42\text{--}0.54$ meV [97,98] agrees reasonably well with our analysis.

In the SF phase, the lower band is pinned at zero energy at Γ due to the continuous rotational symmetry of the classical ground state energy that is spontaneously broken by the noncollinear ground state [99]. The Berry curvature of band $n = 1$ is dominantly positive, and the Chern number C_1 jumps from 0 to -1 . Thus, the magnetic phase transition is accompanied by a topological phase transition and $|\kappa_{xy}|$ is abruptly increased.

Ramping up the magnetic field further, the large Berry curvature around Γ [cf. Fig. 3(b)] becomes redistributed to high-energy magnons [cf. Fig. 3(c)], with the consequence that $|\kappa_{xy}|$ decreases with the B field [cf. Fig. 2(b)].

The second topological phase transition at $g\mu_B B_2^{(t)} = 1.901$ meV is attributed to a band inversion. The Chern numbers of both bands are interchanged; that is,

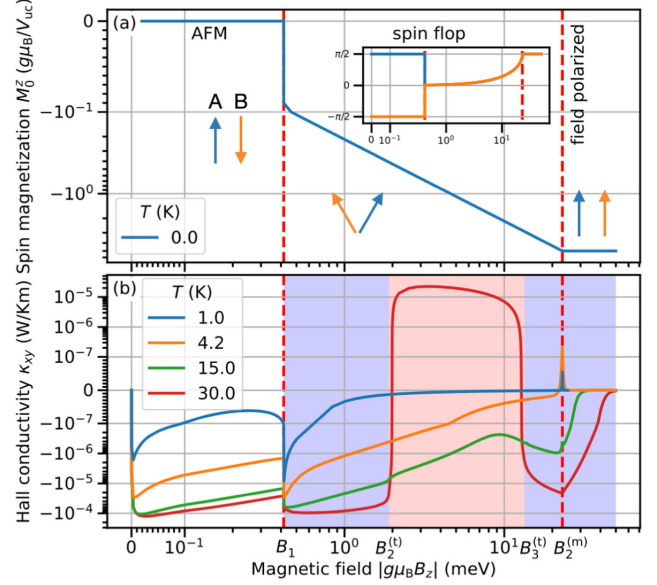


FIG. 2. Magnetic, topological, and transport properties of (bulk) MnPS₃ ($A = 0$). (a) Classical ground state magnetization versus magnetic field. Inset: angles θ_A and θ_B of the sublattice A (blue) and B (orange) spins with the xy plane. (b) Thermal Hall conductivity κ_{xy} for four selected temperatures ($T = 1.0, 4.2, 15,$ and 30 K). The white, blue, red background color indicates topological phases with Chern numbers $C_1 = 0, -1, +1$ of the lowest magnon band. Dashed red lines mark the magnetic phase transitions at the critical fields $B_1^{(m)}$ and $B_2^{(m)}$. All four panels have logarithmic ordinates and abscissae with linear-scale segments around 0, which are identified by equally spaced minor ticks.

$C_1 = -1 \rightarrow C_1 = +1$. This band inversion occurs near the BZ edge: just before $B_2^{(t)}$, e.g., $|g\mu_B B_z| = 1.8$ meV, the dominating positive Berry curvature appears near the BZ edge and is spread along k_x [red in Fig. 3(c)]. And after the transition, e.g., at $|g\mu_B B_z| = 2$ meV, this dominating $\Omega_{n\mathbf{k}}$ has changed sign [blue in Fig. 3(d)]. As a consequence, the band inversion manifests itself in κ_{xy} prominently at elevated temperatures, for which it even causes sign changes [cf. red line in Fig. 2(b)].

The band inversion is reversed again ($C_1 = +1 \rightarrow C_1 = -1$) at $g\mu_B B_3^{(t)} = 13.368$ meV, again most clearly seen in κ_{xy} at 30 K, which, as before, features a sign change. Approaching $B_3^{(t)}$ the elongated distribution of the Berry curvature seen for $B_2^{(t)}$ becomes concentrated around the K and K' points, and the band inversion then occurs at these points at the BZ edge (cf. Supplemental Material, Video 1 [90]). In short, the higher the temperature (but still well below the ordering temperature), the stronger κ_{xy} reflects the topological phase transitions.

The second-order magnetic SF-FP phase transition at $g\mu_B B_2^{(m)} = 23.107$ meV, also identified by a jump in the

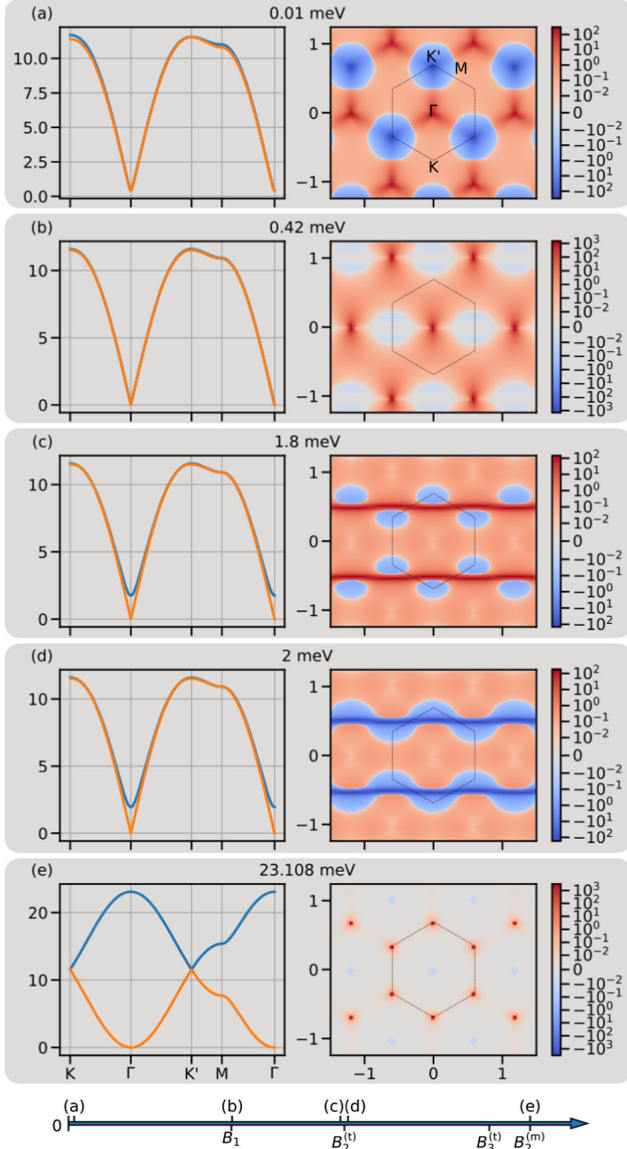


FIG. 3. (a–e) Magnon band structures and Berry curvatures of (bulk) MnPS_3 ($A = 0$) for selected strengths $|g\mu_B B_z|$ of the magnetic field. Magnon-dispersion and Berry-curvature panels appear in pairs, indicated by a common gray background, with identical strength of the magnetic field (in meV; the positioning with respect to the phase transitions is sketched at the bottom). The magnon energies $\varepsilon_{n\mathbf{k}}$ (in meV) are shown along high-symmetry lines of the first Brillouin zone; the Berry curvatures $\Omega_{1\mathbf{k}}$ of the lowest band are displayed as color maps in reciprocal space (the black hexagons indicate the first BZ). The k_x and k_y axes are given in \AA^{-1} . Parameters are chosen as in Fig. 2. For an animation, see Supplemental Material, Video 1 [90].

susceptibility, shows clear temperature-dependent signatures in κ_{xy} [Fig. 2(b)]. On the one hand, the dominating positive contribution of the Berry curvature is located at the BZ edges (magnons with higher energies); on the other hand, a small annular, negative contribution shows up near

the BZ center (low-energy magnons) [Fig. 3(e)]. Thus, the weighting between these competing contributions can be altered by the occupation of the respective magnon states and, therefore, by the temperature. To be more specific, low temperatures freeze out the high-energy contribution, allowing the small low-energy contribution to dominate in the transport and leading to a peak with a sign change in κ_{xy} . At elevated temperatures, however, magnons with positive $\Omega_{n\mathbf{k}}$ are significantly populated. Since the high-energy contribution, being induced by the topological phase transition, exists independently of the magnetic phase transition, it does not show up as a pronounced peak.

At the transition point, the in-plane Néel vector vanishes. The FP phase is hence characterized by a saturated classical magnetization [cf. Fig. 2(a)]. Beyond this second-order transition the magnetic field shifts both bands to higher energies, thereby suppressing thermal transport ($\kappa_{xy} \rightarrow 0$) [Fig. 2(b)].

Based on the above, we conclude that κ_{xy} exhibits clear signatures of magnetic phase transition at low temperatures and of topological phase transitions at higher temperatures.

Thermal Hall magnetoconductivity.—The previous analysis revealed the need for a quantity that precisely measures the sensitivity of $\kappa_{xy}(B_z)$ on the phase transitions. In analogy to the magnetoresistance, we define the thermal Hall magnetoconductivity (THMC) as

$$\text{THMC} = \left| \frac{\kappa_{xy}(\overline{B}_z + \Delta B_z) - \kappa_{xy}(\overline{B}_z - \Delta B_z)}{\kappa_{xy}(\overline{B}_z + \Delta B_z) + \kappa_{xy}(\overline{B}_z - \Delta B_z)} \right|. \quad (8)$$

By definition, the THMC corresponds to the relative change of κ_{xy} upon the phase transition at \overline{B}_z . In Fig. 4, the THMC is shown versus temperature for (i) the AFM-SF transition (B_1 , blue line) and (ii) for the topological phase transition at $B_2^{(t)}$ (orange line) [100]. For (i) the THMC is close to one near 1 K and monotonically decreases with temperature. (ii) The topological phase transition shows the expected behavior, i.e., the THMC is small at low temperatures, indicating that κ_{xy} does not change by much,

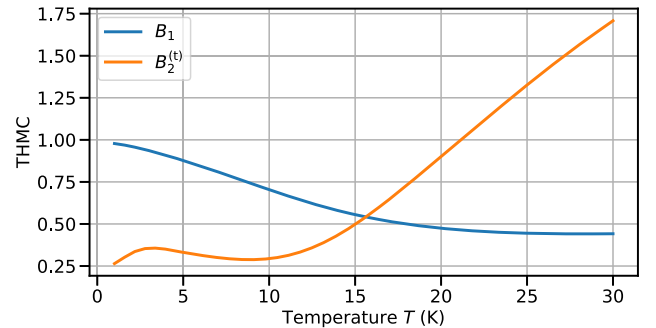


FIG. 4. Thermal Hall magnetoconductivity as a function of temperature T at the AFM-SF transition B_1 (blue line) and the second topological phase transition $B_2^{(t)}$ (orange line).

when the topological transition is crossed, but it escalates and takes values close to 175% at 30 K. Based on these results, the drastic changes of κ_{xy} at the phase transitions can be exploited for a “thermal Hall switch,” in which the transverse heat current (or the transverse temperature gradient) is controlled by the external field.

Results for MnPS₃ on a substrate.—A substrate or a heterostructure that breaks the sublattice symmetry is mimicked by setting $A = 0.1$ meV. There are three key differences to bulk MnPS₃ ($A = 0$): (i) The AFM-SF transition becomes continuous. (ii) The nonmagnetic atoms, which are responsible for $A \neq 0$, break an effective time-reversal symmetry PT and a thermal Hall effect in a collinear antiferromagnet without a magnetic field ensues. A similar situation has been reported for the anomalous Hall effect in an electronic system [84]. (iii) A opens a trivial gap in the FM phase and it dominates over J_a . Since the AFM phase is always trivial, there are no topological phase transitions. We present the magnon spectra, Berry curvature, thermal Hall effect, and heat capacity for $A = 0.1$ meV in the Supplemental Material [90].

Wrap up.—Our theoretical investigation of the temperature and magnetic-field dependence of the transversal heat conductivity κ_{xy} of a honeycomb magnet proves that κ_{xy} is very sensitive to the magnetic structure at low temperatures: it exhibits pronounced peaks at the magnetic phase transitions, but is rather unaffected by topological phase transitions. Conversely, κ_{xy} traces the topological phase transitions at high temperatures, but is insensitive to the magnetic transitions. Its reading may change several orders near a phase transition and it may also change sign. To paraphrase, magnetic and topological phase transition cause distinct signatures in κ_{xy} , the measurement of which may be used to identify the phase transitions. On the other hand, the strong change under the phase transitions may be exploited as a thermal Hall switch in which the transport properties are manipulated by external means.

Detecting topological (edge) magnons is more difficult than for electrons, since transport of bosons is not quantized—what is a clear signature of nontrivial topology in electronic systems. Instead, $\kappa_{xy}(B)$ may be investigated as an indicator, its prominent features provide evidence to infer the existence of topological magnons. Although there are other sources of drastic changes in $\kappa_{xy}(B)$, a combination with measurements of, e.g., heat capacity $C_V(B)$, which is insensitive to topology, could be used to verify the topological nature of the signatures (proof of concept in Supplemental Material [90]).

Our findings call for experimental validation. The numerical results for MnPS₃ suggest that κ_{xy} lies within the experimentally accessible range. We point out that extraordinarily high fields would be required for mapping the entire phase diagram. Nonetheless, the antiferromagnet–spin-flop transition and the topological transition at 2.202 meV are experimentally amenable.

This work is funded by the Deutsche Forschungsgemeinschaft (DFG, German Research Foundation) – Project-ID 328545488 – TRR 227, project B04.

- [1] D. Hsieh, D. Qian, L. Wray, Y. Xia, Y. S. Hor, R. J. Cava, and M. Z. Hasan, A topological Dirac insulator in a quantum spin Hall phase, *Nature (London)* **452**, 970 (2008).
- [2] V. Mourik, K. Zuo, S. M. Frolov, S. R. Plissard, E. P. Bakkers, and L. P. Kouwenhoven, Signatures of Majorana fermions in hybrid superconductor-semiconductor nanowire devices, *Science* **336**, 1003 (2012).
- [3] X.-L. Qi and S.-C. Zhang, Topological insulators and superconductors, *Rev. Mod. Phys.* **83**, 1057 (2011).
- [4] M. Z. Hasan and C. L. Kane, Colloquium: Topological insulators, *Rev. Mod. Phys.* **82**, 3045 (2010).
- [5] X.-B. Li, W.-K. Huang, Y.-Y. Lv, K.-W. Zhang, C.-L. Yang, B.-B. Zhang, Y. B. Chen, S.-H. Yao, J. Zhou, M.-H. Lu, L. Sheng, S.-C. Li, J.-F. Jia, Q.-K. Xue, Y.-F. Chen, and D.-Y. Xing, Experimental Observation of Topological Edge States at the Surface Step Edge of the Topological Insulator ZrTe₅, *Phys. Rev. Lett.* **116**, 176803 (2016).
- [6] E. Prodan and C. Prodan, Topological Phonon Modes and Their Role in Dynamic Instability of Microtubules, *Phys. Rev. Lett.* **103**, 248101 (2009).
- [7] L. Zhang, J. Ren, J.-S. Wang, and B. Li, Topological Nature of the Phonon Hall Effect, *Phys. Rev. Lett.* **105**, 225901 (2010).
- [8] N. Berg, K. Joel, M. Koolyk, and E. Prodan, Topological phonon modes in filamentary structures, *Phys. Rev. E* **83**, 021913 (2011).
- [9] T. Qin, J. Zhou, and J. Shi, Berry curvature and the phonon Hall effect, *Phys. Rev. B* **86**, 104305 (2012).
- [10] Z.-G. Chen and Y. Wu, Tunable Topological Phononic Crystals, *Phys. Rev. Applied* **5**, 054021 (2016).
- [11] B.-Z. Xia, T.-T. Liu, G.-L. Huang, H.-Q. Dai, J.-R. Jiao, X.-G. Zang, D.-J. Yu, S.-J. Zhang, and J. Liu, Topological phononic insulator with robust pseudospin-dependent transport, *Phys. Rev. B* **96**, 094106 (2017).
- [12] S. Zhang, G. Go, K.-J. Lee, and S. K. Kim, SU(3) Topology of Magnon-Phonon Hybridization in 2D Antiferromagnets, *Phys. Rev. Lett.* **124**, 147204 (2020).
- [13] M. Akazawa, M. Shimozawa, S. Kittaka, T. Sakakibara, R. Okuma, Z. Hiroi, H.-Y. Lee, N. Kawashima, J. H. Han, and M. Yamashita, Thermal Hall Effects of Spins and Phonons in Kagome Antiferromagnet Cd-Kapellasite, *Phys. Rev. X* **10**, 041059 (2020).
- [14] R. Y. Chiao and Y.-S. Wu, Manifestations of Berry’s Topological Phase for the Photon, *Phys. Rev. Lett.* **57**, 933 (1986).
- [15] L. Lu, J. D. Joannopoulos, and M. Soljačić, Topological photonics, *Nat. Photonics* **8**, 821 (2014).
- [16] L. Lu, C. Fang, L. Fu, S. G. Johnson, J. D. Joannopoulos, and M. Soljačić, Symmetry-protected topological photonic crystal in three dimensions, *Nat. Phys.* **12**, 337 (2016).
- [17] T. Ozawa, H. M. Price, A. Amo, N. Goldman, M. Hafezi, L. Lu, M. C. Rechtsman, D. Schuster, J. Simon, O. Zilberberg, and I. Carusotto, Topological photonics, *Rev. Mod. Phys.* **91**, 015006 (2019).

- [18] X.-D. Chen, W.-M. Deng, F.-L. Shi, F.-L. Zhao, M. Chen, and J.-W. Dong, Direct Observation of Corner States in Second-Order Topological Photonic Crystal Slabs, *Phys. Rev. Lett.* **122**, 233902 (2019).
- [19] L. Zhang, J. Ren, J.-S. Wang, and B. Li, Topological magnon insulator in insulating ferromagnet, *Phys. Rev. B* **87**, 144101 (2013).
- [20] A. Mook, J. Henk, and I. Mertig, Magnon Hall effect and topology in kagome lattices: A theoretical investigation, *Phys. Rev. B* **89**, 134409 (2014).
- [21] A. Mook, J. Henk, and I. Mertig, Edge states in topological magnon insulators, *Phys. Rev. B* **90**, 024412 (2014).
- [22] S. A. Owerre, Floquet topological magnons, *J. Phys. Commun.* **1**, 021002 (2017).
- [23] P. A. McClarty, X.-Y. Dong, M. Gohlke, J. G. Rau, F. Pollmann, R. Moessner, and K. Penc, Topological magnons in Kitaev magnets at high fields, *Phys. Rev. B* **98**, 060404(R) (2018).
- [24] A. Rückriegel, A. Brataas, and R. A. Duine, Bulk and edge spin transport in topological magnon insulators, *Phys. Rev. B* **97**, 081106 (2018).
- [25] S. A. Díaz, J. Klinovaja, and D. Loss, Topological Magnons and Edge States in Antiferromagnetic Skyrmion Crystals, *Phys. Rev. Lett.* **122**, 187203 (2019).
- [26] X. S. Wang, A. Brataas, and R. E. Troncoso, Bosonic Bott Index and Disorder-Induced Topological Transitions of Magnons, *Phys. Rev. Lett.* **125**, 217202 (2020).
- [27] R. Mukherjee, R. Kundu, A. Singh, and A. Kundu, Schwinger-boson mean-field study of spin-1/2 $J_1 - J_2 - J_\chi$ model in honeycomb lattice: Thermal Hall signature, [arXiv:2108.08801](https://arxiv.org/abs/2108.08801).
- [28] O. Pietzsch, A. Kubetzka, M. Bode, and R. Wiesendanger, Observation of magnetic hysteresis at the nanometer scale by spin-polarized scanning tunneling spectroscopy, *Science* **292**, 2053 (2001).
- [29] M. Bode, M. Heide, K. V. Bergmann, P. Ferriani, S. Heinze, G. Bihlmayer, A. Kubetzka, O. Pietzsch, S. Blügel, and R. Wiesendanger, Chiral magnetic order at surfaces driven by inversion asymmetry, *Nature (London)* **447**, 190 (2007).
- [30] J. Fernández-Rossier, Theory of Single-Spin Inelastic Tunneling Spectroscopy, *Phys. Rev. Lett.* **102**, 256802 (2009).
- [31] J. Fransson, O. Eriksson, and A. V. Balatsky, Theory of spin-polarized scanning tunneling microscopy applied to local spins, *Phys. Rev. B* **81**, 115454 (2010).
- [32] T. Balashov, A. F. Takács, W. Wulfhekel, and J. Kirschner, Magnon Excitation with Spin-Polarized Scanning Tunneling Microscopy, *Phys. Rev. Lett.* **97**, 187201 (2006).
- [33] J. Feldmeier, W. Natori, M. Knap, and J. Knolle, Local probes for charge-neutral edge states in two-dimensional quantum magnets, *Phys. Rev. B* **102**, 134423 (2020).
- [34] F. Zhu, L. Zhang, X. Wang, F. J. d. Santos, J. Song, T. Mueller, K. Schmalzl, W. F. Schmidt, A. Ivanov, J. T. Park *et al.*, Topological magnon insulators in two-dimensional van der Waals ferromagnets CrSiTe_3 and CrGeTe_3 : Towards intrinsic gap-tunability, *Sci. Adv.* **7** (2021).
- [35] Y. Shiomi, R. Takashima, and E. Saitoh, Experimental evidence consistent with a magnon Nernst effect in the antiferromagnetic insulator MnPS_3 , *Phys. Rev. B* **96**, 134425 (2017).
- [36] H. Katsura, N. Nagaosa, and P. A. Lee, Theory of the Thermal Hall Effect in Quantum Magnets, *Phys. Rev. Lett.* **104**, 066403 (2010).
- [37] Y. Onose, T. Ideue, H. Katsura, Y. Shiomi, N. Nagaosa, and Y. Tokura, Observation of the magnon Hall effect, *Science* **329**, 297 (2010).
- [38] R. Matsumoto and S. Murakami, Rotational motion of magnons and the thermal Hall effect, *Phys. Rev. B* **84**, 184406 (2011).
- [39] R. Matsumoto and S. Murakami, Theoretical Prediction of a Rotating Magnon Wave Packet in Ferromagnets, *Phys. Rev. Lett.* **106**, 197202 (2011).
- [40] R. Shindou, R. Matsumoto, S. Murakami, and J.-i. Ohe, Topological chiral magnonic edge mode in a magnonic crystal, *Phys. Rev. B* **87**, 174427 (2013).
- [41] T. Ideue, Y. Onose, H. Katsura, Y. Shiomi, S. Ishiwata, N. Nagaosa, and Y. Tokura, Effect of lattice geometry on magnon Hall effect in ferromagnetic insulators, *Phys. Rev. B* **85**, 134411 (2012).
- [42] M. Hirschberger, R. Chisnell, Y. S. Lee, and N. P. Ong, Thermal Hall Effect of Spin Excitations in a Kagome Magnet, *Phys. Rev. Lett.* **115**, 106603 (2015).
- [43] R. Matsumoto, R. Shindou, and S. Murakami, Thermal Hall effect of magnons in magnets with dipolar interaction, *Phys. Rev. B* **89**, 054420 (2014).
- [44] X. Cao, K. Chen, and D. He, Magnon Hall effect on the Lieb lattice, *J. Phys. Condens. Matter* **27**, 166003 (2015).
- [45] H. Lee, J. H. Han, and P. A. Lee, Thermal Hall effect of spins in a paramagnet, *Phys. Rev. B* **91**, 125413 (2015).
- [46] B. Xu, T. Ohtsuki, and R. Shindou, Integer quantum magnon Hall plateau-plateau transition in a spin-ice model, *Phys. Rev. B* **94**, 220403(R) (2016).
- [47] K. Nakata, J. Klinovaja, and D. Loss, Magnonic quantum Hall effect and Wiedemann-Franz law, *Phys. Rev. B* **95**, 125429 (2017).
- [48] S. A. Owerre, Topological honeycomb magnon Hall effect: A calculation of thermal Hall conductivity of magnetic spin excitations, *J. Appl. Phys.* **120**, 043903 (2016).
- [49] S. A. Owerre, A first theoretical realization of honeycomb topological magnon insulator, *J. Phys. Condens. Matter* **28**, 386001 (2016).
- [50] S. A. Owerre, Magnon Hall effect in AB-stacked bilayer honeycomb quantum magnets, *Phys. Rev. B* **94**, 094405 (2016).
- [51] S. A. Owerre, Chirality-induced magnon transport in AA-stacked bilayer honeycomb chiral magnets, *J. Phys. Condens. Matter* **28**, 47LT02 (2016).
- [52] A. Mook, J. Henk, and I. Mertig, Spin dynamics simulations of topological magnon insulators: From transverse current correlation functions to the family of magnon Hall effects, *Phys. Rev. B* **94**, 174444 (2016).
- [53] B. Madon, D. C. Pham, J.-E. Wegrowe, D. Lacour, M. Hehn, V. Polewczyk, A. Anane, and V. Cros, Anomalous and planar Righi-Leduc effects in $\text{Ni}_{80}\text{Fe}_{20}$ ferromagnets, *Phys. Rev. B* **94**, 144423 (2016).
- [54] A. Okamoto and S. Murakami, Berry curvature for magnons in ferromagnetic films with dipole-exchange interactions, *Phys. Rev. B* **96**, 174437 (2017).

- [55] S. Murakami and A. Okamoto, Thermal Hall effect of magnons, *J. Phys. Soc. Jpn.* **86**, 011010 (2017).
- [56] S. A. Owerre, Topological magnon bands in ferromagnetic star lattice, *J. Phys. Condens. Matter* **29**, 185801 (2017).
- [57] B. Li and A. A. Kovalev, Chiral topological insulator of magnons, *Phys. Rev. B* **97**, 174413 (2018).
- [58] R. Seshadri and D. Sen, Topological magnons in a kagome-lattice spin system with XXZ and Dzyaloshinskii-Moriya interactions, *Phys. Rev. B* **97**, 134411 (2018).
- [59] M. Kawano and C. Hotta, Thermal Hall effect and topological edge states in a square lattice antiferromagnet, *Phys. Rev. B* **99**, 054422 (2019).
- [60] Y.-S. Lu, J.-L. Li, and C.-T. Wu, Topological Phase Transitions of Dirac Magnons in Honeycomb Ferromagnets, *Phys. Rev. Lett.* **127**, 217202 (2021).
- [61] F. Zhuo, H. Li, and A. Manchon, Topological phase transition and thermal Hall effect in kagome ferromagnets, *Phys. Rev. B* **104**, 144422 (2021).
- [62] M. Hirschberger, J. W. Krizan, R. J. Cava, and N. P. Ong, Large thermal Hall conductivity of neutral spin excitations in a frustrated quantum magnet, *Science* **348**, 106 (2015).
- [63] K. A. van Hoogdalem, Y. Tserkovnyak, and D. Loss, Magnetic texture-induced thermal Hall effects, *Phys. Rev. B* **87**, 024402 (2013).
- [64] C. Schütte and M. Garst, Magnon-skyrmion scattering in chiral magnets, *Phys. Rev. B* **90**, 094423 (2014).
- [65] A. Mook, B. Göbel, J. Henk, and I. Mertig, Magnon transport in noncollinear spin textures: Anisotropies and topological magnon Hall effects, *Phys. Rev. B* **95**, 020401 (R) (2017).
- [66] S. A. Owerre, Topological thermal Hall effect in frustrated kagome antiferromagnets, *Phys. Rev. B* **95**, 014422 (2017).
- [67] S. A. Owerre, Magnon Hall effect without Dzyaloshinskii-Moriya interaction, *J. Phys. Condens. Matter* **29**, 03LT01 (2017).
- [68] S. A. Owerre, Topological magnetic excitations on the distorted kagome antiferromagnets: Applications to volborthite, vesignieite, and edwardsite, *Europhys. Lett.* **117**, 37006 (2017).
- [69] S. A. Owerre, Noncollinear antiferromagnetic Haldane magnon insulator, *J. Appl. Phys.* **121**, 223904 (2017).
- [70] E. Iacocca and O. Heinonen, Topologically Nontrivial Magnon Bands in Artificial Square Spin Ices with Dzyaloshinskii-Moriya Interaction, *Phys. Rev. Applied* **8**, 034015 (2017).
- [71] K. Hwang, N. Trivedi, and M. Randeria, Topological Magnons with Nodal-Line and Triple-Point Degeneracies: Implications for Thermal Hall Effect in Pyrochlore Iridates, *Phys. Rev. Lett.* **125**, 047203 (2020).
- [72] P. Laurell and G. A. Fiete, Topological Magnon Bands and Unconventional Superconductivity in Pyrochlore Iridate Thin Films, *Phys. Rev. Lett.* **118**, 177201 (2017).
- [73] P. Laurell and G. A. Fiete, Magnon thermal Hall effect in kagome antiferromagnets with Dzyaloshinskii-Moriya interactions, *Phys. Rev. B* **98**, 094419 (2018).
- [74] S. Owerre, Topological thermal Hall effect due to Weyl magnons, *Can. J. Phys.* **96**, 1216 (2018).
- [75] J. Cookmeyer and J. E. Moore, Spin-wave analysis of the low-temperature thermal Hall effect in the candidate Kitaev spin liquid α -RuCl₃, *Phys. Rev. B* **98**, 060412 (R) (2018).
- [76] S. K. Kim, K. Nakata, D. Loss, and Y. Tserkovnyak, Tunable Magnonic Thermal Hall Effect in Skyrmion Crystal Phases of Ferrimagnets, *Phys. Rev. Lett.* **122**, 057204 (2019).
- [77] A. Mook, J. Henk, and I. Mertig, Thermal Hall effect in noncollinear coplanar insulating antiferromagnets, *Phys. Rev. B* **99**, 014427 (2019).
- [78] D. Watanabe, K. Sugii, M. Shimozawa, Y. Suzuki, T. Yajima, H. Ishikawa, Z. Hiroi, T. Shibauchi, Y. Matsuda, and M. Yamashita, Emergence of nontrivial magnetic excitations in a spin-liquid state of kagomé volborthite, *Proc. Natl. Acad. Sci. U.S.A.* **113**, 8653 (2016).
- [79] Y. Kasahara, K. Sugii, T. Ohnishi, M. Shimozawa, M. Yamashita, N. Kurita, H. Tanaka, J. Nasu, Y. Motome, T. Shibauchi, and Y. Matsuda, Unusual Thermal Hall Effect in a Kitaev Spin Liquid Candidate α -RuCl₃, *Phys. Rev. Lett.* **120**, 217205 (2018).
- [80] Y. Kasahara, T. Ohnishi, Y. Mizukami, O. Tanaka, S. Ma, K. Sugii, N. Kurita, H. Tanaka, J. Nasu, Y. Motome *et al.*, Majorana quantization and half-integer thermal quantum Hall effect in a Kitaev spin liquid, *Nature (London)* **559**, 227 (2018).
- [81] H. Doki, M. Akazawa, H.-Y. Lee, J. H. Han, K. Sugii, M. Shimozawa, N. Kawashima, M. Oda, H. Yoshida, and M. Yamashita, Spin Thermal Hall Conductivity of a Kagome Antiferromagnet, *Phys. Rev. Lett.* **121**, 097203 (2018).
- [82] R. Hentrich, M. Roslova, A. Isaeva, T. Doert, W. Brenig, B. Büchner, and C. Hess, Large thermal Hall effect in α -RuCl₃: Evidence for heat transport by Kitaev-Heisenberg paramagnons, *Phys. Rev. B* **99**, 085136 (2019).
- [83] M. Yamashita, M. Akazawa, M. Shimozawa, T. Shibauchi, Y. Matsuda, H. Ishikawa, T. Yajima, Z. Hiroi, M. Oda, H. Yoshida, H.-Y. Lee, J. H. Han, and N. Kawashima, Thermal-transport studies of kagomé antiferromagnets, *J. Phys. Condens. Matter* **32**, 074001 (2020).
- [84] L. Šmejkal, R. González-Hernández, T. Jungwirth, and J. Sinova, Crystal time-reversal symmetry breaking and spontaneous Hall effect in collinear antiferromagnets, *Sci. Adv.* **6**, eaaz8809 (2020).
- [85] T. Matsumoto and S. Hayami, Nonreciprocal magnons due to symmetric anisotropic exchange interaction in honeycomb antiferromagnets, *Phys. Rev. B* **101**, 224419 (2020).
- [86] A. R. Wildes, S. Okamoto, and D. Xiao, Search for nonreciprocal magnons in MnPS₃, *Phys. Rev. B* **103**, 024424 (2021).
- [87] R. Cheng, S. Okamoto, and D. Xiao, Spin Nernst Effect of Magnons in Collinear Antiferromagnets, *Phys. Rev. Lett.* **117**, 217202 (2016).
- [88] T. J. Hicks, T. Keller, and A. R. Wildes, Magnetic dipole splitting of magnon bands in a two dimensional antiferromagnet, *J. Magn. Magn. Mater.* **474**, 512 (2019).
- [89] R. Hidalgo-Sacoto, R. I. Gonzalez, E. E. Vogel, S. Allende, J. D. Mella, C. Cardenas, R. E. Troncoso, and F. Munoz, Magnon valley Hall effect in CrI₃-based van der Waals heterostructures, *Phys. Rev. B* **101**, 205425 (2020).
- [90] See Supplemental Material at <http://link.aps.org/supplemental/10.1103/PhysRevLett.128.117201>, which contains the parameters of MnPS₃, details on the theoretical

- calculations, results for the spin texture in the spin-flop phase, on order-by-disorder, and the pseudo-Goldstone gaps, on heat capacity, and transport calculations for enhanced spin-orbit parameter J_d . The Supplemental Material also includes videos that show the evolution of the magnon spectra (top left panel) and the Berry curvatures of both bands (lowest band, top right panel; highest band, bottom right panel) for different parameter sets as the magnetic field is varied (bottom left panel). The Supplemental Material includes Refs. [38,77,84,86,91–96].
- [91] T. Holstein and H. Primakoff, Field dependence of the intrinsic domain magnetization of a ferromagnet, *Phys. Rev.* **58**, 1098 (1940).
- [92] A. Jain, S. P. Ong, G. Hautier, W. Chen, W. D. Richards, S. Dacek, S. Cholia, D. Gunter, D. Skinner, G. Ceder, and K. Persson, The Materials Project: A materials genome approach to accelerating materials innovation, *APL Mater.* **1**, 011002 (2013).
- [93] K. Persson, Materials data on MnPS_3 (sg:12) by materials project (2016), [10.17188/1309185](https://doi.org/10.17188/1309185).
- [94] A. R. Wildes, B. Roessli, B. Lebech, and K. W. Godfrey, Spin waves and the critical behaviour of the magnetization in MnPS_3 , *J. Phys. Condens. Matter* **10**, 6417 (1998).
- [95] J. G. Rau, P. A. McClarty, and R. Moessner, Pseudo-Goldstone Gaps and Order-by-Quantum Disorder in Frustrated Magnets, *Phys. Rev. Lett.* **121**, 237201 (2018).
- [96] R. R. Neumann, A. Mook, J. Henk, and I. Mertig, Orbital Magnetic Moment of Magnons, *Phys. Rev. Lett.* **125**, 117209 (2020).
- [97] K. Okuda, K. Kurosawa, S. Saito, M. Honda, Z. Yu, and M. Date, Magnetic properties of layered compound MnPS_3 , *J. Phys. Soc. Jpn.* **55**, 4456 (1986).
- [98] D. J. Goossens and T. J. Hicks, The magnetic phase diagram of $\text{Mn}_x\text{Zn}_{1-x}\text{PS}_3$, *J. Phys. Condens. Matter* **10**, 7643 (1998).
- [99] We neglect a pseudo-Goldstone gap [95] that we show to be irrelevant in the Supplemental Material [90].
- [100] We have set $\overline{B}_z = B_1$ and $\Delta B_z = 2 \mu\text{eV}$ for (i) and $\overline{B}_z = B_2^{(i)}$ and $\Delta B_z = 0.4 \text{ meV}$ for (ii).

6.2.2 Thermal Magnon-Polaron Hall Effect

Motivated by the preceding results on the effects of field-driven phase transitions on the thermal transport properties of antiferromagnets, we collaborated with experimentalists on the heat transport in the cobaltate $\text{Na}_2\text{Co}_2\text{TeO}_6$. The material is a honeycomb antiferromagnet, which has gained attention due to the prediction of a spin liquid phase in materials with $3d$ electrons [170]. However, the material features antiferromagnetic order below $T_N = 27$ K [171]. The experimental data of the thermal HALL effect reported in our paper obtained at temperatures below 2.2 K exhibit a sign change at 10 T driven by the magnetic field.

The theoretical analysis of the paper revealed three main findings:

- The sign change around 10 T can be attributed to a spin-flop phase transition from a collinear zigzag-type antiferromagnetic to a spin-flop phase.
- Intrinsic magnon transport by itself does not explain the observed sign and magnitude of the thermal HALL signal.
- The hybridization of magnons and phonons reverses the sign and can explain the magnitude of the thermal HALL conductivity.

While the magnon model predicts a magnetic phase transition close to 10 T and an accompanying sign change of the thermal HALL conductivity, the global sign is incorrect. Furthermore, the magnon transport only accounts for roughly 10% of the signal.

When spin-lattice coupling is included in the form of a hybridization between magnons and phonons, the crossings between phonon and magnon bands are gapped and magnon polarons emerge (cf. Section 2.4). The hybridization imparts a BERRY curvature to the hybrid excitations, the dominant contribution of which is of opposite sign than that of the dominant magnon BERRY curvature before the hybridization. Consequently, the sign of the thermal HALL conductivity reverses and the magnitude increases depending on the strength of the spin-lattice coupling. Pictorially speaking, magnons and magnon polarons are deflected in opposite directions and their contributions to the transverse heat current compete with each other. Depending on the temperature and spin-lattice coupling, the balance can be tilted in favor of either types of quasiparticles.

Importantly, the study demonstrates that magnon polarons may dominate the thermal HALL conductivity, which exacerbates the detection of topological magnons by heat transport because they are typically higher in energy. The potential of magnon polarons overshadowing topological magnons therefore needs to be considered in proposals for observing the latter.

Reprinted article from N. Li, R. R. Neumann, S. K. Guang, Q. Huang, J. Liu, K. Xia, X. Y. Yue, Y. Sun, Y. Y. Wang, Q. J. Li, Y. Jiang, J. Fang, Z. Jiang, X. Zhao, A. Mook, J. Henk, I. Mertig, H. D. Zhou, and X. F. Sun, *Physical Review B* **108**, L140402 (2023); Ref. [RN3]; <http://dx.doi.org/10.1103/PhysRevB.108.L140402>. Copyright (2023) American Physical Society. Reproduced with permission. All rights reserved.

Magnon-polaron driven thermal Hall effect in a Heisenberg-Kitaev antiferromagnet

N. Li,^{1,*} R. R. Neumann^{2,*} S. K. Guang,^{1,*} Q. Huang,³ J. Liu,³ K. Xia,¹ X. Y. Yue,⁴ Y. Sun,⁴ Y. Y. Wang,⁴ Q. J. Li,⁵ Y. Jiang⁵, J. Fang⁶, Z. Jiang⁶, X. Zhao,⁷ A. Mook⁸, J. Henk², I. Mertig^{2,†}, H. D. Zhou^{3,‡} and X. F. Sun^{1,4,§}

¹Department of Physics, Hefei National Laboratory for Physical Sciences at Microscale, and Key Laboratory of Strongly-Coupled Quantum Matter Physics (CAS), University of Science and Technology of China, Hefei, Anhui 230026, People's Republic of China

²Institute of Physics, Martin Luther University Halle-Wittenberg, Halle (Saale) D-06120, Germany

³Department of Physics and Astronomy, University of Tennessee, Knoxville, Tennessee 37996-1200, USA

⁴Institute of Physical Science and Information Technology, Anhui University, Hefei, Anhui 230601, People's Republic of China

⁵School of Physics and Optoelectronics, Anhui University, Hefei, Anhui 230601, People's Republic of China

⁶School of Physics, Georgia Institute of Technology, Atlanta, Georgia 30332, USA

⁷School of Physical Sciences, University of Science and Technology of China, Hefei, Anhui 230026, People's Republic of China

⁸Institute of Physics, Johannes Gutenberg University, Mainz D-55128, Germany



(Received 28 February 2023; revised 23 August 2023; accepted 7 September 2023; published 4 October 2023)

We investigate the thermal Hall effect in the Heisenberg-Kitaev antiferromagnet $\text{Na}_2\text{Co}_2\text{TeO}_6$, where we observe negative thermal Hall conductivity (THC) with thermal Hall angles up to 2% at low magnetic fields, which changes the sign to positive THC at higher fields. Our theoretical calculations, incorporating spin-lattice coupling, reveal that the quantum-geometric Berry curvature of magnon polarons counteracts the purely magnonic contribution, resulting in a reversed sign and an increased magnitude in THC. This finding emphasizes the significance of spin-lattice coupling in understanding the thermal Hall effect.

DOI: [10.1103/PhysRevB.108.L140402](https://doi.org/10.1103/PhysRevB.108.L140402)

Topological phases of matter have received enormous attention in solid-state physics not only for their exceptional fundamental properties, but also for their potential technological impact. For example, topological band insulators feature protected, dissipationless edge channels [1–3], and topological order in strongly correlated electron systems (e.g., quantum spin liquids [4–6]) may be a route to fault-tolerant quantum computing [7,8]. Harvesting the potential of these exotic phases requires a reliable technique for their detection and characterization. An important probe for topological phases in insulators is the thermal Hall effect (THE), which denotes a transverse heat current response to a longitudinal temperature gradient [9,10]. Its *intrinsic* contribution is an invaluable probe of the Berry curvature, that is, a quantum-geometric property acting on the inherent quasiparticles, e.g., Majorana fermions [11,12], triplons [13,14], photons [15,16], and magnons [17–23], like a fictitious magnetic field. However, the ubiquitous phonons (quanta of lattice vibrations) interact and potentially hybridize with the aforementioned quasiparticles due to spin-lattice coupling (SLC) [24–26]. The band inversions of these quasiparticle-phonon hybrids establish another source of Berry curvature that may even dominate the low-temperature THE because of the low acoustic phonon energies. Hence, a detailed understanding of SLC and its effects on intrinsic heat transport is required.

In this joint experimental and theoretical work, we report the thermal Hall conductivity (THC) κ_{xy} of the Kitaev spin-liquid candidate $\text{Na}_2\text{Co}_2\text{TeO}_6$ (NCTO), which has attracted considerable attention recently [27–42]. Our field- and temperature-dependent measurements reveal a negative THC for out-of-plane magnetic fields below 10 T and a positive THC above 10 T at low temperatures. We attribute this sign change to a field-driven magnetic phase transition. As we demonstrate theoretically, magnons fail to explain not only the overall sign of THC, but also its order of magnitude, as THC is underestimated by a factor of ten. By taking SLC into account, magnons and phonons form hybrid quasiparticles, i.e., magnon polarons. The Berry curvature at the resulting avoided crossing between the lowest magnon and the acoustic phonon band is of opposite sign compared to the low-energy magnon Berry curvature without SLC. Hence, we reproduce both the correct overall sign and the order of magnitude of the experimental THC. The sign reversal of THC due to the hybridization of phonons and magnons is one of our main findings and is visualized in Fig. 1. Our results indicate the pivotal role of SLC in thermal transport, which may be also relevant to the interpretation of THC in related Heisenberg-Kitaev magnets [43–45].

NCTO is composed of Co^{2+} ions, arranged in layers of honeycomb lattices, whose effective $S = 1/2$ spins order in antiferromagnetic (AFM) zigzag chains [cf. Fig. 2(a)]. Employing a three-thermometer setup [Fig. 2(b), cf. Supplemental Material Section I.D. [46]], we have measured the temperature dependence of the longitudinal thermal conductivity $\kappa_{xx}(T)$ of NCTO at zero magnetic field [Fig. 2(c)]. According to previous studies, NCTO enters a magnetically

*These authors contributed equally to this work.

†ingrid.mertig@physik.uni-halle.de

‡hzhou10@utk.edu

§xfsun@ahu.edu.cn

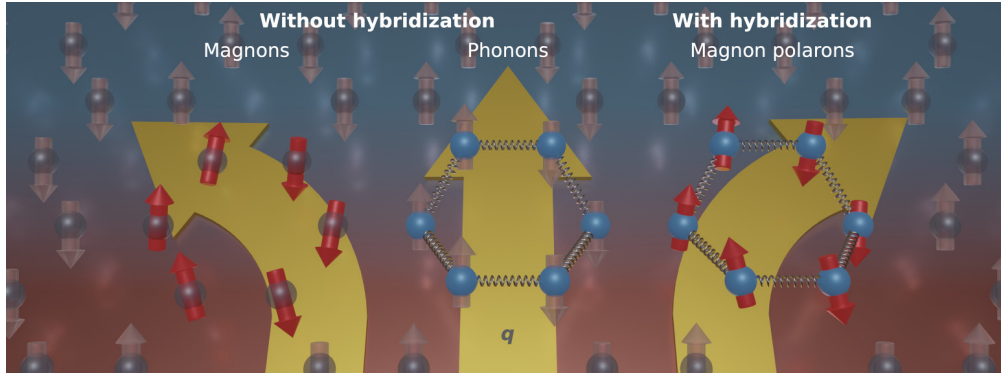


FIG. 1. Qualitative visualization of our theoretical results. Intrinsic thermal transport of distinct quasiparticles moving from hot to cold in a temperature gradient. Without hybridization, magnons contribute to the longitudinal and transversal transport, while phonons only contribute to the longitudinal one (in our approximation). With hybridization, magnons and phonons merge into magnon polarons and the transverse transport direction is reversed.

ordered state below the Néel temperature $T_N = 27$ K, followed by two possible spin reorientations around 16 K and 6 K, respectively [27–31]. Our $\kappa_{xx}(T)$ data show no obvious anomalies around 27 K and 16 K, in agreement with reported $\kappa_{xx}(T)$ data [47], but a slope change is noted below ~ 6 K, possibly related to a spin reorientation [28,30]. At sub-Kelvin temperatures, $\kappa_{xx}(T)$ roughly follows a $T^{1.2}$ behavior, which is at variance with the T^3 or T^2 behavior expected for the

phonon thermal conductivity at low temperatures in three or two dimensions, respectively [48]. Since magnons are frozen out at temperatures corresponding to energies below the spin-wave gap, their contribution does not explain the observed scaling law either. Therefore, this $T^{1.2}$ behavior may indicate the significance of interactions between phonons and magnons.

The field dependence of $\kappa_{xx}(B)$ measured at various temperatures with $\mathbf{B} \parallel \mathbf{c}$ is depicted in Fig. 2(d) and 2(e). At $T < 1.56$ K, $\kappa_{xx}(B)$ decreases quickly with increasing field to reach a minimum around 4 T, and then shows a weak field dependence up to 14 T. At 2.2 K, 2.7 K, and 3.2 K, $\kappa_{xx}(B)$ manifests a double-valley structure, with valleys around 2 T and 10 T, respectively. At even higher temperatures, $\kappa_{xx}(B)$ exhibits a broad valley in the range of 5 to 10 T. Similar observations have been reported in Ref. [49].

Apart from the complex longitudinal thermal conductivity, we find a peculiar field dependence of the THC $\kappa_{xy}(B)$, which we have measured at various temperatures below T_N [cf. Figs. 3(a) and 3(b)]. At $T \leq 2.2$ K, with increasing field, $\kappa_{xy}(B)$ first exhibits a negative Hall response, reaching a minimum around 3 to 5 T, then it changes to a positive sign around 10 T and increases at higher fields. At 3.2 K and 5.4 K, $\kappa_{xy}(B)$ curves show a positive peak at low fields, followed by two zero crossings with increasing field. At 7.8 K, $\kappa_{xy}(B)$ is positive without sign reversal. We have plotted the temperature dependence of κ_{xy}/T at several fields in Fig. 3(c). It is evident that at $B = 3$ T and 5 T, with increasing temperature, κ_{xy} is negative and reaches a minimum around 2 K, and then changes to a positive sign around 3 K to 4 K. The thermal Hall angle κ_{xy}/κ_{xx} possesses a minimum around 4 T and changes to a positive sign around 10 T at temperatures below 2.2 K [cf. Fig. 3(d)]. The largest absolute value of κ_{xy}/κ_{xx} is around 2% at 0.78 K and 4 T.

In a magnetic insulator, the observed κ_{xy} may have several origins, including phonons, magnons, and fractionalized exotic quasiparticles such as spinons. In experiments on non-magnetic insulators, the κ_{xy} of phonons does not exhibit a sign change [49,50], although this possibility cannot be ruled out here. For spinons, a nonzero κ_{xy} has only been observed in a quantum spin liquid with disordered spins [51–53]. Moreover, the 2% thermal Hall angle is exceptionally large for an

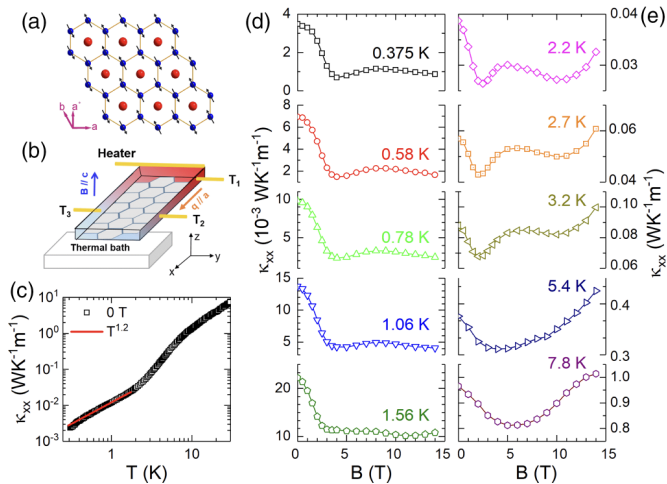


FIG. 2. Longitudinal thermal heat conductivity κ_{xx} of a $\text{Na}_2\text{Co}_2\text{TeO}_6$ single crystal. (a) Crystallographic spin structure of the ab plane of NCTO in the AFM state. The honeycomb lattice consists of cobalt ions (blue spheres) in the zigzag AFM arrangements (indicated by arrows), and the tellurium ions (red spheres) are located at the center of each honeycomb. The a^* axis is the in-plane direction perpendicular to the a axis. (b) Schematic of the experimental setup for the thermal Hall measurements. The heat current and the magnetic field are applied along the a and c axes, respectively. The longitudinal and transverse temperature gradients are determined by the difference between T_1 and T_2 and between T_2 and T_3 , respectively. (c) Temperature dependence of the longitudinal thermal conductivity κ_{xx} at zero magnetic field. The zero-field data roughly display a $T^{1.2}$ behavior at very low temperatures, as the solid line indicates. (d) and (e) Magnetic-field dependence of the thermal conductivity at various temperatures and with $\mathbf{B} \parallel \mathbf{c}$.

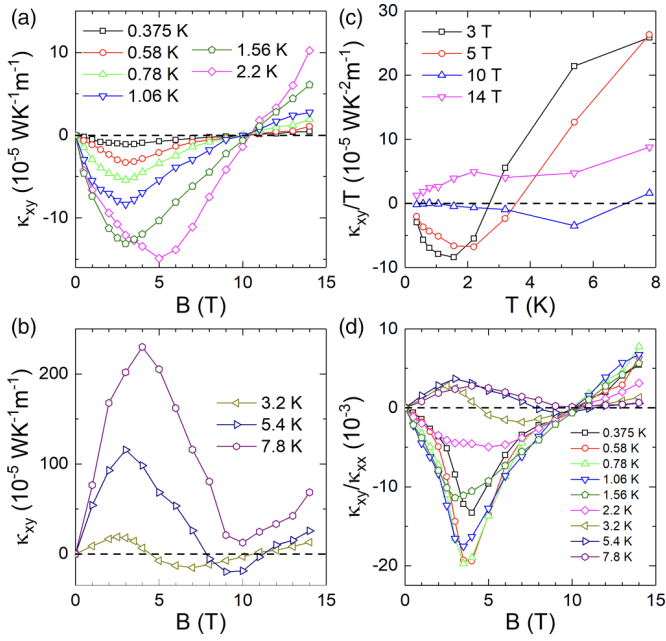


FIG. 3. Thermal Hall conductivity of a $\text{Na}_2\text{Co}_2\text{TeO}_6$ single crystal. (a) and (b) Field dependence of thermal Hall conductivity κ_{xy} for $\mathbf{B} \parallel \mathbf{c}$ at various temperatures. (c) Temperature dependence of κ_{xy}/T at selected magnetic fields. (d) Magnetic field dependence of the thermal Hall angle κ_{xy}/κ_{xx} at various temperatures.

insulator. The expected value, either originating from phonons or magnons, is typically around 0.3% to 0.6% or even lower [54], although similar thermal Hall angles have been observed in the insulating phases of the cuprate $\text{Nd}_{2-x}\text{Ce}_x\text{CuO}_4$ (up to 2%) [55], the iridate $\text{Sr}_2\text{Ir}_{1-x}\text{Rh}_x\text{O}_4$ (up to 3%) [56], and the pyrochlore magnet $\text{Yb}_2\text{Ti}_2\text{O}_7$ in its quantum spin-liquid state (up to 2%) [53].

The experimental results on the transverse transport properties of NCTO are subsequently explained by an effective, semiquantitative model. The starting point is the Heisenberg-Kitaev-Gamma-Gamma' (HKGΓ') Hamiltonian [57–59]

$$H = \frac{1}{2\hbar^2} \sum_{\langle ij \rangle_r} J_r \mathbf{S}_i \cdot \mathbf{S}_j + \frac{1}{2\hbar^2} \sum_{\langle ij \rangle} [K S_i^\alpha S_j^\beta + \Gamma (S_i^\alpha S_j^\beta + S_i^\beta S_j^\alpha) + \Gamma' (S_i^\gamma S_j^\alpha + S_i^\gamma S_j^\beta + S_i^\alpha S_j^\gamma + S_i^\beta S_j^\gamma)]$$

that encompasses the Heisenberg exchange [J_r ($r = 1, 2, 3$)] up to third nearest neighbors, and the Kitaev (K), Gamma (Γ), Gamma' (Γ') interactions between nearest neighbors. The magnetic field \mathbf{B} enters via the Zeeman Hamiltonian

$$H_B = \frac{g\mu_B}{\hbar} \mathbf{B} \cdot \sum_i \mathbf{S}_i.$$

\hbar denotes the reduced Planck constant, μ_B the Bohr magneton and g is the g -factor.

Here, we are interested in out-of-plane fields $\mathbf{B} \parallel \mathbf{c}$. Several parameter sets of the spin Hamiltonian have been determined for NCTO (Supplemental Material Table I [46]). In the following, we choose $J_1 = -3.2$ meV, $J_2 = 0.1$ meV, $J_3 = 1.2$ meV, $K = 2.7$ meV, $\Gamma = -2.9$ meV, $\Gamma' = 1.6$ meV, and $g = 2.3$ Refs. [34,36]. This parameter set (referred to as tc+) reproduces the critical fields

in experimental reports on field-induced magnetic phase transitions (Supplemental Material Section II.C. [46]) and, as presented later, provides the best agreement with the experimental THC. Results for other parameter sets are reported in the Supplemental Material Section II.D. [46]. The weak interlayer coupling is neglected.

The antiferromagnetic ground state of the Hamiltonian at zero field is characterized by zigzag chains with intra-chain ferromagnetic and interchain antiferromagnetic order. Applying a magnetic field cants the spins slightly, but they remain confined to the yz plane [cf. Fig. 4(a), left inset]. At the critical field of $B_{c1} = 10.8$ T the system passes a first-order phase transition into a spin-flop state, in which the spins lie within the zx plane [ferromagnetic component along z and Néel vector along x ; cf. Fig. 4(a), right inset]. The magnetization saturates at $B_{c2} = 31.2$ T, at which the fully field-polarized phase is reached. These critical fields are supported by magnetometry measurements (Supplemental Material Section II.C. [46]).

The diagonalization of the linearized Hamiltonian yields the four magnon bands ε_{nk} ($n = 1, 2, 3, 4$) [60,61]. Because of the spin-1/2 nature of the local magnetic moments, significant quantum fluctuations [62,63] are expected, which we discuss in the Supplemental Material Section II.F. [46]. The intrinsic contribution to THC is computed with the linear response formalism (cf. Supplemental Material Section II.D. [46]) [64].

Figure 4(a) shows κ_{xy} versus B_z as computed from free-magnon calculations for six temperatures. In the low-field phase, κ_{xy} is positive and changes sign at B_{c1} for all temperatures. This sign change is thus linked to the magnetic phase transition. However, the overall sign of κ_{xy} is at variance with the measured data [cf. Fig. 3(a)]. Attributed to the first-order transition, κ_{xy} is discontinuous at the phase transition, with the maximum left and the minimum right of B_{c1} . Moreover, the experimental data are underestimated by a factor of ten. Similar calculations with other parameter sets taken from the literature fail to reproduce the data as well (Supplemental Material Section II.D. [46]).

The foregoing suggests that magnons by themselves are not sufficient to explain the experimental data. It has been shown before that the hybridization of magnons and phonons can give rise to a thermal Hall effect [25,26,65–71]. We therefore consider out-of-plane oscillating phonons described by

$$H_p = \sum_i \frac{(p_i^z)^2}{2M} + \frac{C}{4} \sum_{\langle ij \rangle} (u_i^z - u_j^z)^2,$$

where p_i^z is momentum and u_i^z is displacement, which are subject of a particular SLC arising from spin-orbit coupling [25,26,67,71–73],

$$H_{\text{me}} = \frac{\tilde{\lambda}}{\hbar^2} \sum_i \sum_{\delta} (\mathbf{S}_i \cdot \boldsymbol{\delta}) S_i^z (u_i^z - u_{i+\delta}^z),$$

where $\boldsymbol{\delta}$ are the nearest-neighbor bond vectors for site. We neglect vibrations of nonmagnetic ions and other types of SLC for a minimal description. Furthermore, we consider a single acoustic phonon branch in the crystallographic Brillouin zone (that is, two branches in the magnetic Brillouin

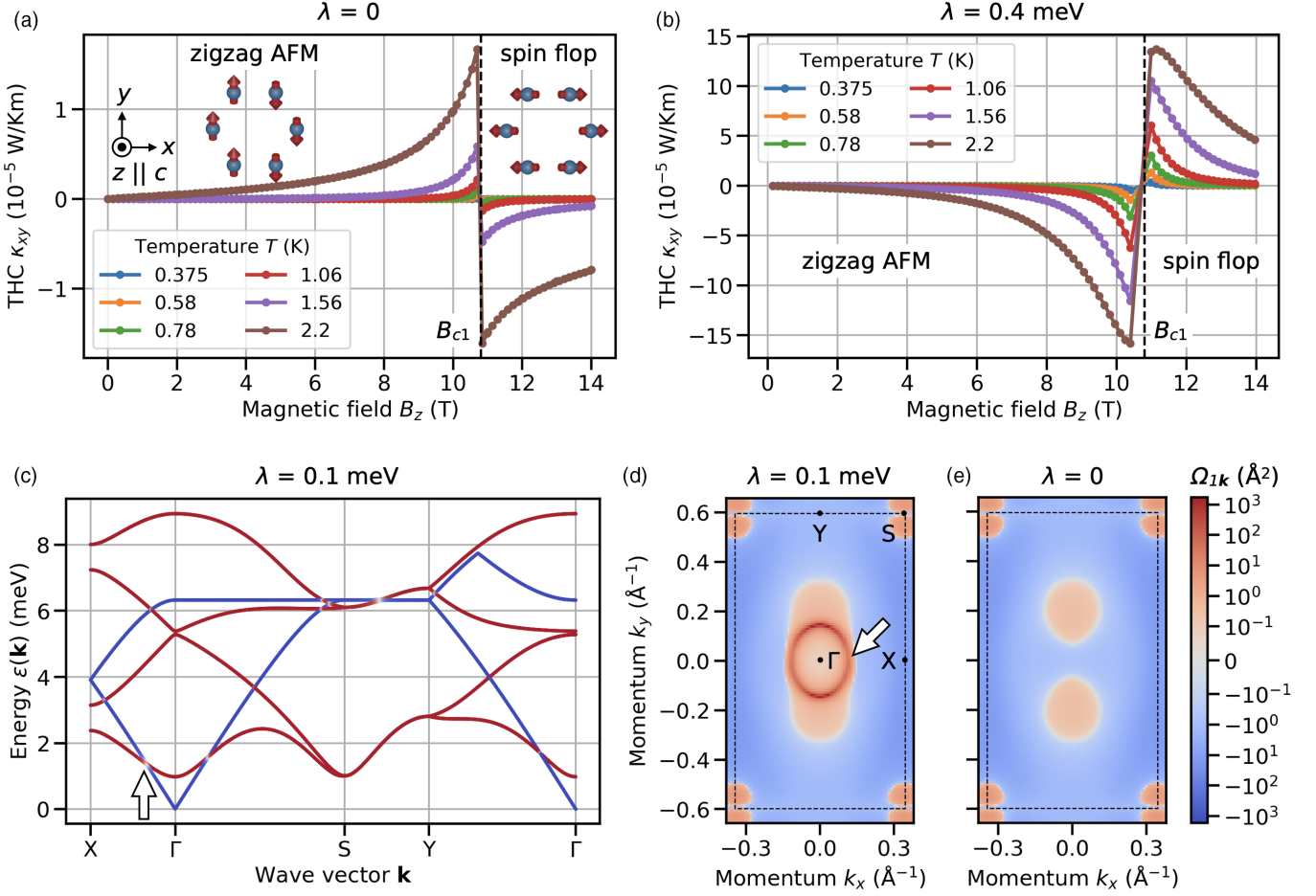


FIG. 4. Model calculations. (a) and (b) Thermal Hall conductivity κ_{xy} versus applied field B_z (a) without ($\lambda = 0$ meV) and (b) with ($\lambda = 0.4$ meV) SLC. Inset: Magnetic ground state of Co^{2+} ions in their two respective phases. (c) Magnon-polaron spectrum ε_{nk} along a high-symmetry path. Red, white, and blue color of the bands indicate the magnon, mixed, phonon character, respectively, of the modes; the magnetic field is 5 T. (d) and (e) Berry curvatures Ω_{nk} of the lowest bands $n = 1$ (d) with SLC ($\lambda = 0.1$ meV) and (e) without SLC ($\lambda = 0$ meV). Dashed rectangles in (d) and (e) mark the first Brillouin zone. The white arrows in (c) and (d) indicate the same avoided crossing. All results are obtained for the model of a two-dimensional honeycomb antiferromagnet with Heisenberg-Kitaev-Gamma-Gamma' interactions ($J_1 = -3.2$ meV, $J_2 = 0.1$ meV, $J_3 = 1.2$ meV, $K = 2.7$ meV, $\Gamma = -2.9$ meV, $\Gamma' = 1.6$ meV, and $g = 2.3$) and coupling of the spins to out-of-plane lattice displacements (see text for further details).

zone). The relevant energy scale $\lambda = \tilde{\lambda} d_{nn} \sqrt{\frac{\hbar}{2\sqrt{CM}}}$ [where M is the mass of Co^{2+} and $d_{nn} = 3.0361$ Å is the (in-plane) nearest-neighbor distance] quantifies the strength of the SLC. The elastic constant C is chosen to yield a phonon velocity of 3000 m/s, which is supported by heat capacity measurements (Supplemental Material Section I.C. [46] [74]). We proceed by bosonizing the spin and position operators, and extend the basis by the two phonon modes. The extended Hamiltonian is then diagonalized, and κ_{xy} is computed as before. The SLC strength $\lambda = 0.4$ meV has been fitted as an effective parameter to reproduce the experimental THC at 2.2 K.

Figure 4(b) displays κ_{xy} versus B_z in the presence of SLC. Compared to exclusive magnon transport, the overall sign of κ_{xy} is reversed and the sign change at the magnetic phase transition remains intact. Furthermore, κ_{xy} 's order of magnitude has increased and matches that of the experimental data. In short, agreement with the experiment has increased significantly.

The sign change and the increase of $|\kappa_{xy}|$ are attributed to hybrid quasiparticles that we refer to as magnon polarons. These normal modes are superpositions of magnons and phonons. Their hybrid nature is prominent in the band structure with SLC [Fig. 4(c)] at avoided crossings: their character changes continuously from magnon-like (red) to phonon-like (blue). The avoided crossing between the acoustic phonon branch and the lower magnon band generates a positive Berry curvature in the lowest band, indicated by a white arrow in Fig. 4(d). This pronounced, low-energy Berry curvature dominates the transport and explains the negative sign in the zigzag antiferromagnetic phase. This finding is contrasted with the Berry curvature in the absence of SLC [Fig. 4(e)]. Ignoring the phonon bands [blue in Fig. 4(c)], the magnon bands exhibit a spin-wave gap, and their lowest energies are at the Γ and S points. The Berry curvature of the lowest magnon band [Fig. 4(e)] at these points is negative and positive, respectively. Since the two lower magnon bands are degenerate at S and the upper band exhibits the opposite Berry curvature at S , the Berry curvature at Γ mostly governs the thermal transport at

low temperatures. This Berry curvature is, however, opposite to the emerging Berry curvature caused by the hybridization. Thus, there is a competition between pure magnon transport and magnon-polaron transport in the presence of SLC.

The gradual suppression and sign reversal of κ_{xy} by the coupling to phonons hold for lower temperatures. At higher temperatures, the magnon bands are strongly populated and the transport coefficient changes sign (Supplemental Material [46]). This competitive interplay between phonons and magnons is contrasted by the results of Zhang *et al.* [26] for the honeycomb ferromagnet VI_3 , which has been modeled with the Dzyaloshinskii-Moriya interaction (DMI) as the source of the magnon Berry curvature. There, an amplification of THC was found due to the SLC. Notably, an attenuation can be found for reversed DMI, which produces the same magnon spectrum, but opposite Berry curvature; hence, both amplification and attenuation of THC are within the reach of the DMI model with SLC. In contrast, the HKGG' model with SLC uniquely fixes both the sign of the magnon and the magnon-polaron Berry curvatures and, therefore, their relative sign. This renders the agreement between theory and experiment nontrivial. Overall, whether SLC leads to an amplification or an attenuation depends on the spin Hamiltonian and the particular form of SLC. Examples for the amplification by SLC in the HKGG' model are reported in the Supplemental Material [46] with different parameters. A systematic study is needed to predict which of these two scenarios can be expected in other systems.

The model including SLC achieves an agreement between theoretical and experimental results in overall sign, magnitude, and the general field dependence, in contrast to the pure magnon calculations. The remaining quantitative disagreement between the effective theoretical model and experiment could be caused by the presence of multiple domains close to the phase transition, which is not accounted for in our model, the restriction to one phonon band and one particular type of SLC, and the disregard of vibrational degrees of freedom of nonmagnetic ions. The deviation between the minima of $\kappa_{xy}(B_z)$ measured at 3 T and computed at 10 T may be attributed to extrinsic contributions to THC, as indicated by the correlation between the measured minima of κ_{xx} and κ_{xy} at similar fields [cf. Figs. 2(d), 2(e), and 3(a)]. Hence, at lower fields, extrinsic contributions appear to be relevant for a better quantitative agreement, while at larger fields, due to the lack of a similar prominent correlation, their relevance might be limited. Therefore, the extrinsic contributions to THC such as magnon-phonon scattering, magnon-magnon

scattering, and scattering of phonons or magnons at (magnetic) impurities should be investigated in a more comprehensive quantitative theory.

An open question for NCTO is whether its ground state is of zigzag antiferromagnetic or of triple-Q nature. While several studies have argued in favor of triple-Q [33,39,40], another reports inconsistent observations with the triple-Q ground state [41]. Our study shows that the zigzag antiferromagnetic ground state is compatible with THC measurements; however, we cannot conclusively rule out the possibility of a triple-Q ground state. In the triple-Q state, the noncollinear spin texture gives rise to a more complex SLC and magnon-phonon hybridization, leading to a larger set of adjustable parameters, which would have to be obtained from density functional theory. Whether the triple-Q ground state is also compatible with our THC measurements needs to be addressed in the future.

Finally, our results—in particular, the fact that magnon polarons and pure magnons can drive opposite heat currents of different magnitudes—demonstrate that SLC may completely alter the low-temperature transport properties and overshadow predicted transport signatures of isolated quasiparticles like topological magnons. Instead of transport signatures of isolated exotic spin excitations, a more unified approach that includes the hybridization with phonons is necessary for the interpretation of such transport experiments. To verify the importance of SLC in NCTO, but also more generally, an independent determination of the SLC by *ab initio* calculations or magnetoelastic experiments is required that should be combined with model calculations to quantify the impact on THC. In short, our results call for a systematic analysis of the role of SLC in THC.

We thank I. Kimchi for insightful discussions, and W. J. Chu and X. H. Zhou for their help with the experiments. This work was supported by the National Natural Science Foundation of China (Grants No. 12274388, No. 12174361, No. 12025408, No. 11904003, and No. 12274001) and the Nature Science Foundation of Anhui Province (Grants No. 1908085MA09, No. 2108085QA22, and No. 2208085MA09). The work at the University of Tennessee and Georgia Tech was supported by the U.S. Department of Energy (Awards No. DE-SC-0020254 and No. DE-FG02-07ER46451). A.M., J.H., and I.M. acknowledge funding from Deutsche Forschungsgemeinschaft (DFG, German Research Foundation) (Projects No. 504261060 and No. SFB TRR 227).

-
- [1] K. v. Klitzing, G. Dorda, and M. Pepper, New method for high-accuracy determination of the fine-structure constant based on quantized Hall resistance, *Phys. Rev. Lett.* **45**, 494 (1980).
- [2] D. J. Thouless, M. Kohmoto, M. P. Nightingale, and M. den Nijs, Quantized Hall conductance in a two-dimensional periodic potential, *Phys. Rev. Lett.* **49**, 405 (1982).
- [3] F. D. M. Haldane, Model for a quantum Hall effect without Landau levels: Condensed-matter realization of the parity anomaly, *Phys. Rev. Lett.* **61**, 2015 (1988).
- [4] P. W. Anderson, Resonating valence bonds: A new kind of insulator? *Mater. Res. Bull.* **8**, 153 (1973).
- [5] R. Moessner and S. L. Sondhi, Resonating valence bond phase in the triangular lattice quantum dimer model, *Phys. Rev. Lett.* **86**, 1881 (2001).
- [6] A. Kitaev, Anyons in an exactly solved model and beyond, *Ann. Phys.* **321**, 2 (2006).
- [7] A. Stern and N. H. Lindner, Topological quantum computation: From basic concepts to first experiments, *Science* **339**, 1179 (2013).

- [8] V. Lahtinen and J. Pachos, A short introduction to topological quantum computation, *SciPost Physics* **3**, 021 (2017).
- [9] H. Katsura, N. Nagaosa, and P. A. Lee, Theory of the thermal Hall effect in quantum magnets, *Phys. Rev. Lett.* **104**, 066403 (2010).
- [10] R. Matsumoto, R. Shindou, and S. Murakami, Thermal Hall effect of magnons in magnets with dipolar interaction, *Phys. Rev. B* **89**, 054420 (2014).
- [11] J. Nasu, J. Yoshitake, and Y. Motome, Thermal transport in the Kitaev model, *Phys. Rev. Lett.* **119**, 127204 (2017).
- [12] Y. Kasahara, T. Ohnishi, Y. Mizukami, O. Tanaka, S. Ma, K. Sugii, N. Kurita, H. Tanaka, J. Nasu, Y. Motome, T. Shibauchi, and Y. Matsuda, Majorana quantization and half-integer thermal quantum Hall effect in a Kitaev spin liquid, *Nature (London)* **559**, 227 (2018).
- [13] J. Romhányi, K. Penc, and R. Ganesh, Hall effect of triplons in a dimerized quantum magnet, *Nat. Commun.* **6**, 6805 (2015).
- [14] P. A. McClarty, F. Krüger, T. Guidi, S. F. Parker, K. Refson, A. W. Parker, D. Prabhakaran, and R. Coldea, Topological triplon modes and bound states in a Shastry–Sutherland magnet, *Nat. Phys.* **13**, 736 (2017).
- [15] S. Raghu and F. D. M. Haldane, Analogs of quantum-Hall-effect edge states in photonic crystals, *Phys. Rev. A* **78**, 033834 (2008).
- [16] L. Lu, J. D. Joannopoulos, and M. Soljačić, Topological photonics, *Nat. Photon* **8**, 821 (2014).
- [17] Y. Onose, T. Ideue, H. Katsura, Y. Shiomi, N. Nagaosa, and Y. Tokura, Observation of the magnon Hall effect, *Science*, **329**, 297 (2010).
- [18] T. Ideue, Y. Onose, H. Katsura, Y. Shiomi, S. Ishiwata, N. Nagaosa, and Y. Tokura, Effect of lattice geometry on magnon Hall effect in ferromagnetic insulators, *Phys. Rev. B* **85**, 134411 (2012).
- [19] R. Shindou, R. Matsumoto, S. Murakami, and J. Ohe, Topological chiral magnonic edge mode in a magnonic crystal, *Phys. Rev. B* **87**, 174427 (2013).
- [20] A. Mook, J. Henk, and I. Mertig, Magnon Hall effect and topology in kagome lattices: A theoretical investigation, *Phys. Rev. B* **89**, 134409 (2014).
- [21] R. Chisnell, J. S. Helton, D. E. Freedman, D. K. Singh, R. I. Bewley, D. G. Nocera, and Y. S. Lee, Topological magnon bands in a kagome lattice ferromagnet, *Phys. Rev. Lett.* **115**, 147201 (2015).
- [22] A. Mook, J. Henk, and I. Mertig, Thermal Hall effect in non-collinear coplanar insulating antiferromagnets, *Phys. Rev. B* **99**, 014427 (2019).
- [23] R. R. Neumann, A. Mook, J. Henk, and I. Mertig, Thermal Hall effect of magnons in collinear antiferromagnetic insulators: Signatures of magnetic and topological phase transitions, *Phys. Rev. Lett.* **128**, 117201 (2022).
- [24] R. Takahashi and N. Nagaosa, Berry curvature in magnon-phonon hybrid systems, *Phys. Rev. Lett.* **117**, 217205 (2016).
- [25] S. Zhang, G. Go, K.-J. Lee, and S. K. Kim, SU(3) topology of magnon-phonon hybridization in 2D antiferromagnets, *Phys. Rev. Lett.* **124**, 147204 (2020).
- [26] H. Zhang, C. Xu, C. Carnahan, M. Sretenovic, N. Suri, D. Xiao, and X. Ke, Anomalous thermal Hall effect in an insulating van der Waals magnet, *Phys. Rev. Lett.* **127**, 247202 (2021).
- [27] L. Viciu, Q. Huang, E. Morosan, H. W. Zandbergen, N. I. Greenbaum, T. McQueen, and R. J. Cava, Structure and basic magnetic properties of the honeycomb lattice compounds $\text{Na}_2\text{Co}_2\text{TeO}_6$ and $\text{Na}_3\text{Co}_2\text{SbO}_6$, *J. Solid State Chem.* **180**, 1060 (2007).
- [28] E. Lefrançois, M. Songvilay, J. Robert, G. Nataf, E. Jordan, L. Chaix, C. V. Colin, P. Lejay, A. Hadj-Azzem, R. Ballou, and V. Simonet, Magnetic properties of the honeycomb oxide $\text{Na}_2\text{Co}_2\text{TeO}_6$, *Phys. Rev. B* **94**, 214416 (2016).
- [29] A. K. Bera, S. M. Yusuf, A. Kumar, and C. Ritter, Zigzag antiferromagnetic ground state with anisotropic correlation lengths in the quasi-two-dimensional honeycomb lattice compound $\text{Na}_2\text{Co}_2\text{TeO}_6$, *Phys. Rev. B* **95**, 094424 (2017).
- [30] G. Xiao, Z. Xia, W. Zhang, X. Yue, S. Huang, X. Zhang, F. Yang, Y. Song, M. Wei, H. Deng, and D. Jiang, Crystal growth and the magnetic properties of $\text{Na}_2\text{Co}_2\text{TeO}_6$ with quasi-two-dimensional honeycomb lattice, *Cryst. Growth Des.* **19**, 2658 (2019).
- [31] W. Yao and Y. Li, Ferrimagnetism and anisotropic phase tunability by magnetic fields in $\text{Na}_2\text{Co}_2\text{TeO}_6$, *Phys. Rev. B* **101**, 085120 (2020).
- [32] M. Songvilay, J. Robert, S. Petit, J. A. Rodríguez-Rivera, W. D. Ratcliff, F. Damay, V. Balédent, M. Jiménez-Ruiz, P. Lejay, E. Pachoud, A. Hadj-Azzem, V. Simonet, and C. Stock, Kitaev interactions in the Co honeycomb antiferromagnets $\text{Na}_3\text{Co}_2\text{SbO}_6$ and $\text{Na}_2\text{Co}_2\text{TeO}_6$, *Phys. Rev. B* **102**, 224429 (2020).
- [33] W. Chen, X. Li, Z. Hu, Z. Hu, L. Yue, R. Sutarto, F. He, K. Iida, K. Kamazawa, W. Yu, X. Lin, and Y. Li, Spin-orbit phase behavior of $\text{Na}_2\text{Co}_2\text{TeO}_6$ at low temperatures, *Phys. Rev. B* **103**, L180404 (2021).
- [34] G. Lin *et al.*, Field-induced quantum spin disordered state in spin-1/2 honeycomb magnet $\text{Na}_2\text{Co}_2\text{TeO}_6$, *Nat. Commun.* **12**, 5559 (2021).
- [35] C. Kim, J. Jeong, G. Lin, P. Park, T. Masuda, S. Asai, S. Itoh, H.-S. Kim, H. Zhou, J. Ma, and J.-G. Park, Antiferromagnetic Kitaev interaction in $J_{\text{eff}} = 1/2$ cobalt honeycomb materials $\text{Na}_3\text{Co}_2\text{SbO}_6$ and $\text{Na}_2\text{Co}_2\text{TeO}_6$, *J. Phys.: Condens. Matter* **34**, 045802 (2021).
- [36] A. M. Samarakoon, Q. Chen, H. Zhou, and V. O. Garlea, Static and dynamic magnetic properties of honeycomb lattice antiferromagnets $\text{Na}_2M_2\text{TeO}_6$, $M = \text{Co}$ and Ni , *Phys. Rev. B* **104**, 184415 (2021).
- [37] G. Xiao, Z. Xia, Y. Song, and L. Xiao, Magnetic properties and phase diagram of quasi-two-dimensional $\text{Na}_2\text{Co}_2\text{TeO}_6$ single crystal under high magnetic field, *J. Phys.: Condens. Matter* **34**, 075801 (2021).
- [38] A. L. Sanders, R. A. Mole, J. Liu, A. J. Brown, D. Yu, C. D. Ling, and S. Rachel, Dominant Kitaev interactions in the honeycomb materials $\text{Na}_3\text{Co}_2\text{SbO}_6$ and $\text{Na}_2\text{Co}_2\text{TeO}_6$, *Phys. Rev. B* **106**, 014413 (2022).
- [39] W. G. F. Krüger, W. Chen, X. Jin, Y. Li, and L. Janssen, Triple-Q order in $\text{Na}_2\text{Co}_2\text{TeO}_6$ from proximity to hidden-SU(2)-symmetric point, [arXiv:2211.16957](https://arxiv.org/abs/2211.16957).
- [40] W. Yao, Y. Zhao, Y. Qiu, C. Balz, J. R. Stewart, J. W. Lynn, and Y. Li, Magnetic ground state of the Kitaev $\text{Na}_2\text{Co}_2\text{TeO}_6$ spin liquid candidate, *Phys. Rev. Res.* **5**, L022045 (2023).
- [41] S. Zhang, S. Lee, A. J. Woods, W. K. Peria, S. M. Thomas, R. Movshovich, E. Brosha, Q. Huang, H. Zhou, V. S. Zapf, and M. Lee, Electronic and magnetic phase diagrams of the Kitaev quantum spin liquid candidate $\text{Na}_2\text{Co}_2\text{TeO}_6$, *Phys. Rev. B* **108**, 064421 (2023).

- [42] S. Guang, N. Li, Q. Huang, K. Xia, Y. Wang, H. Liang, Y. Sun, Q. Li, X. Zhao, R. L. Luo, G. Chen, H. Zhou, and X. Sun, Anisotropic in-plane heat transport of Kitaev magnet $\text{Na}_2\text{Co}_2\text{TeO}_6$, [arXiv:2307.06316](https://arxiv.org/abs/2307.06316).
- [43] Y. Singh, S. Manni, J. Reuther, T. Berlijn, R. Thomale, W. Ku, S. Trebst, and P. Gegenwart, Relevance of the Heisenberg-Kitaev model for the honeycomb lattice iridates A_2IrO_3 , *Phys. Rev. Lett.* **108**, 127203 (2012).
- [44] K. W. Plumb, J. P. Clancy, L. J. Sandilands, V. V. Shankar, Y. F. Hu, K. S. Burch, H.- Y. Kee, and Y.- J. Kim, α - RuCl_3 : A spin-orbit assisted Mott insulator on a honeycomb lattice, *Phys. Rev. B* **90**, 041112 (2014).
- [45] C. Wong, M. Avdeev, and C. D. Ling, Zig-zag magnetic ordering in honeycomb-layered $\text{Na}_3\text{Co}_2\text{SbO}_6$, *J. Solid State Chem.* **243**, 18 (2016).
- [46] See Supplemental Material at <http://link.aps.org/supplemental/10.1103/PhysRevB.108.L140402> for additional experimental results on magnetometry, heat capacity, and longitudinal thermal conductivity measurements as well as theoretical results on critical magnetic fields, thermal Hall conductivity with and without spin-lattice coupling, and spin fluctuations.
- [47] X. Hong, M. Gillig, R. Hentrich, W. Yao, V. Kocsis, A. R. Witte, T. Schreiner, D. Baumann, N. Pérez, A. U. B. Wolter, Y. Li, B. Büchner, and C. Hess, Strongly scattered phonon heat transport of the candidate Kitaev material $\text{Na}_2\text{Co}_2\text{TeO}_6$, *Phys. Rev. B* **104**, 144426 (2021).
- [48] R. Berman, *Thermal Conduction in Solids* (Clarendon Press, Oxford, 1976).
- [49] S. K. Guang, N. Li, R. L. Luo, Q. Huang, Y. Y. Wang, X. Y. Yue, K. Xia, Q. J. Li, X. Zhao, G. Chen, H. D. Zhou, and X. F. Sun, Thermal transport of fractionalized antiferromagnetic and field induced states in the Kitaev material $\text{Na}_2\text{Co}_2\text{TeO}_6$, *Phys. Rev. B* **107**, 184423 (2023).
- [50] C. Strohm, G. L. J. A. Rikken, and P. Wyder, Phenomenological evidence for the phonon Hall effect, *Phys. Rev. Lett.* **95**, 155901 (2005).
- [51] H. Doki, M. Akazawa, H.- Y. Lee, J. H. Han, K. Sugii, M. Shimozawa, N. Kawashima, M. Oda, H. Yoshida, and M. Yamashita, Spin thermal Hall conductivity of a kagome antiferromagnet, *Phys. Rev. Lett.* **121**, 097203 (2018).
- [52] M. Hirschberger, J. W. Krizan, R. J. Cava, and N. P. Ong, Large thermal Hall conductivity of neutral spin excitations in a frustrated quantum magnet, *Science* **348**, 106 (2015).
- [53] M. Hirschberger, P. Czajka, S. M. Koohpayeh, W. Wang, and N. P. Ong, Enhanced thermal Hall conductivity below 1 Kelvin in the pyrochlore magnet $\text{Yb}_2\text{Ti}_2\text{O}_7$, [arXiv:1903.00595](https://arxiv.org/abs/1903.00595).
- [54] L. Chen, M.-E. Boulanger, Z.- C. Wang, F. Tafti, and L. Taillefer, Large phonon thermal Hall conductivity in the antiferromagnetic insulator Cu_3TeO_6 , *Proc. Natl. Acad. Sci. USA* **119**, e2208016119 (2022).
- [55] M.- E. Boulanger, G. Grissonnanche, É. Lefrançois, A. Gourgout, K.- J. Xu, Z.- X. Shen, R. L. Greene, and L. Taillefer, Thermal Hall conductivity of electron-doped cuprates, *Phys. Rev. B* **105**, 115101 (2022).
- [56] A. Ataei, G. Grissonnanche, M.-E. Boulanger, L. Chen, E. Lefrançois, V. Brouet, and L. Taillefer, Impurity-induced phonon thermal Hall effect in the antiferromagnetic phase of Sr_2IrO_4 , [arXiv:2302.03796](https://arxiv.org/abs/2302.03796).
- [57] J. G. Rau, E. K.- H. Lee, and H.- Y. Kee, Generic spin model for the honeycomb iridates beyond the Kitaev limit, *Phys. Rev. Lett.* **112**, 077204 (2014).
- [58] J. Chaloupka and G. Khaliullin, Hidden symmetries of the extended Kitaev-Heisenberg model: Implications for the honeycomb-lattice iridates A_2IrO_3 , *Phys. Rev. B* **92**, 024413 (2015).
- [59] H. Liu, J. Chaloupka, and G. Khaliullin, Kitaev spin liquid in 3D transition metal compounds, *Phys. Rev. Lett.* **125**, 047201 (2020).
- [60] T. Holstein and H. Primakoff, Field dependence of the intrinsic domain magnetization of a ferromagnet, *Phys. Rev.* **58**, 1098 (1940).
- [61] J. H. P. Colpa, Diagonalization of the quadratic boson Hamiltonian, *Physica A* **93**, 327 (1978).
- [62] P. A. Maksimov, Z. Zhu, S. R. White, and A. L. Chernyshev, Anisotropic-exchange magnets on a triangular lattice: Spin waves, accidental degeneracies, and dual spin liquids, *Phys. Rev. X* **9**, 021017 (2019).
- [63] P. A. Maksimov and A. L. Chernyshev, Rethinking α - RuCl_3 , *Phys. Rev. Res.* **2**, 033011 (2020).
- [64] R. Matsumoto and S. Murakami, Theoretical Prediction of a rotating magnon wave packet in ferromagnets, *Phys. Rev. Lett.* **106**, 197202 (2011).
- [65] S. Park and B.- J. Yang, Topological magnetoelastic excitations in noncollinear antiferromagnets, *Phys. Rev. B* **99**, 174435 (2019).
- [66] X. Zhang, Y. Zhang, S. Okamoto, and D. Xiao, Thermal Hall effect induced by magnon-phonon interactions, *Phys. Rev. Lett.* **123**, 167202 (2019).
- [67] G. Go, S. K. Kim, and K.- J. Lee, Topological Magnon-Phonon Hybrid Excitations in two-dimensional ferromagnets with tunable Chern numbers, *Phys. Rev. Lett.* **123**, 237207 (2019).
- [68] S. Park, N. Nagaosa, and B.- J. Yang, Thermal Hall effect, spin Nernst effect, and spin density induced by a thermal gradient in collinear ferrimagnets from magnon-phonon interaction, *Nano Lett.* **20**, 2741 (2020).
- [69] B. Sheikhi, M. Kargarian, and A. Langari, Hybrid topological magnon-phonon modes in ferromagnetic honeycomb and kagome lattices, *Phys. Rev. B* **104**, 045139 (2021).
- [70] B. Ma and G. A. Fiete, Antiferromagnetic insulators with tunable magnon-polaron Chern numbers induced by in-plane optical phonons, *Phys. Rev. B* **105**, L100402 (2022).
- [71] C. Xu, C. Carnahan, H. Zhang, M. Sretenovic, P. Zhang, D. Xiao, and X. Ke, Thermal Hall effect in a van der Waals triangular magnet FeCl_2 , *Phys. Rev. B* **107**, L060404 (2023).
- [72] E. Thingstad, A. Kamra, A. Brataas, and A. Sudbø, Chiral phonon transport induced by topological magnons, *Phys. Rev. Lett.* **122**, 107201 (2019).
- [73] N. Bazazzadeh, M. Hamdi, S. Park, A. Khavasi, S. M. Mohseni, and A. Sadeghi, Magnetoelastic coupling enabled tunability of magnon spin current generation in two-dimensional antiferromagnets, *Phys. Rev. B* **104**, L180402 (2021).
- [74] A. Tari, *The Specific Heat of Matter at Low Temperatures* (Imperial College Press, London, 2003).

6.3 Electrical Activity of Topological Magnons

Electronic edge states travelling unidirectionally around the boundaries of a sample produce an orbital magnetization [152, 172]. Magnons, on the other hand, do not transport charge, but their edge modes constitute a spin current flowing at the edges of the magnet. By virtue of the vacuum magnetoelectric effect, a moving magnetic dipole moment, which is associated with the magnon's spin, must entail an electric dipole moment locked perpendicular to their propagation direction (cf. Section 5.1). For a set of edge states, which do not have a collective preference of a propagation direction, the electric dipole moments cancel. Chiral edge states have a preferred propagation direction by definition; it is determined by the CHERN number of the bulk magnon bands (cf. Section 3.3).

The following paper studies the implications of the electric dipole moment of the topological magnons. Two main properties are investigated.

1. The electric polarization at the edges in thermal equilibrium, which can exist even in centrosymmetric systems as long as the net polarization vanishes.
2. The absorption of alternating electric fields by magnons in nonequilibrium.

The microscopic electric dipole moments of the topological magnons give rise to a macroscopic electric edge polarization, whose direction depends on the chirality. Since the occupation depends on temperature, the polarization increases with temperature. Moreover, thermally activated internal electric fields and electrical voltages are demonstrated to ensue from the presence of topological magnons. However, a more comprehensive model deems these predictions incomplete as trivial edge magnons may feature lower energies and overshadow the contributions of the topological magnons due to their larger population.

This drawback of thermal equilibrium can be avoided by a resonant excitation of topological magnons. We find that topological magnons can be activated by alternating electric fields. The fluctuations of their electric dipole moments directly couple to the external electric fields and give rise to one-magnon processes, in which the photon energy is completely transferred to the topological magnons. Importantly, the one-magnon processes dominate in ferromagnets at low temperatures. These topological electromagnons give rise to an in-gap resonance in the electrical absorption spectrum, which we propose can be used to detect topological magnons. By combining inelastic neutron scattering and the proposed THz spectroscopy, the bulk band structure including potential topological band gaps can be identified by neutron scattering, which cannot distinguish between topologically trivial and nontrivial gaps because it does not resolve in-gap edge states. By performing electric absorption measurements in the energy window of the gap, in-gap states can be potentially identified.

Electrical Activity of Topological Chiral Edge Magnons

Robin R. Neumann,¹ Jürgen Henk,¹ Ingrid Mertig,¹ and Alexander Mook²

¹*Institut für Physik, Martin-Luther-Universität Halle-Wittenberg, D-06099 Halle (Saale), Germany*

²*Institut für Physik, Johannes Gutenberg-Universität Mainz, D-55128 Mainz, Germany*

(Dated: December 20, 2023)

Topological magnon insulators support chiral edge excitations, whose lack of electric charge makes them notoriously difficult to detect experimentally. We show that relativistic magnetoelectric coupling universally renders chiral edge magnons electrically active, thereby facilitating *electrical* probes of magnon topology. Considering a two-dimensional out-of-plane magnetized topological magnon insulator, we predict a fluctuation-activated electric polarization perpendicular to the sample edges. Furthermore, the chiral topological electromagnons give rise to a unique in-gap signal in electrical absorption experiments. These results suggest THz spectroscopy as a promising probe for topological magnons.

Introduction. Topology has become a key concept in condensed matter physics, with the quantized Hall conductance being a prominent example [1, 2]. Although topological band structure theory can be carried over to magnons [3–8], i.e. the elementary excitations of magnetic order [9], their bosonic statistics does not give rise to quantized transport [10–17]. Furthermore, magnons lack electric charge, which, although being an attractive trait for technologies free of Joule heating [18], renders them “dark” in charge-probing spectroscopies. In addition, inelastic neutron scattering, which is the conventional probe of magnons, reveals their bulk band gaps, but fails to detect edge states [19, 20]. In short, the state of the art does not offer an appropriate tool for the detection of topological magnons and new ideas are needed [21–28].

Despite their charge neutrality, magnons can respond to external electric fields. Those electrically active magnons, so-called *electromagnons*, have been studied by THz spectroscopy [29–34], by magnon-photon coupling in cavities [35–37], and by parametric amplification of topological magnons [22]. The experimental proof of principle for driving magnons electrically has already been provided [38].

Herein, we investigate the electrical activity of topological chiral edge magnons in ferromagnets in order to explore their spectroscopic signatures. Knowing that a flow of magnons induces electric fields [39, 40] by virtue of the vacuum magnetoelectric (VME) effect [41–43], we first show that a flow of chiral edge magnons universally causes an electric edge polarization. Motivated by this result, we consider the Katsura-Nagaosa-Balatsky (KNB) mechanism [44] to study the electric polarization of a two-dimensional topological magnon insulator (TMI) and to disentangle contributions from topologically trivial and nontrivial magnons. Second, we investigate the response of topological magnons to external alternating electric fields in TMI nanoribbons and flakes, in which edge magnons cause electric absorption peaks within the magnon bulk band gap. Our results suggest that chiral edge magnons are electrically active and that terahertz spectroscopy could evidence their existence experimentally.

Intuitive expectations. Magnons carry a magnetic moment \mathbf{m} , giving rise to a relativistic electric dipole $\mathbf{p} = \mathbf{v} \times \mathbf{m}/c^2$ (\mathbf{v} magnon velocity, c speed of light), which is the VME effect resulting from Lorentz transformation from the magnon’s rest

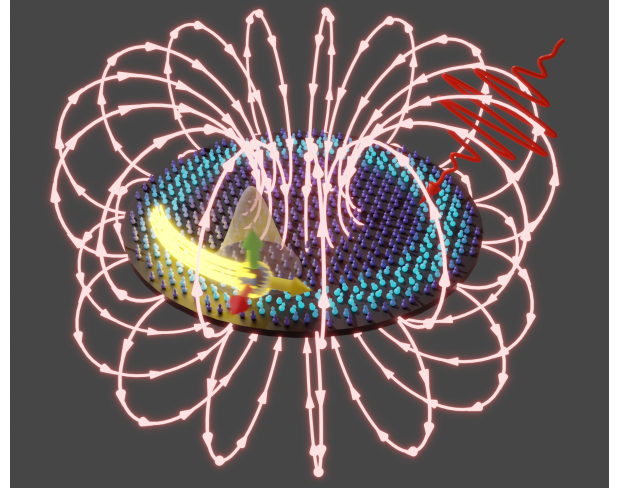


FIG. 1. Propagating chiral edge magnon in a disk-shaped topological magnon insulator. Arrows indicate velocity (yellow), magnetic dipole moment (green), and electric dipole moment (red, due to the vacuum magnetoelectric effect) of the wave packet (transparent sphere). The electric field (light red lines) follows from the generalized Biot-Savart law. The dark (light) blue arrows represent localized spins in their ground state (excited) state. The red oscillating curve illustrates an external alternating electric field, which excites and probes chiral edge magnons.

frame to the lab frame [39, 41–43]. For chiral edge magnons in two-dimensional and out-of-plane magnetized TMI, $\mathbf{m} \parallel \hat{z}$ and $\mathbf{p} \parallel \mathbf{v} \times \hat{z}$ points along the local edge normal, as indicated in Fig. 1. The sign of \mathbf{p} depends on the magnetization direction and on the velocity (hence, on the chirality) of the edge magnons. The chiral magnon edge current causes an electric field $\mathbf{E} = -\nabla\phi$, whose scalar potential

$$\phi(\mathbf{r}) = \frac{\mu_0 I_m}{4\pi} \oint [\mathrm{d}\mathbf{r}' \times \hat{\mathbf{m}}(\mathbf{r}')] \cdot \frac{\mathbf{r} - \mathbf{r}'}{|\mathbf{r} - \mathbf{r}'|^3}, \quad (1)$$

is obtained from a generalized Biot-Savart law [39, 40] (μ_0 vacuum permeability, I_m magnetization current, $\hat{\mathbf{m}}$ direction of the magnetic dipole).

For a magnetic current carried by chiral magnons on a cir-

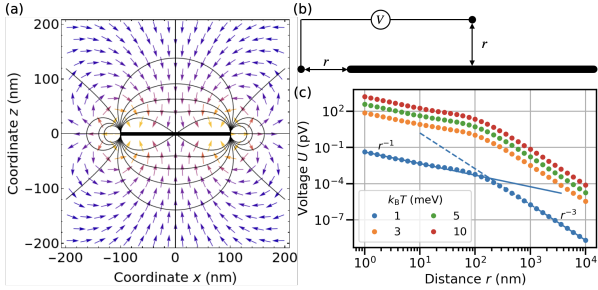


FIG. 2. Electric field of a magnetic disk in the xy plane and with a radius of 100 nm. (a) Field distribution in the xz -plane ($y = 0$). Arrows and arrow colors indicate directions and magnitude of the electric field, respectively, while black lines indicate equipotential lines. The disk is indicated by the black rectangle at $z = 0$. (b) Schematic of a voltage measurement setup. (c) Estimated distance dependence of the voltage due to the vacuum magnetoelectric effect of topological magnons for the setup of panel (b). Dots represent numerical data, while straight and dashed lines are linear fits to $U(r)$ for $k_B T = 1$ meV (11.6 K). For parameters, see text.

cular trajectory of radius R , we write $\mathbf{r} = \rho \hat{\mathbf{e}}_\rho(\varphi) + z \hat{\mathbf{e}}_z$ in cylindrical coordinates; $\hat{\mathbf{e}}_z$ ($\hat{\mathbf{e}}_\rho$) is out-of-plane (radial) to the magnetic current loop. If $R \ll \rho$, we approximate

$$\phi(\rho, \varphi, z) \approx \frac{\mu_0 I_m R^2 (\rho^2 - 2z^2)}{4 (\rho^2 + z^2)^{5/2}}, \quad (2)$$

while for $\rho = 0$ the exact potential reads

$$\phi(0, \varphi, z) = -\frac{\mu_0 I_m R^2}{2 (R^2 + z^2)^{3/2}} \quad (3)$$

[see Supplemental Material (SM) [45]]. Thus, the potential drops with distance as z^{-3} in the far field limit. The sign of I_m , i.e., the chirality of the edge magnons, determines the direction of the electric field \mathbf{E} . As expected, the \mathbf{E} field lines point radially outward from the edge of the disk and resemble a dipole field close to the edge [see Fig. 2(a)]. The largest electric field is found in the vicinity of the edges hosting the chiral edge magnons.

In order to estimate \mathbf{E} , we compute $I_m = \frac{g\mu_B v}{2\pi} \int_{-\pi/a}^{\pi/a} dk \rho(\varepsilon_k)$ (g Landé g -factor, μ_B Bohr magneton, a lattice constant, v edge magnon's group velocity). The occupation is given by $\rho(\varepsilon) = [\exp(\varepsilon/(k_B T)) - 1]^{-1}$ (k_B Boltzmann constant, T temperature). We assume $a = 1$ nm and, in order to describe van-der-Waals magnets [20, 46], $v = 1000$ m s $^{-1}$, $\varepsilon_k = \hbar v k + 12$ meV (i.e., the topological band gap is 4 meV). The voltage $U(r) = \phi(r, 0, 0) - \phi(0, 0, r)$ between two leads at a distance r from the edge and the center of the disk is evaluated numerically [Fig. 2(b)]. Its r -dependence, shown in Fig. 2(c) for selected temperatures, exhibits two regimes: $r \ll R$ with a r^{-1} -dependence and $r \gg R$ with a r^{-3} -dependence. The crossover is around $R = 100$ nm. These results suggest that a nanovolt-sensitive measurement could prove the existence of chiral edge magnons. We now contrast this intuitive picture with a microscopic theory.

Microscopic theory. We consider a two-dimensional TMI on a honeycomb lattice, which is an effective model for van-der-Waals magnets. The Hamiltonian

$$\mathcal{H} = - \sum_{r=1}^3 \frac{J_r}{2\hbar^2} \sum_{\langle ij \rangle_r} \mathbf{S}_i \cdot \mathbf{S}_j + \frac{1}{2\hbar^2} \sum_{\langle ij \rangle_2} \mathbf{D}_{ij} \cdot (\mathbf{S}_i \times \mathbf{S}_j) - \frac{A}{\hbar^2} \sum_i (S_i^z)^2 \quad (4)$$

includes Heisenberg exchange interactions J_r up to 3rd nearest neighbors, out-of-plane Dzyaloshinskii-Moriya interaction (DMI) $\mathbf{D}_{ij} = \pm D_z \hat{\mathbf{z}}$ between 2nd nearest neighbors, and out-of-plane anisotropy A (\hbar reduced Planck constant). In the following we choose relative parameters: $J_1 = 1$, $J_2 = 0.25$, $J_3 = 0$, $D_z = -0.1$, $A = 0.1$, and $S = 1$. The ground state is an out-of-plane collinear ferromagnet.

The model (4) is known to yield topological magnons in linear spin-wave theory [7, 8], which are shown for the arm-chair nanoribbon geometry in Fig. 3(b). The in-gap states have positive (negative) group velocity and are localized on the left (right) edge. The relation between velocity and localization depends on the Chern number, which can be reversed with the magnetization or the sign of D_z .

The relativistic electric dipole between two spins at sites i and j reads $\mathbf{p}_{ij} = q_{ij} \mathbf{e}_{ij} \times (\mathbf{S}_i \times \mathbf{S}_j) / \hbar^2$ according to the spin-current [or Katsura-Nagaosa-Balatsky (KNB)] mechanism [44, 47] (q_{ij} effective charge, \mathbf{e}_{ij} bond vector between site i and j , \mathbf{S}_i and \mathbf{S}_j spin operators). As shown in the SM [45], the VME and the KNB effects are equivalent for magnons in Heisenberg ferromagnets, but the KNB effect can be around 5 to 6 orders of magnitude larger.

We expand $\mathbf{p}_{ij} = \mathbf{p}_{ij}^{(0)} + \mathbf{p}_{ij}^{(1)} + \mathbf{p}_{ij}^{(2)} + \dots$ by means of the Holstein-Primakoff transformation [48], where the superscript denotes the number of bosons (explicit expressions for the operators are provided in the SM [45]). $\mathbf{p}_{ij}^{(0)}$ is the classical ground state polarization, which is zero in our case. $\mathbf{p}_{ij}^{(1)}$ vanishes in equilibrium, but encodes the dynamic electric dipole moment associated with spin dynamics, and the bilinear $\mathbf{p}_{ij}^{(2)}$ tells about the expectation value per magnon. In equilibrium, the fluctuation-induced $\mathbf{p}_{ij}^{(2)}$ is the dominant contribution to the macroscopic polarization.

Below, we consider the layer-resolved polarization

$$\mathbf{P}_n = \frac{q}{\hbar^2 L} \sum_{i \in L_n} \mathbf{e}_{ij} \times (\mathbf{S}_i \times \mathbf{S}_j), \quad (5)$$

of layer n in the nanoribbon, which is a sum over all inter-site electric dipole moments \mathbf{p}_{ij} in that layer (L_n set of all sites in layer n , L circumference of the nanoribbon). The thermal equilibrium expectation value of \mathbf{P}_n (originating from $\mathbf{p}_{ij}^{(2)}$) projected onto the in-plane normal vector $\hat{\mathbf{n}}$ of the left edge, shown in Fig. 3(a), features nonzero values at the edges of the nanoribbon, while it vanishes in the bulk. Inversion symmetry dictates that the polarizations at opposite edges are antiparallelly oriented. However, based on the intuitive expectations

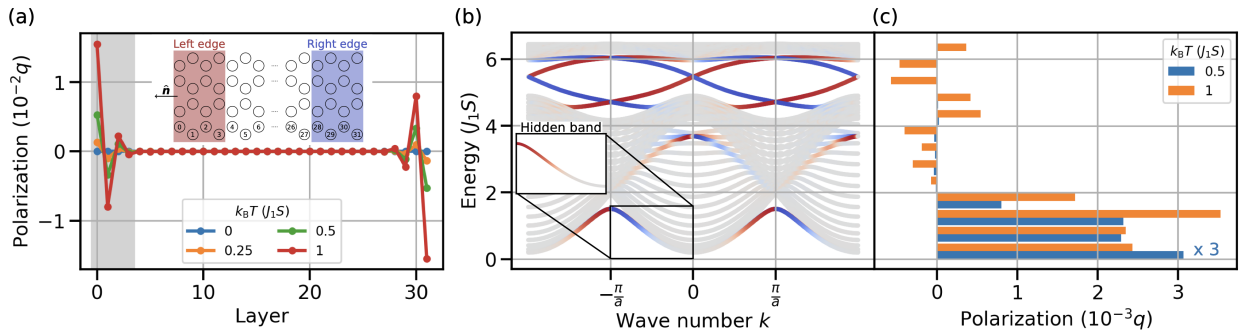


FIG. 3. Electric polarization and magnons of a nanoribbon in armchair nanoribbon geometry with 32 layers. (a) Layer-resolved electric polarization due to the Katsura-Nagaosa-Balatsky effect for various temperatures (as indicated) projected onto the outward-facing in-plane normal vector \hat{n} of the left edge. Inset: section of the nanoribbon including layer labels and the normal vector \hat{n} . The system is finite (infinite) along the horizontal (vertical) direction. (b) Magnon spectrum. Probability amplitudes of the left (red) and right (blue) edge [defined as the 4 outermost layers at each edge side; cf. the inset in panel (a)] are encoded by color. Inset: hidden band covered by the lowest band. (c) Energy-resolved contributions of the magnons to the electric polarization at the left edge [highlighted in panel (a) by a gray background] for two selected temperatures (as indicated). Each bar comprises contributions accumulated in an energy interval of $J_1S/2$. The blue bars are multiplied by 3 for better visibility. Parameters read $J_1 = 1, J_2 = 0.25, J_3 = 0, D_z = -0.1, A = 0.1,$ and $S = 1$. Results for other terminations can be found in the SM [45].

following from the VME effect and the chirality of the edge magnons [cf. Fig. 3(b)], one would expect a *negative* projected polarization at the left edge, which is opposite to the numerical results.

This discrepancy is understood by analyzing the energy-resolved contributions to the left-edge polarization $\sum_{n=0}^3 \mathbf{P}_n$ [see Fig. 3(c); layers 0–3 are highlighted in Fig. 3(a)]. There exist not only contributions from within the topological band gap, but also much larger ones from energies below the gap. The latter arise from trivial sub-gap edge modes [see Fig. 3(b)], whose thermal occupation is larger than that of the nontrivial in-gap states. The existence of trivial sub-gap edge modes is unavoidable: these arise from the weaker effective internal magnetic field for spins at the edges (missing neighbor sites). The sub-gap states highlighted in the inset of Fig. 3(b) (these are hidden below the lowest band) have a velocity opposite to that of the nontrivial mode localized at the same edge, and, therefore, an opposite electric dipole moment. The contributions of trivial sub-gap modes to $\sum_{n=0}^3 \mathbf{P}_n$ dominate over those of the nontrivial in-gap modes at all temperatures. Furthermore, the trivial contributions proved robust against disorder and manipulations of the edges (see SM [45]).

In short, the equilibrium properties of the topological magnons are overshadowed by those of trivial magnons, and the intuitive picture is incomplete.

Absorption of alternating electric fields. The above discussion demonstrates the need to go beyond thermal equilibrium, in which sub-gap states are favored over in-gap states. As we show in the SM [45], the in-gap states do not respond to alternating magnetic fields. Therefore, we study the possibility to address resonantly the magnons with alternating *electric* fields

$\mathbf{E}(t)$ by including a perturbation

$$\mathcal{H}' = -V\mathbf{P} \cdot \mathbf{E}(t) = \frac{q}{\hbar^2} \sum_{\langle ij \rangle} (\mathbf{e}_{ij} \times \mathbf{E}(t)) \cdot (\mathbf{S}_i \times \mathbf{S}_j) \quad (6)$$

to the Hamiltonian (4) (\mathbf{P} total electric polarization). This form suggests that the external electric field induces a time-varying DMI, the corresponding DMI vector of which is out-of-plane (in-plane) for in-plane (out-of-plane) fields.

The linear response of \mathbf{P} to the perturbation, $\Delta \langle \mathbf{P}_\mu(\omega) \rangle = \chi_{\mu\nu}(\omega) E_\nu(\omega)$, is quantified by the electric susceptibility $\chi_{\mu\nu}(\omega)$ ($\mu, \nu = x, y, z$; implicit summation over ν). In Kubo's formalism [49, 50], $\chi_{\mu\nu}(\omega) = -VC_{P_\mu, P_\nu}^R(\omega)$ is obtained from the retarded polarization autocorrelation function $C_{P_\mu, P_\nu}^R(\omega)$, which is evaluated in the SM [45]. There are various types of contributions $\chi_{\mu\nu}^{(i)}$ to $\chi_{\mu\nu}$, among them one- ($i = 1$; leading order derived from $\mathbf{p}_{ij}^{(1)}$) and two-magnon processes ($i = 2$; leading order derived from $\mathbf{p}_{ij}^{(2)}$). While the one-magnon processes are governed by the (out-of-plane or transversal) fluctuations of the magnons' electric dipole moments about their mean value, the two-magnon processes are governed by the bilinear part of the total dipole moment that is also responsible for the finite mean value in equilibrium (longitudinal fluctuations). Therefore, one-magnon processes appear for out-of-plane, while two-magnon processes appear for in-plane electric fields. Since according to Eq. (6) only the former induces in-plane DMI, which breaks magnon-number conservation, only one-magnon processes may change the magnon number, while two-magnon processes can only cause interband transitions of thermally excited magnons. Thus, contrary to $\chi_{\mu\nu}^{(1)}, \chi_{\mu\nu}^{(2)}$ can be frozen out. We therefore focus on one-magnon processes in the rest of the paper, while delegating further details, mathematical expressions, derivations, and results for two-magnon processes to the SM [45].

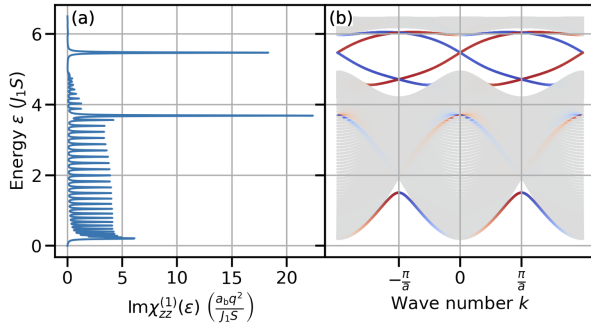


FIG. 4. Electric susceptibility of a 120 layers wide nanoribbon with armchair terminations. (a) Imaginary part of the one-magnon susceptibility vs. energy. (b) Magnon spectrum with localization at the left (red) and right (blue) edge encoded by color. a_b is the bulk lattice constant of the underlying honeycomb lattice, while $a = \sqrt{3}a_b$ is the lattice constant of the nanoribbon. The width of the Lorentzians is $\eta = 0.01J_1 S$. Parameters as for Fig. 3. Results for other terminations can be found in the SM [45].

The imaginary part

$$\text{Im}\chi_{\mu\mu}^{(1)}(\omega) = \pi V \sum_{n=1}^N \left| (\mathcal{P}_{\mu}^{(1)})_n \right|^2 \delta(\hbar\omega - \epsilon_{n,k=0}) \quad (7)$$

of the diagonal electric one-magnon susceptibility ($\omega > 0$, N number of bands) contains the linear electric dipole element $(\mathcal{P}_{\mu}^{(1)})_n$ for component μ and band n , whose general expression is derived in the SM [45]. The δ -distribution, which we replace by a Lorentzian of width η for numerical calculations, ensures energy conservation, such that resonance frequencies appear at the eigenfrequencies of the system, while only magnons at $\mathbf{k} = \mathbf{0}$ can be probed due to momentum conservation.

Returning to the honeycomb model, absorption appears only for $\mu = z$: it shows a pronounced in-gap peak just below $\epsilon/(J_1 S) = 6$, which is attributed to topological magnons (see Fig. 4). In the SM [45], we show that *the absorption only takes place at the edges*, therefore, only modes with nonzero probability amplitude at the edges may contribute. Bulk modes have nonzero probability amplitudes at the edges as well, but cause peaks above and below the gap.

Together with inelastic neutron scattering, which can locate gaps in the bulk magnon spectrum, in-gap peaks of $\text{Im}\chi_{zz}^{(1)}(\omega)$ could allow to detect topological magnons in principle. Momentum conservation tells that only topological magnons with $\mathbf{k} = \mathbf{0}$ contribute to the signal; however, it is not guaranteed that topological magnons exist at this particular \mathbf{k} (see SM for a counterexample [45]). Thus, in-gap peaks are no necessary consequence of topological edge modes. Furthermore, absorption at a sample's edge could be overshadowed by other sources and hence might be hard to resolve in experiment.

The above suggests that momentum conservation has to be lifted. We therefore consider the electric absorption of flakes instead of nanoribbons. While a large flake is roughly similar to a nanoribbon, increasing deviations are expected

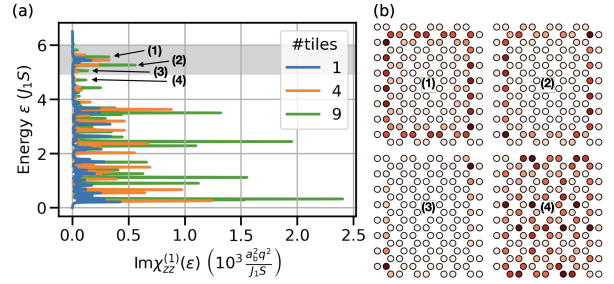


FIG. 5. Electric susceptibility of a flake of 1152 spins cut into four (nine) smaller equally sized tiles [see legend in panel (a)]. (a) Energy-resolved imaginary part of the electric one-magnon susceptibility. For the 9-tile spectrum (green line), selected in-gap resonances (1)–(4) are marked with arrows. The gray background indicates the topological bulk band gap. (b) Real-space probability distributions of the four electrically active magnon modes (1)–(4) marked in panel (a), one tile for each mode (as indicated). Nine of these tiles make up the green absorption spectrum in panel (a). The width of the Lorentzians is $\eta = 0.01J_1 S$. Parameters as for Fig. 3.

upon shrinking the flake. We have computed the electric one-magnon absorption of a flake encompassing 1152 spins [blue line in Fig. 5(a)] that is “cut” into 4 (orange line) and 9 equally sized smaller tiles (green line). This cutting increases the signal magnitude of infinite-wavelength peaks due to the introduction of internal edges and leads to additional peaks from in-gap states with smaller wavelengths.

To prove the topological origin of the in-gap peaks for the green line, we have selected four peaks [labeled (1)–(4) in Fig. 5(a)], for which the real-space probability distribution of the corresponding magnon states is shown in Fig. 5(b). Each flake depicts one of the 9 tiles responsible for the green absorption spectrum in Fig. 5(a). The darker the color, the stronger the localization of the corresponding magnon mode at that site. In the cases (1), (2), and (3), the electrically active modes have vanishing weights in the bulk. In contrast, mode (4) is delocalized throughout the bulk. The topological bulk gap, indicated by a horizontal gray stripe in the background of Fig. 5(a), includes modes (1)–(3), while (4) falls outside this energy window, demonstrating the topological origin of the *in-gap* absorption peaks.

Quantitative estimate. The effective charge is estimated as $q \approx 10^{-4}|e|$ to $10^{-3}|e|$ for GaV_4S_8 [51], CrBr_3 [52], and YIG [53] (cf. SM [45]; $|e|$ elementary charge). Here, we present calculations based on Heisenberg-DMI and Heisenberg-Kitaev models for the experimental parameters of CrI_3 [54] (cf. SM [45]), a putative TMI. The three-dimensional electric edge polarization, which depends on the weight of the edges in the probed volume, is estimated to about $10 \mu\text{C m}^{-2}$ within the first four layers. For the imaginary part of the three-dimensional electric susceptibility, which is inversely proportional to the linewidth η , we obtain $6 \times 10^{-3} \epsilon_0$ for $\eta = 0.1 \text{ meV}$ (ϵ_0 vacuum permittivity). This value decreases with increasing size of the nanoribbon, as is expected for edge effects.

We expect that our prediction qualitatively applies as well to other ferromagnetic TMI, such as $\text{Lu}_2\text{V}_2\text{O}_7$ [12], $\text{Cu}(\text{1,3-benzenedicarboxylate})$ [14, 19], CrSiTe_3 and CrGeTe_3 [20], and VI_3 [55].

Discussion. We have investigated the electric properties of topological chiral edge magnons in equilibrium and nonequilibrium. In an intuitive picture of the vacuum magnetoelectric effect, topological magnons give rise to an electric edge polarization by thermal fluctuations even in centrosymmetric systems. However, the model calculations based on the KNB effect identified further contributions by trivial edge modes, which dominate the overall signal. Nonetheless, by addressing the topological magnons directly with alternating electric fields of corresponding frequencies, we demonstrated that these modes may be electrically active, as is indicated by peaks in the one-magnon electric susceptibility. These topological electromagnons have infinite wavelengths and, depending on their specific dispersion relation, might not be present in every nanoribbon. The electric absorption by topological edge magnons in flakes can be tuned by the edge-to-area ratio, such that additional peaks from magnons with a finite wavelength appear and the signal of magnons with infinite wavelength is increased. Hence, we believe that THz spectroscopy can be regarded a probe for topological magnons.

Future research in “topological electromagnonics” could be directed at a *local* THz probe of chiral edge states, as provided by scattering-type scanning near-field optical microscopy [56–59], at a topological electromagnon-polariton formation in THz cavities [36], and at the existence of topological electromagnons beyond the relativistic KNB mechanism [47]. We hope that our results provide additional impetus to search for candidate materials with nontrivial magnon band structures and strong magnetoelectric coupling, and to explore the relation of electromagnons to magnon orbitronics [60, 61].

Acknowledgments. This work was funded by the Deutsche Forschungsgemeinschaft (DFG, German Research Foundation) – Project-ID 328545488 – TRR 227, project B04; and Project No. 504261060 (Emmy Noether Programme).

-
- [1] K. v. Klitzing, G. Dorda, and M. Pepper, New Method for High-Accuracy Determination of the Fine-Structure Constant Based on Quantized Hall Resistance, *Physical Review Letters* **45**, 494 (1980).
 - [2] F. D. M. Haldane, Model for a Quantum Hall Effect without Landau Levels: Condensed-Matter Realization of the “Parity Anomaly”, *Physical Review Letters* **61**, 2015 (1988).
 - [3] R. Matsumoto and S. Murakami, Theoretical Prediction of a Rotating Magnon Wave Packet in Ferromagnets, *Physical Review Letters* **106**, 197202 (2011).
 - [4] L. Zhang, J. Ren, J.-S. Wang, and B. Li, Topological magnon insulator in insulating ferromagnet, *Physical Review B* **87**, 144101 (2013).
 - [5] R. Shindou, R. Matsumoto, S. Murakami, and J.-i. Ohe, Topological chiral magnonic edge mode in a magnonic crystal, *Physical Review B* **87**, 174427 (2013).
 - [6] A. Mook, J. Henk, and I. Mertig, Edge states in topological magnon insulators, *Physical Review B* **90**, 024412 (2014).
 - [7] S. A. Owerre, A first theoretical realization of honeycomb topological magnon insulator, *Journal of Physics: Condensed Matter* **28**, 386001 (2016).
 - [8] S. K. Kim, H. Ochoa, R. Zarzuela, and Y. Tserkovnyak, Realization of the Haldane-Kane-Mele Model in a System of Localized Spins, *Physical Review Letters* **117**, 227201 (2016).
 - [9] F. Bloch, Zur Theorie des Ferromagnetismus, *Zeitschrift für Physik* **61**, 206 (1930).
 - [10] R. Tao and K. Maki, Quantum hall effect of two-dimensional interacting boson systems, *Physics Letters A* **116**, 277 (1986).
 - [11] H. Katsura, N. Nagaosa, and P. A. Lee, Theory of the Thermal Hall Effect in Quantum Magnets, *Physical Review Letters* **104**, 066403 (2010).
 - [12] Y. Onose, T. Ideue, H. Katsura, Y. Shiomi, N. Nagaosa, and Y. Tokura, Observation of the Magnon Hall Effect, *Science* **10.1126/science.1188260** (2010).
 - [13] R. Matsumoto, R. Shindou, and S. Murakami, Thermal Hall effect of magnons in magnets with dipolar interaction, *Physical Review B* **89**, 054420 (2014).
 - [14] M. Hirschberger, R. Chisnell, Y. S. Lee, and N. P. Ong, Thermal Hall Effect of Spin Excitations in a Kagome Magnet, *Physical Review Letters* **115**, 106603 (2015).
 - [15] K. Nakata, J. Klinovaja, and D. Loss, Magnonic quantum Hall effect and Wiedemann-Franz law, *Physical Review B* **95**, 125429 (2017).
 - [16] A. Mook, B. Göbel, J. Henk, and I. Mertig, Taking an electron-magnon duality shortcut from electron to magnon transport, *Physical Review B* **97**, 140401 (2018).
 - [17] R. R. Neumann, A. Mook, J. Henk, and I. Mertig, Thermal Hall Effect of Magnons in Collinear Antiferromagnetic Insulators: Signatures of Magnetic and Topological Phase Transitions, *Physical Review Letters* **128**, 117201 (2022).
 - [18] A. V. Chumak, V. I. Vasyuchka, A. A. Serga, and B. Hillebrands, Magnon spintronics, *Nature Physics* **11**, 453–461 (2015).
 - [19] R. Chisnell, J. S. Helton, D. E. Freedman, D. K. Singh, R. I. Bewley, D. G. Nocera, and Y. S. Lee, Topological Magnon Bands in a Kagome Lattice Ferromagnet, *Physical Review Letters* **115**, 147201 (2015).
 - [20] F. Zhu, L. Zhang, X. Wang, F. J. dos Santos, J. Song, T. Mueller, K. Schmalzl, W. F. Schmidt, A. Ivanov, J. T. Park, J. Xu, J. Ma, S. Lounis, S. Blügel, Y. Mokrousov, Y. Su, and T. Brückel, Topological magnon insulators in two-dimensional van der Waals ferromagnets CrSiTe_3 and CrGeTe_3 : Toward intrinsic gap-tunability, *Science Advances* **7**, eabi7532 (2021).
 - [21] B. Perreault, J. Knolle, N. B. Perkins, and F. J. Burnell, Raman scattering in correlated thin films as a probe of chargeless surface states, *Phys. Rev. B* **94**, 060408 (2016).
 - [22] D. Malz, J. Knolle, and A. Nunnenkamp, Topological magnon amplification, *Nature Communications* **10**, 3937 (2019).
 - [23] J. Feldmeier, W. Natori, M. Knap, and J. Knolle, Local probes for charge-neutral edge states in two-dimensional quantum magnets, *Phys. Rev. B* **102**, 134423 (2020).
 - [24] A. Rustagi, I. Bertelli, T. van der Sar, and P. Upadhyaya, Sensing chiral magnetic noise via quantum impurity relaxometry, *Phys. Rev. B* **102**, 220403 (2020).
 - [25] V. Guemard and A. Manchon, Unified formulation of interfacial magnonic pumping from noncollinear magnets, *Phys. Rev. B* **105**, 054433 (2022).
 - [26] B. Hetényi, A. Mook, J. Klinovaja, and D. Loss, Long-distance coupling of spin qubits via topological magnons, *Phys. Rev. B* **106**, 235409 (2022).
 - [27] A. Mitra, A. Corticelli, P. Ribeiro, and P. A. McClarty, Magnon

- interference tunneling spectroscopy as a probe of 2d magnetism, *Phys. Rev. Lett.* **130**, 066701 (2023).
- [28] E. Viñas Boström, T. S. Parvini, J. W. McIver, A. Rubio, S. V. Kusminskiy, and M. A. Sentef, Direct optical probe of magnon topology in two-dimensional quantum magnets, *Phys. Rev. Lett.* **130**, 026701 (2023).
- [29] T. Moriya, Far Infrared Absorption by Two Magnon Excitations in Antiferromagnets, *Journal of the Physical Society of Japan* **21**, 926 (1966).
- [30] T. Moriya, Theory of Absorption and Scattering of Light by Magnetic Crystals, *Journal of Applied Physics* **39**, 1042 (1968).
- [31] T. Moriya, Light Scattering by Two-Magnon Excitations in Ferromagnets, *Progress of Theoretical Physics Supplement* **46**, 121 (1970).
- [32] A. Pimenov, A. A. Mukhin, V. Y. Ivanov, V. D. Travkin, A. M. Balbashov, and A. Loidl, Possible evidence for electromagnons in multiferroic manganites, *Nature Physics* **2**, 97 (2006).
- [33] A. Pimenov, A. Loidl, A. A. Mukhin, V. D. Travkin, V. Yu. Ivanov, and A. M. Balbashov, Terahertz spectroscopy of electromagnons in $\text{Eu}_{1-x}\text{Y}_x\text{MnO}_3$, *Physical Review B* **77**, 014438 (2008).
- [34] N. Kida, Y. Ikebe, Y. Takahashi, J. P. He, Y. Kaneko, Y. Yamasaki, R. Shimano, T. Arima, N. Nagaosa, and Y. Tokura, Electrically driven spin excitation in the ferroelectric magnet DyMnO_3 , *Physical Review B* **78**, 104414 (2008).
- [35] T. Hirose, A. Mook, J. Klinovaja, and D. Loss, Magnetolectric Cavity Magnonics in Skyrmion Crystals, *PRX Quantum* **3**, 040321 (2022).
- [36] J. B. Curtis, A. Grankin, N. R. Poniatowski, V. M. Galitski, P. Narang, and E. Demler, Cavity magnon-polaritons in cuprate parent compounds, *Phys. Rev. Res.* **4**, 013101 (2022).
- [37] Z. Toklikishvili, L. Chotorlishvili, R. Khomeriki, V. Jandieri, and J. Berakdar, Electrically controlled entanglement of cavity photons with electromagnons, *Physical Review B* **107**, 115126 (2023).
- [38] T. Kubacka, J. A. Johnson, M. C. Hoffmann, C. Vicario, S. de Jong, P. Beaud, S. Grübel, S.-W. Huang, L. Huber, L. Patthey, Y.-D. Chuang, J. J. Turner, G. L. Dakovski, W.-S. Lee, M. P. Minitti, W. Schlotter, R. G. Moore, C. P. Hauri, S. M. Koohpayeh, V. Scagnoli, G. Ingold, S. L. Johnson, and U. Staub, Large-Amplitude Spin Dynamics Driven by a THz Pulse in Resonance with an Electromagnon, *Science* **343**, 1333 (2014).
- [39] F. Meier and D. Loss, Magnetization Transport and Quantized Spin Conductance, *Physical Review Letters* **90**, 167204 (2003).
- [40] F. Schütz, M. Kollar, and P. Kopietz, Persistent Spin Currents in Mesoscopic Heisenberg Rings, *Physical Review Letters* **91**, 017205 (2003).
- [41] J. E. Hirsch, Overlooked contribution to the Hall effect in ferromagnetic metals, *Physical Review B* **60**, 14787 (1999).
- [42] V. Hnizdo, Magnetic dipole moment of a moving electric dipole, *American Journal of Physics* **80**, 645 (2012).
- [43] D. J. Griffiths and V. Hnizdo, Mansuripur's paradox, *American Journal of Physics* **81**, 570 (2013).
- [44] H. Katsura, N. Nagaosa, and A. V. Balatsky, Spin Current and Magnetolectric Effect in Noncollinear Magnets, *Physical Review Letters* **95**, 057205 (2005).
- [45] The Supplemental Material includes details about the solution of the Biot-Savart law, linear spin wave theory, magnon expansion of total and local electric polarization operators, estimation of the effective charge, comparison between the VME and KNB mechanisms, derivation for the electric and magnetic susceptibilities as well as additional results for the electric polarization and electric and magnetic susceptibilities for Heisenberg-DMI and Heisenberg-Kitaev models. Moreover, the influence of increased easy-axis anisotropies at the edges and on-site disorder on the local electric polarization is studied. The Supplemental Material cites Refs 5, 7, 8, 39, 40, 44, 48–54, 62–81. URL: [url inserted by publisher].
- [46] L. Chen, J.-H. Chung, M. B. Stone, A. I. Kolesnikov, B. Winn, V. O. Garlea, D. L. Abernathy, B. Gao, M. Augustin, E. J. G. Santos, and P. Dai, Magnetic Field Effect on Topological Spin Excitations in CrI_3 , *Physical Review X* **11**, 031047 (2021).
- [47] Y. Tokura, S. Seki, and N. Nagaosa, Multiferroics of spin origin, *Reports on Progress in Physics* **77**, 076501 (2014).
- [48] T. Holstein and H. Primakoff, Field Dependence of the Intrinsic Domain Magnetization of a Ferromagnet, *Physical Review* **58**, 1098 (1940).
- [49] R. Kubo, Statistical-Mechanical Theory of Irreversible Processes. I. General Theory and Simple Applications to Magnetic and Conduction Problems, *Journal of the Physical Society of Japan* **12**, 570 (1957).
- [50] H. Bruus and K. Flensberg, *Many-Body Quantum Theory in Condensed Matter Physics: An Introduction* (OUP Oxford, 2004).
- [51] S. A. Nikolaev and I. V. Solov'yev, Microscopic theory of electric polarization induced by skyrmionic order in GaV_4S_8 , *Physical Review B* **99**, 100401 (2019).
- [52] A. O. Fumega and J. L. Lado, Moiré-driven multiferroic order in twisted CrCl_3 , CrBr_3 and CrI_3 bilayers, *2D Materials* **10**, 025026 (2023).
- [53] T. Liu and G. Vignale, Electric Control of Spin Currents and Spin-Wave Logic, *Physical Review Letters* **106**, 247203 (2011).
- [54] L. Chen, J.-H. Chung, B. Gao, T. Chen, M. B. Stone, A. I. Kolesnikov, Q. Huang, and P. Dai, Topological Spin Excitations in Honeycomb Ferromagnet CrI_3 , *Physical Review X* **8**, 041028 (2018).
- [55] H. Zhang, C. Xu, C. Carnahan, M. Sretenovic, N. Suri, D. Xiao, and X. Ke, Anomalous Thermal Hall Effect in an Insulating van der Waals Magnet, *Physical Review Letters* **127**, 247202 (2021).
- [56] A. Cvitkovic, N. Ocelic, and R. Hillenbrand, Analytical model for quantitative prediction of material contrasts in scattering-type near-field optical microscopy, *Optics Express* **15**, 8550 (2007).
- [57] A. J. L. Adam, Review of Near-Field Terahertz Measurement Methods and Their Applications, *Journal of Infrared, Millimeter, and Terahertz Waves* **32**, 976 (2011).
- [58] X. Chen, D. Hu, R. Mescall, G. You, D. N. Basov, Q. Dai, and M. Liu, Modern Scattering-Type Scanning Near-Field Optical Microscopy for Advanced Material Research, *Advanced Materials* **31**, 1804774 (2019).
- [59] M. M. Wiecha, A. Soltani, and H. G. Roskos, *Terahertz Nano-Imaging with s-SNOM* (IntechOpen, 2021).
- [60] R. S. Fishman, J. S. Gardner, and S. Okamoto, Orbital Angular Momentum of Magnons in Collinear Magnets, *Physical Review Letters* **129**, 167202 (2022).
- [61] G. Go, D. An, H.-W. Lee, and S. K. Kim, *Intrinsic Magnon Orbital Hall Effect in Honeycomb Antiferromagnets* (2023), arxiv:2303.11687 [cond-mat].
- [62] M. Lein and K. Sato, Krein-Schrödinger formalism of bosonic Bogoliubov-de Gennes and certain classical systems and their topological classification, *Physical Review B* **100**, 075414 (2019).
- [63] J. H. P. Colpa, Diagonalization of the quadratic boson hamiltonian, *Physica A: Statistical Mechanics and its Applications* **93**, 327 (1978).
- [64] V. Cherepanov, I. Kolokolov, and V. L'vov, The saga of YIG: Spectra, thermodynamics, interaction and relaxation of magnons in a complex magnet, *Physics Reports* **229**, 81 (1993).
- [65] S. Weinberg, *The Quantum Theory of Fields: Volume 1: Foundations*, Vol. 1 (Cambridge University Press, Cambridge, 1995).

- [66] J. Habel, A. Mook, J. Willsher, and J. Knolle, [Breakdown of Chiral Edge Modes in Topological Magnon Insulators](#) (2023), [arxiv:2308.03168 \[cond-mat\]](#).
- [67] G. D. Mahan, *Many-Particle Physics* (Springer US, Boston, MA, 2000).
- [68] A. Gurevich and G. Melkov, *Magnetization Oscillations and Waves* (Taylor & Francis, 1996).
- [69] Y. O. Kvashnin, A. Bergman, A. I. Lichtenstein, and M. I. Katsnelson, Relativistic exchange interactions in CrX_3 ($X = \text{Cl, Br, I}$) monolayers, *Physical Review B* **102**, 115162 (2020).
- [70] B. Huang, G. Clark, E. Navarro-Moratalla, D. R. Klein, R. Cheng, K. L. Seyler, D. Zhong, E. Schmidgall, M. A. McGuire, D. H. Cobden, W. Yao, D. Xiao, P. Jarillo-Herrero, and X. Xu, Layer-dependent ferromagnetism in a van der Waals crystal down to the monolayer limit, *Nature* **546**, 270 (2017).
- [71] M. A. McGuire, H. Dixit, V. R. Cooper, and B. C. Sales, Coupling of Crystal Structure and Magnetism in the Layered, Ferromagnetic Insulator CrI_3 , *Chemistry of Materials* **27**, 612 (2015).
- [72] E. Ruff, S. Widmann, P. Lunkenheimer, V. Tsurkan, S. Bordács, I. Kézsmárki, and A. Loidl, Multiferroicity and skyrmions carrying electric polarization in GaV_4S_8 , *Science Advances* **1**, e1500916 (2015).
- [73] T. Kimura, T. Goto, H. Shintani, K. Ishizaka, T. Arima, and Y. Tokura, Magnetic control of ferroelectric polarization, *Nature* **426**, 55 (2003).
- [74] M. Kenzelmann, A. B. Harris, S. Jonas, C. Broholm, J. Schefer, S. B. Kim, C. L. Zhang, S.-W. Cheong, O. P. Vajk, and J. W. Lynn, Magnetic Inversion Symmetry Breaking and Ferroelectricity in TbMnO_3 , *Physical Review Letters* **95**, 087206 (2005).
- [75] J. Chaloupka, G. Jackeli, and G. Khaliullin, Kitaev-Heisenberg Model on a Honeycomb Lattice: Possible Exotic Phases in Iridium Oxides A_2IrO_3 , *Physical Review Letters* **105**, 027204 (2010).
- [76] J. G. Rau, E. K.-H. Lee, and H.-Y. Kee, Generic Spin Model for the Honeycomb Iridates beyond the Kitaev Limit, *Physical Review Letters* **112**, 077204 (2014).
- [77] V. M. Katukuri, S. Nishimoto, V. Yushankhai, A. Stoyanova, H. Kandpal, S. Choi, R. Coldea, I. Rousochatzakis, L. Hozoi, and J. van den Brink, Kitaev interactions between $j = 1/2$ moments in honeycomb Na_2IrO_3 are large and ferromagnetic: Insights from ab initio quantum chemistry calculations, *New Journal of Physics* **16**, 013056 (2014).
- [78] E. Aguilera, R. Jaeschke-Ubiergo, N. Vidal-Silva, L. E. F. F. Torres, and A. S. Nunez, Topological magnonics in the two-dimensional van der Waals magnet CrI_3 , *Physical Review B* **102**, 024409 (2020).
- [79] A. Kitaev, Anyons in an exactly solved model and beyond, *Annals of Physics* **321**, 2 (2006), [arxiv:cond-mat/0506438](#).
- [80] P. A. McClarty, X.-Y. Dong, M. Gohlke, J. G. Rau, F. Pollmann, R. Moessner, and K. Penc, Topological magnons in Kitaev magnets at high fields, *Physical Review B* **98**, 060404 (2018).
- [81] A. Mook, S. A. Díaz, J. Klinovaja, and D. Loss, Chiral hinge magnons in second-order topological magnon insulators, *Physical Review B* **104**, 024406 (2021).

CONCLUSION AND OUTLOOK

In this thesis, multiple routes for the detection of topological magnons have been studied theoretically. Linear spin wave theory, the second quantization of phonons, and linear response theory have been applied to correlate microscopic properties of the bosonic quasiparticles of magnetic insulators with their macroscopic observables in equilibrium and nonequilibrium. This includes magnetic and electrical properties as well as the thermal transport in ferromagnets, collinear and noncollinear antiferromagnets.

For the detectability of topological magnons, the following conclusions can be drawn.

- The thermal HALL effect can exist both in topologically trivial and nontrivial phases and does not indicate topological magnons. However, *transitions* between trivial and nontrivial phases or between different nontrivial phases have been found to imprint characteristic signatures in the thermal HALL effect. The topological phase transitions can be distinguished from magnetic ones by tuning the thermal HALL effect sensitive to either one in collinear antiferromagnets. In addition, combining transverse heat transport measurements with equilibrium measurements such as the heat capacity supports the search of topological phase transitions.
- Magnon polarons may play an important role in the thermal HALL effect in the collinear antiferromagnet $\text{Na}_2\text{Co}_2\text{TeO}_6$. While a pure magnon transport theory is unable to explain the experimental data qualitatively, a theory that allows for a hybridization of magnons and phonons is able to install an agreement between theory and experiment. The theory demonstrates that the hybridization can reverse the sign of the thermal HALL effect and increase its magnitude. Thus, topological phases of magnons can be obscured in the heat transport properties by magnon polarons.
- Despite being charge-neutral, (topological) magnons were shown to possess an electric dipole that manifests in the electric polarization in equilibrium and the electric susceptibility in nonequilibrium. The electric dipole moment imparted by the spin current mechanism is locked to the group velocity and, hence, is coupled to the chirality of the topological chiral edge magnons. Topological magnon insulators exhibit an electric edge polarization that partially stems from the topological magnons. On the other hand, detailed microscopic calculations have revealed that the main contribution is of nontopological origin.

More promising for the detection of topological magnons are one-magnon processes in the electric absorption. While magnetic fields are unable to excite topological magnons resonantly, external electric fields directly couple to the in-gap modes allowing for their activation. Microscopic calculations in nanoribbons and flakes exposed the in-gap peaks of topological origin in the electric absorption spectrum at THz frequencies. In short, topological magnons are electromagnons.

7 Conclusion and Outlook

The work shows that resonant probes of topological magnons are most promising for their detection, one of which is the one-magnon electrical absorption. With the help of inelastic neutron scattering band gaps in the bulk magnon spectrum can be identified, which can be checked for in-gap states by THz spectroscopy, which are not visible to neutrons. These results await experimental confirmation.

Future theoretical research on topological electromagnons could address other magnetoelectric mechanisms and identify candidate materials for topological magnon insulators with strong magnetoelectric effects. One shortcoming of the one-magnon absorption is the need of topological magnons with long wavelengths. Even though small flakes lift this requirement partially, local geometries could be explored in the future. Instead of homogeneously exciting all spins in the sample with electrical fields, near-field techniques such as scattering-type scanning near-field optical microscopy motivate the development of a theory of local electrical response properties.

Since heat transport measurements on insulators are gaining more experimental attention, a theoretical study of regimes in which topological magnons may be relevant to the thermal transport constitutes another possible future research direction. Most theoretical results rely on noninteracting magnons in clean crystals neglecting magnon-magnon, magnon-impurity, and magnon-phonon scattering. Applying an interacting transport theory could clarify if topological magnons can dominate the transport properties because of their proposed immunity against backscattering.

LIST OF PUBLICATIONS

Publications Appearing in This Work

- [RN1] [R. R. Neumann](#), A. Mook, J. Henk, and I. Mertig, “Orbital Magnetic Moment of Magnons,” [Physical Review Letters](#) **125**, 117209 (2020).
- [RN2] [R. R. Neumann](#), A. Mook, J. Henk, and I. Mertig, “Thermal Hall Effect of Magnons in Collinear Antiferromagnetic Insulators: Signatures of Magnetic and Topological Phase Transitions,” [Physical Review Letters](#) **128**, 117201 (2022).
- [RN3] N. Li*, [R. R. Neumann](#)*, S. K. Guang*, Q. Huang, J. Liu, K. Xia, X. Y. Yue, Y. Sun, Y. Y. Wang, Q. J. Li, Y. Jiang, J. Fang, Z. Jiang, X. Zhao, A. Mook, J. Henk, I. Mertig, H. D. Zhou, and X. F. Sun, “Magnon-polaron driven thermal Hall effect in a Heisenberg-Kitaev antiferromagnet,” [Physical Review B](#) **108**, L140402 (2023).
- [RN4] [R. R. Neumann](#), J. Henk, I. Mertig, and A. Mook, *Electrical Activity of Topological Chiral Edge Magnons*, Dec. 2023, [arXiv:2312.12316 \[cond-mat\]](#).

* These authors contributed equally.

Publications Not Appearing in This Work

- [RN5] A. Mook, [R. R. Neumann](#), J. Henk, and I. Mertig, “Spin Seebeck and spin Nernst effects of magnons in noncollinear antiferromagnetic insulators,” [Physical Review B](#) **100**, 100401 (2019).
- [RN6] A. Mook, [R. R. Neumann](#), A. Johansson, J. Henk, and I. Mertig, “Origin of the magnetic spin Hall effect: Spin current vorticity in the Fermi sea,” [Physical Review Research](#) **2**, 023065 (2020).
- [RN7] B. K. Hazra, B. Pal, J.-C. Jeon, [R. R. Neumann](#), B. Göbel, B. Grover, H. Deniz, A. Styervoyedov, H. Meyerheim, I. Mertig, S.-H. Yang, and S. S. P. Parkin, “Generation of out-of-plane polarized spin current by spin swapping,” [Nature Communications](#) **14**, 4549 (2023).
- [RN8] B. H. Rimmler, B. K. Hazra, B. Pal, K. Mohseni, J. M. Taylor, A. Bedoya-Pinto, H. Deniz, M. Tangi, I. Kostanovskiy, C. Luo, [R. R. Neumann](#), A. Ernst, F. Radu, I. Mertig, H. L. Meyerheim, and S. S. P. Parkin, “Atomic Displacements Enabling the Observation of the Anomalous Hall Effect in a Non-Collinear Antiferromagnet,” [Advanced Materials](#) **35**, 2209616 (2023).

BIBLIOGRAPHY

- [1] J. M. Ziman, *Electrons and Phonons: The Theory of Transport Phenomena in Solids* (Oxford University Press, Feb. 2001).
- [2] R. Gross and A. Marx, *Festkörperphysik* (De Gruyter, Jan. 2018).
- [3] M. Z. Hasan and C. L. Kane, “Colloquium: Topological insulators,” *Reviews of Modern Physics* **82**, 3045–3067 (2010).
- [4] M. Z. Hasan and J. E. Moore, “Three-Dimensional Topological Insulators,” *Annual Review of Condensed Matter Physics* **2**, 55–78 (2011).
- [5] X.-L. Qi and S.-C. Zhang, “Topological insulators and superconductors,” *Reviews of Modern Physics* **83**, 1057–1110 (2011).
- [6] K. v. Klitzing, G. Dorda, and M. Pepper, “New Method for High-Accuracy Determination of the Fine-Structure Constant Based on Quantized Hall Resistance,” *Physical Review Letters* **45**, 494–497 (1980).
- [7] D. J. Thouless, M. Kohmoto, M. P. Nightingale, and M. den Nijs, “Quantized Hall Conductance in a Two-Dimensional Periodic Potential,” *Physical Review Letters* **49**, 405–408 (1982).
- [8] Y. Hatsugai, “Chern number and edge states in the integer quantum Hall effect,” *Physical Review Letters* **71**, 3697–3700 (1993).
- [9] Y. Hatsugai, “Edge states in the integer quantum Hall effect and the Riemann surface of the Bloch function,” *Physical Review B* **48**, 11851–11862 (1993).
- [10] F. Bloch, “Zur Theorie des Ferromagnetismus,” *Zeitschrift für Physik* **61**, 206–219 (1930).
- [11] T. Holstein and H. Primakoff, “Field Dependence of the Intrinsic Domain Magnetization of a Ferromagnet,” *Physical Review* **58**, 1098–1113 (1940).
- [12] F. J. Dyson, “General Theory of Spin-Wave Interactions,” *Physical Review* **102**, 1217–1230 (1956).
- [13] R. Matsumoto and S. Murakami, “Theoretical Prediction of a Rotating Magnon Wave Packet in Ferromagnets,” *Physical Review Letters* **106**, 197202 (2011).
- [14] L. Zhang, J. Ren, J.-S. Wang, and B. Li, “Topological magnon insulator in insulating ferromagnet,” *Physical Review B* **87**, 144101 (2013).
- [15] R. Shindou, R. Matsumoto, S. Murakami, and J.-i. Ohe, “Topological chiral magnonic edge mode in a magnonic crystal,” *Physical Review B* **87**, 174427 (2013).
- [16] A. Mook, J. Henk, and I. Mertig, “Magnon Hall effect and topology in kagome lattices: A theoretical investigation,” *Physical Review B* **89**, 134409 (2014).
- [17] A. Mook, J. Henk, and I. Mertig, “Edge states in topological magnon insulators,” *Physical Review B* **90**, 024412 (2014).

- [18] S. A. Owerre, “A first theoretical realization of honeycomb topological magnon insulator,” *Journal of Physics: Condensed Matter* **28**, 386001 (2016).
- [19] S. K. Kim, H. Ochoa, R. Zarzuela, and Y. Tserkovnyak, “Realization of the Haldane-Kane-Mele Model in a System of Localized Spins,” *Physical Review Letters* **117**, 227201 (2016).
- [20] K. Nakata, J. Klinovaja, and D. Loss, “Magnonic quantum Hall effect and Wiedemann-Franz law,” *Physical Review B* **95**, 125429 (2017).
- [21] A. Mook, K. Plekhanov, J. Klinovaja, and D. Loss, “Interaction-Stabilized Topological Magnon Insulator in Ferromagnets,” *Physical Review X* **11**, 021061 (2021).
- [22] D. Malz, J. Knolle, and A. Nunnenkamp, “Topological magnon amplification,” *Nature Communications* **10**, 3937 (2019).
- [23] “Magnetic neutron scattering,” in *Modern Techniques for Characterizing Magnetic Materials*, edited by Y. Zhu (Springer US, Boston, MA, 2005), pp. 3–64.
- [24] R. Chisnell, J. S. Helton, D. E. Freedman, D. K. Singh, R. I. Bewley, D. G. Nocera, and Y. S. Lee, “Topological Magnon Bands in a Kagome Lattice Ferromagnet,” *Physical Review Letters* **115**, 147201 (2015).
- [25] F. Zhu, L. Zhang, X. Wang, F. J. dos Santos, J. Song, T. Mueller, K. Schmalzl, W. F. Schmidt, A. Ivanov, J. T. Park, J. Xu, J. Ma, S. Lounis, S. Blügel, Y. Mokrousov, Y. Su, and T. Brückel, “Topological magnon insulators in two-dimensional van der Waals ferromagnets CrSiTe₃ and CrGeTe₃: Toward intrinsic gap-tunability,” *Science Advances* **7**, eabi7532 (2021).
- [26] H. Ibach and H. Lüth, *Festkörperphysik*, Springer-Lehrbuch (Springer, Berlin, Heidelberg, 2009).
- [27] M. Born and R. Oppenheimer, “Zur Quantentheorie der Molekeln,” *Annalen der Physik* **389**, 457–484 (1927).
- [28] J. M. Ziman, *Prinzipien der Festkörpertheorie*, 2nd ed. (Akademie-Verlag, Berlin, 1974).
- [29] J. Callaway, *Quantum Theory of the Solid State* (Elsevier Science & Technology, Saint Louis, UNITED STATES, 1991).
- [30] E. K. U. Gross, E. Runge, and O. Heinonen, *Many Particle Theory* (Institute of Physics Publishing, Bristol, May 1992).
- [31] E. J. Heller, “The Semiclassical Way to Dynamics and Spectroscopy,” in *The Semiclassical Way to Dynamics and Spectroscopy* (Princeton University Press, June 2018).
- [32] N. W. Ashcroft and N. D. Mermin, *Festkörperphysik* (Oldenbourg Wissenschaftsverlag, Jan. 2001).
- [33] C. Kittel, *Introduction to solid state physics*, 8th ed (Wiley, Hoboken, NJ, 2005).
- [34] J. Goldstone, A. Salam, and S. Weinberg, “Broken Symmetries,” *Physical Review* **127**, 965–970 (1962).
- [35] H. B. Nielsen and S. Chadha, “On how to count Goldstone bosons,” *Nuclear Physics B* **105**, 445–453 (1976).

- [36] T. Schäfer, D. T. Son, M. A. Stephanov, D. Toublan, and J. J. M. Verbaarschot, “Kaon condensation and Goldstone’s theorem,” [Physics Letters B](#) **522**, 67–75 (2001).
- [37] H. Watanabe and H. Murayama, “Unified Description of Nambu-Goldstone Bosons without Lorentz Invariance,” [Physical Review Letters](#) **108**, 251602 (2012).
- [38] L. Sheng, D. N. Sheng, and C. S. Ting, “Theory of the Phonon Hall Effect in Paramagnetic Dielectrics,” [Physical Review Letters](#) **96**, 155901 (2006).
- [39] G. D. Mahan, *Many-Particle Physics* (Springer US, Boston, MA, 2000).
- [40] H. Bruus and K. Flensberg, *Many-Body Quantum Theory in Condensed Matter Physics: An Introduction* (OUP Oxford, Sept. 2004).
- [41] D. J. Griffiths, *Quantenmechanik, 2.*, aktualisierte Auflage (Pearson Studium, München, 2012).
- [42] W. Nolting and A. Ramakanth, *Quantum Theory of Magnetism* (Springer, Berlin, Heidelberg, 2009).
- [43] I. Mazin and The PRX Editors, “Editorial: Altermagnetism—A New Punch Line of Fundamental Magnetism,” [Physical Review X](#) **12**, 040002 (2022).
- [44] L. Néel, “Magnetism and Local Molecular Field,” [Science](#) **174**, 985–992 (1971).
- [45] L. Šmejkal, J. Sinova, and T. Jungwirth, “Emerging Research Landscape of Altermagnetism,” [Physical Review X](#) **12**, 040501 (2022).
- [46] S.-W. Cheong and X. Xu, “Magnetic chirality,” [npj Quantum Materials](#) **7**, 1–6 (2022).
- [47] W. Heisenberg, “Mehrkörperproblem und Resonanz in der Quantenmechanik,” [Zeitschrift für Physik](#) **38**, 411–426 (1926).
- [48] J. Hubbard and B. H. Flowers, “Electron correlations in narrow energy bands,” [Proceedings of the Royal Society of London. Series A. Mathematical and Physical Sciences](#) **276**, 238–257 (1963).
- [49] E. C. Stoner, “Collective electron ferromagnetism,” [Proceedings of the Royal Society of London. Series A. Mathematical and Physical Sciences](#) **165**, 372–414 (1938).
- [50] E. C. Stoner, “Collective electron ferromagnetism II. Energy and specific heat,” [Proceedings of the Royal Society of London. Series A. Mathematical and Physical Sciences](#) **169**, 339–371 (1939).
- [51] C. Zener, “Interaction Between the d Shells in the Transition Metals,” [Physical Review](#) **81**, 440–444 (1951).
- [52] T. Kasuya, “A Theory of Metallic Ferro- and Antiferromagnetism on Zener’s Model,” [Progress of Theoretical Physics](#) **16**, 45–57 (1956).
- [53] J. Kondo, “Resistance Minimum in Dilute Magnetic Alloys,” [Progress of Theoretical Physics](#) **32**, 37–49 (1964).
- [54] P. Mohn, *Magnetism in the Solid State*, 1st ed., Vol. 134, Solid-State Sciences (Springer-Verlag, Berlin, Heidelberg, June 2006).

- [55] W. Nolting, *Quantentheorie des Magnetismus: Teil 1: Grundlagen* (Vieweg+Teubner Verlag, Wiesbaden, 1986).
- [56] P. Fröbrich and P. J. Kuntz, “Many-body Green’s function theory of Heisenberg films,” *Physics Reports* **432**, 223–304 (2006).
- [57] W. Pauli, “The Connection Between Spin and Statistics,” *Physical Review* **58**, 716–722 (1940).
- [58] H. Haken and H. C. Wolf, *Atom- und Quantenphysik*, Springer-Lehrbuch (Springer, Berlin, Heidelberg, 2004).
- [59] F. Hund, “Zur Deutung der Molekelspektren. I,” *Zeitschrift für Physik* **40**, 742–764 (1927).
- [60] F. Hund, “Zur Deutung der Molekelspektren. II,” *Zeitschrift für Physik* **42**, 93–120 (1927).
- [61] E. Rastelli, *Statistical Mechanics of Magnetic Excitations: From Spin Waves to Stripes and Checkerboards*, Vol. 18, Series on Advances in Statistical Mechanics (WORLD SCIENTIFIC, Mar. 2013).
- [62] T. Yildirim, A. B. Harris, A. Aharony, and O. Entin-Wohlman, “Anisotropic spin Hamiltonians due to spin-orbit and Coulomb exchange interactions,” *Physical Review B* **52**, 10239–10267 (1995).
- [63] R. F. L. Evans, W. J. Fan, P. Chureemart, T. A. Ostler, M. O. A. Ellis, and R. W. Chantrell, “Atomistic spin model simulations of magnetic nanomaterials,” *Journal of Physics: Condensed Matter* **26**, 103202 (2014).
- [64] S. Toth and B. Lake, “Linear spin wave theory for single-Q incommensurate magnetic structures,” *Journal of Physics: Condensed Matter* **27**, 166002 (2015).
- [65] A. Mook, “Topological magnon materials and transverse magnon transport,” PhD thesis (Martin-Luther-Universität Halle-Wittenberg, Halle, Oct. 2017).
- [66] B. D. Cullity and C. D. Graham, *Introduction to Magnetic Materials* (John Wiley & Sons, Feb. 2008).
- [67] E. Ising, “Beitrag zur Theorie des Ferromagnetismus,” *Zeitschrift für Physik* **31**, 253–258 (1925).
- [68] I. Dzyaloshinsky, “A thermodynamic theory of “weak” ferromagnetism of antiferromagnetics,” *Journal of Physics and Chemistry of Solids* **4**, 241–255 (1958).
- [69] T. Moriya, “Anisotropic Superexchange Interaction and Weak Ferromagnetism,” *Physical Review* **120**, 91–98 (1960).
- [70] A. Kitaev, “Anyons in an exactly solved model and beyond,” *Annals of Physics* **321**, 2–111 (2006), [arXiv:cond-mat/0506438](https://arxiv.org/abs/cond-mat/0506438).
- [71] V. M. Katukuri, S. Nishimoto, V. Yushankhai, A. Stoyanova, H. Kandpal, S. Choi, R. Coldea, I. Rousochatzakis, L. Hozoi, and J. van den Brink, “Kitaev interactions between $j = 1/2$ moments in honeycomb Na₂IrO₃ are large and ferromagnetic: insights from ab initio quantum chemistry calculations,” *New Journal of Physics* **16**, 013056 (2014).
- [72] J. G. Rau, E. K.-H. Lee, and H.-Y. Kee, “Generic Spin Model for the Honeycomb Iridates beyond the Kitaev Limit,” *Physical Review Letters* **112**, 077204 (2014).

- [73] J. Chaloupka and G. Khaliullin, “Hidden symmetries of the extended Kitaev-Heisenberg model: Implications for the honeycomb-lattice iridates $A_2\text{IrO}_3$,” *Physical Review B* **92**, 024413 (2015).
- [74] P. A. McClarty, X.-Y. Dong, M. Gohlke, J. G. Rau, F. Pollmann, R. Moessner, and K. Penc, “Topological magnons in Kitaev magnets at high fields,” *Physical Review B* **98**, 060404 (2018).
- [75] M. Maksymenko, V. R. Chandra, and R. Moessner, “Classical dipoles on the kagome lattice,” *Physical Review B* **91**, 184407 (2015).
- [76] D. J. Griffiths, *Elektrodynamik: eine Einführung*, trans. by G. Radons, 4., aktualisierte Auflage, ph - Physik (Pearson, Hallbergmoos, 2018).
- [77] L. D. Landau and E. Lifshitz, “On the theory of the dispersion of magnetic permeability in ferromagnetic bodies,” *Phys. Z. Sowjet.* **8**, 153 (1935).
- [78] T. Gilbert, “A Phenomenological Theory of Damping in Ferromagnetic Materials,” *IEEE Transactions on Magnetics* **40**, 3443–3449 (2004).
- [79] W. Brown, “Thermal fluctuation of fine ferromagnetic particles,” *IEEE Transactions on Magnetics* **15**, 1196–1208 (1979).
- [80] A. Lyberatos, D. V. Berkov, and R. W. Chantrell, “A method for the numerical simulation of the thermal magnetization fluctuations in micromagnetics,” *Journal of Physics: Condensed Matter* **5**, 8911 (1993).
- [81] J. L. García-Palacios and F. J. Lázaro, “Langevin-dynamics study of the dynamical properties of small magnetic particles,” *Physical Review B* **58**, 14937–14958 (1998).
- [82] U. Nowak, O. N. Mryasov, R. Wieser, K. Guslienko, and R. W. Chantrell, “Spin dynamics of magnetic nanoparticles: Beyond Brown’s theory,” *Physical Review B* **72**, 172410 (2005).
- [83] J. G. Rau, P. A. McClarty, and R. Moessner, “Pseudo-Goldstone Gaps and Order-by-Quantum Disorder in Frustrated Magnets,” *Physical Review Letters* **121**, 237201 (2018).
- [84] J. H. P. Colpa, “Diagonalization of the quadratic boson hamiltonian,” *Physica A: Statistical Mechanics and its Applications* **93**, 327–353 (1978).
- [85] R. Kubo, “The Spin-Wave Theory of Antiferromagnetics,” *Physical Review* **87**, 568–580 (1952).
- [86] J. A. Eisele and F. Keffer, “Effects of Anisotropy on Thermodynamic Properties of Antiferromagnets,” *Physical Review* **96**, 929–933 (1954).
- [87] N. Okuma, “Magnon Spin-Momentum Locking: Various Spin Vortices and Dirac magnons in Noncollinear Antiferromagnets,” *Physical Review Letters* **119**, 107205 (2017).
- [88] N. D. Mermin and H. Wagner, “Absence of Ferromagnetism or Antiferromagnetism in One- or Two-Dimensional Isotropic Heisenberg Models,” *Physical Review Letters* **17**, 1133–1136 (1966).
- [89] C. Kittel, “Model of Exchange-Inversion Magnetization,” *Physical Review* **120**, 335–342 (1960).

- [90] S. Park and B.-J. Yang, “Topological magnetoelastic excitations in noncollinear antiferromagnets,” *Physical Review B* **99**, 174435 (2019).
- [91] S. Li and S. Okamoto, “Thermal Hall effect in the Kitaev-Heisenberg system with spin-phonon coupling,” *Physical Review B* **106**, 024413 (2022).
- [92] S. Li, H. Yan, and A. H. Nevidomskyy, *Magnons, Phonons, and Thermal Hall Effect in Candidate Kitaev Magnet α -RuCl₃*, Jan. 2023, [arXiv:2301.07401 \[cond-mat\]](#).
- [93] R. Takahashi and N. Nagaosa, “Berry Curvature in Magnon-Phonon Hybrid Systems,” *Physical Review Letters* **117**, 217205 (2016).
- [94] E. Thingstad, A. Kamra, A. Brataas, and A. Sudbø, “Chiral Phonon Transport Induced by Topological Magnons,” *Physical Review Letters* **122**, 107201 (2019).
- [95] G. Go, S. K. Kim, and K.-J. Lee, “Topological Magnon-Phonon Hybrid Excitations in Two-Dimensional Ferromagnets with Tunable Chern Numbers,” *Physical Review Letters* **123**, 237207 (2019).
- [96] S. Zhang, G. Go, K.-J. Lee, and S. K. Kim, “SU(3) Topology of Magnon-Phonon Hybridization in 2D Antiferromagnets,” *Physical Review Letters* **124**, 147204 (2020).
- [97] N. Bazazzadeh, M. Hamdi, S. Park, A. Khavasi, S. M. Mohseni, and A. Sadeghi, “Magnetoelastic coupling enabled tunability of magnon spin current generation in two-dimensional antiferromagnets,” *Physical Review B* **104**, L180402 (2021).
- [98] H. Zhang, C. Xu, C. Carnahan, M. Sretenovic, N. Suri, D. Xiao, and X. Ke, “Anomalous Thermal Hall Effect in an Insulating van der Waals Magnet,” *Physical Review Letters* **127**, 247202 (2021).
- [99] C. Xu, C. Carnahan, H. Zhang, M. Sretenovic, P. Zhang, D. Xiao, and X. Ke, “Thermal Hall effect in a van der Waals triangular magnet FeCl₂,” *Physical Review B* **107**, L060404 (2023).
- [100] D.-Q. To, C. Y. Ameyaw, A. Suresh, S. Bhatt, M. J. H. Ku, M. B. Jungfleisch, J. Q. Xiao, J. M. O. Zide, B. K. Nikolic, and M. F. Doty, *Giant spin Nernst effect in a two-dimensional antiferromagnet due to magnetoelastic coupling-induced gaps and interband transitions between magnon-like bands*, May 2023, [arXiv:2305.06020 \[cond-mat\]](#).
- [101] Z.-X. Lin and S. Zhang, *Topological magnon-polaron transport in a bilayer van der Waals magnet*, Dec. 2023, [arXiv:2312.07463 \[cond-mat, physics:quant-ph\]](#).
- [102] J. N. Kløgetvedt and A. Qaiumzadeh, “Tunable topological magnon-polaron states and intrinsic anomalous Hall phenomena in two-dimensional ferromagnetic insulators,” *Physical Review B* **108**, 224424 (2023).
- [103] X. Zhang, Y. Zhang, S. Okamoto, and D. Xiao, “Thermal Hall Effect Induced by Magnon-Phonon Interactions,” *Physical Review Letters* **123**, 167202 (2019).
- [104] S. Park, N. Nagaosa, and B.-J. Yang, “Thermal Hall Effect, Spin Nernst Effect, and Spin Density Induced by a Thermal Gradient in Collinear Ferrimagnets from Magnon-Phonon Interaction,” *Nano Letters* **20**, 2741–2746 (2020).

- [105] F. Foggetti and S. Artyukhin, “Soft magnon contributions to dielectric constant in spiral magnets with domain walls,” (2020).
- [106] B. Sheikhi, M. Kargarian, and A. Langari, “Hybrid topological magnon-phonon modes in ferromagnetic honeycomb and kagome lattices,” [Physical Review B **104**, 045139 \(2021\)](#).
- [107] B. Ma and G. A. Fiete, “Antiferromagnetic insulators with tunable magnon-polaron Chern numbers induced by in-plane optical phonons,” [Physical Review B **105**, L100402 \(2022\)](#).
- [108] S. Bao, Z.-L. Gu, Y. Shangguan, Z. Huang, J. Liao, X. Zhao, B. Zhang, Z.-Y. Dong, W. Wang, R. Kajimoto, M. Nakamura, T. Fennell, S.-L. Yu, J.-X. Li, and J. Wen, “Direct observation of topological magnon polarons in a multiferroic material,” [Nature Communications **14**, 6093 \(2023\)](#).
- [109] R. Schmidt and P. W. Brouwer, “Theory of the low-temperature longitudinal spin Seebeck effect,” [Physical Review B **103**, 014412 \(2021\)](#).
- [110] J. Cui, E. V. Boström, M. Ozerov, F. Wu, Q. Jiang, J.-H. Chu, C. Li, F. Liu, X. Xu, A. Rubio, and Q. Zhang, “Chirality selective magnon-phonon hybridization and magnon-induced chiral phonons in a layered zigzag antiferromagnet,” [Nature Communications **14**, 3396 \(2023\)](#).
- [111] J. Luo, S. Li, Z. Ye, R. Xu, H. Yan, J. Zhang, G. Ye, L. Chen, D. Hu, X. Teng, W. A. Smith, B. I. Yakobson, P. Dai, A. H. Nevidomskyy, R. He, and H. Zhu, “Evidence for Topological Magnon–Phonon Hybridization in a 2D Antiferromagnet down to the Monolayer Limit,” [Nano Letters, **10.1021/acs.nanolett.3c00351** \(2023\)](#).
- [112] N. Vidal-Silva, E. Aguilera, A. Roldán-Molina, R. A. Duine, and A. S. Nunez, “Magnon polarons induced by a magnetic field gradient,” [Physical Review B **102**, 104411 \(2020\)](#).
- [113] S. G. Bahoosh, J. M. Wesselinowa, and S. Trimper, “The magnetoelectric effect and double-perovskite structure,” [physica status solidi \(b\) **249**, 1602–1606 \(2012\)](#).
- [114] S. G. Bahoosh, J. M. Wesselinowa, and S. Trimper, “Phonon excitations and magnetoelectric coupling in multiferroic RMn₂O₅,” [The European Physical Journal B **86**, 201 \(2013\)](#).
- [115] W. Nolting, *Theoretical Physics 7* (Springer International Publishing, Cham, 2017).
- [116] M. V. Berry, “Quantal phase factors accompanying adiabatic changes,” [Proceedings of the Royal Society of London. A. Mathematical and Physical Sciences, **10.1098/rspa.1984.0023** \(1984\)](#).
- [117] J. K. Asbóth, L. Oroszlány, and A. Pályi, *A Short Course on Topological Insulators*, Vol. 919, Lecture Notes in Physics (Springer International Publishing, Cham, 2016).
- [118] N. Nagaosa and Y. Tokura, “Emergent electromagnetism in solids,” [Physica Scripta **2012**, 014020 \(2012\)](#).
- [119] F. Wilczek and A. Shapere, *Geometric Phases in Physics*, Vol. 5, Advanced Series in Mathematical Physics (WORLD SCIENTIFIC, July 1989).

- [120] F. Pientka, “Geometrical Concepts in the Band Theory of Solids,” Diploma Thesis (Martin-Luther-Universität Halle-Wittenberg, Halle (Saale), Nov. 2010).
- [121] J. Zak, “Berry’s phase for energy bands in solids,” *Physical Review Letters* **62**, 2747–2750 (1989).
- [122] D. Xiao, M.-C. Chang, and Q. Niu, “Berry phase effects on electronic properties,” *Reviews of Modern Physics* **82**, 1959–2007 (2010).
- [123] D. R. Hartree, “The Wave Mechanics of an Atom with a Non-Coulomb Central Field. Part I. Theory and Methods,” *Mathematical Proceedings of the Cambridge Philosophical Society* **24**, 89–110 (1928).
- [124] D. R. Hartree, “The Wave Mechanics of an Atom with a Non-Coulomb Central Field. Part II. Some Results and Discussion,” *Mathematical Proceedings of the Cambridge Philosophical Society* **24**, 111–132 (1928).
- [125] J. A. Gaunt, “A Theory of Hartree’s Atomic Fields,” *Mathematical Proceedings of the Cambridge Philosophical Society* **24**, 328–342 (1928).
- [126] W. Kohn and L. J. Sham, “Self-Consistent Equations Including Exchange and Correlation Effects,” *Physical Review* **140**, A1133–A1138 (1965).
- [127] F. Bloch, “Über die Quantenmechanik der Elektronen in Kristallgittern,” *Zeitschrift für Physik* **52**, 555–600 (1929).
- [128] M.-C. Chang and Q. Niu, “Berry Phase, Hyperorbits, and the Hofstadter Spectrum,” *Physical Review Letters* **75**, 1348–1351 (1995).
- [129] M.-C. Chang and Q. Niu, “Berry phase, hyperorbits, and the Hofstadter spectrum: Semiclassical dynamics in magnetic Bloch bands,” *Physical Review B* **53**, 7010–7023 (1996).
- [130] R. Matsumoto, R. Shindou, and S. Murakami, “Thermal Hall effect of magnons in magnets with dipolar interaction,” *Physical Review B* **89**, 054420 (2014).
- [131] A. Mook, J. Henk, and I. Mertig, “Thermal Hall effect in noncollinear coplanar insulating antiferromagnets,” *Physical Review B* **99**, 014427 (2019).
- [132] J. Cayssol and J. N. Fuchs, “Topological and geometrical aspects of band theory,” *Journal of Physics: Materials* **4**, 034007 (2021).
- [133] T. Fukui, Y. Hatsugai, and H. Suzuki, “Chern Numbers in Discretized Brillouin Zone: Efficient Method of Computing (Spin) Hall Conductances,” *Journal of the Physical Society of Japan* **74**, 1674–1677 (2005).
- [134] M. Kohmoto, “Topological invariant and the quantization of the Hall conductance,” *Annals of Physics* **160**, 343–354 (1985).
- [135] F. D. M. Haldane, “Model for a Quantum Hall Effect without Landau Levels: Condensed-Matter Realization of the ”Parity Anomaly”,” *Physical Review Letters* **61**, 2015–2018 (1988).
- [136] J. Fransson, A. M. Black-Schaffer, and A. V. Balatsky, “Magnon Dirac materials,” *Physical Review B* **94**, 075401 (2016).

- [137] D. Carpentier, “Topology of Bands in Solids: From Insulators to Dirac Matter,” in *Dirac Matter*, edited by B. Duplantier, V. Rivasseau, and J.-N. Fuchs, Progress in Mathematical Physics (Springer International Publishing, Cham, Jan. 2017), pp. 95–129.
- [138] A. S. T. Pires, *A Brief Introduction to Topology and Differential Geometry in Condensed Matter Physics* (Morgan & Claypool Publishers, 2019).
- [139] F. Schwabl, *Statistische Mechanik*, Springer-Lehrbuch (Springer, Berlin, Heidelberg, 2006).
- [140] R. Kubo, “Statistical-Mechanical Theory of Irreversible Processes. I. General Theory and Simple Applications to Magnetic and Conduction Problems,” *Journal of the Physical Society of Japan* **12**, 570–586 (1957).
- [141] R. Kubo, “The fluctuation-dissipation theorem,” *Reports on Progress in Physics* **29**, 255 (1966).
- [142] H. B. Callen and T. A. Welton, “Irreversibility and Generalized Noise,” *Physical Review* **83**, 34–40 (1951).
- [143] J. M. Luttinger, “Theory of Thermal Transport Coefficients,” *Physical Review* **135**, A1505–A1514 (1964).
- [144] T. Qin, Q. Niu, and J. Shi, “Energy Magnetization and the Thermal Hall Effect,” *Physical Review Letters* **107**, 236601 (2011).
- [145] V. A. Zyuzin and A. A. Kovalev, “Magnon Spin Nernst Effect in Antiferromagnets,” *Physical Review Letters* **117**, 217203 (2016).
- [146] B. Li, A. Mook, A. Raeliarijaona, and A. A. Kovalev, “Magnonic analog of the Edelstein effect in antiferromagnetic insulators,” *Physical Review B* **101**, 024427 (2020).
- [147] L. Smrcka and P. Streda, “Transport coefficients in strong magnetic fields,” *Journal of Physics C: Solid State Physics* **10**, 2153 (1977).
- [148] N. R. Cooper, B. I. Halperin, and I. M. Ruzin, “Thermoelectric response of an interacting two-dimensional electron gas in a quantizing magnetic field,” *Physical Review B* **55**, 2344–2359 (1997).
- [149] D. Bohm, “Note on a Theorem of Bloch Concerning Possible Causes of Superconductivity,” *Physical Review* **75**, 502–504 (1949).
- [150] N. Yamamoto, “Generalized Bloch theorem and chiral transport phenomena,” *Physical Review D* **92**, 085011 (2015).
- [151] A. Kapustin and L. Spodyneiko, “Absence of Energy Currents in an Equilibrium State and Chiral Anomalies,” *Physical Review Letters* **123**, 060601 (2019).
- [152] H. Watanabe, “A Proof of the Bloch Theorem for Lattice Models,” *Journal of Statistical Physics* **177**, 717–726 (2019).
- [153] S. Bachmann and M. Fraas, “On the absence of stationary currents,” *Reviews in Mathematical Physics* **33**, 2060011 (2021).
- [154] H. Kobayashi and H. Watanabe, “Vanishing and Nonvanishing Persistent Currents of Various Conserved Quantities,” *Physical Review Letters* **129**, 176601 (2022).

- [155] Y. Tokura, S. Seki, and N. Nagaosa, “Multiferroics of spin origin,” *Reports on Progress in Physics* **77**, 076501 (2014).
- [156] F. Thöle, A. Keliri, and N. A. Spaldin, “Concepts from the linear magnetoelectric effect that might be useful for antiferromagnetic spintronics,” *Journal of Applied Physics* **127**, 213905 (2020).
- [157] D. Khomskii, “Classifying multiferroics: Mechanisms and effects,” *Physics* **2**, 20 (2009).
- [158] T. Kimura, T. Goto, H. Shintani, K. Ishizaka, T. Arima, and Y. Tokura, “Magnetic control of ferroelectric polarization,” *Nature* **426**, 55–58 (2003).
- [159] M. Mostovoy, “Ferroelectricity in Spiral Magnets,” *Physical Review Letters* **96**, 067601 (2006).
- [160] A. Bolens, “Theory of electronic magnetoelectric coupling in d 5 Mott insulators,” *Physical Review B* **98**, 125135 (2018).
- [161] H. Katsura, N. Nagaosa, and A. V. Balatsky, “Spin Current and Magnetoelectric Effect in Noncollinear Magnets,” *Physical Review Letters* **95**, 057205 (2005).
- [162] T. Moriya, “Theory of Absorption and Scattering of Light by Magnetic Crystals,” *Journal of Applied Physics* **39**, 1042–1049 (1968).
- [163] A. Pimenov, A. A. Mukhin, V. Y. Ivanov, V. D. Travkin, A. M. Balbashov, and A. Loidl, “Possible evidence for electromagnons in multiferroic manganites,” *Nature Physics* **2**, 97–100 (2006).
- [164] A. Mook, B. Göbel, J. Henk, and I. Mertig, “Taking an electron-magnon duality shortcut from electron to magnon transport,” *Physical Review B* **97**, 140401 (2018).
- [165] R. Valdés Aguilar, M. Mostovoy, A. B. Sushkov, C. L. Zhang, Y. J. Choi, S.-W. Cheong, and H. D. Drew, “Origin of Electromagnon Excitations in Multiferroic $RMnO_3$,” *Physical Review Letters* **102**, 047203 (2009).
- [166] S. Miyahara and N. Furukawa, “Theory of electric field induced one-magnon resonance in cycloidal spin magnets,” (2008).
- [167] I. A. Sergienko and E. Dagotto, “Role of the Dzyaloshinskii-Moriya interaction in multiferroic perovskites,” *Physical Review B* **73**, 094434 (2006).
- [168] M. Kenzelmann, A. B. Harris, S. Jonas, C. Broholm, J. Schefer, S. B. Kim, C. L. Zhang, S.-W. Cheong, O. P. Vajk, and J. W. Lynn, “Magnetic Inversion Symmetry Breaking and Ferroelectricity in $TbMnO_3$,” *Physical Review Letters* **95**, 087206 (2005).
- [169] M. Seemann, D. Ködderitzsch, S. Wimmer, and H. Ebert, “Symmetry-imposed shape of linear response tensors,” *Physical Review B* **92**, 155138 (2015).
- [170] H. Liu, J. Chaloupka, and G. Khaliullin, “Kitaev Spin Liquid in 3d Transition Metal Compounds,” *Physical Review Letters* **125**, 047201 (2020).
- [171] E. Lefrançois, M. Songvilay, J. Robert, G. Nataf, E. Jordan, L. Chaix, C. V. Colin, P. Lejay, A. Hadj-Azzem, R. Ballou, and V. Simonet, “Magnetic properties of the honeycomb oxide $Na_2Co_2TeO_6$,” *Physical Review B* **94**, 214416 (2016).

- [172] T. Thonhauser, “Theory of orbital magnetization in solids,” [International Journal of Modern Physics B](#) **25**, 1429–1458 (2011).

ACKNOWLEDGEMENT

I would like to express my deep gratitude toward all the people that have accompanied me during the last few years. Firstly, I thank my colleagues, collaborators, mentors, and proofreaders for their scientific support and for enriching my time as a PhD student.

I would like to extend special thanks to Prof. Dr. INGRID MERTIG. Thanks to her recommendation, I dedicated my bachelor thesis the research field of magnonics. Since then, her support enabled me to continuously pursue my research, ultimately leading to this PhD thesis. In addition to her scientific support, which included frequent open and inspiring discussions, her personal and professional support has been invaluable. I appreciate her motivating interest in my work and professional future, and I am grateful for all the opportunities she has provided me.

Furthermore, I am particularly grateful to Dr. ALEXANDER MOOK. Scientifically, I have learned much from him, and I still highly benefit from our discussions. Beyond the scientific aspects, the collaboration with him is motivating, inspiring, and enjoyable on a personal level.

Abschließend möchte ich meiner Familie und meinen Freunden meinen tiefen Dank aussprechen. Ihr Rückhalt und die Art und Weise, wie sie mein persönliches Leben bereichern, sind für mich von unschätzbarem Wert.

CURRICULUM VITAE

Personal Information

Name Robin Richard Neumann
Gender Male
Nationality German

Education

since Feb 2022 Member of Max Planck Graduate Center for Quantum Materials
since Aug 2021 Member of International Max Planck Research School for Science and Technology of Nano-Systems
since Oct 2020 **PhD studies**, *Martin Luther University, Halle*
Supervisor: Prof. Dr. Ingrid Mertig
2018 – 2020 **Master of Science in Physics**, *Martin Luther University, Halle*
Master thesis: “Orbital Magnetic Moment of Magnons”
Final grade: 1.0
2015 – 2018 **Bachelor of Science in Physics**, *Martin Luther University, Halle*
Bachelor thesis: “Spintransport in isolierenden, nichtkollinearen Antiferromagneten”
Final grade: 1.0
2007 – 2015 **Grammar school**, *Christian-Wolff-Gymnasium, Halle*
Final grade: 1.0
2006 – 2007 **Elementary school**, *Heideschule, Halle*
2003 – 2006 **Elementary school**, *Glauchaschule, Halle*

Academic Career

since May 2018 Research assistant, Institute of Physics, Martin Luther University
2017 – 2018 Student assistant, Institute of Physics, Martin Luther University

EIDESSTATTLICHE ERKLÄRUNG

Hiermit erkläre ich, Robin Richard Neumann, dass ich die vorliegende Arbeit selbstständig und ohne fremde Hilfe verfasst, keine anderen als die von mir angegebenen Quellen und Hilfsmittel verwendet und die wörtlich oder inhaltlich entnommenen Stellen aus benutzten Werken als solche kenntlich gemacht habe. Weiterhin erkläre ich, keine früheren vergeblichen Versuche zur Erlangung des Doktorgrades unternommen und diese Arbeit weder in der gegenwärtigen noch in einer anderen Fassung einer anderen Fakultät vorgelegt zu haben. Gegen mich sind weder Vorstrafen verhängt worden, noch sind gegen mich Ermittlungsverfahren anhängig.

Halle (Saale), den 18. November 2024
Robin Richard Neumann